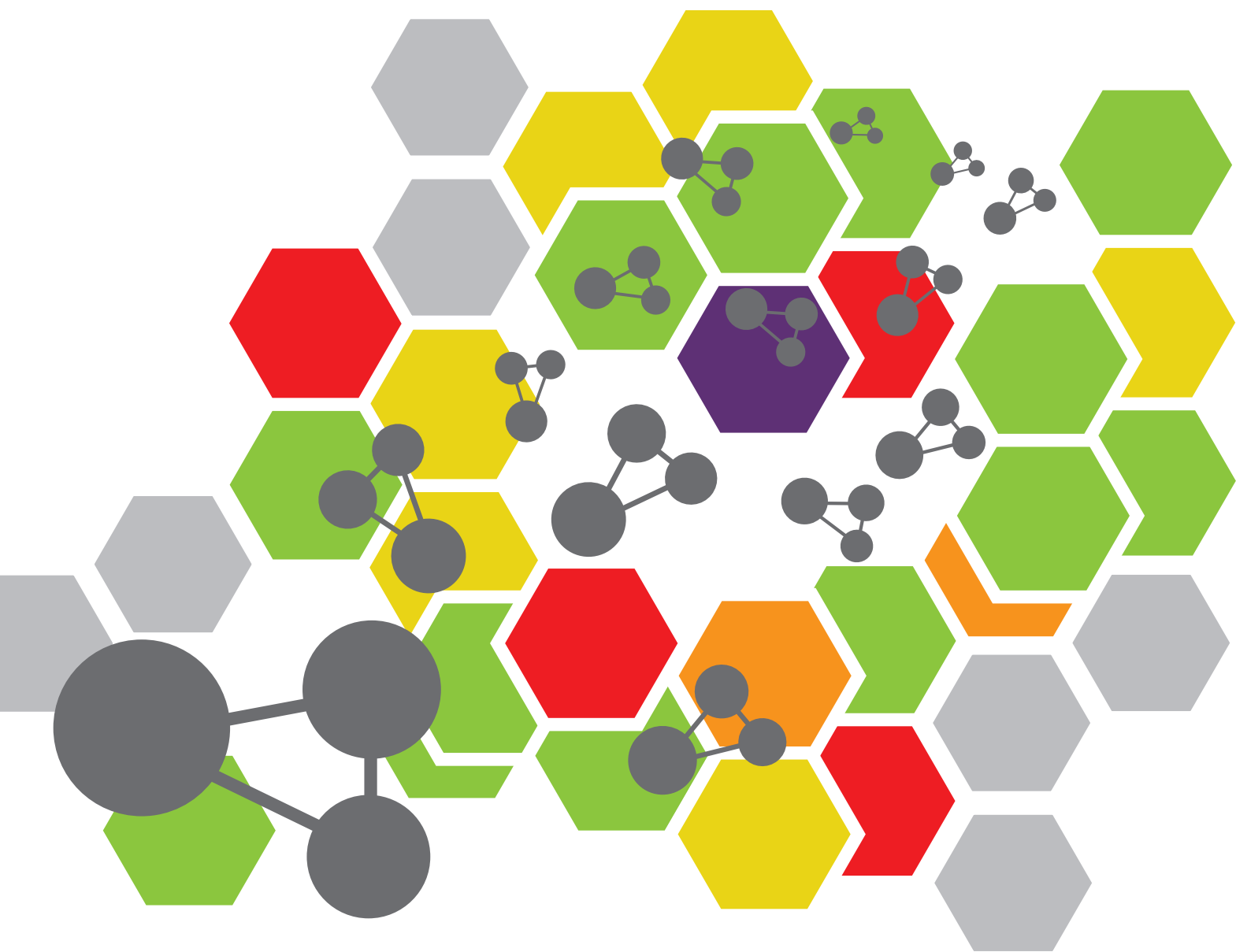# ADVANCED SELF-ASSEMBLED MATERIALS WITH PROGRAMMABLE FUNCTIONS

EDITED BY: Huacheng Zhang, Isurika R. Fernando, Jie Han,
Truc Kim Nguyen and Jingbo Louise Liu

frontiers Research Topics

About Frontiers

Frontiers is more than just an open-access publisher of scholarly articles: it is a pioneering approach to the world of academia, radically improving the way scholarly research is managed. The grand vision of Frontiers is a world where all people have an equal opportunity to seek, share and generate knowledge. Frontiers provides immediate and permanent online open access to all its publications, but this alone is not enough to realize our grand goals.

Frontiers Journal Series

The Frontiers Journal Series is a multi-tier and interdisciplinary set of open-access, online journals, promising a paradigm shift from the current review, selection and dissemination processes in academic publishing. All Frontiers journals are driven by researchers for researchers; therefore, they constitute a service to the scholarly community. At the same time, the Frontiers Journal Series operates on a revolutionary invention, the tiered publishing system, initially addressing specific communities of scholars, and gradually climbing up to broader public understanding, thus serving the interests of the lay society, too.

Dedication to Quality

Each Frontiers article is a landmark of the highest quality, thanks to genuinely collaborative interactions between authors and review editors, who include some of the world's best academicians. Research must be certified by peers before entering a stream of knowledge that may eventually reach the public - and shape society; therefore, Frontiers only applies the most rigorous and unbiased reviews.
Frontiers revolutionizes research publishing by freely delivering the most outstanding research, evaluated with no bias from both the academic and social point of view. By applying the most advanced information technologies, Frontiers is catapulting scholarly publishing into a new generation.

What are Frontiers Research Topics?

Frontiers Research Topics are very popular trademarks of the Frontiers Journals Series: they are collections of at least ten articles, all centered on a particular subject. With their unique mix of varied contributions from Original Research to Review Articles, Frontiers Research Topics unify the most influential researchers, the latest key findings and historical advances in a hot research area! Find out more on how to host your own Frontiers Research Topic or contribute to one as an author by contacting the Frontiers Editorial Office: frontiersin.org/about/contact

ADVANCED SELF-ASSEMBLED MATERIALS WITH PROGRAMMABLE FUNCTIONS

Topic Editors:
Huacheng Zhang, Xi'an Jiaotong University, China
Isurika R. Fernando, University of Sri Jayewardenepura, Sri Lanka
Jie Han, Nankai University, China
Truc Kim Nguyen, The Ohio State University, United States
Jingbo Louise Liu, Texas A&M University Kingsville, United States

Table of Contents

Editorial: Advanced Self-assembled Materials with Programmable Functions

Huacheng Zhang[1]*, Isurika R. Fernando[2], Jie Han[3], Kim Truc Nguyen[4] and Jingbo Louise Liu[5,6]

[1]School of Chemical Engineering and Technology, Xi'an Jiaotong University, Xi'an, China, [2]Department of Chemistry, Faculty of Applied Sciences, University of Sri Jayewardenepura, Nugegoda, Sri Lanka, [3]Key Laboratory of Advanced Energy Materials Chemistry (Ministry of Education), College of Chemistry, Nankai University, Tianjin, China, [4]William G. Lowrie Department of Chemical and Biomolecular Engineering, The Ohio State University, Columbus, OH, United States, [5]Department of Chemistry, Texas A&M University-Kingsville, Kingsville, TX, United States, [6]Texas A&M Energy Institute, College Station, TX, United States

Editorial on the Research Topic

Advanced Self-assembled Materials with Programmable Functions

The process of self-assembly—where building units of a system organize into an ordered and/or functional structure via the internal arrangement of molecules—has attracted researchers from a broad range of disciplines which varies from chemistry and material science to engineering and technology. Over the last two decades, the new knowledge generated through the concept of "self-assembly" based fundamental research has opened up the doors for potential applications in engineering (Cao et al., 2021). In particular, this novel and inspiring methodological strategy of fabricating functional materials via self-assembly provides more opportunities for acquiring and optimizing the desired morphological and physicochemical properties of a material through proper design and synthesis of molecular building blocks. Thus, amalgamating the chemistry of self-assembly along with materials science will lead to the efficient fabrication of innovative materials with programmable functions.

Scientists involved in "self-assembly" related research not only focus on extending a significant fundamental study, but also target on solving practical issues in applied engineering during the development of advanced materials (Wang et al., 2019). The current research topic entitled as "Advanced Self-assembled Materials with Programmable Functions" embraced related but diverse research disciplines and areas such as organic chemistry, inorganic chemistry, supramolecular chemistry polymer chemistry, coordination chemistry, colloid and surface chemistry, biomaterials, environmental science, nanotechnology, nano-science, as well as functional materials science.

In fact, supramolecular chemistry was originated from mimicking of nature, especially some particular biological phenomena and catalytic studies (Zhang et al., 2020). In this research topic, Dang et al. provided an interesting view on protein dimerization with molecular approaches, and discussed opportunities for supramolecular chemistry in depth. Furthermore, Zhu et al. recently carried out the research of G-motif construction and chirality in deoxyguanosine monophosphate nucleotide complexes, revealing that supramolecular crystals overcomes the inherent limitations of self-assembly. In addition, Liu et al. employed the man-made active catalysts with Pd(0) and phosphine-based bulky ligand to synthesize the thiophene-containing conjugated polymers. Supramolecular interactions utilized in these researches including π–π stacking, charge transfer interactions, and metal-ion coordination driven self-assembly render novel mechanisms and efficient

strategies to create materials whose properties could not be obtained only by using conventional covalent bonds. Here, Kong et al. investigated diverse driving forces such as hydrogen bonding and covalent bonding with tannic acid as the natural cross-linker for catalyst-free silicone elastomers. Additionally, those non-covalent driving forces were further employed in the potential application to biomedicines, for example, Abbasi et al. utilized the strong capacity of RNA aptamer B40t77 in specifically binding gp-120, and reported the liquid crystal based binding assay for detecting HIV-1 surface glycoprotein. Interestingly, these supramolecular interactions could further pave the way for preparing other advanced supramolecular architectures, such as mechanically interlocked molecules.

In particular, during the study of supramolecular interactions, scientists like to use the term "host" and "guest" to classify different roles among those valuable species. In this research topic, Sun et al. utilized traditional macrocyclic molecules to fabricate interesting calix[4]crown-based 1,3,4-oxadiazole, and further explored the possible application to fluorescent chemosensor for Cu(II) ion detections. Meanwhile, Huang and Tan. recently investigated the host-guest interactions between metal-organic frameworks and air-sensitive complex at high temperature. In fact, the concept of host-guest chemistry was not limited only in "organic" and "polymeric" substances, and a lot of "inorganic" materials could also fall under the concept of host and guest species (Li et al., 2020). Here, Sun et al. introduced microwave-assisted solvothermal method for preparing MoO_2 nanospheres, which played a role as host material for the detection of H_2S guest in wide concentration range at low temperature. In addition, Zhang et al. found that the general industrial by-product fluid catalytic cracking catalyst could be recycled as raw material, such as host species, for solidification of

heavy metals, and guest species, for prevention of groundwater pollution caused by inadequate disposal.

Moreover, self-assembly could be used to control morphology and dimensions of thus obtained materials from the one dimensional (1D), two dimensional (2D), and three dimensional (3D) nanoscale, as well as make those materials programmable and reversible based on internal/external stimuli and by selectively introducing diverse functional groups (Fernando et al., 2015). In this research topic, Zhou et al. found that building blocks, especially efficient nitrogen-donors, could be used for building multifunctional 3D supramolecular co-coordination polymeric materials, which exhibited interesting applications in CO_2 adsorption, antibacterial activity, as well as selective sensing of Fe(III)/Cr(III) ions and 2,4,6-trinitrophenol. Further, the reversible modifying method and diverse functional groups could assist in achieving different geometries/topologies of materials, leading to the construction of multi-dimensional smart materials. Here, Shinmori et al. studied porphyrin photoabsorption and fluorescence variation by adsorptive loading on gold nanoparticles. In addition, Dong et al. prepared self-assembled particle systems, and further carried out experimental investigations on profile control in Fuyu oilfield. Finally, advanced self-assembled materials with programmable functions could balance morphologies and physiochemical properties, and have wide prospective applications in crystals and chirality, chemosensors, biosensors, absorption of pollutants in air and ground water as environmental protection materials, biomaterials, and optical materials.

AUTHOR CONTRIBUTIONS

HZ wrote the draft of this Editorial article. All authors have provided corrections and suggestions on the article.

REFERENCES

Cao, S., Zhang, H., Zhao, Y., and Zhao, Y. (2021). Pillararene/Calixarene-based Systems for Battery and Supercapacitor Applications. *eScience* 1 (1), 28–43. doi:10.1016/j.esci.2021.10.001

Fernando, I. R., Ferris, D. P., Frasconi, M., Malin, D., Strekalova, E., Yilmaz, M. D., et al. (2015). Esterase- and pH-Responsive Poly(β-Amino Ester)-capped Mesoporous Silica Nanoparticles for Drug Delivery. *Nanoscale* 7, 7178–7183. doi:10.1039/C4NR07443B

Li, C., Hu, R., Lu, X., Bashir, S., and Liu, J. L. (2020). Efficiency Enhancement of Photocatalytic Degradation of Tetracycline using Reduced Graphene Oxide Coordinated Titania Nanoplatelet. *Catal. Today* 350, 171–183. doi:10.1016/j.cattod.2019.06.038

Wang, R., Zhang, Q., Zhang, Y., Shi, H., Nguyen, K. T., and Zhou, X. (2019). Unconventional Split Aptamers Cleaved at Functionally Essential Sites Preserve Biorecognition Capability. *Anal. Chem.* 91 (24), 15811–15817. doi:10.1021/acs.analchem.9b04115

Zhang, J., Hao, J., Huang, Z., Han, J., and He, Z. (2020). PIII-mediated Intramolecular Cyclopropanation and Metal-free Synthesis of Cyclopropane-

Fused Heterocycles. *Chem. Commun.* 56, 10251–10254. doi:10.1039/D0CC04086J

Liquid Crystal Based Binding Assay for Detecting HIV-1 Surface Glycoprotein

Amna Didar Abbasi[1], Zakir Hussain[1]*, Usman Liaqat[1], Dooa Arif[1] and Kun-Lin Yang[2]

[1] Department of Materials Engineering, School of Chemical and Materials Engineering, National University of Sciences and Technology, Islamabad, Pakistan, [2] Department of Chemical and Biomolecular Engineering, National University of Singapore, Singapore, Singapore

Surface protein gp-120 of HIV-1 virus plays an important role in the infection of HIV-1, but detection of gp-120 during the early stage of infection is very difficult. Herein, we report a binding bioassay based on an RNA aptamer B40t77, which binds specifically to gp-120. The bioassay is built upon a hydrophobic glass slide with surface immobilized gp-120. When the glass surface is incubated in a solution containing B40t77, the aptamer is able to bind to gp-120 specifically and remove it from the surface after a short incubation time of 30 min. The result of the binding event can be amplified by using liquid crystal (LC) into optical signals in the final step. By using this bioassay, we are able to detect as low as 1 μg/ml of gp-120 with high specificity within 30 min. No response is obtained when gp-120 is replaced by other protein such as bovine serum albumin (BSA). This is the first qualitative bioassay which provides a simple way for the detection of gp-120 with the naked eye. The assay is robust, low-cost and does not require additional labeling. Thus, the bioassay is potentially useful for the early detection of HIV-1 in resources-limited regions.

Keywords: liquid crystals, aptamer, gp-120, binding assay, PDMS

INTRODUCTION

Gp-120 is a surface glycoprotein of HIV-1 virion. It plays a central role in early immune dysfunction which is a characteristic of HIV-1 infection (Rychert et al., 2010). It is able to recognize and interact with specific receptors (e.g., CD4 in combination with either CCR5 or CXCR4) present on target cells (Wyatt and Sodroski, 1998; Banerjee and Mukhopadhyay, 2016). Therefore, targeting this step of gp-120 and CD4 interaction is very critical for diagnosis, inhibition and therapeutics of HIV-1 (Galdiero et al., 2011). Even though antibody-based immunoassays have been widely used in the detection of HIV-1, they do not allow early detection of HIV-1 due to low levels of antibodies present in the early stage of HIV-1 infection (Jangam et al., 2013). Detection HIV-1 infection in the so-called "window period" requires an analytical method that does not rely on antibodies (Branson and Stekler, 2012). Although there are molecular techniques that are readily available for the detection of gp-120, such as enzyme linked immunoassay (ELISA) (Rychert et al., 2010) and western blotting (Lee et al., 2000). However, these methods are very time-consuming, costly and require additional labeling, experienced personnel and well-equipped laboratories (Tsang et al., 2018). Therefore, there is a need to develop a new analytical method which is sensitive, simple, label-free and economical for the detection of gp-120.

Recently, aptamers have been exploited as molecular probes in various types of bioassays due to their high specificity, low cost, thermal stability, and ease of modification (Huang et al., 2015; Wen et al., 2015; Rahimizadeh et al., 2017). Aptamers are synthetic single-strand oligonucleotides (DNA or RNA) which bind to specific target molecules with high affinity (Robertson and Joyce, 1990; Tuerk and Gold, 1990). Because of their properties, aptamers can replace antibodies in various bioassays. For the diagnosis of HIV-1, aptamers are able to detect both early (viral genes and gp-120 protein) and late (antibodies) infection markers (Wandtke et al., 2015). In the literature, Dey et al. in 2005 isolated and characterized two anti-gp-120 RNA aptamers B40 and B40t77. Both of them are able to neutralize R5 strain of HIV-1 by binding specifically to its surface gp-120 (Dey et al., 2005). Recently, John et al. in 2014 presented an electrochemical biosensor based on 4 poly(propylene imine) dendrimer/streptavidin platform for immobilization of B40 aptamer to detect gp-120 (John et al., 2014). However, B40 is susceptible to nucleases and that caused some reliability issues. In contrast, B40t77 (77 nucleotide-long, the truncated form of B40) is resistant to nuclease because its 2' position of nucleobases is substituted by fluoro, amino or O-methyl groups (Osborne and Ellington, 1997; Dey et al., 2005). Despite of its short length, it is able to neutralize infectivity of HIV-1 R5 strains by binding specifically to its surface gp-120 and blocking viral entry (Dey et al., 2005). However, B40t77 has not been used for the development of a bioassay for gp-120 so far, because it was created for the purpose of HIV-1 therapeutics initially. In this study, we chose B40t77 as a molecular probe to develop a bioassay for detecting gp-120.

In traditional bioassays, detection signal was amplified by using fluorescence or enzyme-linked antibodies. However, these approaches require labeling of biomolecules with additional probes (fluorophores or enzymes). Recently, liquid crystals received much attention due to their unique optical properties and long-range orientational orders (Li et al., 2014; Hussain et al., 2016; Kim et al., 2018). Many research groups have exploited orientational response of liquid crystal to surface-bound biomolecules as a mechanism to develop various bioassays and biosensors which enable naked eye detection. In the literature, it has been reported that the orientational response of liquid crystal can be amplified by an intrinsic cooperative behavior associated with long-range interactions. The orientational response of liquid crystal also produces optical readouts which are visible to the naked eye under crossed polarizers. Thus, LC-based biosensors eliminate the need of labeling, amplification, and expensive instrumentation (Hussain et al., 2016). It can be used as a portable biosensor in resource-limited regions. Previously, there are many reports of LC-based biosensors for the detection of bacteria (Xu et al., 2010; Zafiu et al., 2016), viruses (Han et al., 2014), enzymes (Hu and Jang, 2012), proteins (Xue and Yang, 2008; Alino et al., 2012; Kim et al., 2018; Kim and Jang, 2019), organophosphate (Yang, 2005), DNA (Yang, 2005; Price and Schwartz, 2008; Chen and Yang, 2010), and glucose (Zhong and Jang, 2014) etc., but it has not been used for the detection of gp-120 due to the lack of specific molecular probes.

In this paper, we aim to combine liquid crystal and the molecular probe B40t77 to develop a bioassay which is suitable for the detection of gp-120. The bioassay consists of a hydrophobic glass slide, which allows non-specific adsorption of gp-120 on the surface. Liquid crystal is applied to the surface to report the spatial distribution of gp-120 on the surface. In an event that the glass surface is incubated in a solution containing B40t77 aptamer, we hypothesize that the aptamer is able to bind to gp-120 and remove it from the surface. The binding event can be probed by using LC after the incubation step. Recently, integration of biosensing platforms into lab-on-a-chip systems by introducing microfluidics has been an increasing interest (Haeberle and Zengerle, 2007). As previously reported, microfluidic based bioassays have attracted a lot of attention due to their high sensitivity, fast response and short assay time due to their large surface-to-volume ratios (Sia and Whitesides, 2003). In this study, we also aimed to combine the bioassay with a microfluidic device to shorten the response time of the bioassay. This is the first report showing the application of LC and aptamers combined together for the detection of gp-120 and potentially for the early detection of HIV-1.

EXPERIMENTAL SECTION

Materials

N, N-dimethyl-n-octadecyl-3aminopropyltrimethoxy-silylchloride (DMOAP), bovine serum albumin (BSA), RNase free water, RNase ZAP and magnesium chloride were purchased from Sigma Aldrich (Singapore) and used as received. Microscopic glass slides were obtained from Merienfield (Germany). Liquid crystal 4-cyano-4-pentylbiphenyl (5CB) was purchased from Merck (Japan). Tris EDTA ($1\times$TE, pH 8) and PBS buffer ($10\times$, pH 7.4) were purchased from 1st BASE (Singapore). TEM grids (copper, 100 parallel lines) were obtained from Electron Microscopy Sciences (U.S.A). Sylgard 184 (PDMS monomer and curing agent) was purchased from Dow Corning (U.S.A). Decon-90 was purchased from VWR (Singapore). Mylar transparency mask was purchased from Infinite Graphics (Singapore). Silicon tubing (ID $0.031\times$ OD 0.094 inches) was purchased from Cole Parmer (U.S.A). Protein gp-120 was purchased from Abcam (U.K.). 2-fluoro pyrimidine substituted 77 nucleotides long B40t77 RNA aptamer was custom synthesized by Gene Link (U.S.A). Apt 8 (anti-IgG Aptamer) was purchased from IDT (Singapore). Aptamer stock solution was prepared by dissolving B40t77 in RNase-free water at room temperature and diluted by using TE buffer with 100 mM of magnesium chloride. Prior to use, the aptamer solution was heated to 95°C for 3 min, cooled at room temperature for 5 min and then cooled on ice to ensure correct spatial folding of the aptamer. All buffer solutions were prepared in 0.2 μm filtered milli Q water.

Chemical Modification of Glass Slides

Glass slides were first rinsed with deionized water two times and then immersed in a 5% (v/v) Decon-90 solution overnight. Then, the glass slides were cleaned ultrasonically in deionized water for 15 min and rinsed with copious amount of deionized water. To prepare DMOAP-coated glass slides, the cleaned glass

slides were immersed in a 0.1% (v/v) DMOAP solution for 5 min. Subsequently, the slides were rinsed with deionized water five times to remove unreacted DMOAP from the surface and then dried under a stream of compressed nitrogen gas. Finally, the immobilized DMOAP was cross-linked in a vacuum oven at 100°C for 15 min.

Immobilization of gp-120 on a DMOAP-Coated Slide

All stock and working solutions of gp-120 and BSA were prepared in 0.01 M of phosphate buffered saline (PBS, pH 7.4). Next, TEM copper grids with parallel lines were used as a template to generate parallel protein lines on DMOAP coated glass slides as shown in **Figure 1B**. The TEM copper grids were cleaned by sonication with ethanol, methanol and acetone for 15 min sequentially followed by drying in an oven at 100°C overnight.

To immobilize gp-120, a TEM copper grid was placed on a DMOAP-coated slide, and gp-120 solution with a concentration of 1 μg/ml was pipetted to cover the entire grid (∼2 μl). After 1 h of incubation in a humidified chamber, the glass slide was blown dried under a stream of nitrogen and the TEM grid was removed with the help of a micropipette. To check the specificity and cross reactivity of proposed bioassay, patterns of BSA were also prepared by following the same procedure as described for gp-120, except that the BSA concentration was 6 μg/ml.

Fabrication of Microfluidic Devices

The surface of PDMS with embossed microfluidic channels was prepared by casting Sylgard 184 on a silicon master with raised features (Width × Depth × Length/0.2 × 0.04 × 40 mm). Silicon master was fabricated by defining the channel patterns through photolithography onto a negative photoresist (SU-8).

FIGURE 1 | (A) The working principle for the detection of gp-120 by using an RNA aptamer B40t77 and LC. **(B)** Optical images of surface-immobilized gp-120 (left) and corresponding LC images (right) showing that the pattern of surface-immobilized gp-120 on the glass slide closely ensembles a TEM grid. **(C)** Top view of a microfluidic device for the proposed binding assay. The inlet of the microfluidic device was connected to a piece of silicon tubing for delivering a solution containing B40t77 at a controlled flow rate.

Microfluidic channels were then molded from PDMS using standard soft lithography techniques (Xue et al., 2009; Alino et al., 2012). In brief, silicon elastomer and curing agent were mixed in a weight ratio of 10:1 and the mixture was degassed for 60 min after pouring on silicon master to remove air bubbles. After degassing, PDMS was cured at 65°C for 4 h. Finally, the cured PDMS with micro-channels was carefully peeled off from silicon master and cut into appropriate size. Holes were punched out on the PDMS to form inlets and outlets. To clean the PDMS, it was soaked in absolute ethanol overnight, washed with deionized water and dried under a stream of nitrogen. Finally, a closed microfluidic device was prepared by binding the PDMS with a piece of DMOAP-coated slide with surface-immobilized gp-120. The microfluidic channel was carefully aligned with the immobilized gp-120 on the surface as shown in **Figure 1C**. To ensure good sealing, pressure was applied to the system for 30 s.

Removal of Surface-Immobilized gp-120

The gp-120 adsorbed glass slides in parallel patterns was incubated with different concentrations (10, 16, 20, and 40 μg/ml) of B40t77 (~2 μl) aqueous solution for 1 h at room temperature in a home-made humidified chamber to allow B40t77 to bind with adsorbed gp-120 on glass slide and subsequently pulling these proteins off the surface of glass slide. Thereafter, these slides were rinsed with filtered Milli Q water and dried under a stream of nitrogen gas. Finally, results were examined by using LC as signal reporter as depicted in working principle shown in **Figure 1A**.

LC-Based Binding Bioassay by Using Microfluidic Device and Syringe Pump

To further streamline the assay, we used microfluidic flow channel device which is connected to the syringe pump (PHD Ultra, Harvard) through silicone tubing. Fifteen microliter of aptamer solution with different concentrations was flowed through the micro-channels by using the infuse function of the syringe pump. The volume of the aptamer solution was controlled by using the withdrawal function of syringe pump. After washing the micro-channels with 2 μl of water under a continuous flow mode, the PDMS microfluidic device was peeled off from glass slide followed by blow drying of the sample glass slide under stream of compressed nitrogen gas. Finally, results of this assay were analyzed by using LC as signal reporter.

Preparation of LC Optical Cells for Imaging Protein Patterns

A piece of sample glass slide and a piece of DMOAP-coated slide were used to prepare an LC optical cell. The two glass slides were put together and separated by Mylar films (thickness ~6 μm) at both ends of the glass slides. The optical cell was secured at both ends with binder clips. Approximately 10 μl of LC was loaded into the empty space between the two glass slides by using capillary force. After 15 min, the prepared LC optical cell was analyzed by using 1x objective lens under a polarized optical microscope Nikon ECLIPSE LV100POL (Japan) in the transmission mode.

RESULTS AND DISCUSSION

Detection of Surface-Immobilized gp-120 Using LC

We first investigated whether LC can be used to detect surface-immobilized gp-120 and effect of gp-120 concentrations on the LC optical responses. In this experiment, a piece of DMOAP-coated glass slide was chosen as a platform to immobilize gp-120. In literatures, the DMOAP-coated slide has been widely used to control the orientations of LC and for immobilization of biomolecules (Naemura, 1980; Xue and Yang, 2008). To understand the effect of gp-120 on the orientations of LC, we spotted droplets of gp-120 solution (~0.5 μl) with different concentrations on the DMOAP-coated slide in an array format. After 1 h of incubation in a humidified chamber at room temperature, the slide was blown-dried and used to make an LC optical cell. Optical images of LC under crossed polarizers were shown in **Figure 2A**. It can be seen that the orientation of LC was disrupted by the surface immobilized gp-120 and gave a bright spot only when the concentration of gp-120 was 1 μg/ml or higher. In other regions without any gp-120 or in regions where the gp-120 concentration was lower than 1 μg/ml, the orientation of LC was not disrupted, as is evident by the dark color. This result suggests that the lowest concentration of gp-120 which can disrupt the orientation of LC on the DMOAP-coated slide is 1 μg/ml. Moreover, **Figure 2A** shows that the degree of disruption and brightness increased with increasing concentration of gp-120 from 1 to 10 μg/ml. In the literature, the interference color of LC can be used as a means to report concentration of an analyte (Chen and Yang, 2012). Herein, we also observed that a higher concentration (10–2 μg/ml) led to a bright color whereas a low concentration (1 μg/ml) led to a white or gray color. For comparison, we also spotted different concentrations of BSA and observed how they have disrupted the orientations of LC. **Figure 2B** shows that the lowest concentration of BSA which can disrupt LC and gave a bright signal is 6 μg/ml. When the concentration of BSA was lower than 6 μg/ml, the LC remained dark, because the surface density of BSA was too low to disrupt LC orientation. The lowest concentrations (gp-120, 1 μg/ml and BSA, 6 μg/ml) which can disrupt LC were chosen to generate parallel lines pattern of gp-120 and BSA for subsequent experiments of competitive binding bioassay.

Removal of Surface-Immobilized gp-120 by Using B40t77

Next, we investigated if the surface-immobilized gp-120 can be removed by incubating it in a B40t77 solution. Firstly, a TEM grid was used as a template to immobilize gp-120 on a DMOAP-coated glass slide. Successful immobilization of gp-120 was confirmed by using the optical image of LC as shown in **Figure 1B**. The line pattern of the surface-immobilized gp-120 resembled the shape of the TEM grid. Following the procedure, ~2 μl of a solution containing B40t77 was dispensed onto the surface to cover the immobilized gp-120 completely. After 1 h of incubation, the solution was blown dried and LC
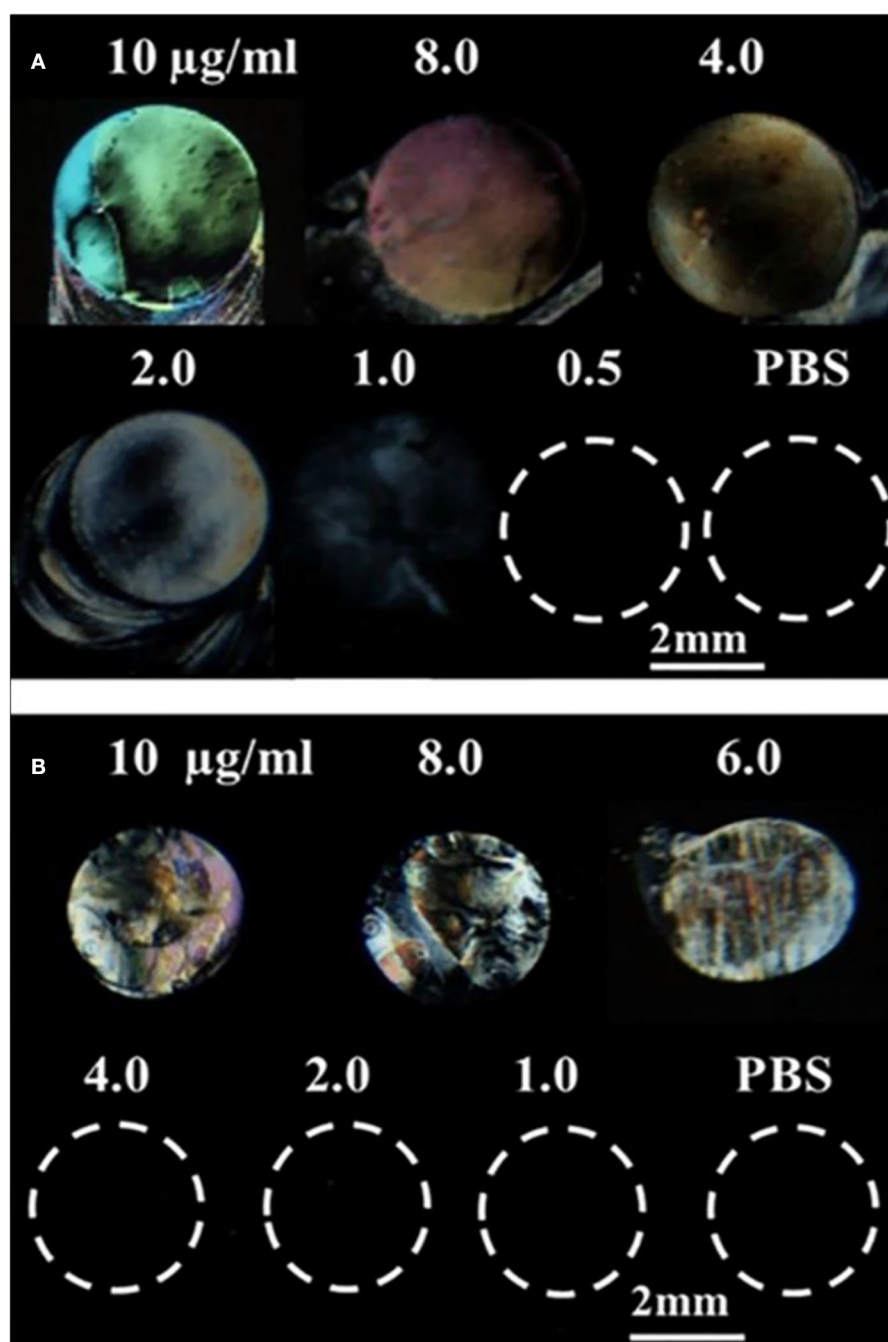
FIGURE 2 | Optical images of LCs supported on a DMOAP-coated surface immobilized with different concentrations of **(A)** gp-120 and **(B)** BSA. Number above each spot is the protein concentration (μg/ml).

was used to examine the remaining gp-120 pattern on the surface. **Figure 3A** shows that when the B40t77 concentration was 40 μg/ml, no gp-120 could be detected. This result suggests that B40t77 is able to bind to the surface-immobilized gp-120 and remove it from the surface. The result was expected because the B40t77 was specifically designed and constructed for binding gp-120 with high affinity (Dey et al., 2005). From

Figure 3A, it can also be seen that the binding event is concentration-dependent. When the concentration of B40t77 was decreased to 16 μg/ml, no gp-120 could be detected. At this condition, the amount of B40t77 was still sufficient to reduce the density of surface-bound gp-120 below the limit of detection. However, when the B40t77 concentration was further reduced to 10 μg/ml, LC gave a bright signal which can
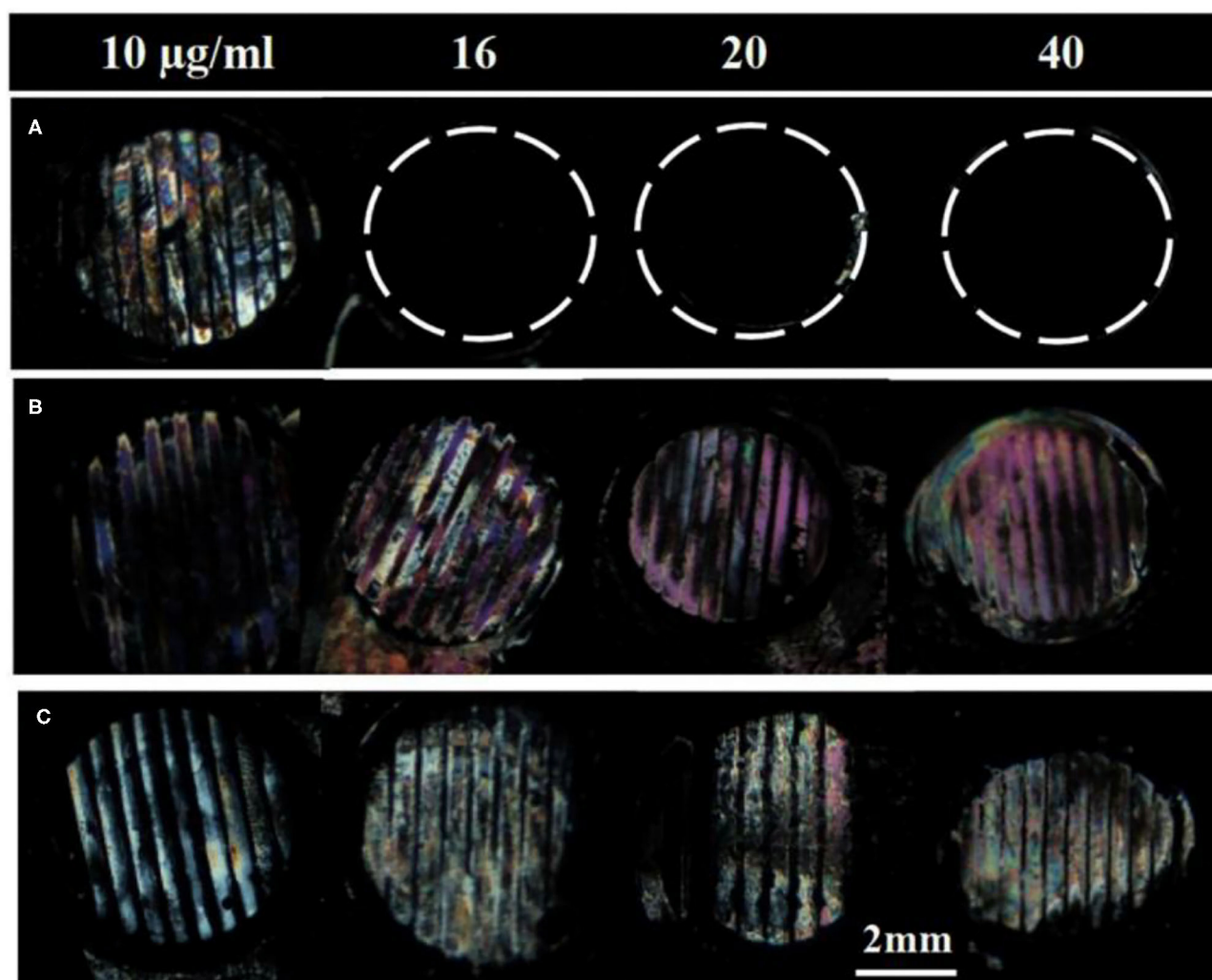
FIGURE 3 | Effect of aptamers solution concentrations on the removal of surface-immobilized **(A)** gp-120, **(B)** BSA, and **(C)** gp-120. Numbers above are concentration of Aptamer solution used in the study, B40t77 in **(A,B)** whereas Apt 8 in case of **(C)**. Optical images of LC show that surface-immobilized gp-120 can be released from the surface only when the concentration of B40t77 was 16 µg/ml or higher whereas bright images were observed in case of BSA treated with B40t77and gp-120 treated with Apt 8 instead of B40t77.
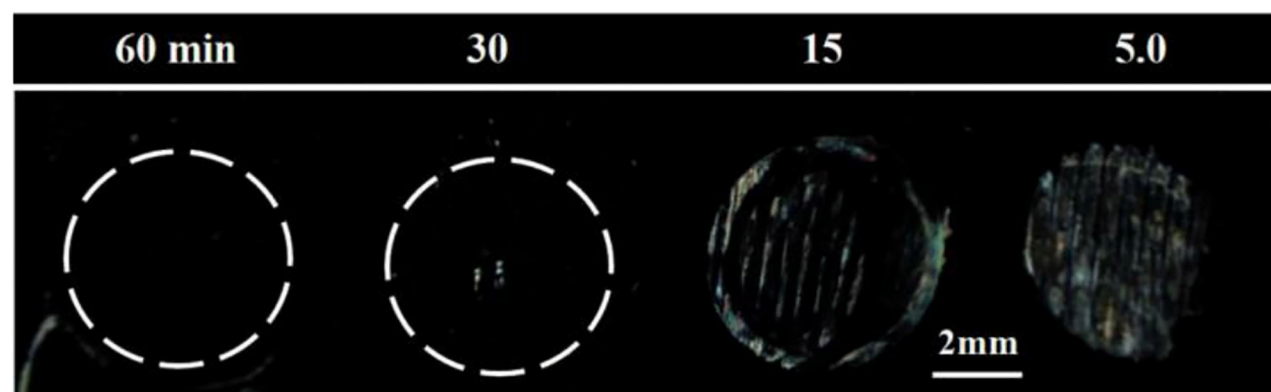
FIGURE 4 | Effect of incubation time on removal of surface-immobilized gp-120. Optical images of LC supported on DMOAP coated glass slide decorated with gp-120 patterns after incubation in a B40t77 solution (16 µg/ml) for different incubation times (60, 30, 15, and 5 min).

be easily distinguished from the dark background. The bright signal was caused by gp-120 which remained on the surface. Thus, it was proposed that 16 μg/ml is the minimal B40t77 concentration which is needed to clear surface-immobilized gp-120. Whereas, in **Figure 3B**, B40t77 shows no binding for BSA, even if the B40t77 concentration was 40 μg/ml. As a result, remaining BSA on the surface was still able to disrupt the orientation of LC supported on DMOAP-coated slide and
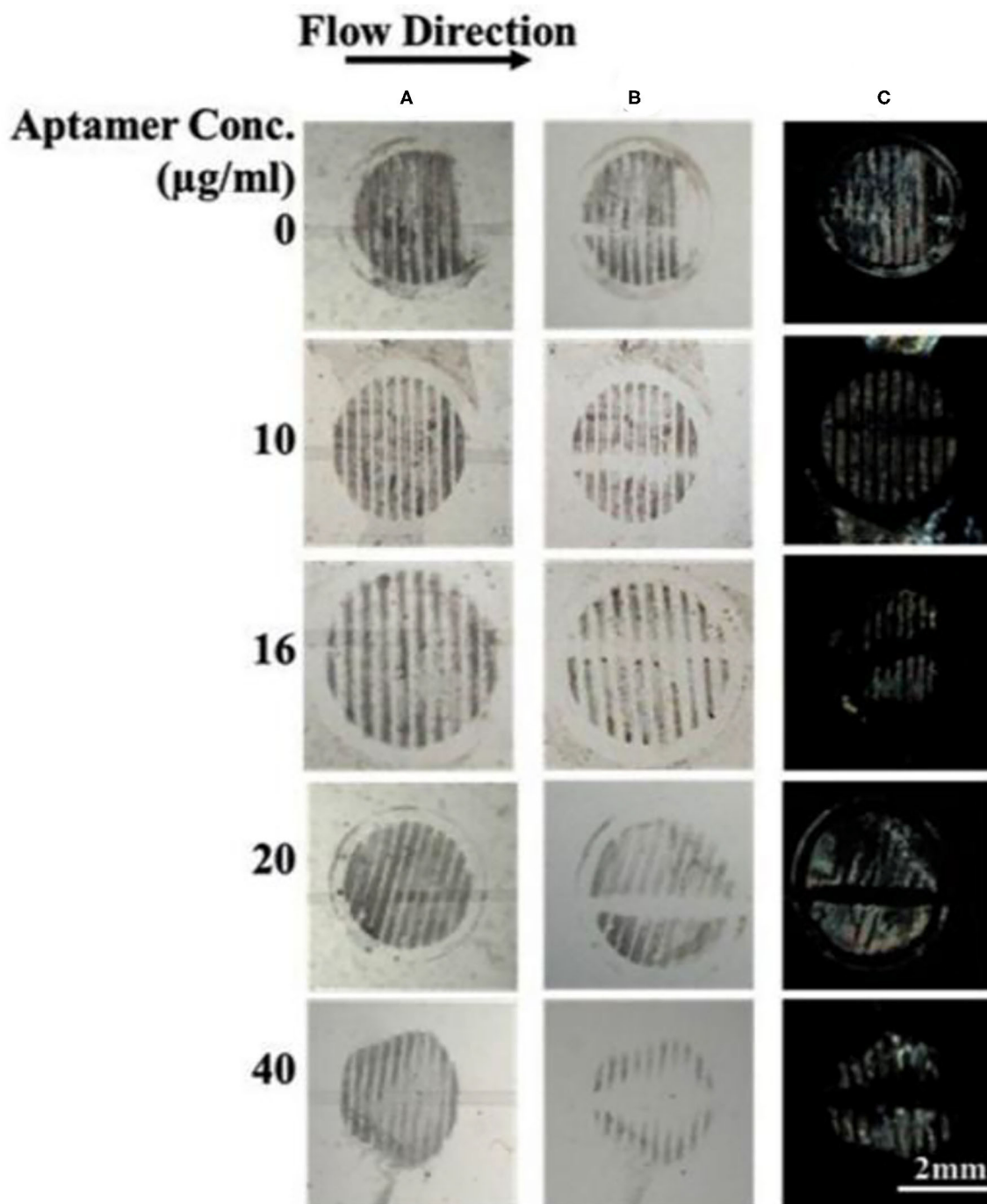
FIGURE 5 | Effect of aptamer concentration on the removal of surface-immobilized gp-120 from a DMOAP-coated surface. **(A,B)** Optical images of gp-120 patterns before and after flowing of different concentrations of B40t77 (0, 10, 16, 20, and 40 μg/ml), respectively. **(C)** Optical images of LC after the assay was completed. The flow rate was 0.5 μl/min.

gave a bright spot. To test binding specificity, we replaced the B40t77 solution with an anti-IgG aptamer (Apt 8) solution at four different concentrations. As shown in **Figure 3C**, no interaction of Apt 8 with gp-120 was found in these control experiments. LC was still disrupted by surface-bound gp-120 after the incubation.

To investigate whether the incubation time also played a role in the binding event, we varied the incubation time from 5 to 60 min while fixing the B40t77 concentration at 16 μg/ml. As shown in **Figure 4**, an incubation time of 60 min was required; otherwise, the surface-immobilized gp-120 could not be removed completely by using B40t77. A shorter incubation time led to incomplete removal of surface-immobilized gp-120, as shown in **Figure 4**.

Development of a Microfluidic Bioassay

To streamline the procedures, we further developed a binding assay for the detection of gp-120 in a microfluidic device. Firstly, gp-120 was patterned on the surface as shown in **Figure 5A**. Next, we prepared a closed microfluidic channel by aligning an open PDMS micro-channel with the surface-immobilized gp-120 pattern on a DMOAP-coated slide by physical attachment as shown in **Figure 1C**, Fifteen microliters of TE buffer containing aptamer with different concentrations (0, 10, 16, 20, and 40 μg/ml) were flowed at a constant flow rate of 0.5 μl/min through the micro-channel. The total assay time was 30 min. As shown in **Figure 5B**, surface-patterned gp-120 can be removed after the aptamer solution passed through the micro-channel. The same result can be obtained by using LC as a signal reporter as shown in **Figure 5C**. From the results, it can be concluded that aptamer concentration at 16 μg/ml or higher could lead to complete removal of surface-immobilized gp-120 from the flow path. However, when the aptamer concentration was 10 μg/ml, the surface-immobilized gp-120 could be removed only partially. Moreover, in the case of TE buffer with no aptamer, we found that the pattern of gp-120 before and after the flow remained unchanged. These results clearly showed that the removal of surface-immobilized gp-120 (1 μg/ml) was caused by binding of B40t77 and gp-120. Furthermore, the comparison of the present work with already available HIV-1 gp-120 detection methods in literature is listed in **Table 1**. Despite of the fact that the limit of detection (LoD) is not the lowest but the present biosensing technique is easy to operate, simple and requires minimal sample volume as compared to other methods e.g., ELISA.

Effect of Flow Rate

One of the advantages of using a microfluidic device to deliver B40t77 is that the flow rate can be controlled precisely by using a syringe pump. To check the effect of flow rate on the performance of the assay, we repeated the experiment by varying the flow rates from 0.1 to 1 μl/min. The total B40t77 solution volume was fixed at 15 μl and concentration used was 16 μg/ml. From **Table 2**, it is apparent that a higher flow rate leads to a decrease in the residence time (Aubin et al., 2009). As shown in **Figure 6**, when the flow rate was in the range of 0.1–0.5 μl/min, the surface-immobilized gp-120 was completely

TABLE 1 | Comparison of present work with available HIV-1 detection techniques.

Method	Matrix	LoD (ng/ml)	References
ELISA	Blood	0.5	Rychert et al., 2010
Plasmonic ELISA	Physiological buffer	10^{-8}	Cecchin et al., 2014
Microcantilever deflection	Physiological buffer	8×10^3	Lam et al., 2006
Laser-induced fluorescence detection	Physiological buffer	120	Zhou et al., 2000
LC- based binding assay	Physiological buffer	1×10^3	This work

TABLE 2 | Residence time, time to complete assay, and working outcomes of bioassay under different flow rates.

Volumetric flow rate (μl/min)	Residence time (sec)	Total assay time (min)	Assay works or not (Yes/No)
0.1	180	150	Yes
0.3	60	50	Yes
0.5	36	30	Yes
1	18	15	No

cleared by the flowing solution inside the flow path due to the interaction of B40t77 with target protein gp-120. On the other hand, flow rate was >0.5 μl/min leads to assay failure as shown in **Figure 6**, when flow rate was 1.0 μl/min; the surface-immobilized gp-120 remained on the surface. On the basis of our observation during the experiment, a higher flow rate inevitably led to solution leakage from the side of the micro-channel. Thus, the surface-immobilized gp-120 could not be removed by the aptamer solution. These results suggest that a low flow rate is better than high flow rate. However, a very low flow rate at 0.1 μl/min led to a long assay time which is also not desirable. These results, when combined, suggest that a flow rate of 0.5 μl/min is suitable for the assay.

Specificity, Stability, and Reproducibility

One of the reasons to choose B40t77 as a molecular probe for detecting gp-120 protein was the high specificity of B40t77 toward gp-120. To test the specificity, we used BSA to check cross reactivity of the proposed bioassay. All experimental conditions and procedures were same except that gp-120 was replaced by BSA. Next, solutions containing different concentrations of aptamer (10, 16, and 40 μg/ml) were flowed through the surface coated with BSA. **Figure 7** shows that the surface pattern of BSA before and after the flow of B40t77 were same, indicating that the aptamer did not interact with BSA even at the highest concentration (40 μg/ml) tested. As a result, it can be concluded that the

FIGURE 6 | Effect of flow rate on the removal of surface-immobilized gp-120 from a DMOAP-coated surface by using B40t77. **(A)** Before flowing B4077 solution. **(B)** After flowing B40t77 solution at different flow rates (0.1, 0.3, 0.5, and 1 µl/min). **(C)** Optical images of LC after the assay was completed. The B40t77 concentration used was 16 µl/ml and the sample volume was 15 µl.
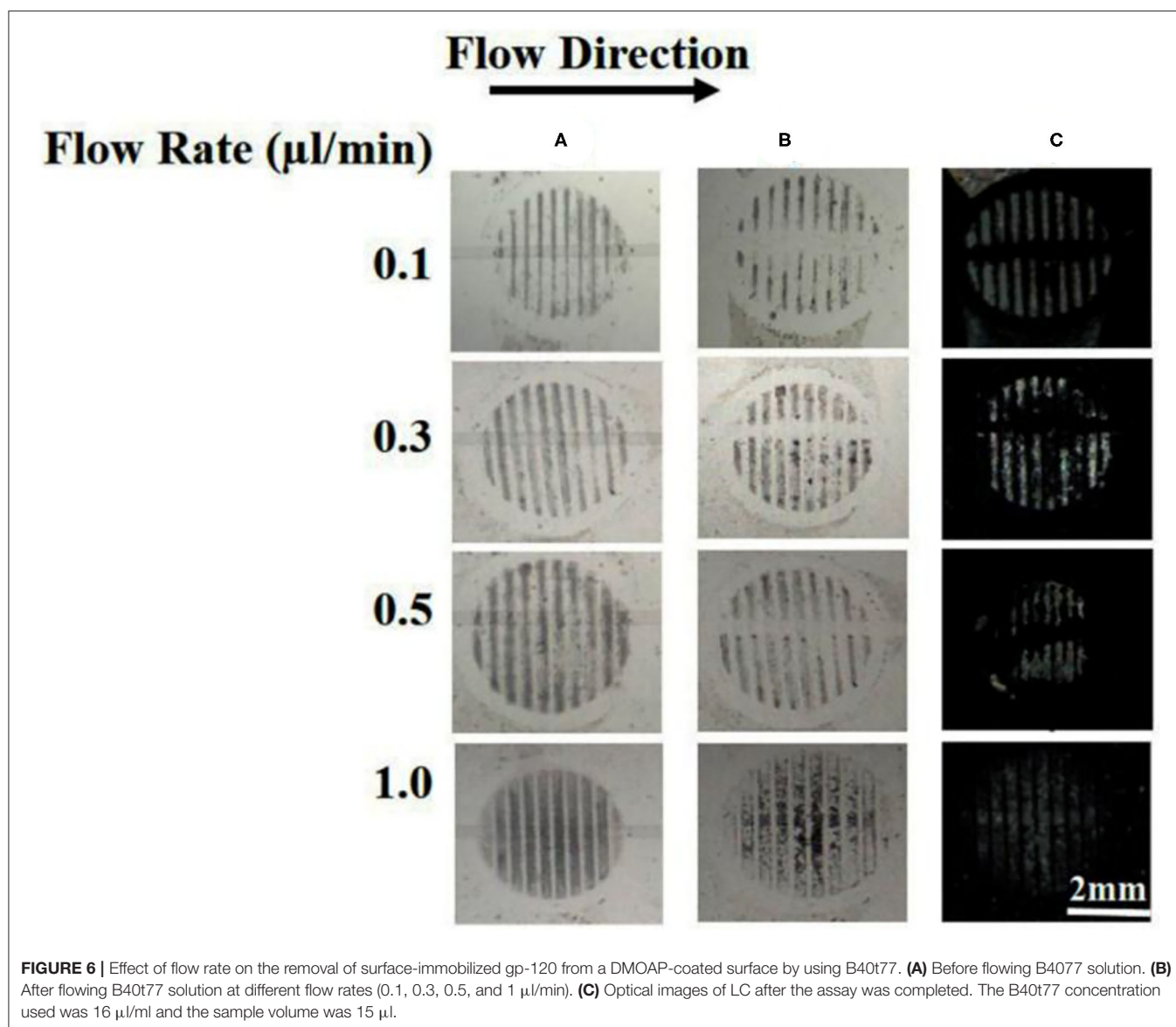
bioassay shows no cross-reactivity against other proteins such as BSA.

Due to various influencing factors, the stability and reproducibility of biosensors are worthy of research attention. In order to make our microfluidic device more stable and reproducible all the influencing factors were kept same while preparing sensor substrate. We observed that the protein pattern on our substrate remained stable for more than 2 weeks at 4°C and can be used to prepare closed microfluidic flow channel device by placing PDMS flow channels on dried glass substrate with little pressure for 30 s. Moreover, the thickness of LC film is also of keen interest, we have used mylar film (∼6 µm) while making the LC optical cell. All experiments were carried out at room temperature and

the flow rate and reaction time were also kept constant after optimization.

CONCLUSIONS

In summary, we have successfully developed a binding bioassay for gp-120 by using aptamer B40t77 as a molecular probe and liquid crystal as a signal reporter. This bioassay shows high specificity against gp-120 without any cross-reactivity with BSA. The bioassay was integrated with a microfluidic device to control the flow rate and the total assay time was 30 min. At the optimal flow rate of 0.5 µl/min, the surface-immobilized gp-120 can be released from the surface by flowing 16 µg/ml of B40t77 through binding events. For detection purposes, this
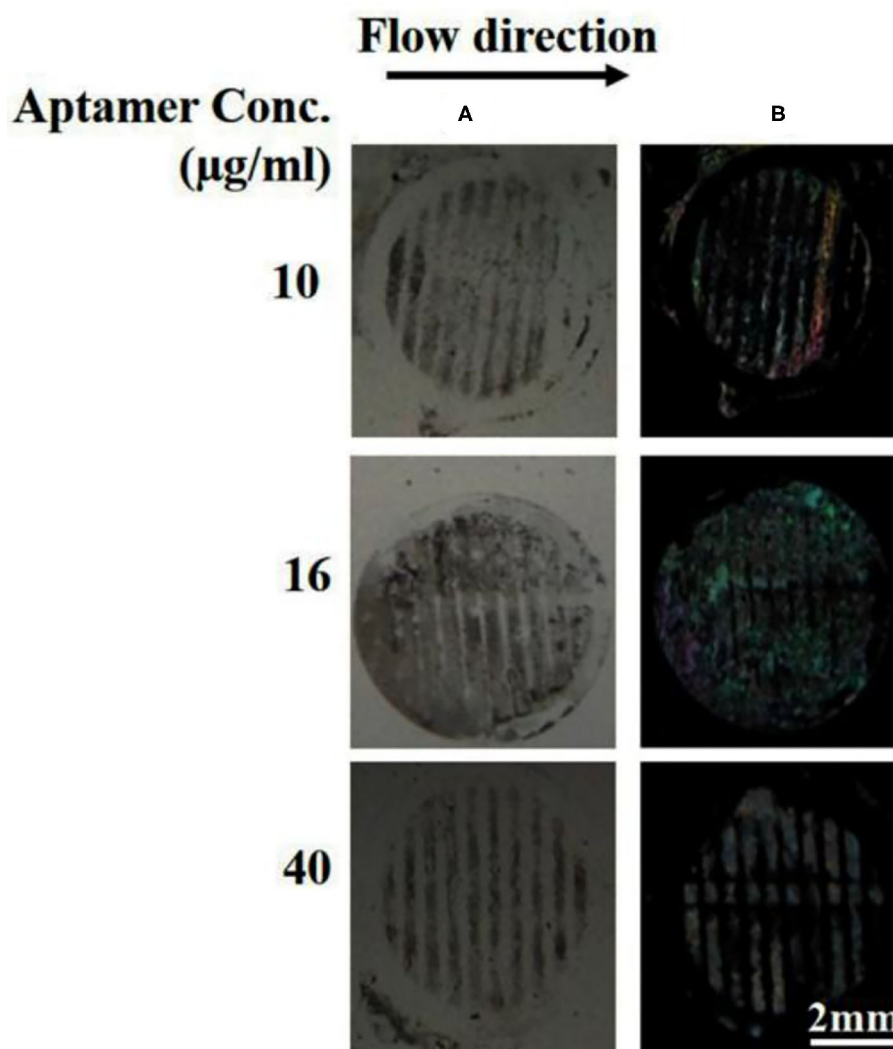
FIGURE 7 | Specificity by using BSA protein as a control experiment. **(A)** Optical image of BSA patterns after flowing different concentrations of B40t77 (10, 16, and 40 μg/ml). **(B)** Optical images of LC after the assay was completed. The flow rate was 0.5 μl/min.

event can be transduced and amplified by using liquid crystal into optical signal visible with the naked eye. The simple and low-cost microfluidic device has the potential to detect HIV-1 in early stages.

DATA AVAILABILITY STATEMENT

The original contributions presented in the study are included in the article/supplementary material, further inquiries can be directed to the corresponding author.

AUTHOR CONTRIBUTIONS

AA: experimentation, data acquisition, and write up. DA: data acquisition and manuscript preparation. UL:

data interpretation and manuscript corrections. K-LY: supervision, proof reading, and data interpretation. ZH: conceptualization, supervision, data interpretation, and proof reading. All authors contributed to the article and approved the submitted version.

FUNDING

REFERENCES

Alino, V. J., Sim, P. H., Choy, W. T., Fraser, A., and Yang, K.-L. (2012). Detecting proteins in microfluidic channels decorated with liquid crystal sensing dots. *Langmuir* 28, 17571–17577. doi: 10.1021/la303213h

Aubin, J., Prat, L., Xuereb, C., and Gourdon, C. (2009). Effect of microchannel aspect ratio on residence time distributions and the axial dispersion coefficient. *Chem. Eng. Process. Process Intensif.* 48, 554–559. doi: 10.1016/j.cep.2008.08.004

Banerjee, N., and Mukhopadhyay, S. (2016). Viral glycoproteins: biological role and application in diagnosis. *Virusdisease* 27, 1–11. doi: 10.1007/s13337-015-0293-5

Branson, B. M., and Stekler, J. D. (2012). Detection of acute HIV infection: we can't close the window. *J. Infect. Dis.* 205, 521–524. doi: 10.1093/infdis/jir793

Cecchin, D., De La Rica, R., Bain, R. E. S., Finnis, M. W., Stevens, M. M., and, G., et al. (2014). Plasmonic ELISA for the detection of gp120 at ultralow concentrations with the naked eye. *Nanoscale* 6, 9559–9562. doi: 10.1039/C3NR06167A

Chen, C.-H., and Yang, K.-L. (2010). Detection and quantification of DNA adsorbed on solid surfaces by using liquid crystals. *Langmuir* 26, 1427–1430. doi: 10.1021/la9033468

Chen, C. H., and Yang, K. L. (2012). Liquid crystal-based immunoassays for detecting hepatitis B antibody. *Anal. Biochem.* 421, 321–323. doi: 10.1016/j.ab.2011.11.007

Dey, A. K., Griffiths, C., Lea, S. M., and James, W. (2005). Structural characterization of an anti-gp120 RNA aptamer that neutralizes R5 strains of HIV-1. *RNA* 11, 873–884. doi: 10.1261/rna.7205405

Galdiero, S., Falanga, A., Vitiello, M., Cantisani, M., Marra, V., and Galdiero, M. (2011). Silver nanoparticles as potential antiviral agents. *Molecules* 16, 8894–8918. doi: 10.3390/molecules16108894

Haeberle, S., and Zengerle, R. (2007). Microfluidic platforms for lab-on-a-chip applications. *Lab Chip* 7, 1094–1110. doi: 10.1039/b706364b

Han, G.-R., Song, Y.-J., and Jang, C.-H. (2014). Label-free detection of viruses on a polymeric surface using liquid crystals. *Colloids Surf. B Biointerfaces* 116, 147–152. doi: 10.1016/j.colsurfb.2013.12.037

Hu, Q.-Z., and Jang, C.-H. (2012). Using liquid crystals for the label-free detection of catalase at aqueous–LC interfaces. *J. Biotechnol.* 157, 223–227. doi: 10.1016/j.jbiotec.2011.11.010

Huang, X., Li, Y., Huang, X., Chen, Y., and Gao, W. (2015). Combining a loop-stem aptamer sequence with methylene blue: a simple assay for thrombin detection by resonance light scattering technique. *RSC Adv.* 5, 30268–30274. doi: 10.1039/C4RA14729D

Hussain, Z., Qazi, F., Ahmed, M. I., Usman, A., Riaz, A., and Abbasi, A. D. (2016). Liquid crystals based sensing platform-technological aspects. *Biosens. Bioelectron.* 85, 110–127. doi: 10.1016/j.bios.2016.04.069

Jangam, S. R., Agarwal, A. K., Sur, K., and Kelso, D. M. (2013). A point-of-care PCR test for HIV-1 detection in resource-limited settings. *Biosens. Bioelectron.* 42, 69–75. doi: 10.1016/j.bios.2012.10.024

John, S. V., Rotherham, L. S., Khati, M., Mamba, B. B., and Arotiba, O. A. (2014). Towards HIV detection: novel poly (propylene) dendrimer-streptavidin platform for electrochemical DNA and gp-120 aptamer biosensors. *Int. J. Electrochem. Sci.* 9, 5425–5437. doi: 10.13140/2.1.2378.5606

Kim, H., An, Z., and Jang, C.-H. (2018). Label-free optical detection of thrombin using a liquid crystal-based aptasensor. *Microchem. J.* 141, 71–79. doi: 10.1016/j.microc.2018.05.010

Kim, H. J., and Jang, C.-H. (2019). Liquid crystal-based aptasensor for the detection of interferon-γ and its application in the diagnosis of tuberculosis using human blood. *Sens. Actuators B* 282, 574–579. doi: 10.1016/j.snb.2018.11.104

Lam, Y., Abu-Lail, N. I., Alam, M. S., and Zauscher, S. (2006). Using microcantilever deflection to detect HIV-1 envelope glycoprotein gp120.

Nanomed. Nanotechnol. Biol. Med. 2, 222–229. doi: 10.1016/j.nano.2006.10.002

Lee, M. K., Martin, M. A., and Cho, M. W. (2000). Higher western blot immunoreactivity of glycoprotein 120 from R5 HIV type 1 isolates compared with X4 and X4R5 isolates. *AIDS Res. Hum. Retroviruses* 16, 765–775. doi: 10.1089/088922200308765

Li, X., Tan, H., Li, Y.-L., Wu, Z.-Y., Shen, G.-L., Yu, R.-Q., et al. (2014). Aptamer-based liquid crystal biosensor for detection of platelet-derived growth factor BB. *Chinese J. Anal. Chem.* 42, 629–635. doi: 10.1016/S1872-2040(13)60729-X

Naemura, S. (1980). Polar and nonpolar contributions to liquid-crystal orientations on substrates. *J. Appl. Phys.* 51, 6149–6159. doi: 10.1063/1.327602

Osborne, S. E., and Ellington, A. D. (1997). Nucleic acid selection and the challenge of combinatorial chemistry. *Chem. Rev.* 97, 349–370. doi: 10.1021/cr960009c

Price, A. D., and Schwartz, D. K. (2008). DNA Hybridization-induced reorientation of liquid crystal anchoring at the nematic liquid crystal/aqueous interface. *J. Am. Chem. Soc.* 130, 8188–8194. doi: 10.1021/ja0774055

Rahimizadeh, K., AlShamaileh, H., Fratini, M., Chakravarthy, M., Stephen, M., Shigdar, S., et al. (2017). Development of cell-specific aptamers: recent advances and insight into the selection procedures. *Molecules* 22:2070. doi: 10.3390/molecules22122070

Robertson, D. L., and Joyce, G. F. (1990). Selection *in vitro* of an RNA enzyme that specifically cleaves single-stranded DNA. *Nature* 344, 467–468. doi: 10.1038/344467a0

Rychert, J., Strick, D., Bazner, S., Robinson, J., and Rosenberg, E. (2010). Detection of HIV gp120 in plasma during early HIV infection is associated with increased proinflammatory and immunoregulatory cytokines. *AIDS Res. Hum. Retroviruses* 26, 1139–1145. doi: 10.1089/aid.2009.0290

Sia, S. K., and Whitesides, G. M. (2003). Microfluidic devices fabricated in poly(dimethylsiloxane) for biological studies. *Electrophoresis* 24, 3563–3576. doi: 10.1002/elps.200305584

Tsang, H. F., Chan, L. W., Tong, J. C., Wong, H. T., Lai, C. K., Au, T. C., et al. (2018). Implementation and new insights in molecular diagnostics for HIV infection. *Expert Rev. Mol. Diagn.* 18, 433–441. doi: 10.1080/14737159.2018.1464393

Tuerk, C., and Gold, L. (1990). Systematic evolution of ligands by exponential enrichment: RNA ligands to bacteriophage T4 DNA polymerase. *Science (80-.)* 249, 505–510. doi: 10.1126/science.2200121

Wandtke, T., Wozniak, J., and Kopinski, P. (2015). Aptamers in diagnostics and treatment of viral infections. *Viruses* 7, 751–780. doi: 10.3390/v7020751

Wen, W., Hu, R., Bao, T., Zhang, X., and Wang, S. (2015). An insertion approach electrochemical aptasensor for mucin 1 detection based on exonuclease-assisted target recycling. *Biosens. Bioelectron.* 71, 13–17. doi: 10.1016/j.bios.2015.04.001

Wyatt, R., and Sodroski, J. (1998). The HIV-1 envelope glycoproteins: fusogens, antigens, and immunogens. *Science (80-.)* 280, 1884–1888. doi: 10.1126/science.280.5371.1884

Xu, H., Hartono, D., and Yang, K. L. (2010). Detecting and differentiating Escherichia coli strain TOP10 using optical textures of liquid crystals. *Liq. Cryst.* 37, 1269–1274. doi: 10.1080/02678292.2010.498061

Xue, C.-Y., Khan, S. A., and Yang, K.-L. (2009). Exploring optical properties of liquid crystals for developing label-free and high-throughput microfluidic immunoassays. *Adv. Mater. Weinheim* 21, 198–202. doi: 10.1002/adma.200801803

Xue, C. Y., and Yang, K. L. (2008). Dark-to-bright optical responses of liquid crystals supported on solid surfaces decorated with proteins. *Langmuir* 24, 563–567. doi: 10.1021/la7026626

Yang, K. (2005). Use of self-assembled monolayers, metal ions, and smectic liquid crystals to detect organophosphonates. *Sens. Actuators B Chem.* 104, 50–56. doi: 10.1016/j.snb.2004.04.098

Zafiu, C., Hussain, Z., Küpcü, S., Masutani, A., Kilickiran, P., and Sinner, E.-K. (2016). Liquid crystals as optical amplifiers for bacterial detection. *Biosens. Bioelectron.* 80, 161–170. doi: 10.1016/j.bios.2016.01.017

Zhong, S., and Jang, C.-H. (2014). Highly sensitive and selective glucose sensor based on ultraviolet-treated nematic liquid crystals. *Biosens. Bioelectron.* 59, 293–299. doi: 10.1016/j.bios.2014.03.070

Zhou, W., Tomer, K. B., and Khaledi, M. G. (2000). Evaluation of the binding between potential anti-HIV DNA-based drugs and viral envelope

glycoprotein gp120 by capillary electrophoresis with laser-induced fluorescence detection. *Anal. Biochem.* 284, 334–341. doi: 10.1006/abio.2000.4651

Conflict of Interest: The authors declare that the research was conducted in the absence of any commercial or financial relationships that could be construed as a potential conflict of interest.

Utilization of Spent FCC Catalyst as Fine Aggregate in Non-sintered Brick: Alkali Activation and Environmental Risk Assessment

Dandan Zhang[1], Shiping Fang[1], Hongzhe Zhang[1,2], Zhengwei Liu[1], Zhiyuan Zhang[1] and Shucai Zhang[1]*

[1] State Key Laboratory of Safety and Control for Chemicals, SINOPEC Research Institute of Safety Engineering, Qingdao, China, [2] National Registration Center for Chemicals of the State Administration of Work Safety, Qingdao, China

This study focuses on the recycling of a spent fluid catalytic cracking (FCC) catalyst to produce catalyst-based non-sintered bricks (CN-bricks) for the recovery of its aluminosilicate components and the solidification of heavy metals. The effects of the content of cement (10–20%), the proportion of FCC (10–40%), and the type of an activator ($NaOH/Na_2SiO_3/Na_2SO_4$) on the performance of a CN-brick were investigated in terms of the mechanical strength and leaching behavior. The results show that an optimal binder system of 20% cement + Na_2SO_4 could promote the compressive strength up to 42.3 MPa; the proportion of an optimal spent FCC catalyst of 20% could achieve the lowest porosity and water absorption. The microscopic mechanism of a cementitious process was analyzed by x-ray diffraction (XRD), Fourier transform infrared spectroscopy (FTIR), and scanning electron microscopy (SEM), proving that C-S-H and ettringite (AFt) are the two main hydration products of a CN-brick. Na_2SO_4 is superior to NaOH or Na_2SiO_3 as an activator since Na_2SO_4 takes advantage of the aluminum-rich property of a spent FCC catalyst and specifically promote the formation of a needle-like AFt. Quantitative environmental risk assessment for the utilization of a CN-brick on roads was carried out based on the leaching test of a toxicity characteristic leaching procedure (TCLP), NEN 7371 maximum availability test, and the hazard Index (HI) identification, and a final HI 0.0045 (<1.0) indicates an acceptable risk for environment and nearby residents as CN-bricks are utilized on roads for 30 years.

Keywords: spent FCC catalyst, reclycing, non-sintered brick, environmental risk, alkali activation

INTRODUCTION

A fluid catalytic cracking (FCC) catalyst is widely used in FCC units in petrochemical industries to convert crude oil into gasoline and other lighter fuel products, and its worldwide supply can reach 840,000 tons every year (Vogt and Weckhuysen, 2015). FCC catalysts mainly consist of a clay matrix, binder, and zeolite. Due to the accumulation of heavy metals and coke on the surface, a FCC catalyst will gradually get deactivated due to the site coverage and pore blockage (Zhang et al., 2020), and the catalysts with low catalytic activity will be discharged from a work unit. A spent FCC catalyst has been identified as a hazardous waste HW50 according to the Chinese National Directory of Hazardous Wastes (HW, 2016), due to excessive contents of heavy metals

[vanadium (V) and nickel (Ni)]. Nowadays, a main handling way of a spent FCC catalyst is landfilling, yet many factors will restrict this approach in the future, especially its economic costs brought by a land use right, and the environmental impact after a landfill leachate penetrates into the soil. Instead, a spent FCC catalyst has widely been explored as a replacement of the raw materials in the production (laboratory scale) of a cement mortar (Al-Jabri et al., 2013; Payá et al., 2013), a concrete (Neves et al., 2015), ceramics (Ramezani et al., 2017), a geopolymer (Font et al., 2017), a zeolite (Ferella et al., 2019), an asphalt (Xue et al., 2020), and a brick (Taha et al., 2012).

Brick is a widely used material in the construction industry, and its consumption can reach 23–30 million pieces annually in the USA alone (Meng et al., 2018). Most of the used bricks belonging to the "sintered brick" are made from clay and sintered at around 900°C, which consume a high amount of clay and energy and release a high level of CO_2. Therefore, many countries have enacted policies to restrict the use of sintered bricks. In this case, a non-sintered brick (NS-brick) has attracted more attention because of its environmental benefit: an NS-brick is generally conserved at room temperature and hardly consumes much energy. Pozzolanic materials such as furnace slag, fly ash, iron-ore tailing, and FCC catalyst are often utilized in the production of NS-bricks, since their silica-aluminum structure can react with $Ca(OH)_2$ to form a cementitious substance like calcium silicate hydrates (CSH) and calcium aluminate hydrates (CAH), contributing to the strength development. Dabaieh et al. (2020) proved that the replacement of sintering by an NS-brick can result in a reduction of the energy consumption of 5,305 MJ and the CO_2 emission of 5,907 kg for 1,000 bricks. Wang Y. et al. (2019) adopted an electrolytic manganese residue (EMR) to produce NS-bricks. Lang et al. (2020) mixed dredged sludge, cement, lime, fly ash, and nano-SiO_2 to produce high-strength bricks. Weishi et al. (2018) prepared an NS-brick made from iron-ore tailing and two minor additives such as triethanolamine and stearic acids. Taha et al. (2012) focuses on the recycled spent FCC catalyst to produce an NS-brick, which proved that 15% of the catalyst replacement and the addition of a cement kiln dust (CKD) can yield a higher compressive strength, showing that a spent FCC catalyst has a potential for use in road base and masonry block construction.

A spent FCC catalyst generally contains Ni and V and other heavy metals, which may pose a threat to the environment when recycled, so the kernel problem of a catalyst-based non-sintered brick (CN-brick) concerns whether their environmental risk can be acceptable when they are used on roads, embankments, and other scenarios. The study by Taha et al. (2012) have included the test of a toxicity characteristic leaching procedure (TCLP), but fails to consider in detail the extent of contaminants leached to groundwater and ingested by nearby residents through drinking water. In this study, all the processes have been considered and precisely calculated. Beyond that, the methods for improving the mechanical property of a CN-brick has not been discussed earlier. Numerous studies have included the alkali activation as an approach for the strength improvement for construction products (Guo et al., 2010; Liu et al., 2021), since an alkali environment could dissolve Si-O and Al-O from the former

structure and react with $Ca(OH)_2$ to produce more C-S-H and C-A-S-H gels. Alkali reagents such as NaOH, Na_2SiO_3, Na_2SO_4 all have the potential to improve the strength of a CN-brick to a higher level.

This study was designed to evaluate the utilization of a spent FCC catalyst to produce CN-bricks for use on roads and embankments. The content of cement, type of an activator, and proportion of FCC were explored for an optimal design. The compressive strength and flexural strength were tested to evaluate the physical and mechanical properties of CN-bricks. The solidification mechanism of cement and an activator was investigated by means of x-ray diffraction (XRD), scanning electron microscopy (SEM), and Fourier transform infrared spectroscopy (FTIR). In addition, quantitative environmental risk assessment for CN-bricks including a leaching test of heavy metals and an exposure scenario analysis was carried out.

MATERIALS AND METHODS

Sample Sources
The spent FCC catalyst sample used in this study was taken from an oil refinery in Shandong, China. X-ray fluorescence (XRF) spectrometry (**Table 1**) shows its major components, which are aluminum oxide (54.2%) and silicon dioxide (37.1%), and the sum of these components accounts for more than 93% of the total. The XRD pattern (**Figure 1A**) shows that the main phase of a spent FCC catalyst is zeolite Y, dealuminated, which is consistent with its crystal structure. **Figure 4A** shows that the surface appearance of a spent FCC catalyst is a fairly regular sphere with impurities attached to the surface. The average particle size of a spent FCC catalyst is 80.055 μm as shown in **Figure 1B**, which is quite low just like the other pozzolanic materials such as fly ash and furnace slag (around 20 μm).

A coarse aggregate is gravel, the main (83%) particle size of a coarse aggregate was between 3 and 5 mm and the remaining (17%) was between 1 and 3 mm in diameter. The gravels were filtered through a 1.0-mm sieve, and the gravels larger than 1.0 mm were selected for use. A fine aggregate is ISO standard sand, the diameter of a fine aggregate is mainly distributed between 0.08 and 1.0 mm. The basic cementitious material is ordinary Portland P42.5 cement. In order to improve the cementitious effect of a binder, three chemical reagents such as NaOH (96% purity), $Na_2SiO_3 \cdot 9H_2O$, and Na_2SO_4 (99% purity) were sampled as the activators and were purchased from Sinopharm Company Ltd.

Production Process of CN-Bricks
The production process of CN-bricks mainly includes mixing, molding, compacting, and curing. This study established 12 groups to investigate the effect of a binder system ("BS-series") and the proportion of a spent FCC catalyst ("FC-series") on the properties of CN-bricks, as summarized in **Table 2**. Samples BS-C10/C15/C20 correspond to 10, 15, and 20% content of ordinary Portland cement by weight in their raw materials. Three types of activators, NaOH, Na_2SiO_3, and Na_2SO_4, were tested for their activating function, and their samples were labeled as BS-C20A, BS-20B, and BS-20C, respectively. The additive amount

TABLE 1 | The main chemical composition of a spent fluid catalytic cracking (FCC) catalyst.

Component	Al_2O_3	SiO_2	NiO	V_2O_5	Sb_2O_3	Else
Contents (wt%)	54.2	37.1	1.4	0.46	0.39	6.45

FIGURE 1 | X-ray diffraction (XRD) pattern **(A)** and particle size distribution **(B)** of spent fluid catalytic cracking (FCC) catalyst.
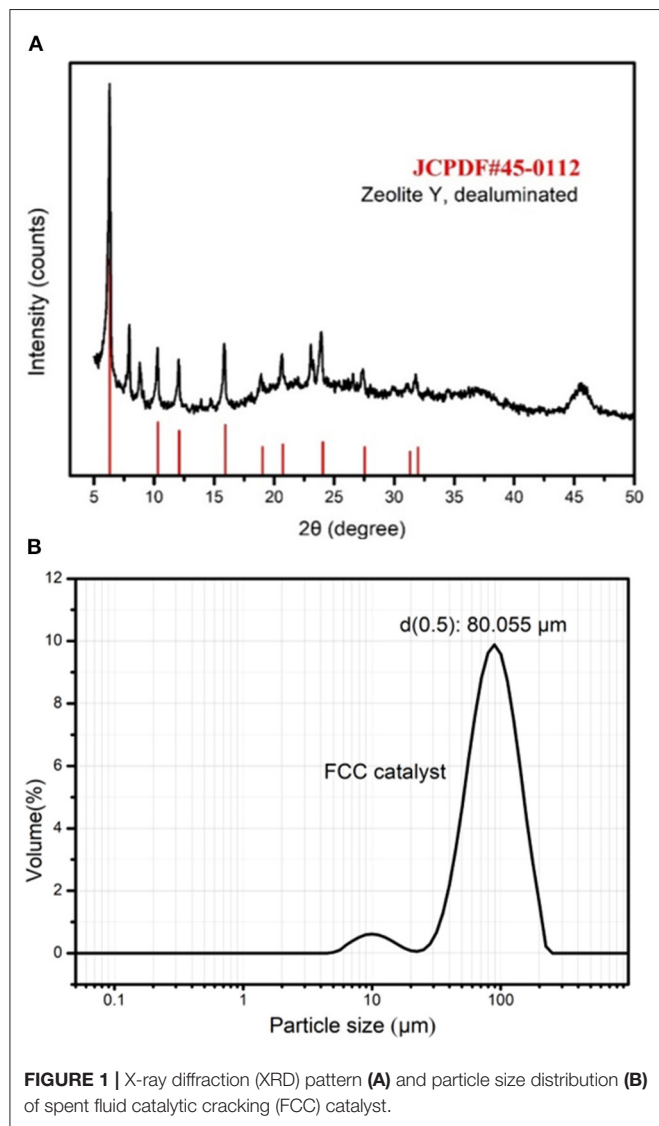
of activators was set as 2.5% (wt%) referring to relevant alkali activating studies (Abdel-Gawwad et al., 2020b). Each sample of FC-10/15/20/25/30/40 represents 10, 15, 20, 25, 30, and 40% of a spent FCC catalyst by weight used in a raw material when the proportion of a gravel gets reduced from 55 to 25%.

In the making process of each sample, raw materials were mixed in the blender for 5 min and added with water to maintain its moisture with the water/cement ratio set as 0.40. After full blending, the materials were put in a mold and compacted with a pressure of 20 MPa to be shaped as $240 \times 115 \times 53$ mm. After 24 h, the CN-bricks were demolded and conserved in curing boxes at $20°C$ and 60–90% moisture for 28 days. After 28 days, various properties of bricks were tested by the standard methods that are listed as follows.

Mechanical and Physical Properties

The compressive strength test and flexural strength test of CN-bricks were conducted according to the Chinese Standard GB/T 4111-2013 (GB/T 4111, 2013), which were tested by Instron 5969 and Sinter WDW-50 pressure testing machines at a rate of 4.0 kN/s until the bricks got damaged. The bulk density and water absorption were also tested according to GB/T 4111-2013 by soaking the samples in a tank at $20°C$ for 24 h when the upper surface was at least 20 mm lower than the water surface, and then the samples were taken out, wiped, and immediately weighed as m_1. Afterward, the samples were dried in an oven at $105°C$ to achieve constant weight and weighed as m. The water absorption was calculated as follows:

$$\text{Water absorption} = \frac{m_1 - m}{m} \times 100\% \tag{1}$$

The bulk density was calculated according to Equation (2)

$$\text{Bulk density (kg/m}^3) = \frac{m}{V} \tag{2}$$

where m stands for the dry weight of CN-bricks and V is the volume of a brick. Each index was measured thrice and reported with error bars in the final result.

Microstructure Characterization

For subsequent microstructure analysis, the chosen samples were roughly crushed and pulverized in a laboratory grinding machine for 5 min, and then dried in an oven at $50°C$ until reaching a constant weight. The samples that could pass through a 0.45-μm filter were chosen for the XRD test and FTIR test. XRD analysis was carried out to obtain the crystal structure and phase characteristics of a CN-brick on a Bruker D8 Advance with the scanning angle ranging from 5 to $75°$ at a scanning rate of $4°$/min. FTIR analysis was carried out to identify the functional groups of organic compounds on a Thermo Nicolet iS5 in the range of $4,000–500$ cm^{-1}. The crushed samples were analyzed by SEM to study the microstructure of the specimens on a Tescan Mira 3 machine.

Environmental Risk Assessment of CN-Bricks
Determination of Total Metal Content

The detection of the total heavy metal content of heavy metals V, chromium (Cr), manganese (Mn), cobalt (Co), Ni, Cu, Zn, antimony (Sb), Ba, and Pb in raw materials and CN-bricks was done by following the Chinese Standard HJ 781-2016 (HJ 781, 2016). To sum up, the solid wastes were added

Samples	Aggregate			Binder system				W/C ratio
	Spent FCC catalyst/%	Sand/%	Gravel/%	Cement/%	NaOH/%	Na$_2$SiO$_3$/%	Na$_2$SO$_4$/%	
BS-C10	23	17	50	10	0	0	0	0.4
BS-C15	21	16	48	15	0	0	0	0.4
BS-C20	20	15	45	20	0	0	0	0.4
BS-C20A	20	15	45	20	2.5	0	0	0.4
BS-C20B	20	15	45	20	0	2.5	0	0.4
BS-C20C	20	15	45	20	0	0	2.5	0.4
FC-10	10	15	55	20	0	0	0	0.4
FC-15	15	15	50	20	0	0	0	0.4
FC-20	20	15	45	20	0	0	0	0.4
FC-25	25	15	40	20	0	0	0	0.4
FC-30	30	15	35	20	0	0	0	0.4
FC-40	40	15	25	20	0	0	0	0.4

with acids including HCL, HF, HNO$_3$, and HClO'$_4$ and then digested in an electric hot plate at 180°C for 1–2 h. Digested solution was then brought into plasma emission spectrometer [inductively coupled plasma optical emission spectroscopy (ICP-OES), Thermo iCAP 7000], and the characteristic spectrum of elements being atomized will be used to represent the element content.

Toxicity Characteristic Leaching Procedure

The TCLP test was conducted under a protocol EPA SW-846 Method 1311 (EPA 1311, 1992) to simulate a leaching process induced by acid rain when CN-bricks are used in a pedestrian street. In short, samples were mixed with the leaching solution, which contains acetic acid solution (0.57% v/v) with a liquid-to-solid (L/S) ratio set as 20:1 L/kg and pH set as 2.88 ± 0.05. The mixed solution was then vibrated for 18 h under a temperature of 23°C at a rate of 30 revolutions/min. The leachate was then filtered and analyzed by ICP-OES to determine the leaching concentration of heavy metals V, Cr, Mn, Co, Ni, Cu, Zn, Sb, Ba, and Pb.

Maximum Availability Leaching Test

Heavy metals V, Cr, Co, Ni, Sb, and Ba are tested for their maximum availability in CN-bricks according to the EA NEN 7371 protocol (EA NEN 7371, 2004), which includes two extraction stages. Samples were filtered through a 125 μm membrane and mixed with the extract liquid at an L/S ratio of 50:1 L/kg, with pH maintained at 7.0 ± 0.5 by adjusting HNO$_3$ in deionized water. After the first extraction, the leachate was filtered through 0.45 μm and be prepared for second extraction stage, during which the pH is changed to 4.0 ± 0.5. The contact time was set as 3 h for both extraction process. At last, the two leachates were mixed and analyzed by ICP-OES. The maximum leaching rate is calculated in Equation (3):

$$\text{Maximum leaching rate (\%)} = \frac{\text{Maximum availability}}{\text{Total metal content}} \quad (3)$$

RESULTS AND DISCUSSION

Mechanical and Physical Properties of CN-Bricks

Compressive Strength and Flexural Strength

The effect of the cement content and alkali activators on the mechanical properties of a CN-brick was examined. A review of Gupta et al. (2020) illustrates that cement (10–30%) and lime (5–30%) are the main cementitious binders used in unfired bricks/blocks. In this study, 10, 15, and 20% of the cement were tested, and the compressive strength increases from 14.3 to 23.4 MPa, flexural strength increases from 2.3 to 4.6 MPa as the cement content increases from 10 to 20% (**Figure 2A**). The main components of Portland cement are 3CaO · SiO$_2$ (C$_3$S), 2CaO · SiO$_2$ (C$_2$S), and 3CaO · Al$_2$O$_3$ (C$_3$A), which could react with H$_2$O to form C-S-H, C-A-H, ettringite (AFt), and Ca(OH)$_2$ to improve the strength of a brick, and the mechanisms of the reaction are shown in Equations (4)–(7):

$$3CaO \cdot SiO_2 + nH_2O \rightarrow xCaO \cdot SiO_2 \cdot yH_2O + (3-x)Ca(OH)_2 \quad (4)$$
$$2CaO \cdot SiO_2 + nH_2O \rightarrow xCaO \cdot SiO_2 \cdot yH_2O + (2-x)Ca(OH)_2 \quad (5)$$
$$3CaO \cdot Al_2O_3 + 6H_2O \rightarrow 3CaO \cdot Al_2O_3 \cdot 6H_2O \quad (6)$$
$$3CaO \cdot Al_2O_3 + 3CaSO_4 \cdot 2H_2O$$
$$+26H_2O \rightarrow 3CaO \cdot Al_2O_3 \cdot 3CaSO_4 \cdot 32H_2O(AFt) \quad (7)$$
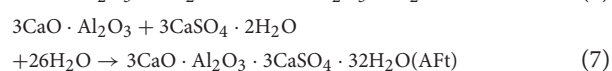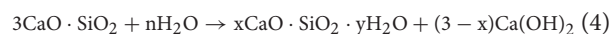
A higher content of the cement indicates a higher content of hydration products that would wrap an aggregate more tightly, which then indicates a lower porosity, denser structure, and higher mechanical strength. According to the relevant national standard GB 11945-1999 (GB 11945, 1999), the compressive strength and flexural strength of the MU20-degree brick should exceed 20.0 and 4.0 MPa. Hence, only the cement content of 20% could achieve the MU20 degree. To further improve the mechanical property of a brick, alkali activators were introduced into a binder system. **Figure 2** shows that NaOH slightly increases the compressive strength
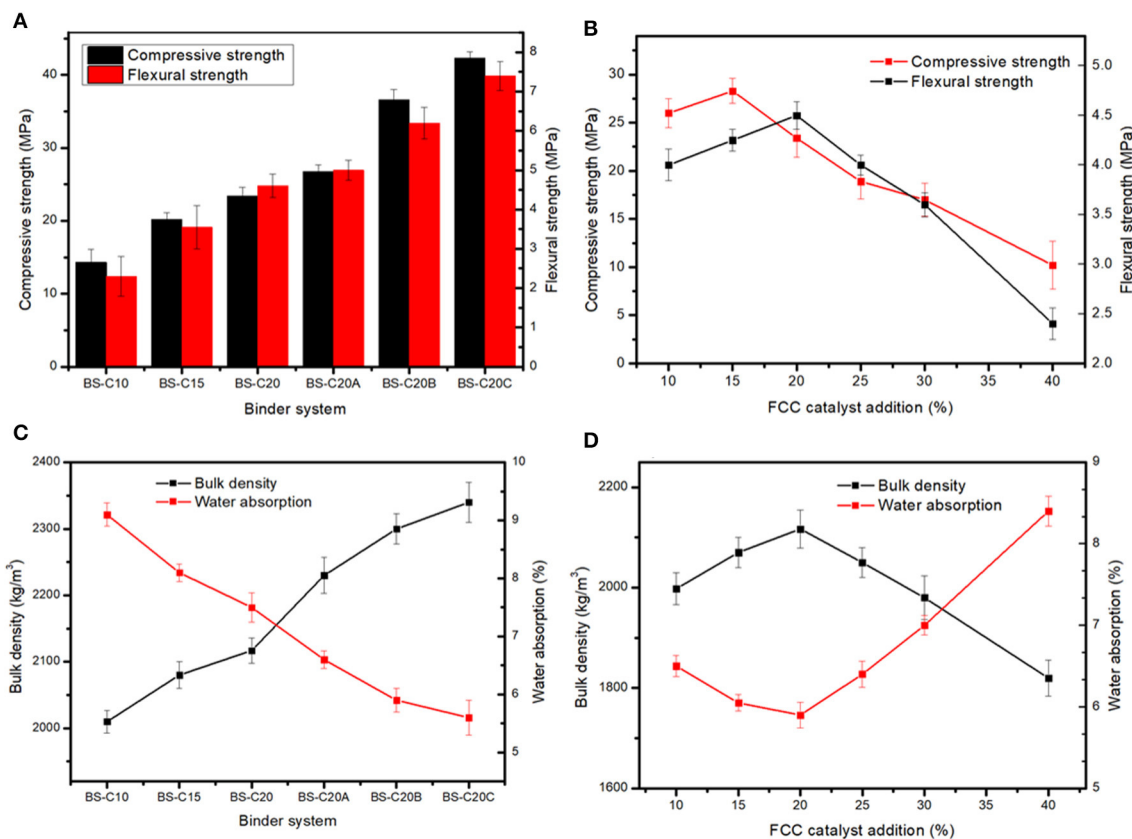
FIGURE 2 | Compressive strength, flexural strength **(A,B)** water absorption, and bulk density **(C,D)** of catalyst-based non-sintered bricks (CN-bricks).

of a brick from 23.4 to 26.7 MPa, while Na_2SiO_3 and Na_2SO_4 significantly lift the compressive strength up to 36.6 and 42.3 MPa, respectively. Na_2SO_4 is an optimal activator for a CN-brick, the mechanism of which will be illustrated later in detail.

With the determination of an optimal binder system, the effect of the FCC content on the mechanical properties were then evaluated. Among raw materials, gravels (1.0–5.0 mm) act as a skeleton, sands (0.08–1.0 mm) can fill the pores between the gravels, and a spent FCC catalyst (80.1 μm) can fill the remaining interspace. An ideal grain size distribution can reduce the overall porosity and induces a higher strength. **Figure 2** shows 20% FCC proportion could achieve the most ideal compressive strength and flexural strength at the same time, the strength at this point can meet the MU20 class according to the Chinese standard GB 11945-1999, yet up to 25% addiction amount will reduce the strength of bricks to MU15 class. Flexural strength changes in the same trend as compressive strength, the cement content < 20% could improve the flexural strength, but a proportion higher than 20% would deteriorate the strength of a CN-brick, the mechanism of which will be illustrated later. In sum, an optimal formula of the production of a CN-brick is gravel:sand:FCC:cement:Na_2SO_4 = 45:15:20:20:2.5.

Water Absorption and Bulk Density

The water absorption and bulk density of CN-bricks with various binders and the FCC content are summarized in **Figure 2**. The bulk density of a CN-brick increases from 2,010 to 2,340 kg/m^3 when the cement content increases from 10 to 20%, and then added with three types of activators. This is because cement and activators increased the amount of hydration products like C-S-H and AFt, as illustrated by XRD and FTIR in later sections, which could fill the micropores of an aggregate and bind them more tightly. This is also the reason why the water absorption of BS-series decreases gradually from 9.1 to 5.6%. The water absorption represents the water-resistance ability of bricks that is closely related to the porosity of bricks. When aggregates are bound more tightly by cement and activators, open porosity will decrease, so does the water absorption value (Lang et al., 2020). Even though the water absorption rates of samples are different, all are below the threshold set by the Chinese standard JC/T 422-2007, which is 18%.
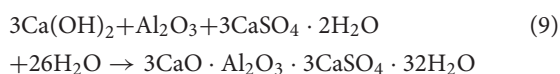
The bulk density and water absorption of a CN-brick with different values of FCC content are illustrated in **Figure 2D**. The bulk density increases when the proportion of FCC gets increased from 10 to 20% and the content of gravel decreases from 55 to 45%, this is because macropores between the gravels (1–5 mm) could be filled more tightly by a fine aggregate of a spent FCC

catalyst (0.08 mm), which reduces the porosity and improves the compactness, so the water absorption rate of a CN-brick decreases from 6.5 to 5.9%. However, when more FCCs are added from 25 to 40% and the content of gravel gets reduced from 40 to 25%, a spent FCC catalyst replaces gravels as a main raw material in a system, the properties of a CN-brick get deteriorated. The bulk density of bricks gradually decreases from 2,117 to 1,820 kg/m^3 accompanied with the compressive strength from 23.4 to 10.2 MPa (**Figure 2B**), while the water absorption rate increases from 5.9 to 8.4%. A higher proportion of fine aggregates than coarse aggregates would induce an incompact grain size distribution. Fine aggregates that could not be compacted by large particles would be scattered in the system. The above mentioned research shows that too much coarse aggregates or fine aggregates are neither good for the properties of bricks, 20% of a spent FCC catalyst and 45% of a gravel could achieve the most ideal stacking structure in a CN-brick.

Microstructure of CN-Bricks Under Alkali Activation

XRD Characterization

The mechanical strength of a CN-brick is mainly attributed by the hydration reaction caused by binders including cement, NaOH, Na_2SiO_3, and Na_2SO_4, in this study. **Figure 3A** illustrate the XRD pattern of CN-bricks added with 10, 15, and 20% cement (BS-C10, BS-C15, and BS-C20) at 28 days and 10% cement at 56 days. It can be seen that the crystalline phase in the CN-bricks are AFt (9.1, 15.8, 22.9, 34.5, 40.8°, 2θ), quartz (SiO_2, 26.5°), C_3S (Ca_3SiO_5, 29.2°, 32.1°, 34.2°, 2θ), C_2S (Ca_2SiO_4, 32.0°, 32.5°, 34.3°, 2θ), and C-S-H (29.3°, 32.0°, 50.0°, 2θ). The two hydration products with higher peaks that assume a main responsibility for the strength of CN-bricks are AFt and C-S-H. These two products can be formed by ordinary Portland cement alone as illustrated in Equations (5–8). Apart from that, they can also be formed by a chemical reaction between an aggregate and cement. The $Ca(OH)_2$ produced from the cement hydration (Equations 4 and 5) could react with SiO_2 and Al_2O_3 that exists in a gravel, sand, and a spent FCC catalyst, and then form C-S-H and AFt directly according to Equations (8) and (9):

$$3Ca(OH)_2 + 2SiO_2 \rightarrow 3CaO \cdot 2SiO_2 \cdot 3H_2O \quad (8)$$

$$3Ca(OH)_2 + Al_2O_3 + 3CaSO_4 \cdot 2H_2O \quad (9)$$
$$+26H_2O \rightarrow 3CaO \cdot Al_2O_3 \cdot 3CaSO_4 \cdot 32H_2O$$

An interesting phenomenon in the XRD pattern of a CN-brick is that the crystalline phase of AFt is far more distinct compared with the bricks made from the other wastes, such as fly ash, furnace slag, or degraded sludge (Wang C.-Q., et al., 2019; Akinyemi et al., 2021). This is because of the proportion of Al_2O_3 in a spent FCC catalyst, 54.2%, which is significantly higher than that of fly ash (18–25%), furnace slag (6–11%), and degraded sludge (7–21%) and it is referenced in many relevant literature studies. Multiple researches related to the spent FCC catalyst recycling (Al-Jabri et al., 2013; Font et al., 2017; Xue et al., 2020) also recorded that the proportion of Al_2O_3 in a spent FCC

catalyst ranges between 47 and 66%, which is in a relatively high level. A higher content of Al_2O_3 would react with $Ca(OH)_2$, and then form more AFt than the other materials, during which the content of $CaSO_4$ is a limiting factor.

With an increase in the proportion of cement from 10 to 20%, all of the peaks have increased including SiO_2, C_3S, C_2S, C-S-H, and AFt (**Figure 3A**). This is because of the cement hydration itself illustrated in Equations (5–8). **Figure 3A** also compares the XRD pattern of BS-C10 at 28 and 56 days. Some crystalline phases like SiO_2, C_3S, and C_2S get decreased and the peaks of C-S-H (29.3°, 50.0°, 2θ) have increased in BS-C10 (56 days). Hydration products like C-S-H and AFt could be continuously produced as the curing time gets prolonged, yet 28 days are enough for the mechanical construction in a CN-brick.

The XRD pattern of BS-C20A/B/C is shown in **Figure 3B**. Compared to BS-C20, crystalline phases of AFt and C-S-H in BS-20A show a slight improvement. NaOH could dissolve $[SiO_4]^{4-}$ and $[AlO_4]^{5-}$ from a spent FCC catalyst and aggregates, and promote their reaction with Ca^{2+} to produce more C-S-H and C-A-H gels. Compared to BS-C20A, the peaks of SiO_2 and C_3S in a sample BS-C20B were obviously increased, since Na_2SiO_3 could produce SiO_2, $CaSiO_3$, and NaOH as shown in Equation (10):

$$NaO \cdot nSiO_2 + Ca(OH)_2 \rightarrow (n\text{-}1)SiO_2 + CaSiO_3 + 2NaOH \quad (10)$$
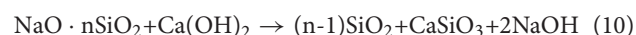
The increased content of SiO_2 reacts with $Ca(OH)_2$ to produce more C_3S and C-S-H as XRD results show, thus increasing the compressive strength of a CN-brick. In addition, the generated NaOH will dissolve Si-O and Al-O and promote the formation of C-S-H and C-A-H at the same time like the BS-C20A does.

When Na_2SO_4 are added into BS-C20C, significant increases in the peak heights of AFt are at 9.1, 15.8, and 22.9°. This is because of bringing more SO_4^{2-} in the system, and more $CaSO_4$ and NaOH can be formed in Equation (11):

$$Na_2SO_4 + Ca(OH)_2 \rightarrow CaSO_4 \cdot 2H_2O + 2NaOH \quad (11)$$

It is mentioned above that AFt is a characteristic hydration product of a CN-brick, which is transformed from a high content of Al_2O_3, during which $CaSO_4$ is a limiting factor. The addiction of an activator Na_2SO_4 could promote the formation of $CaSO_4 \cdot 2H_2O$ and then react with excessive Al_2O_3 to increase the content of AFt as the XRD results show. This is a main reason why Na_2SO_4 could increase the compressive strength of a CN-brick from 23.4 to 42.3 MPa. This rule has not been found in the previous studies on the recycling of a spent FCC catalyst. Na_2SO_4 is more suitable to be an activator in a NS-bricks made from a spent FCC catalyst.

FTIR Analysis

The FTIR pattern of BS-C10/15/20 and BS-C20A/B/C is summarized in **Figures 3C,D**. These absorption peaks mainly represent the stretching O-H vibration (3,650 cm^{-1}), stretching H-O-H vibration in water (3,406 and 1,654 cm^{-1}), asymmetric stretching CO_3^{2-} vibration (1,428 cm^{-1}), asymmetric stretching Si-O-Si(Al) bond (1,098 cm^{-1}), and bending O-Si-O vibration
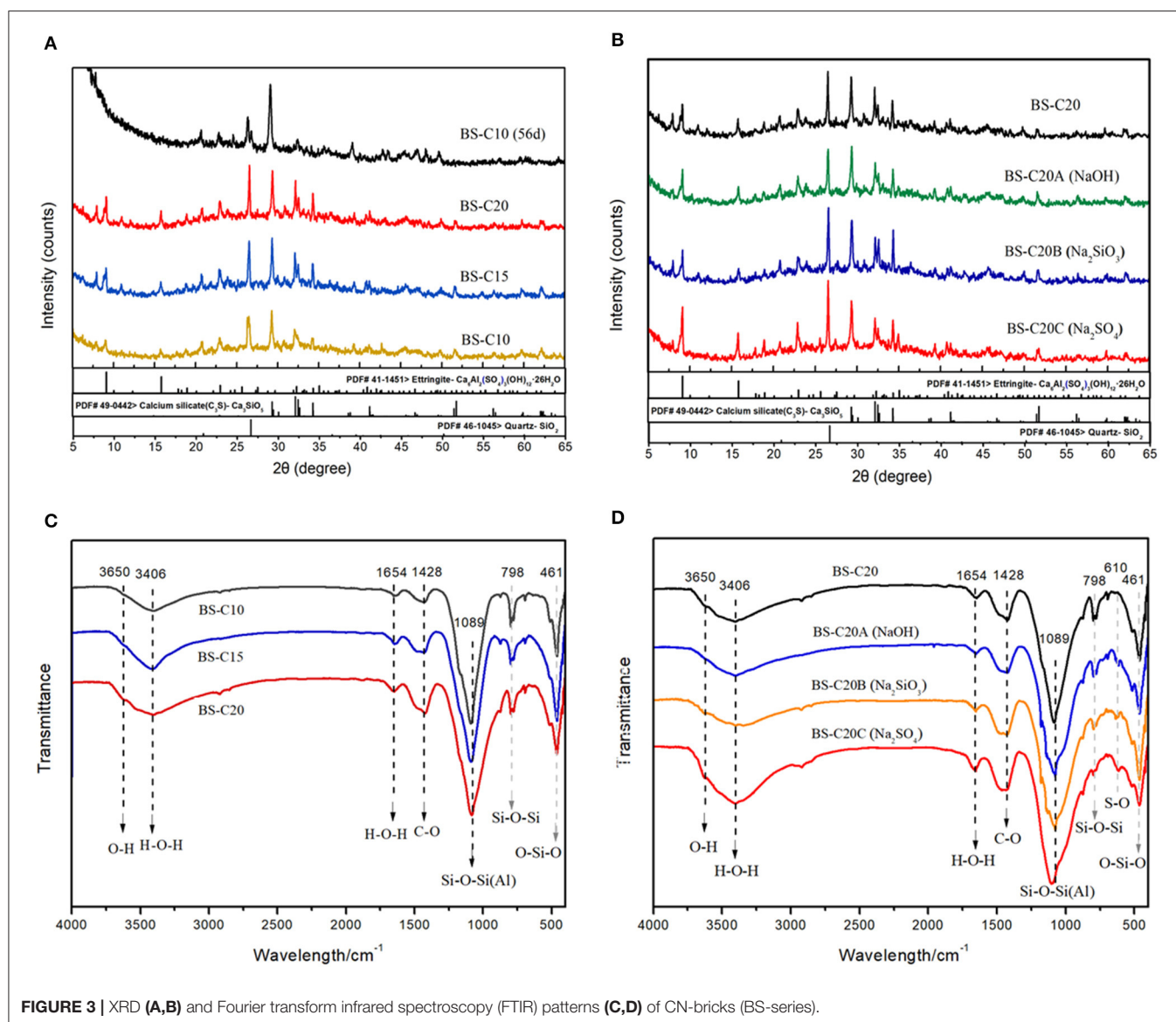
FIGURE 3 | XRD **(A,B)** and Fourier transform infrared spectroscopy (FTIR) patterns **(C,D)** of CN-bricks (BS-series).

(461 cm^{-1}) in a gel matrix. The predominant peaks shown in the spectra mainly refer to silicate, aluminate, and carbonate compounds just like the other construction materials made from industrial wastes and binders (Abdel-Gawwad et al., 2020a; Liu et al., 2021). When the cement content increases from 10 to 20%, there is an increase in the intensity of peak in 3,650 cm^{-1}, which indicates that more Si-OH and Al-OH are produced from $[SiO_4]^{4-}$ and $[AlO_4]^{4-}$. Absorption of peaks in 3,406 and 1,654 cm^{-1} also shows an increase in intensity, which indicates that more free water has been transferred to structural water. The absorption peak of Si-O-Si(Al) is located between 1,150 and 1,008 cm^{-1}, which has been apparently sharpened since more Si-O are produced in the form of C-S-H and AFt, which is consistent with the result of XRD. The absorption peak at 1,428 cm^{-1} is associated with CO_3^{2-} existing in carbonates like calcite and dolomite, which has been increased because of the reaction of

Ca^{2+} and atmospheric CO_2. The intensity of 798 cm^{-1} peak has been decreased since more SiO_2 has been involved in the hydration process. A higher cement content is proved to be effective in promoting the hydration process.

The FTIR pattern of CN-bricks added with NaOH, Na_2SiO_3, and Na_2SO_4 as activators are summarized in **Figure 3D**. Many peak intensities have increased when various activators are added including bands at 3,650, 1,654, 1,428, 1,089, and 461 cm^{-1}. Peaks near 3,650 cm^{-1} indicates the extent of Si-OH and Al-OH dissolution rate from $[SiO_4]^{4-}$ and $[AlO_4]^{4-}$, Na_2SiO_3, and Na_2SO_4 exhibits higher dissolving ability than NaOH, which explains why Na_2SiO_3 and Na_2SO_4 exhibit higher strength enhancement capacity. The increase of band 1,428 cm^{-1} intensity (CO_3^{2-}) indicates that activators promote the formation of carbonates and improve the strength of a brick. The absorption peak at 798 cm^{-1} (SiO_2) gradually disappears when activators
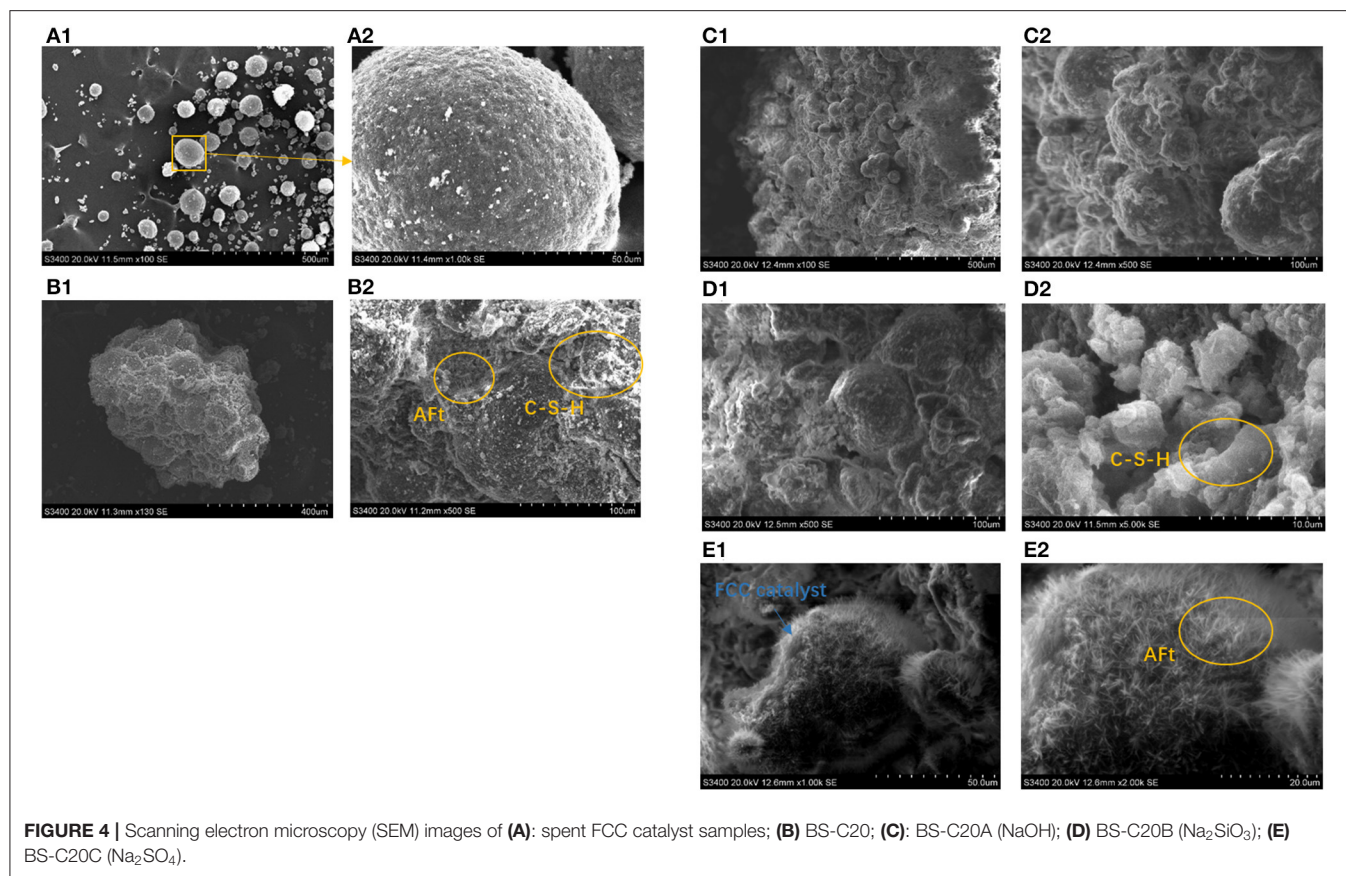
FIGURE 4 | Scanning electron microscopy (SEM) images of **(A)**: spent FCC catalyst samples; **(B)** BS-C20; **(C)**: BS-C20A (NaOH); **(D)** BS-C20B (Na$_2$SiO$_3$); **(E)** BS-C20C (Na$_2$SO$_4$).

are added, which represents the extent to which SiO$_2$ gets transformed to C-S-H and C-A-S-H gel. The enhancement of Si-O-Si(Al) bands at 1,098 cm^{-1} and a slight shift toward higher wavenumbers indicate the polymerization reaction and the increased amount of C-S-H and C-A-H in hydration products. The absorption peak near 610 cm^{-1} represents the bond of S-O in SO$_4^{2-}$, which has been sharpened in BS-C20C compared to BS-C20, due to an addictive amount of SO$_4^{2-}$ and AFt brought from an activator Na$_2$SO$_4$. In sum, FTIR spectrums prove that a higher content of cement and alkali activators could promote the formation of C-S-H, AFt, and carbonates in hydration products.

SEM Analysis

The scanning electron microscopy test was conducted for a more intuitive observation of the effect of a binder system on a CN-brick. **Figure 4** shows that spent FCC catalysts are regular spheres with particle size lower than 100 μm, attached with certain impurities (around 1 μm) that are likely to be the chemical compounds produced from heavy metals in crude oil. These heavy metals would cover the exterior surface of a spent FCC catalyst and clog the access to active sites inside the zeolite, causing a spent FCC catalyst to be deactivated. When a spent FCC catalyst is recycled and reused in a CN-brick, it is tightly wrapped in the gel materials along with the aggregates as a whole (**Figure 4B**). The gel materials that bind them together are mainly flake-like C-S-H and needle-like AFt, which are consistent with

the XRD results. AFt is usually found in a system added with gypsum, and is recorded to have a setting retarding effect for the too quick hydration speed of cement caused by C$_3$A. AFt is also widely known as capable of improving early stage strength of the construction materials.

The effect of activators on hydration products is examined by SEM as shown in **Figure 4**. When NaOH is added into the system, the microstructure of BS-20A is generally similar to that of BS-20, with a slight difference that the surface of aggregates and a spent FCC catalyst are little bit rougher than the original one. About 3% addition of NaOH creates an alkali environment that would corrode the aluminosilicate material, dissolve more activated Si-O unit from a Si-O-Si network, and form more C-S-H gels. When Na$_2$SiO$_3$ is added into a system (**Figure 4D**), the interface of aggregate and gel materials is more compact and tight. A main gel material in the BS-C20B system is still a flake-like C-S-H, the density of which is obviously increased, since the addition of Na$_2$SiO$_3$ introduces a higher content of SiO$_2$ and CaSiO$_3$ and further a higher content of a hydration product C-S-H. When Na$_2$SO$_4$ is added into a binder, as shown in **Figure 4E**, the surface of a spent FCC catalyst and its interface with other aggregates are covered with a thick layer of a needle-like AFt, since SO$_4^{2-}$ in an activator would react with Al$_2$O$_3$ to form more AFt (XRD result). The amount of AFt formed on the FCC surface is higher than on the surface of gravel and sand, proving that Na$_2$SO$_4$ could specifically activate an aluminum-rich material.

Among NaOH, Na_2SiO_3, and Na_2SO_4, the activator Na_2SO_4 can specifically make full use of a characteristic of the FCC catalyst as a high-aluminum material.

In summary, the mechanism of hydration reactions happened in a CN-brick is illustrated in **Figure 5**. C-S-H and AFt are the main hydration products generated from cement, reinforced by activators, and mainly contribute to the mechanical strength of CN-bricks.

Quantitative Environmental Risk Assessment
Determination of Characteristic Pollutants of CN-Bricks

The characteristic pollutants in CN-bricks were determined from the total metal content (**Figure 6**) and leaching concentration (**Table 4**). Metals V, Cr, Mn, Co, Ni, Cu, Zn, Sb, Ba, and Pb were chosen to be examined in raw materials and CN-bricks, since they are conventional indicators in Chinese hazardous waste identification standard (GB 5085.3, 2007) and groundwater quality standard (GB/T 14848, 2017). **Figure 6A** shows that the concentration of Ni, V, and Sb is particularly higher than the other heavy metals in a spent FCC catalyst, which are 11,510.5, 3,700.0, and 2,610.2 mg/kg, respectively. Ni and V have been widely acknowledged as the main pollutants of a FCC catalyst (Etim et al., 2016; Ferella et al., 2016). The deposition of Ni and V from crude oil on the catalyst surface makes the selectivity of the catalyst worse and leads to catalyst poisoning. V is the most dangerous metal since V in V^{5+} state reacts to form H_3VO_4, which could destroy the structure of zeolite dramatically (Busca et al., 2014). Ni is less detrimental, but still has a strong dehydrogenation activity, which would suppress the production of gasoline. One of the solutions is the addition of Sb to from Ni-Sb alloys, $Ni_xSb_yO_z$, to inhibit the strong dehydrogenation activity of Ni and increase the yield of gasoline (Bohmer et al., 1990), so Sb is in high content. Wai et al. (1999) also confirmed that the concentration of V, Ni, and Sb gets significantly increased from 2–33 ppm to 1,326–3,930 ppm when a FCC catalyst gets deactivated in an unit. Apart from the spent FCC samples, the raw material aggregates (gravel and sand) and cement also brought in a high level of Mn and Cr in the product. Elements Ni, V, Sb, Mn, and Cr are the pollutants with a high total content in CN-bricks.

Instead of the total content, the leaching behavior is usually a main concern of the hazard identification. Samples "FC-10," "FC-15," and "FC-20" were analyzed to investigate the leaching behavior of CN-bricks with different amounts of a spent FCC catalyst. TCLP test (**Table 3**) show that the leaching concentration of all metals is significantly lower than their total content, attributed by the above-mentioned hydration reaction. The regulatory level of relevant metals in China and USA are also listed in **Table 3** according to the Chinese Standard (GB 5085.3, 2007) and USA 40 CFR 261.24 (USEPA, 2011), which confines the leaching concentration limits above which the solid waste will be defined as hazardous wastes. The leaching concentration of all heavy metals are much lower than the regulatory levels, thus the CN-bricks produced in this study should not be considered as hazardous materials.

In the long-term environmental risk of CN-bricks, six metal elements V, Cr, Co, Ni, Sb, and Ba are identified as the characteristic pollutants of CN-bricks according to the result of TCLP, since the other elements Mn, Cu, Zn, and Pb are either in low concentration or pose a little threat to human health.

Impact of CN-Bricks on Groundwater

An exposure scenario analysis of CN-bricks is depicted in **Figure 7B**, which generally includes: (1) determination of the concentration of pollution source, which refers to the daily leaching amount ($C_{Daily-Lea}$) of a CN-brick; (2) calculation of the concentration of contaminants in groundwater (C_{gw}); and (3) human health risk assessment considering an average daily intake dose (ADD) of nearby residents and hazard quotient (HQ) of CN-bricks.

FIGURE 5 | Microscopic mechanism diagram of a CN-brick.
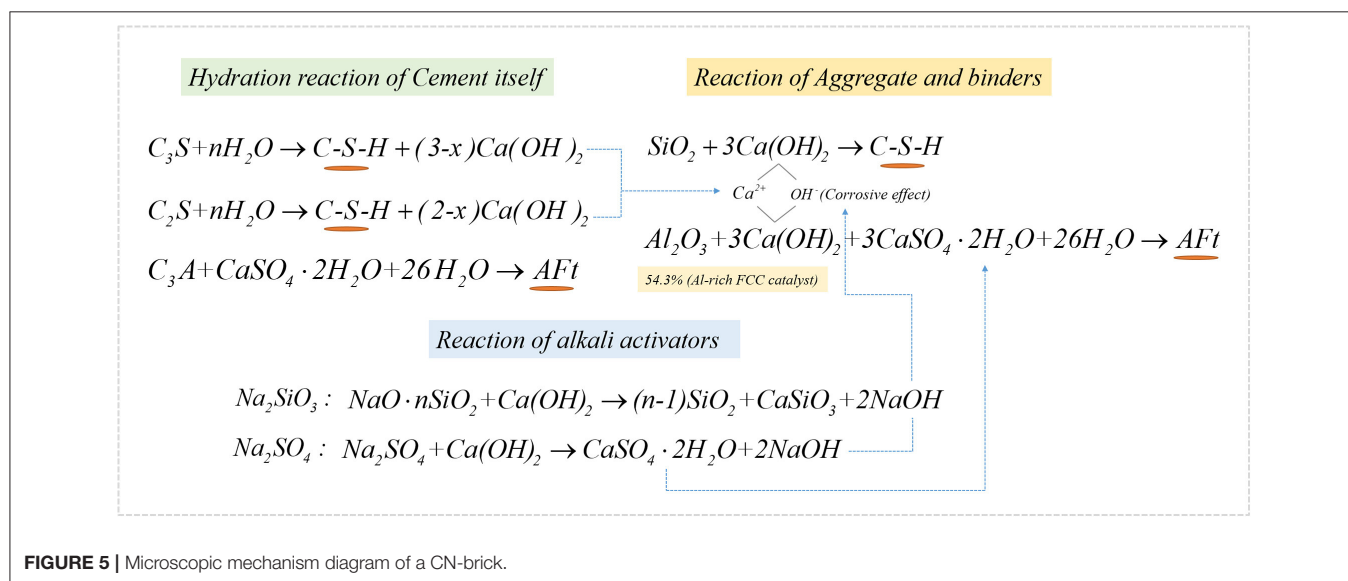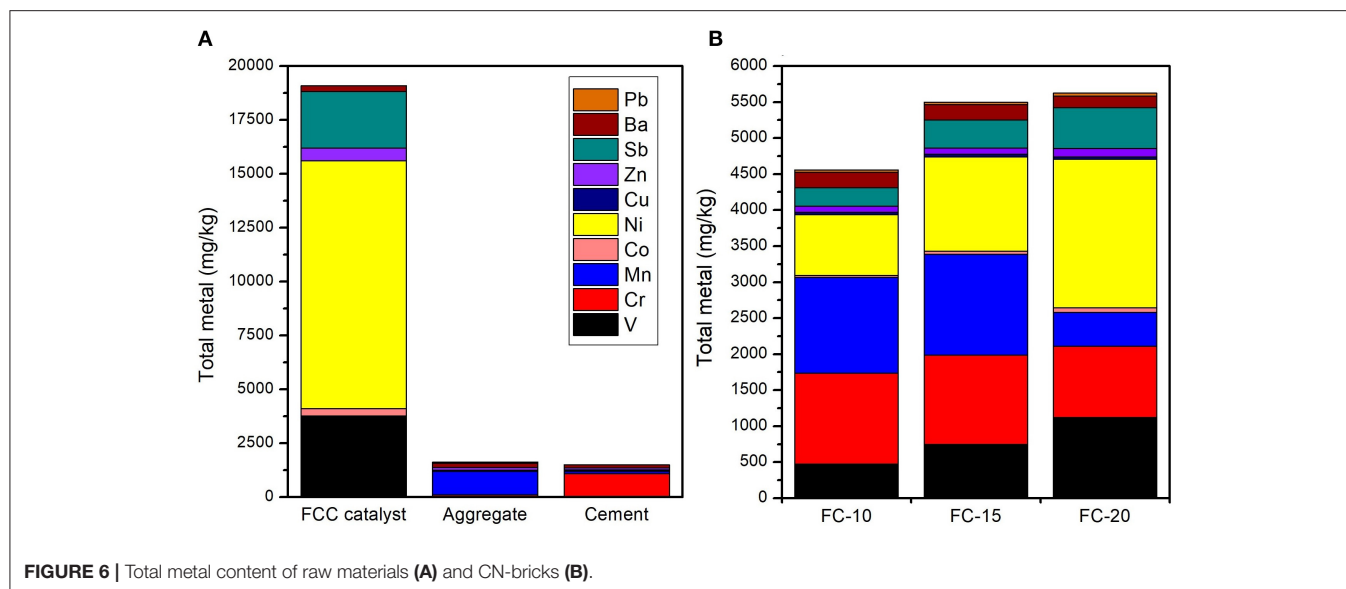
FIGURE 6 | Total metal content of raw materials **(A)** and CN-bricks **(B)**.

TABLE 3 | Toxicity characteristic leaching procedure (TCLP) result of catalyst-based non-sintered bricks (CN-bricks; ug/L).

Samples	V	Cr	Mn	Co	Ni	Cu	Zn	Sb	Ba	Pb
FC-10	3.34 ± 0.82	6.12 ± 0.00	ND	0.13 ± 0.01	1.20 ± 0.11	0.35 ± 0.01	6.22 ± 1.51	13.20 ± 0.63	126.07 ± 15.79	0.4 ± 0.06
FC-15	6.94 ± 0.62	6.05 ± 0.23	ND	0.11 ± 0.01	0.76 ± 0.12	0.38 ± 0.18	1.23 ± 0.96	21.26 ± 0.38	52.03 ± 3.13	0.05 ± 0.01
FC-20	78.68 ± 4.78	40.26 ± 5.70	ND	0.55 ± 0.02	0.71 ± 0.10	0.60 ± 0.10	1.12 ± 0.87	55.46 ± 1.27	19.32 ± 0.89	ND
Regul limit 1	N.	5,000	N.	N.	5,000	100,000	100,000	N.	100,000	5,000
Regu limit 2	N.	5,000	N.	N.	N.	N.	N.	N.	100,000	5,000
LOD	0.01	0.01	0.02	0.005	0.01	0.01	0.006	0.01	0.004	0.05

ND, Not detected.

N., Not mentioned in reference level regulations.

"Regulatory limit 1" is referred to Chinese Standard GB 5085.3 (GB 5085.3, 2007).

"Regulatory limit 2" is referred to the USA standard 40 CFR 261.

LOD, limit of detection.

Each data are based on three replicates.

TABLE 4 | Maximum availability and daily leaching amount of CN-bricks and concentration of contaminants in groundwater.

Samples	V	Cr	Co	Ni	Sb	Ba
Maximum availability of leaching ($C_{Max-Lea}$), mg/kg						
FC-10	25.34 ± 1.23	1.59 ± 0.28	0.84 ± 0.11	7.21 ± 0.61	12.21 ± 0.69	15.3 ± 2.13
FC-15	28.04 ± 5.67	3.57 ± 1.23	1.62 ± 0.19	13.79 ± 1.43	23.09 ± 1.28	23.58 ± 1.96
FC-20	40.31 ± 4.24	4.97 ± 0.53	0.85 ± 0.78	12.35 ± 5.28	24.99 ± 2.62	12.20 ± 1.30
Daily leaching amount ($C_{Daily-Lea}$), mg/L						
FC-10	4.90E-03	3.07E-04	1.62E-04	1.39E-03	2.36E-03	2.96E-03
FC-15	5.42E-03	6.90E-04	3.13E-04	2.67E-03	4.46E-03	4.56E-03
FC-20	7.79E-03	9.61E-04	1.64E-04	2.39E-03	4.83E-03	2.36E-03
Concentration of contaminants in groundwater (C_{gw}), mg/L						
FC-10	4.61E-05	2.82E-06	2.71E-06	3.13E-05	3.94E-05	7.57E-05
FC-15	5.10E-05	6.34E-06	5.22E-06	5.99E-05	7.45E-05	1.17E-04
FC-20	7.34E-05	8.82E-06	2.74E-06	5.36E-05	8.06E-05	6.04E-05
DAF	106.20	108.94	59.95	44.54	59.95	39.06
Standard limits of groundwater and surface water's quality, mg/L						
GB/T14848-2017 limits III	–	≤ 0.05	≤ 0.05	≤ 0.02	≤ 0.005	≤ 0.70
GB3838-2002	≤ 0.05	≤ 0.05	≤ 0.05	≤ 0.02	≤ 0.005	≤ 0.70

The maximum availability of a CN-brick was tested under EA NEN 7371. **Figure 7A** shows that the leaching level tested under NEN 7371 is significantly higher than that tested under TCLP, by almost three orders of magnitude. This is because the pH level maintained in the NEN 7371 test is more stable by continuously adding HNO₃ in two leaching stages, which make it more ideal to represent the long-term leaching behavior of materials (Youcai and Sheng, 2017). Moreover, the solidification effect of different metals is different, for example, the total content of Ni is higher than that of Sb (1,311 and 386 mg/kg), but the maximum availability of Ni is lower than Sb (12.35 and 24.99 mg/kg). But in general, a higher FCC content indicates a higher metal leaching risk of a CN-brick.

Afterward, the daily leaching amount ($C_{Daily-Lea}$) is calculated from maximum availability in Equation (12):

$$C_{Daily-Lea} = \frac{C_{Max-Lea} \times p}{a \times d} \tag{12}$$

where p is the density of a CN-brick, which is equal to 2,117 kg/m³; a is the service life of a CN-brick, which is equal to 30 years; d is the days of use in a year, which is set as 365 days. The concentration of contaminants in groundwater (C_{gw}) was calculated from $C_{Daily-Lea}$ in Equations (13)–(15):

$$C_{gw} = C_{Daily-Lea}/DAF \tag{13}$$

$$DAF = DF \times AF \tag{14}$$

$$DF = \frac{(H' \times \theta_{as} + \theta_{ws} + K_d \times \rho_b) \times (1 + \frac{U_{gw} \times \delta_{gw}}{I_f \times W_{gw}})}{\rho_b} \times \frac{L_2}{L_1} \tag{15}$$

where DAF is the dilution attenuation factor. AF is selected as 1.0 since the maximum risk is considered. DF is calculated according to Equation (15) which is quoted from the Chinese standard HJ 25.3-2014 (HJ 25.3, 2014) and Wyoming Voluntary Remediation Program report (VRP, 2000). Equation (15) is widely utilized to represent the dilution effect of soil pollutants mitigating into groundwater. The reference values in the DF equation are listed in **Supplementary Table 1**, which are all quoted from the Chinese standard of risk assessment of contaminated sites (HJ 25.3, 2014), and the estimated DAFs are listed in **Table 4**. The values of C_{gw} are then determined in Equation (13) and compared with the Chinese groundwater quality standard (GB/T 14848, 2017) and surface water quality standard (GB 3838, 2002; **Table 4**). The groundwater concentrations of six heavy metals range from 2.74E-06 to 1.17E-04 mg/L, which are all way below the regulatory limit of quality standards, indicating that CN-bricks will not pollute the groundwater to an unacceptable level.

Human Health Risk Assessment

The final step of risk assessment is the human health risk assessment, which considers the hazards faced by nearby residents when they ingest pollutants through groundwater intake. The main exposure pathway discussed in this study is through drinking water, since other pathways (inhalation, skin, or food) can be far less harmful than a drinking water route. The daily intake of pollutants by an adult is calculated according to

Equation (16), which is quoted from Risk Assessment Guidance for Superfund RAGS (1989) of USEPA:

$$ADD = \frac{C_i \times IngR \times EF \times ED}{BW \times AT} \tag{16}$$

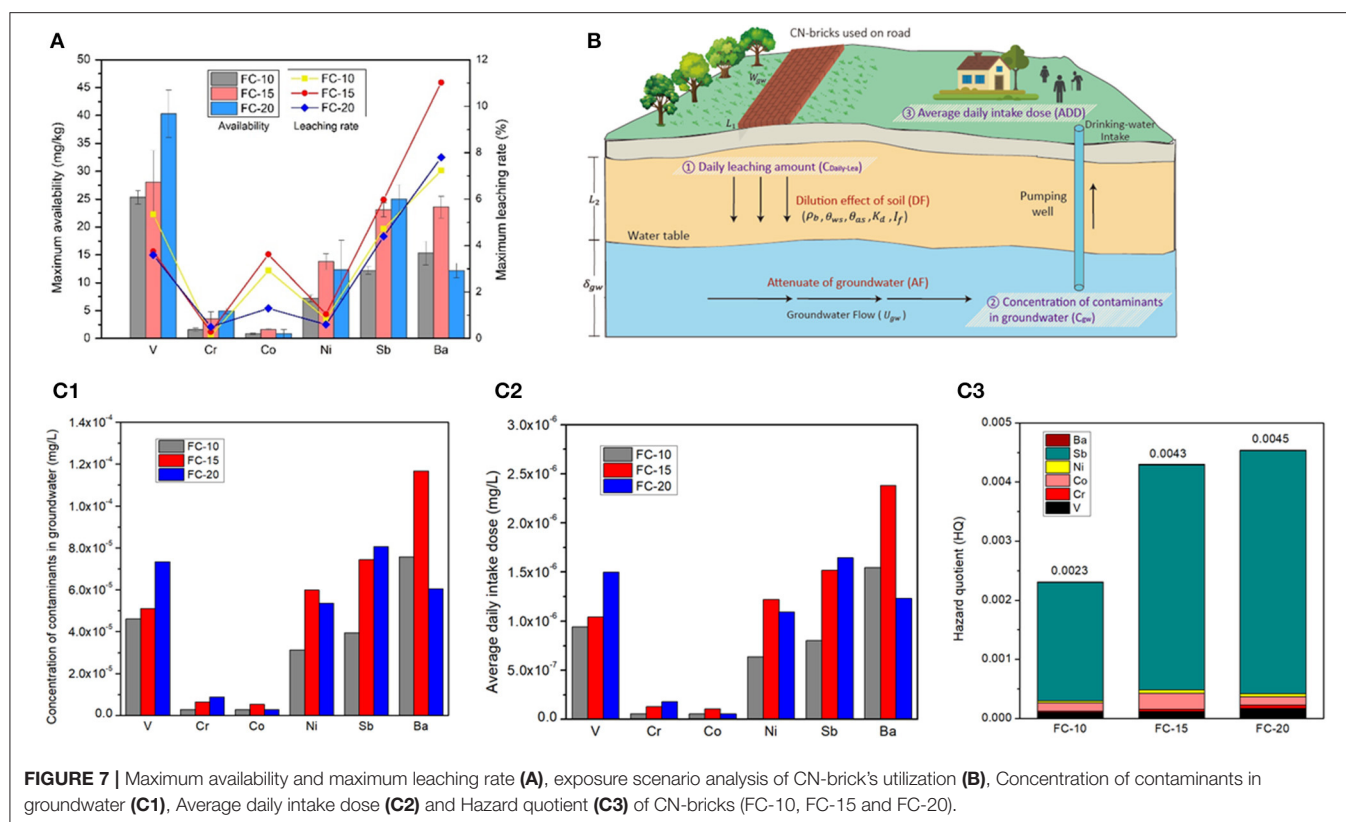where ADD is the average daily intake dose of an element i (mg/kg · day), and C_i is the concentration of a metal i in drinking water, which equals to C_{gw}. IngR is the ingestion rate; EF is exposure frequency; ED is the exposure duration; BW is the body weight; and AT is the average exposure time. The units and values of the above-mentioned parameters are summarized in **Supplementary Table 2**, and the results of ADD results are shown in **Figure 7C**. Then, the HQ is authenticated based on the ADD level. According to US Environmental Protection Agency (USEPA), chemicals are classified as carcinogens and non-carcinogens, the risk of which are, respectively, represented as cancer risk (CR) and HQ. According to USEPA, integrated risk information system (IRIS, 1989), and Chinese Standard HJ 25.3-2014 (HJ 25.3, 2014), only arsenic (As) in heavy metals is considered as carcinogen, all the six metals discussed earlier are not included. Thus, only non-carcinogenic risk is considered in this research, and the HQ is calculated as follows (RAGS, 1989):

$$HQ = \frac{ADD}{RfD_i} \tag{17}$$

where RfD_i is the referenced dose that is interpreted as "an exposure level that is likely to be without an appreciable risk of deleterious effects during a lifetime," and the RfD_i value of six elements is listed in **Supplementary Table 3** according to IRIS (1989). The RAGS guidance indicates that a HQ index lower than 1.0 shows an acceptable risk, whereas the potential of non-carcinogenic risk for human may occur when HQ > 1.0 (RAGS, 1989). To assess the overall non-carcinogenic risk of a CN-brick, the HQs of each contaminant should be summed up and presented as hazard index (HI).

$$HI = \sum_1^i HQ \tag{18}$$

The non-carcinogenic risk assessment results of three different CN-bricks are summarized in **Figure 7C**. CN-bricks with different proportions of a spent FCC catalyst have different HI, the more the spent FCC catalyst were added, the higher the HI will be, which are 0.0023, 0.0043, and 0.0045, respectively. All the HIs of three CN-bricks are all significantly lower than 1.0, proving that when a person is exposed to this dose level over a lifetime, no non-carcinogenic effects is expected to be detected in his/her body over a lifetime. In sum, CN-brick will not pose a threat to environment and human bodies, which can be utilized on road pavement for 30 years without environmental hazard. The environmental risk assessment result in this study can provide a technical basic for the assessment of the utilization of a CN-brick on roads and embankments in the future. For future application of CN-bricks on road, the groundwater detection well should be set nearby for regular detection of groundwater quality.

FIGURE 7 | Maximum availability and maximum leaching rate **(A)**, exposure scenario analysis of CN-brick's utilization **(B)**, Concentration of contaminants in groundwater **(C1)**, Average daily intake dose **(C2)** and Hazard quotient **(C3)** of CN-bricks (FC-10, FC-15 and FC-20).

In the process of using pavement materials, operators should take necessary protection to avoid working in windy weather.

It deserves attention from **Figure 7C** that the HQ of Sb accounts for 86.9, 88.4, and 90.6% of whole HI of FC-10, FC-15, and FC-20, respectively, which constitute a main environmental risk of CN-bricks. The reference dose of Sb, 0.0004 mg/kg · d, is much lower than other metals (**Supplementary Table 3**). Sb belongs to the same group as As and have a potential carcinogenic risk, so it has been listed as priority pollutant by US EPA and hazardous wastes by European Union. Sb is the third most abundant element in CN-bricks (**Figure 6**) due to the addition of Sb-type Ni passivator in the sampling unit, which is used to suppress the negative effects of metal Ni. Element Co also has a strict reference dose, 0.0004 mg/kg · d, but the daily intake dose of Co is way lower than Sb (**Figure 7C**), making it accounting for only a small part of the HI. For future production and utilization of a CN-brick, a raw material of spent FCC catalyst should be cautiously selected. The catalyst coming from units without a Sb-type Ni passivator should be given priority. For catalytic cracking unit in refinery plants, innoxious metal passivators without Sb should be preferred according to the result of environmental risk assessment in this study.

The environmental risk assessment of a CN-brick entails certain uncertainty, which is inevitable in quantitative risk assessment. In the calculation of contaminants in groundwater and ADD, the actual measured data should be given priority, so the reference date may induce a certain

deviation. However, there is no absolute accurate assessment, the exposure analysis in this study is based on a well-defined calculation and could represent the actual environmental risk of CN-bricks.

CONCLUSION

This paper focuses on utilizing a spent FCC catalyst as a partial replacement of a fine aggregate in the production of a NS-brick. 20% cement $+Na_2SO_4$ is proven to be an optimal binder system, which could improve the compressive strength up to 42.3 MPa. Best grain size distribution occurs at 20% spent FCC catalyst + 45% gravel, which could achieve the lowest porosity and water absorption rate, yet a higher spent FCC catalyst proportion would deteriorate the property of a CN-brick. The main hydration products of a CN-brick are C-S-H and AFt. Alkali activators could create an alkaline environment that dissolve more $[SiO_4]^{4-}$ and $[AlO_4]^{5-}$ from the raw materials, and Na_2SO_4 can particularly promote the formation of a needle-like AFt to a large extent. The TCLP test shows that V, Cr, Co, Ni, Sb, and Ba are the characteristic pollutants of CN-bricks. An exposure scenario analysis based on the NEN 7371 leaching test works out a final HI from 0.0023 to 0.0045 for a CN-brick, indicating its acceptable risk for environment and humans. Thus, it can be said that producing NS-bricks from a spent FCC catalyst is technically feasible and environment friendly.

DATA AVAILABILITY STATEMENT

The original contributions presented in the study are included in the article/**Supplementary Material**, further inquiries can be directed to the corresponding author/s.

AUTHOR CONTRIBUTIONS

SZ, SF, and HZ came up with the conception and directed the study. DZ, ZL, and ZZ carried out the experiments. DZ and ZL performed the statistical analysis. DZ finished the manuscript. All authors have revised the final version of the manuscript and approve of submission.

SUPPLEMENTARY MATERIAL

The Supplementary Material for this article can be found online at: https://www.frontiersin.org/articles/10.3389/fchem.2021.674271/full#supplementary-material

REFERENCES

Abdel-Gawwad, H. A., Mohammed, M. S., and Ads, E. N. (2020a). A novel eco-sustainable approach for the cleaner production of ready-mix alkali activated cement using industrial solid wastes and organic-based activator powder. *J. Clean. Prod.* 256:120705. doi: 10.1016/j.jclepro.2020.120705

Abdel-Gawwad, H. A., Mohammed, M. S., and Zakey, S. E. (2020b). Preparation, performance, and stability of alkali-activated-concrete waste-lead-bearing sludge composites. *J. Clean. Prod.* 259:120924. doi: 10.1016/j.jclepro.2020.120924

Akinyemi, B. A., Orogbade, B. O., and Okoro, C. W. (2021). The potential of calcium carbide waste and termite mound soil as materials in the production of unfired clay bricks. *J. Clean. Prod.* 279:123693. doi: 10.1016/j.jclepro.2020.123693

Al-Jabri, K., Baawain, M., Taha, R., Al-Kamyani, Z. S., Al-Shamsi, K., and Ishtieh, A. (2013). Potential use of FCC spent catalyst as partial replacement of cement or sand in cement mortars. *Construct. Build. Mater.* 39, 77–81. doi: 10.1016/j.conbuildmat.2012.05.035

Bohmer, R. W., McKay, D. L., and Knopp, K. G. (eds.). (1990). *Development and Application of FCC Catalyst Metals Passivation*. Washington, DC: American Chemical Society. doi: 10.1021/bk-1991-0452.ch011

Busca, G., Riani, P., Garbarino, G., Ziemacki, G., Gambino, L., Montanari, E., et al. (2014). The state of nickel in spent fluid catalytic cracking catalysts. *Appl. Catalysis A: Gene.* 486, 176–186. doi: 10.1016/j.apcata.2014.08.011

Dabaieh, M., Heinonen, J., El-Mahdy, D., and Hassan, D. M. (2020). A comparative study of life cycle carbon emissions and embodied energy between sun-dried bricks and fired clay bricks. *J. Clean. Prod.* 275:122998. doi: 10.1016/j.jclepro.2020.122998

EA NEN 7371 (2004). *Leaching Characteristics-Determination of the Availability of Inorganic Components for Leaching-Solid Earthy and Stony Materials*. Delft: Netherlands Standardization Institute.

EPA 1311 (1992). *Toxicity Characteristic Leaching Procedure*, Washington, DC: Environmental Protection Agency.

Etim, U. J., Xu, B., Bai, P., Ullah, R., Subhan, F., and Yan, Z. (2016). Role of nickel on vanadium poisoned FCC catalyst: a study of physiochemical properties. *J. Energy Chem.* 25, 667–676. doi: 10.1016/j.jechem.2016.04.001

Ferella, F., Innocenzi, V., and Maggiore, F. (2016). Oil refining spent catalysts: a review of possible recycling technologies. *Resour. Conserv. Recycl.* 108, 10–20. doi: 10.1016/j.resconrec.2016.01.010

Ferella, F., Leone, S., Innocenzi, V., Michelis, I., de, Taglieri, G., and Gallucci, K. (2019). Synthesis of zeolites from spent fluid catalytic cracking catalyst. *J. Clean. Prod.* 230, 910–926. doi: 10.1016/j.jclepro.2019.05.175

Font, A., Borrachero, M. V., Soriano, L., Monzó, J., and Payá, J. (2017). Geopolymer eco-cellular concrete (GECC) based on fluid catalytic cracking catalyst residue (FCC) with addition of recycled aluminium foil powder. *J. Clean. Prod* 168, 1120–1131. doi: 10.1016/j.jclepro.2017.09.110

GB 11945 (1999). *Autoclaved Lime-Sand Brick*. Beijing: National Standard of China.

GB 3838 (2002). *Environmental Quality Standards for Surface Water*. Beijing: National Standard of China.

GB 5085.3 (2007). *Identification Standards for Hazardous Wastes-Identification for Extraction Toxicity*. Beijing: National Standard of China.

GB/T 14848 (2017). *Standard for Groundwater Quality*. Beijing: National Standard of China.

GB/T 4111 (2013). *Test Method for the Concrete Block and Brick*. Beijing: National Standard of China.

Guo, X., Shi, H., Chen, L., and Dick, W. A. (2010). Alkali-activated complex binders from class C fly ash and Ca-containing admixtures. *J. Hazard. Mater.* 173, 480–486. doi: 10.1016/j.jhazmat.2009.08.110

Gupta, V., Chai, H. K., Lu, Y., and Chaudhary, S. (2020). A state of the art review to enhance the industrial scale waste utilization in sustainable unfired bricks. *Construct. Build. Mater.* 254:119220. doi: 10.1016/j.conbuildmat.2020.119220

HJ 25.3 (2014). *Technical Guidelines for Risk Assessment of Contaminated Sites*. Beijing: National Standard of China.

HJ 781 (2016). *Solid Waste- Determination of 22 Metal Elements-Inductively Coupled Plasma Optical Emission Spectrometry*. Beijing: National Standard of China.

HW (2016). *National Directory of Hazardous Wastes*. Beijing: Ministry of Ecology and Environment of the People's Republic of China.

IRIS (1989). *Integrated Risk Information System*. Washington, DC: U.S. Environmental Protection Agency, Office of Research and Development.

Lang, L., Chen, B., and Pan, Y. (2020). Engineering properties evaluation of unfired sludge bricks solidified by cement-fly ash-lime admixed nano-SiO2 under compaction forming technology. *Construct. Build. Mater.* 259:119879. doi: 10.1016/j.conbuildmat.2020.119879

Liu, J., Hu, L., Tang, L., and Ren, J. (2021). Utilisation of municipal solid waste incinerator (MSWI) fly ash with metakaolin for preparation of alkali-activated cementitious material. *J. Hazard. Mater.* 402:123451. doi: 10.1016/j.jhazmat.2020.123451

Meng, Y., Ling, T.-C., and Mo, K. H. (2018). Recycling of wastes for value-added applications in concrete blocks: an overview. *Resourc. Conserv. Recycl.* 138, 298–312. doi: 10.1016/j.resconrec.2018.07.029

Neves, R., Vicente, C., Castela, A., and Montemor, M. F. (2015). Durability performance of concrete incorporating spent fluid cracking catalyst. *Cement Concrete Comp.* 55, 308–314. doi: 10.1016/j.cemconcomp.2014.09.018

Payá, J., Monzó, J., Borrachero, M. V., and Velázquez, S. (2013). Cement equivalence factor evaluations for fluid catalytic cracking catalyst residue. *Cement Concrete Comp.* 39, 12–17. doi: 10.1016/j.cemconcomp.2013.03.011

RAGS (1989). *Risk-Assessment Guidance for Superfund (RAGS), Volume 1, Human Health Evaluation Manual (Part A)*. Washington, DC: Office of Emergency and Remedial Response.

Ramezani, A., Emami, S. M., and Nemat, S. (2017). Reuse of spent FCC catalyst, waste serpentine and kiln rollers waste for synthesis of cordierite and cordierite-mullite ceramics. *J. Hazard. Mater.* 338, 177–185. doi: 10.1016/j.jhazmat.2017.05.029

Taha, R., Al-Kamyani, Z., Al-Jabri, K., Baawain, M., and Al-Shamsi, K. (2012). Recycling of waste spent catalyst in road construction and masonry blocks. *J. Hazard. Mater.* 229–230, 122–127. doi: 10.1016/j.jhazmat.2012.05.083

USEPA (2011). *Toxicity Characteristic (40 CFR 261.24)*. Washington, DC: United States Environmental Protection Agency.

Vogt, E. T. C., and Weckhuysen, B. M. (2015). Fluid catalytic cracking: recent developments on the grand old lady of zeolite catalysis. *Chem. Soc. Rev.* 44, 7342–7370. doi: 10.1039/C5CS00376H

VRP (2000). *Using Fate and Transport Models to Evaluate Cleanup Levels. Voluntary Remediation Program*. cheyenne: Wyoming Department of Environmental Protection.

Wai, C. M., Frye, J. G., Fulton, J. L., Le, B., Silva, L. J., and Gerber, M. A. (1999). *Regeneration of Hydrotreating and FCC Catalysts*. doi: 10.2172/12208

Wang, C.-Q., Lin, X.-Y., Mei, X.-D., and Luo, X-G. (2019). Performance of non-fired bricks containing oil-based drilling cuttings pyrolysis residues of shale gas. *J. Clean. Prod.* 206, 282–296. doi: 10.1016/j.jclepro.2018.09.128

Wang, Y., Gao, S., Liu, X., Tang, B., Mukiza, E., and Zhang, N. (2019). Preparation of non-sintered permeable bricks using electrolytic manganese residue: environmental and NH3-N recovery benefits. *J. Hazard. Mater.* 378:120768. doi: 10.1016/j.jhazmat.2019.120768

Weishi, L., Guoyuan, L., Ya, X., and Qifei, H. (2018). The properties and formation mechanisms of eco-friendly brick building materials fabricated from low-silicon iron ore tailings. *J. Clean. Prod.* 204, 685–692. doi: 10.1016/j.jclepro.2018.08.309

Xue, Y., Wei, X., Zhao, H., Wang, T., and Xiao, Y. (2020). Interaction of spent FCC catalyst and asphalt binder: Rheological properties, emission of VOCs and immobilization of metals. *J. Clean. Prod.* 259:120830. doi: 10.1016/j.jclepro.2020.120830

Youcai, Z., and Sheng, H. (eds.). (2017). "Pretreatment and analysis methods of heavy metals and organic pollutants existing in construction and demolition waste," in: *Pollution Control and Resource Recovery. Butterworth-Heinemann* (Oxford). doi: 10.1016/B978-0-12-811754-5.00003-8

Zhang, Y. S., Lu, X., Owen, R. E., Manos, G., Xu, R., Wang, F. R., et al. (2020). Fine structural changes of fluid catalytic catalysts and characterization of coke formed resulting from heavy oil devolatilization. *Appl. Cataly. B: Environ.* 263:118329. doi: 10.1016/j.apcatb.2019.118329

MoO$_2$ Nanospheres Synthesized by Microwave-Assisted Solvothermal Method for the Detection of H$_2$S in Wide Concentration Range at Low Temperature

Fei An, Shanjun Mu, Shucai Zhang, Wei Xu, Na Li, Haozhi Wang, Shiqiang Wang, Chenyang Zhao, Junjie Feng, Lin Wang and Bing Sun*

State Key Laboratory of Safety and Control for Chemicals, SINOPEC Research Institute of Safety Engineering, Qingdao, China

It is crucial to develop highly energy-efficient and selective sensors for wide concentration range of H$_2$S, a common toxic gas that widely exists in petrochemical industries. In this work, MoO$_2$ nanospheres were rapidly synthesized by microwave-assisted solvothermal method, and were subsequently fabricated into H$_2$S gas sensor. The MoO$_2$ nanospheres-based sensor exhibited excellent response toward H$_2$S with good linearity in a wide concentration range (10–240 ppm). Besides, this sensor presented low working temperature, good repeatability, and selectivity against CH$_4$, H$_2$, and CO. The outstanding sensing performance results from the reaction between H$_2$S and abundant chemisorbed oxygen introduced by oxygen vacancies of MoO$_2$. This result indicates that MoO$_2$ nanosphere synthesized by microwave-assisted solvothermal method is a promising sensing material for H$_2$S detection.

Keywords: MoO$_2$ nanospheres, microwave, solvothermal, H$_2$S, broad range, gas sensor

INTRODUCTION

H$_2$S, a common gas in petroleum refining and storage, would cause serious pollution to air and great damage to human body once leaked (Hu et al., 2018). Therefore, the detection and monitoring of H$_2$S are vital for both environmental conservation and human health. In recent years, different kinds of H$_2$S sensors have been developed, such as electrochemical sensors, surface acoustic wave sensors and resistive sensors (Mirzaei et al., 2018; Zhao et al., 2018; Khan et al., 2019; Tang et al., 2019). Among them, resistive sensors based on metal oxide nanoparticles have attracted great attention due to the high sensitivity and short recovery time. The metal oxide nanoparticles applied for resistive sensors can be classified into two categories: n-type (ZnO, SnO$_2$, Fe$_2$O$_3$, and MoO$_3$) and p-type (CuO, Cr$_2$O$_3$, and Co$_3$O$_4$) semiconductors (Fine et al., 2010; Walker et al., 2019). However, both of them need high operation temperature to achieve good sensing performance, which results in energy consumption issues and gas explosions risks (Gupta Chatterjee et al., 2015). Besides, the detection range of H$_2$S for current nanoparticle based resistive sensors is mainly around the low end (<50 ppm), leading to inaccurate measurement of high concentration H$_2$S (Guo Y. et al., 2016; Sukunta et al., 2017; Tian et al., 2017).

MoO$_2$, a n-type semiconductor, has been applied as catalysts, photochromic, and electrochromic materials, due to good electronic conductivity and ion transport property (Ni et al., 2015; Jin et al., 2016; Zhang B. et al., 2017; Xia et al., 2018). However, there have been few reports on H$_2$S sensors fabricated with MoO$_2$. The preparation methodology of MoO$_2$ needs to be improved as well–MoO$_2$ is usually synthesized by the reduction of MoO$_3$ with H$_2$ or CO at ultrahigh temperature, which exhibits enormous risk of explosion (Wang L. et al., 2017; Prabhakar et al., 2018); conventional solvothermal/hydrothermal methods are milder ways to prepare MoO$_2$, however, the long processing time, additional surfactants and low yield restricts its application (Xiang et al., 2015; Wang et al., 2016; Zhang et al., 2019). Microwave-assisted solvothermal method is a promising alternative method for the preparation of MoO$_2$. Compared to traditional heat source, microwave irradiation generates a rapid heating to attain the desired temperature, due to the direct heating to polar molecules and conducting ions (Zhu and Chen, 2014). In contrast to the conventional solvothermal/hydrothermal methods, which suffer from large thermal gradients between the inner and outer media, the direct heating provides negligible thermal gradients through the reaction system (Mirzaei and Neri, 2016). The uniform heat distribution is beneficial for preparing regular products. Although MoO$_2$ nanoparticles prepared with microwave-assisted hydrothermal method has been reported, which still need additional carbon or graphene, the resultant MoO$_2$ nanoparticles shows irregular morphology (Palanisamy et al., 2015; Fattakhova and Zakharova, 2020). There are few works about MoO$_2$ nanospheres prepared with microwave-assisted solvothermal method without additional surfactants.

In this report, a new method to synthesize MoO$_2$ nanospheres without surfactant template by the microwave-assisted solvothermal method was presented. The morphology, crystalline, chemical state and stability of samples were investigated by SEM, XRD, XPS, and TGA. The working temperature, response, repeatability, and selectivity of the gas sensors based on MoO$_2$ nanospheres were further studied in a gas sensing measurement system. Finally, the gas sensing mechanism of MoO$_2$ nanospheres was discussed.

EXPERIMENTAL

Materials

MoCl$_5$ was purchased from Sigma-Aldrich (China), absolute ethanol was purchased from Sinopharm (China). All reagents were of analytical grade without further purification, and the deionized water was used in all experiments.

Fabrication of MoO$_2$ Nanospheres

MoO$_2$ nanospheres were synthesized by microwave-assisted solvothermal method. In a typical synthesis procedure, 0.57 g of MoCl$_5$ was dissolved in 240 ml absolute ethanol with vigorous stirring for 30 min. The MoCl$_5$ solution was transferred into autoclaves and heated at 200°C for 3 h in a microwave oven (Multiwave PRO, Anton Paar). After cooled to room temperature, the resulting precipitate was collected and washed by centrifuging in deionized water and absolute ethanol, followed by freeze-drying under vacuum for 2 days. The resultant MoO$_2$ nanospheres were named as MMOs. MMO-180 and MMO-160 were prepared at 180°C and 160°C for 3 h, respectively. For comparison, MoO$_2$ nanospheres were also synthesized by conventionally solvothermal method, in which the MoCl$_5$ solution was transferred into autoclaves and heated at 200°C for 24 h in an oven. The resultant MoO$_2$ nanospheres were named as CMOs.

Characterization

A scanning electron microscope (SEM, JEOL JSM-7610F) was used to observe the morphologies of MoO$_2$. X-ray diffraction (XRD) patterns were obtained on a Bruker D8 Advance Xray diffractometer with a Cu Kα radiation of 0.154 nm at a generator voltage of 40 kV. The chemical compositions of MoO$_2$ were measured using Thermo Fisher ESCALAB 250 XI X-ray photoelectron spectroscopy (XPS). Thermogravimetric analysis (TGA) was performed in air atmosphere with a heating rate of 10°C/min by using a Shimadzu DTG-60 A thermogravimetric analyzer.

Fabrication and Test of Gas Sensors

The MoO$_2$ powder was ground and mixed with terpineol at the mass ratio of 1:1 to form a paste. The paste was uniformly coated on the surface of alumina ceramic tube attached with a pair of gold electrodes, which were connected by Pt wires. A Ni-Cr heating wire was inserted into the tube to heat the gas sensor. Before the tests, the sensors were aged at 100°C for 5 days to improve stability. Gas sensing tests were performed on a commercial CGS-8 Gas Sensing Measurement System (Beijing Elite Tech Company Limited) with a test chamber (500 mL in volume). After the sensors' resistance was stabilized at the target temperature, a calculated volume of gas was injected into the chamber. All tests were conducted at a room temperature of 25 ± 5°C and at 40 ± 5% relative humidity.

The gas response is defined as (R$_{air}$-R$_{gas}$)/R$_{air}$ (R$_{air}$ and R$_{gas}$ are the sensors' resistance in air and target gas, respectively). The response time and recovery time is defined as the time taken for the response to reach 90% of total change after testing atmosphere changed.

RESULTS AND DISCUSSION

Morphology and Structure

Figure 1 shows the morphology of MoO$_2$ nanospheres prepared from microwave-assisted and conventional solvothermal method. The diameter of MMOs is in the range of 400–1,000 nm and the average diameter is about 740 nm. In contrast, CMOs own broader distribution of diameter and larger particle size, which affects the homogeneity and sensitivity of gas sensors. Besides, the process of microwave-assisted solvothermal method takes much less time than conventionally solvothermal method, because of the rapid microwave heating (Wang B. et al., 2017). The heating temperature is vital for the regular
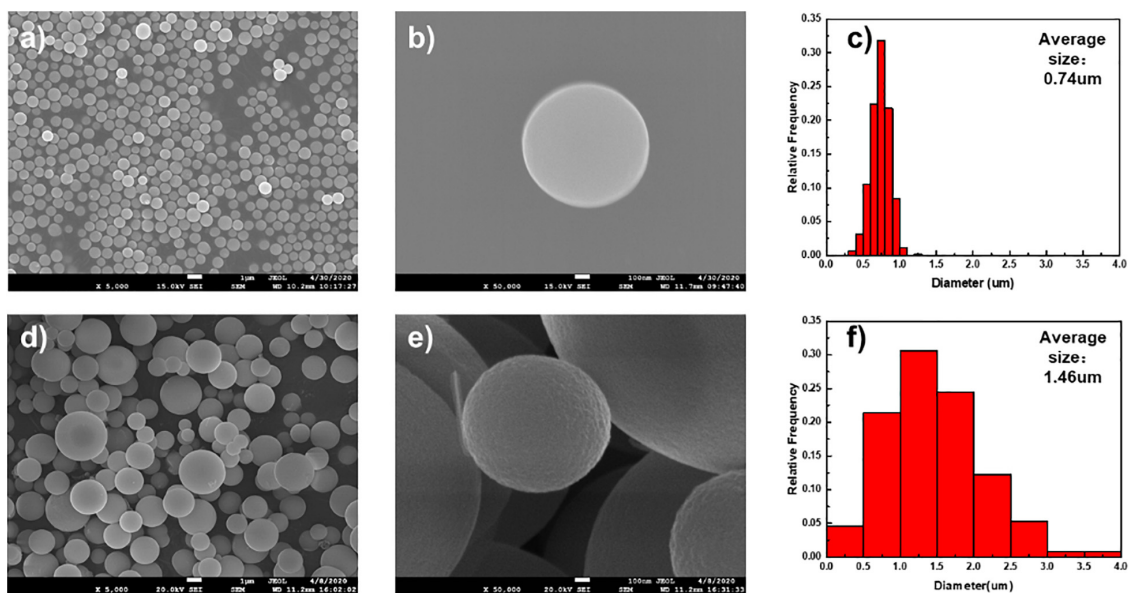
FIGURE 1 | SEM images and diameter statistics of **(a–c)** MMOs and **(d–f)** CMOs.
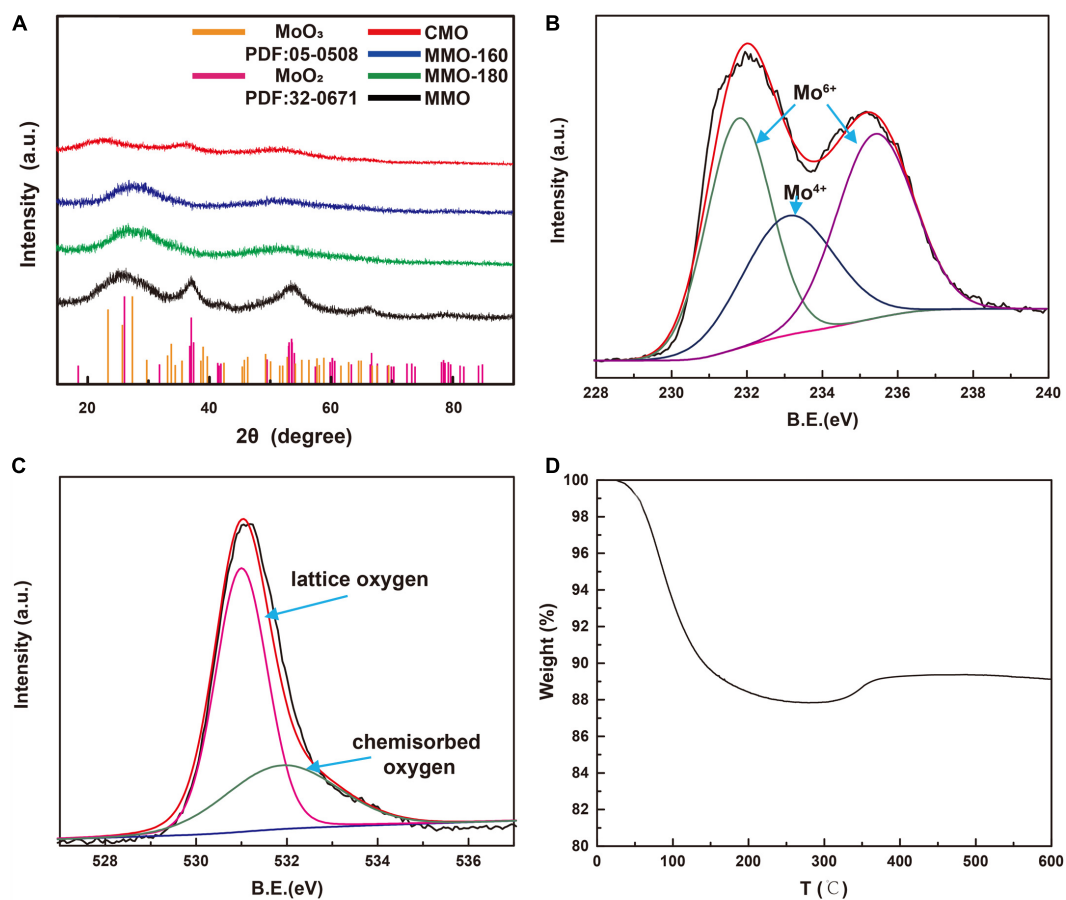
FIGURE 2 | (A) XRD patterns of MMO, MMO-180, MMO-160, and CMO; XPS spectra of **(B)** Mo 3d and **(C)** O1s, and **(D)** TGA curves of MMOs.
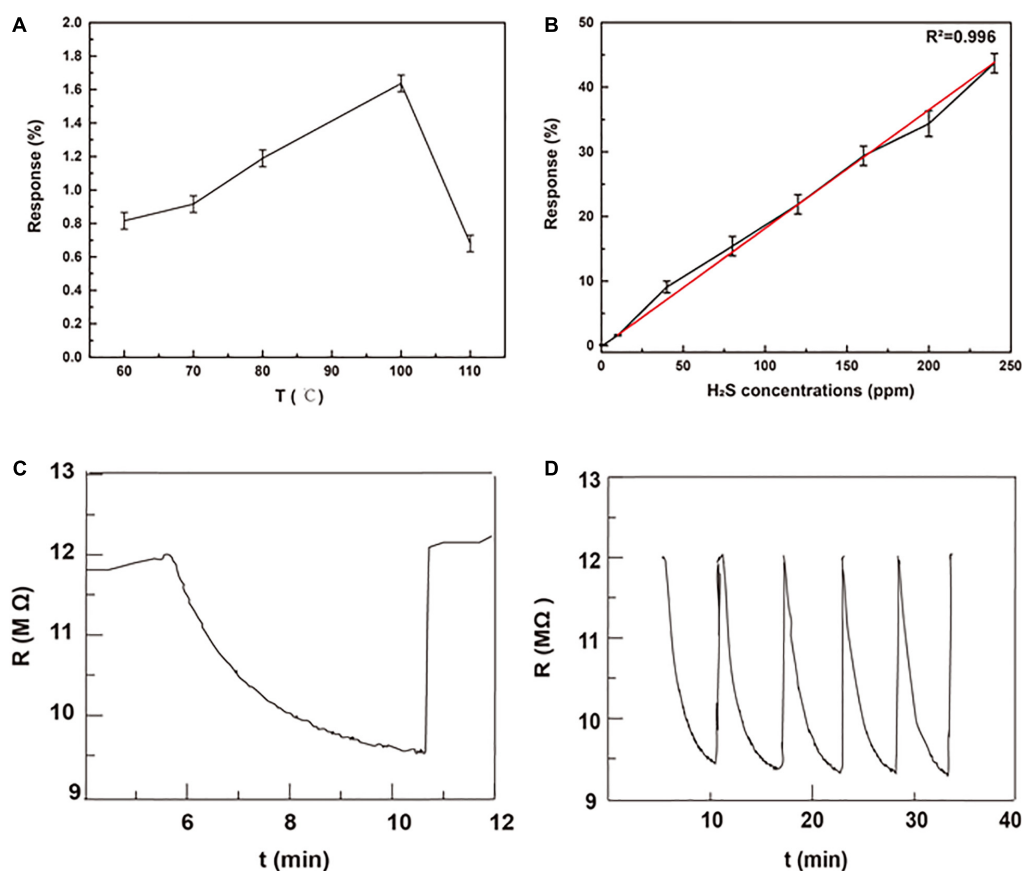
FIGURE 3 | (A) The response of MMOs to 10 ppm H$_2$S at different working temperature; **(B)** the response of MMOs to different H$_2$S concentration at 100°C; **(C)** the real-time response of MMOs to 40 ppm H$_2$S at 100°C; **(D)** five response cycles of MMOs to 40 ppm H$_2$S at 100°C.
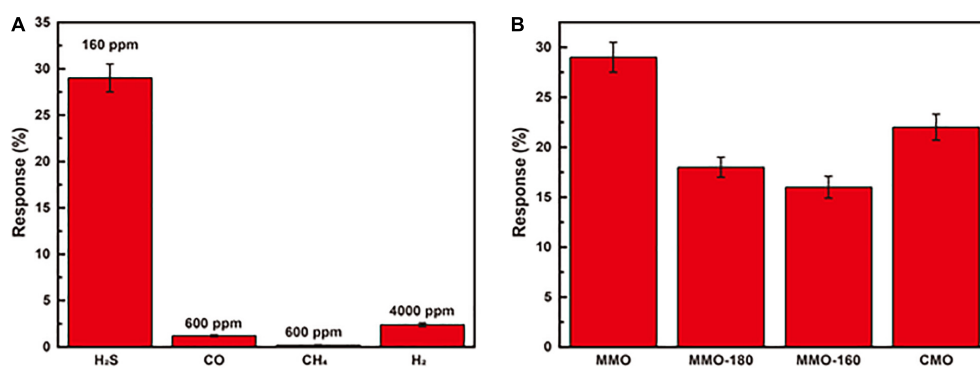
FIGURE 4 | (A) the response of MMOs to various gases; **(B)** the response of MMO, MMO-180, MMO-160, and CMO to 160 ppm H$_2$S.

morphology of MoO$_2$ nanospheres during microwave-assisted solvothermal method. As shown in **Supplementary Figure 1**, MMO-180 and MMO-160, prepared at lower temperature, exhibit irregular morphology, which may affect their sensing properties (Cai et al., 2015). Therefore, MMO is chosen to do further characterization and gas tests.

The crystal structure and chemical composition of MMOs were inspected by XRD and XPS. As shown in **Figure 2A**, MMO

has distinct diffraction peaks at 2θ = 26.03°, 36.852°, 53.512°, and 66.456°, which could be indexed to (−1 1 1), (1 1 1), (−3 1 2), and (2 0 2) planes of monoclinic MoO$_2$ phase according to the JCPDS 32-0671 (Kim et al., 2009). This suggests MoO$_2$ was successfully synthesized by microwave-assisted solvothermal method. On the contrary, MMO-180, MMO-160, and CMO have broader and weaker diffraction peaks, applying to the incomplete crystalline phase, which is consisted with the SEM images. To identify the

valence of Mo and the chemisorption of O, we characterized the MMOs by XPS. As shown in **Figure 2B**, XPS spectra of Mo consists of three peaks: two peaks at 231.7 and 235.6 eV present the Mo 3d$_{5/2}$ and Mo 3d$_{3/2}$ spin-obit components of Mo^{6+}, respectively; the peak at 233.1 eV is assigned to Mo 3d$_{5/2}$ of Mo^{4+} (Choi and Thompson, 1996). The appearance of Mo^{6+} indicates the slightly oxidation at the surface of MoO$_2$ by the exposure to air at room temperature, considering no distinguishing peaks of MoO$_3$ observed at XRD patterns as shown in **Figure 2A**. **Figure 2C** shows the XPS spectra of O 1 s, consisted of two peaks at 531 and 531.9 eV, corresponding to lattice and chemisorbed oxygen, respectively. The appearance of chemisorbed oxygen results from the coordination unsaturation of Mo, implying the presence of oxygen vacancy (Yang et al., 2015). The abundant chemisorbed oxygen is beneficial for the sensitivity of MoO$_2$, since the resistance change is mainly occurred by the reaction between chemisorbed oxygen and target gas (Jian et al., 2020). TGA curves of MMO (**Figure 2D**) shows a decrease of mass before 300°C, due to the loss of adsorbed water. During this temperature range, there is no obvious increase of mass, which implies MMOs are relative stable at low temperature. The stability of MMOs at low temperature is crucial for the repeatability of gas sensors. At higher temperature, a slight increase of mass occurred, corresponding to the oxidation of MoO$_2$.

Gas Sensing Properties

The response to H$_2$S depends on the physical and chemical absorption of gas, which is strongly affected by the working temperature (Su et al., 2019). Thus, we investigated the optimal working temperature of MMO gas sensor. As shown in **Figure 3A**, the response of MMO gas sensors to 10 ppm H$_2$S increased first and then decreased as the working temperature rising. The optimal working temperature is 100°C, which is much

TABLE 1 | Comparison of sensing performance between MMO and other metal oxide.

Materials	Optimal working temperature (°C)	Range of H$_2$S concentration (ppm)	Reference
Pt-WO$_3$	365	1–5	Kim et al., 2018
Pt-SnO$_2$	250	1–5	Bulemo et al., 2018
Fe$_2$O$_3$/TiO$_2$	120	1–50	Xu et al., 2019
NiO-SnO$_2$	200	1–10	Ngoc Hoa et al., 2019
MoO$_3$	177	1–100	Zhang et al., 2016
SnO$_2$-CuO	150	1–40	Park et al., 2020
MoO$_2$	100	1–240	This work

lower than that of other metal oxide gas sensors and beneficial for energy saving (Guo W. et al., 2016; Wang et al., 2019; Nguyen et al., 2020). The low working temperature may come from the abundant chemisorbed oxygen and oxygen vacancy in MMO (Shen et al., 2019). Therefore, further tests of sensing properties are all completed at 100°C.

Figure 3B presents the response of MMO to H$_2$S at different concentrations (1–240 ppm). It can be seen the response increases significantly with increasing concentration of H$_2$S, and there is good linear relationship (R^2 = 0.996) between response and the concentration of H$_2$S in the whole range. Unlike other sensors' narrow range of linear relationship, sensors of MMO with good linear relationship in a broad range are suitable for detection of H$_2$S with large change of concentration (Na et al., 2019; Teng et al., 2020). The response and recovery curve of MMO to 40 ppm H$_2$S at 100°C is shown in **Figure 3C** with a response time of ∼6 min and recovery time of ∼1 min. The repeatability presented in **Figure 3D** is also important for gas sensors and other devices (Kong et al., 2021a,b). The curves of response
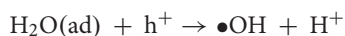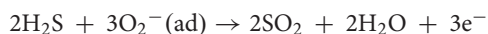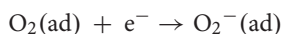

FIGURE 5 | Schematic diagram of H$_2$S sensing mechanism of MMOs.
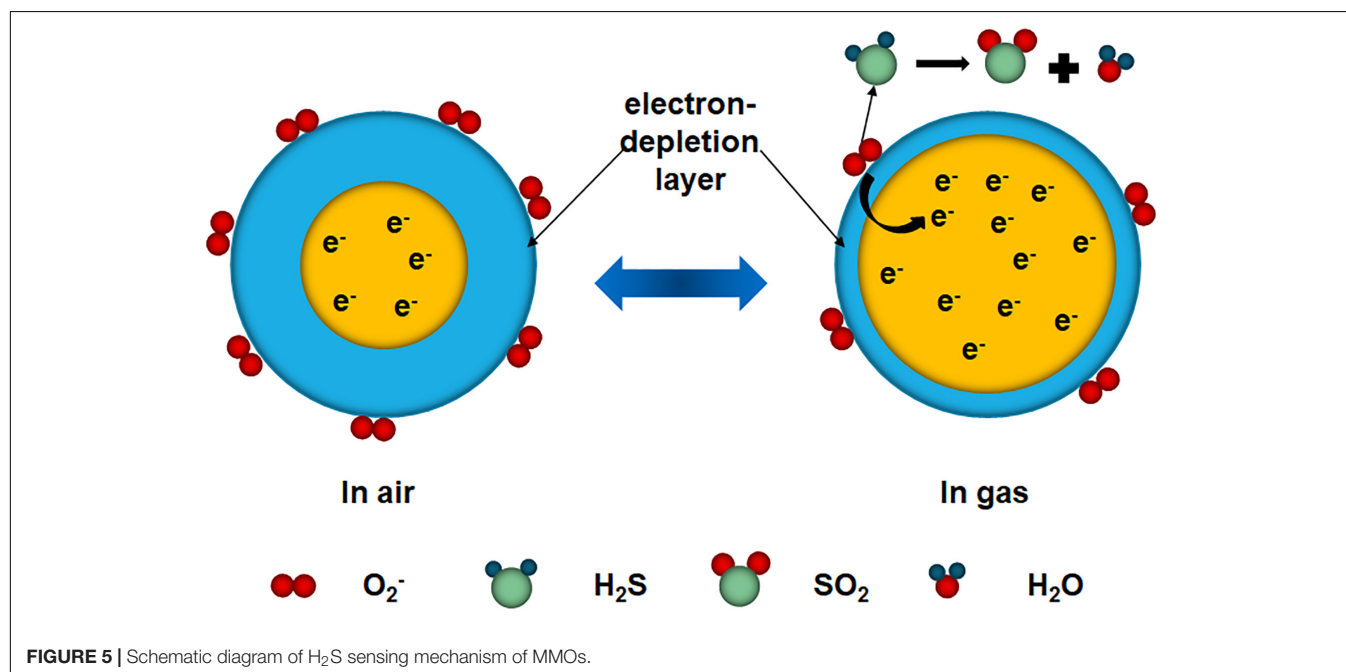
show negligible difference after repeating five cycles of tests to 40 ppm H_2S, which implies good repeatability and stability of MMO. To investigate the selectivity of MMO sensor, it was exposed to various gases, including CH_4, H_2, and CO. As shown in **Figure 4A**, the sensor exhibits higher response to H_2S than other gases, which could greatly weaken the interference of non-target gases. The response of MMO, MMO-180, MMO-160, and CMO are shown in **Figure 4B**, in which MMO has the highest response to H_2S.

Table 1 summarizes the sensing performance of different metal oxide to H_2S. Compared to other metal oxide in early work, MMO sensor exhibits lower working temperature and wider concentration range to detect H_2S. Besides, the good repeatability and selectivity makes MMO sensor suitable for detection of H_2S leakage in chemical petrochemical companies.

Gas Sensing Mechanism

As a typical *n*-type semiconductor, the sensing performance of MMO strongly depends on the free electron density (**Figure 5**). According to the density functional theory (DFT), the adsorption and dissociation of O_2 on MoO_2 surface could occur rapidly at room temperature, due to the high adsorption energy and low dissociation barrier (Zhang Q. et al., 2017). Therefore, when MMO exposed to air, oxygen molecules adsorb onto the surface of MMO and take free electrons from MMO, forming chemisorbed oxygen (O_2^-) and resistant electron-depletion layer (EDL) as the working temperature below 150°C (Franke et al., 2006). This leads to decreased free electron density and increased resistance (Mirzaei et al., 2018). After H_2S was injected into the chamber, H_2S molecules react with O_2^- to form SO_2 and water vapor. In this process, free electrons trapped by O_2^- come back to the MMO, causing the increased free electron density and decreased resistance (Katoch et al., 2015). After exposed to air again, the oxygen molecules will be re-adsorbed and reconstruct the EDL. During the tests, H_2O also participated in the reaction *via* reacting with hole (h^+) to render the radical hydroxyl($\bullet OH$), which justifies the optimal working temperature is 100°C.

The whole reaction is described below:

$$O_2(g) \leftrightarrow O_2(ad)$$

$$O_2(ad) + e^- \rightarrow O_2^-(ad)$$

$$2H_2S + 3O_2^-(ad) \rightarrow 2SO_2 + 2H_2O + 3e^-$$

$$H_2O(ad) + h^+ \rightarrow \bullet OH + H^+$$

As discussed in XPS characterization before, there is abundant chemisorbed oxygen on the surface of MMO, which could react with a large of H_2S molecules without saturation. This causes the good linear relationship in a broad range of MMO sensors to H_2S.

REFERENCES

Bulemo, P. M., Cho, H. J., Kim, D. H., and Kim, I. D. (2018). Facile synthesis of Pt-functionalized meso/macroporous SnO_2 hollow spheres through in situ templating with SiO_2 for H_2S sensors. *ACS Appl. Mater. Interfaces* 10, 18183–18191. doi: 10.1021/acsami.8b00901

CONCLUSION

MoO_2 nanospheres was rapidly synthesized by microwave-assisted solvothermal method at 200°C for 3 h. The resultant MMO exhibit more regular dimension than CMON prepared by conventionally solvothermal method. At an optical working temperature of 100°C, the MMO-based sensors exhibit excellent response, linear relationship, repeatability and selectivity toward a broad concentration range of H_2S (10–240 ppm). The oxygen vacancies on the surface of MMO results in abundant chemisorbed oxygen which could react with H_2S, causing outstanding sensing performance of MMO sensors. In a word, MoO_2 nanosphere with abundant chemisorbed oxygen is a promising sensing material for detection of H_2S leakage in chemical companies.

DATA AVAILABILITY STATEMENT

The original contributions presented in the study are included in the article/**Supplementary Material**, further inquiries can be directed to the corresponding author/s.

AUTHOR CONTRIBUTIONS

FA, SM, BS, and SZ contributed to conception and design of the study. WX organized the database. NL performed the statistical analysis. HW wrote the first draft of the manuscript. SW, CZ, JF, and LW wrote sections of the manuscript. All authors contributed to manuscript revision, read, and approved the submitted version.

FUNDING

SUPPLEMENTARY MATERIAL

The Supplementary Material for this article can be found online at: https://www.frontiersin.org/articles/10.3389/fmats.2021.670044/full#supplementary-material

Supplementary Figure 1 | SEM images of **(A,B)** MMO-180 and **(C,D)** MMO-160.

Cai, Z.-X., Yang, X.-N., Li, H.-Y., and Guo, X. (2015). NO sensing by single crystalline WO_3 nanowires. *Sens. Actuators B* 219, 346–353. doi: 10.1016/j.snb.2015.05.036

Choi, J. G., and Thompson, L. T. (1996). XPS study of as-prepared and reduced molybdenum oxides. *Appl. Surf. Sci.* 93, 143–149. doi: 10.1016/0169-4332(95)00317-7

Fattakhova, Z. A., and Zakharova, G. Z. (2020). MoO$_2$/C composites: synthesis, properties, and formation mechanism. *Russ. J. Inorg. Chem.* 65, 480–487. doi: 10.1134/S0036023620040051

Fine, G. F., Cavanagh, L. M., Afonja, A., and Binions, R. (2010). Metal oxide semi-conductor gas sensors in environmental monitoring. *Sensors* 10, 5469–5502. doi: 10.3390/s100605469

Franke, M., Koplin, T., and Simon, U. (2006). Metal and metal oxide nanoparticles in chemiresistors: does the nanoscale matter? *Small* 2, 36–50. doi: 10.1002/smll.200500261

Guo, W., Mei, L., Wen, J., and Ma, J. (2016). High-response H$_2$S sensor based on ZnO/SnO$_2$ heterogeneous nanospheres. *RSC Adv.* 6, 15048–15053. doi: 10.1039/C5RA22187K

Guo, Y., Gong, M., Li, Y., Liu, Y., and Dou, X. (2016). Sensitive, selective, and fast detection of ppb-level H$_2$S gas boosted by ZnO-CuO mesocrystal. *Nanoscale Res. Lett.* 11:475. doi: 10.1186/s11671-016-1688-y

Gupta Chatterjee, S., Chatterjee, S., Ray, A. K., and Chakraborty, A. K. (2015). Graphene–metal oxide nanohybrids for toxic gas sensor: a review. *Sens. Actuators B* 221, 1170–1181. doi: 10.1016/j.snb.2015.07.070

Hu, X., Zhu, Z., Li, Z., Xie, L., Wu, Y., and Zheng, L. (2018). Zheng, heterostructure of CuO microspheres modified with CuFe$_2$O$_4$ nanoparticles for highly sensitive H$_2$S gas sensor. *Sens. Actuators B* 264, 139–149. doi: 10.1016/j.snb.2018.02.110

Jian, Y., Hu, W., Zhao, Z., Cheng, P., Haick, H., Yao, M., et al. (2020). Gas sensors based on chemi-resistive hybrid functional nanomaterials. *Nano Micro Lett.* 12:71. doi: 10.1007/s40820-020-0407-5

Jin, Y., Wang, H., Li, J., Yue, X., Han, Y., Shen, P. K., et al. (2016). Porous MoO$_2$ nanosheets as non-noble bifunctional electrocatalysts for overall water splitting. *Adv. Mater.* 28, 3785–3790. doi: 10.1002/adma.201506314

Katoch, A., Choi, S. W., Kim, J. H., Lee, J. H., Lee, J. S., and Sang, S. K. (2015). Importance of the nanograin size on the H$_2$S-sensing properties of ZnO–CuO composite nanofibers. *Sens. Actuators B* 214, 111–116. doi: 10.1016/j.snb.2015.03.012

Khan, M., Rao, M., and Li, Q. (2019). Recent advances in electrochemical sensors for detecting toxic gases: NO$_2$, SO$_2$ and H$_2$S. *Sensors* 19:905. doi: 10.3390/s19040905

Kim, M. H., Jang, J. S., Koo, W. T., Choi, S. J., Kim, S. J., Kim, D. H., et al. (2018). Bimodally porous WO$_3$ microbelts functionalized with Pt catalysts for selective H$_2$S sensors. *ACS Appl. Mater. Interfaces* 10, 20643–20651. doi: 10.1021/acsami.8b00588

Kim, W.-S., Kim, H.-C., and Hong, S.-H. (2009). Gas sensing properties of MoO$_3$ nanoparticles synthesized by solvothermal method. *J. Nanopar. Res.* 12, 1889–1896. doi: 10.1007/s11051-009-9751-6

Kong, D., Li, J., Guo, A., and Xiao, X. (2021a). High temperature electromagnetic shielding shape memory polymer composite. *Chem. Eng. J.* 408:127365. doi: 10.1016/j.cej.2020.127365

Kong, D., Li, J., Guo, A., Yu, J., and Xiao, X. (2021b). Smart polyimide with recovery stress at the level of high temperature shape memory alloys. *Smart Mater. Strut.* 30:035027. doi: 10.1088/1361-665X/abe182

Mirzaei, A., Kim, S. S., and Kim, H. W. (2018). Resistance-based H$_2$S gas sensors using metal oxide nanostructures: a review of recent advances. *J. Hazard. Mater.* 357, 314–331. doi: 10.1016/j.jhazmat.2018.06.015

Mirzaei, A., and Neri, G. (2016). Microwave-assisted synthesis of metal oxide nanostructures for gas sensing application: a review. *Sens. Actuators B* 237, 749–775. doi: 10.1016/j.snb.2016.06.114

Na, H.-B., Zhang, X.-F., Zhang, M., Deng, Z.-P., Cheng, X.-L., Huo, L.-H., et al. (2019). A fast response/recovery ppb-level H$_2$S gas sensor based on porous CuO/ZnO heterostructural tubule via confined effect of absorbent cotton. *Sens. Actuators B* 297, 126816–126826. doi: 10.1016/j.snb.2019.126816

Ngoc Hoa, T. T., Hoa, N. D., Van Duy, N., Hung, C. M., Thanh Le, D. T., Van Toan, N., et al. (2019). An effective H$_2$S sensor based on SnO$_2$ nanowires decorated with NiO nanoparticles by electron beam evaporation. *RSC Adv.* 9, 13887–13895. doi: 10.1039/C9RA01105F

Nguyen, H. T. T., Truong, T. H., Nguyen, T. D., Dang, V. T., Vu, T. V., Nguyen, S. T., et al. (2020). Ni-doped WO$_3$ flakes-based sensor for fast and selective detection of H$_2$S. *J. Mater. Sci. Mater. Electron.* 31, 12783–12795. doi: 10.1007/s10854-020-03830-9

Ni, J., Zhao, Y., Li, L., and Mai, L. (2015). Ultrathin MoO$_2$ nanosheets for superior lithium storage. *Nano Energy* 11, 129–135. doi: 10.1016/j.nanoen.2014.10.027

Palanisamy, K., Kim, Y., Kim, H., Kim, J. M., and Yoon, W. S. (2015). Self-assembled porous MoO$_2$/graphene microspheres towards high performance anodes for lithium ion batteries. *J. Power Sour.* 275, 351–361. doi: 10.1016/j.jpowsour.2014.11.001

Park, K.-R., Cho, H.-B., Lee, J., Song, Y., Kim, W.-B., and Choa, Y.-H. (2020). Design of highly porous SnO$_2$-CuO nanotubes for enhancing H$_2$S gas sensor performance. *Sens. Actuators B* 302, 127179–127185. doi: 10.1016/j.snb.2019.127179

Prabhakar, R. K., Mhamane, N. B., Kumar, G. M., and Gopinath, C. S. (2018). Mapping valence band and interface electronic structure changes during oxidation of Mo to MoO$_3$ via MoO$_2$ and MoO$_3$ reduction to MoO$_2$: a nappes study. *J. Phys. Chem. C* 122, 23034–23044. doi: 10.1021/acs.jpcc.8b07024

Shen, S., Zhang, X., Cheng, X., Xu, Y., Gao, S., Zhao, H., et al. (2019). Oxygen-vacancy-enriched porous α-MoO$_3$ nanosheets for trimethylamine sensing. *ACS Appl. Nano Mater.* 2, 8016–8026. doi: 10.1021/acsanm.9b02072

Su, Y., Chen, P., Wang, P., Ge, J., Hu, S., Zhao, Y., et al. (2019). Pd-loaded SnO$_2$ hierarchical nanospheres for a high dynamic range H$_2$S micro sensor. *RSC Adv.* 9, 5987–5994. doi: 10.1039/C8RA09156K

Sukunta, J., Wisitsoraat, A., Tuantranont, A., Phanichphant, S., and Liewhiran, C. (2017). Highly-sensitive H$_2$S sensors based on flame-made V-substituted SnO$_2$ sensing films. *Sens. Actuators B* 242, 1095–1107. doi: 10.1016/j.snb.2016.09.140

Tang, Q. B., Guo, Y. J., Tang, Y. L., Long, G. D., Wang, J. L., Li, D. J., et al. (2019). Highly sensitive and selective love mode surface acoustic wave ammonia sensor based on graphene oxides operated at room temperature. *J. Mater. Sci.* 54, 11925–11935. doi: 10.1007/s10853-019-03764-6

Teng, Y., Zhang, X.-F., Xu, T.-T., Deng, Z.-P., Xu, Y.-M., Huo, L.-H., et al. (2020). A spendable gas sensor with higher sensitivity and lowest detection limit towards H$_2$S: porous α-Fe$_2$O$_3$ hierarchical tubule derived from poplar branch. *Chem. Eng. J.* 392, 123679–123688. doi: 10.1016/j.cej.2019.123679

Tian, K., Wang, X. X., Yu, Z. Y., Li, H. Y., and Guo, X. (2017). Hierarchical and hollow Fe$_2$O$_3$ nanoboxes derived from metal-organic frameworks with excellent sensitivity to H$_2$S. *ACS Appl. Mater. Interfaces* 9, 29669–29676. doi: 10.1021/acsami.7b07069

Walker, J. M., Akbar, S. A., and Morris, P. A. (2019). Synergistic effects in gas sensing semiconducting oxide nano-heterostructures: a review. *Sens. Actuators B* 286, 624–640. doi: 10.1016/j.snb.2019.01.049

Wang, B., He, J., Liu, F., and Ding, L. (2017). Rapid synthesis of Cu$_2$O/CuO/rGO with enhanced sensitivity for ascorbic acid biosensing. *J. Alloys Compd.* 693, 902–908. doi: 10.1016/j.jallcom.2016.09.291

Wang, L., Bu, C.-Y., Zhang, G.-H., Wang, J.-S., and Chou, K.-C. (2017). Study of the reduction of industrial grade MoO$_3$ powders with CO or CO-CO$_2$ gases to prepare MoO$_2$. *Metall. Mater. Trans. B* 48, 2047–2056. doi: 10.1007/s11663-017-0979-8

Wang, P., Hui, J., Yuan, T., Chen, P., Su, Y., Liang, W., et al. (2019). Ultrafine nanoparticles of W-doped SnO$_2$ for durable H$_2$S sensors with fast response and recovery. *RSC Adv.* 9, 11046–11053. doi: 10.1039/C9RA00944B

Wang, Y., Yu, L., and Lou, X. W. (2016). Formation of triple-shelled molybdenum-polydopamine hollow spheres and their conversion into MoO$_2$/carbon composite hollow spheres for lithium-ion batteries. *Angew. Chem.* 55, 14668–14672. doi: 10.1002/anie.201608410

Xia, C., Zhou, Y., Velusamy, D. B., Farah, A. A., Li, P., Jiang, Q., et al. (2018). Anomalous Li storage capability in atomically thin two-dimensional sheets of nonlayered MoO$_2$. *Nano Lett.* 18, 1506–1515. doi: 10.1021/acs.nanolett.7b05298

Xiang, Z., Zhang, Q., Zhang, Z., Xu, X., and Wang, Q. (2015). Preparation and photoelectric properties of semiconductor MoO$_2$ micro/nanospheres with wide bandgap. *Ceram. Int.* 41, 977–981. doi: 10.1016/j.ceramint.2014.09.017

Xu, Z., Liu, H., Tong, X., Shen, W., Chen, X., and Bloch, J.-F. (2019). A low operating temperature and high performance sensor for H$_2$S detection based on α-Fe$_2$O$_3$/TiO$_2$ heterojunction nanoparticles composite. *J. Mater. Sci. Mater. Electron.* 30, 12695–12709. doi: 10.1007/s10854-019-01634-0

Yang, S., Wang, Z., Hu, Y., Luo, X., Lei, J., Zhou, D., et al. (2015). Highly responsive room-temperature hydrogen sensing of alpha-MoO$_3$ nanoribbon membranes. *ACS Appl. Mater. Interfaces* 7, 9247–9253. doi: 10.1021/acsami.5b01858

Zhang, B., Xue, Y., Jiang, A., Xue, Z., Li, Z., and Hao, J. (2017). Ionic liquid as reaction medium for synthesis of hierarchically structured one-dimensional

MoO$_2$ for efficient hydrogen evolution. *ACS Appl. Mater. Interfaces* 9, 7217–7223. doi: 10.1021/acsami.7b00722

Zhang, L., Liu, Z., Jin, L., Zhang, B., Zhang, H., Zhu, M., et al. (2016). Self-assembly gridding α-MoO$_3$ nanobelts for highly toxic H$_2$S gas sensors. *Sens. Actuators B* 237, 350–357. doi: 10.1016/j.snb.2016.06.104

Zhang, Q., Zhang, M., and Wiltowski, T. (2017). Adsorption and dissociation of O$_2$ on MoO$_2$(111) surfaces: a DFT study. *Phys. Chem. Chem. Phys.* 43, 29244–29254. doi: 10.1039/C7CP06456J

Zhang, W., Wang, B., Luo, H., Jin, F., Ruan, T., and Wang, D. (2019). MoO$_2$ nanobelts modified with an MOF-derived carbon layer for high performance lithium-ion battery anodes. *J. Alloys Compd.* 803, 664–670. doi: 10.1016/j.jallcom.2019.06.337

Zhao, Y., Yang, Y., Cui, L., Zheng, F., and Song, Q. (2018). Electroactive Au@Ag nanoparticles driven electrochemical sensor for endogenous H$_2$S detection. *Biosens. Bioelectron.* 117, 53–59. doi: 10.1016/j.bios.2018.05.047

Zhu, Y. J., and Chen, F. (2014). Microwave-assisted preparation of inorganic nanostructures in liquid phase. *Chem. Rev.* 114, 6462–6555. doi: 10.1021/cr400366s

The Research of G–Motif Construction and Chirality in Deoxyguanosine Monophosphate Nucleotide Complexes

Yanhong Zhu[1], Zhongkui Li[1], Pengfei Wang[1], Qi–Ming Qiu[1], Hongwei Ma[2] and Hui Li[1]*

[1]Key Laboratory of Cluster Science of Ministry of Education, School of Chemistry and Chemical Engineering, Beijing Institute of Technology, Beijing, China, [2]Analytical and Testing Centre, Beijing Institute of Technology, Beijing, China

A detailed understanding of the mismatched base-pairing interactions in DNA will help reveal genetic diseases and provide a theoretical basis for the development of targeted drugs. Here, we utilized mononucleotide fragment to simulate mismatch DNA interactions in a local hydrophobic microenvironment. The bipyridyl-type bridging ligands were employed as a mild stabilizer to stabilize the GG mismatch containing complexes, allowing mismatch to be visualized based on X-ray crystallography. Five single crystals of 2′-deoxyguanosine–5′–monophosphate (dGMP) metal complexes were designed and obtained *via* the process of self-assembly. Crystallographic studies clearly reveal the details of the supramolecular interaction between mononucleotides and guest intercalators. A novel guanine–guanine base mismatch pattern with unusual (*high anti*)–(*high anti*) type of arrangement around the glycosidic angle conformations was successfully constructed. The solution state ^{1}H–NMR, ESI–MS spectrum studies, and UV titration experiments emphasize the robustness of this g–motif in solution. Additionally, we combined the methods of single-crystal and solution-, solid-state CD spectrum together to discuss the chirality of the complexes. The complexes containing the g–motif structure, which reduces the energy of the system, following the solid-state CD signals, generally move in the long-wave direction. These results provided a new mismatched base pairing, that is g–motif. The interaction mode and full characterizations of g–motif will contribute to the study of the mismatched DNA interaction.

Keywords: base-pair mismatch, g–motif, self-assembly, chirality, crystal structure

INTRODUCTION

The non–B-DNA secondary structures (Afek et al., 2020; Xiong et al., 2021), which are folded in a different manner from B-DNA or form unnatural base pairs that are not used for Watson–Crick (G≡C and A = T) base pairing (Watson and Crick, 1953; Brovarets' et al., 2018), can induce genetic instability and cause a variety of human diseases (Brovarets' et al., 2019; Li et al., 2020). However, the research of mismatched base-pairing interactions has great significance because they play an important role in various processes related to the biological function of nucleic acids (Iyer et al., 2006; Granzhan et al., 2014; Mondal et al., 2016), helping to reveal genetic diseases caused by the non–B-DNA structures. In biological systems, for example, aberrant amplification of the hexanucleotide GGGGCC (G4C2) repeated in the human *C9ORF72* gene is the most common
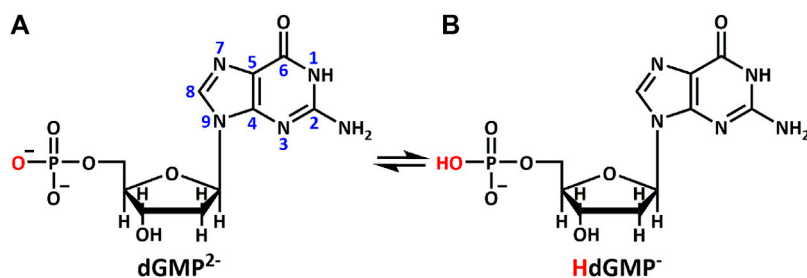
SCHEME 1 | Different protonation states of (A) dGMP^{2-} and (B) HdGMP^{-} in aqueous solution.

genetic factor found behind frontotemporal dementia (FTD) and amyotrophic lateral sclerosis (ALS) (DeJesus-Hernandez et al., 2011). Recently, Tuân Phan group have shown the structures of DNA and RNA duplexes formed by G4C2 repeats, which alternately contain two types of GG mismatched base pair (Maity et al., 2021). Based on the structural analysis of mismatched base pairs in a variety of sequence contexts, it is shown that mismatches are highly polymorphic in nature; many of the mismatched base pairs can exist as protonated bases, such as bifurcated hydrogen bonds, wobble pairs, and various pairing conformations involving *syn–syn*, *anti–ant*, and *anti–syn* isomerization (Faibis et al., 1996; Varani and McClain, 2000; Ghosh et al., 2014).

How to construct and describe mismatched base-pairing interactions in structural details is a key issue for understanding the mechanism of the formation of non–B-DNA and finding effective ways to treat some genetic diseases. Numerous studies have shown that many small-molecule intercalators with pharmaceutical and/or diagnostic potential (Satange et al., 2018; Pages et al., 2019) can recognize mismatched DNA or RNA duplexes and induce various degrees of structural deformations. The existence of unstable mismatches in nucleic acid sequences may cause nucleobases flipping into additional helical positions, which itself is a significant phenomenon observed during the binding of small-molecule ligands to DNA or RNA duplexes (Jourdan et al., 2012; Tseng et al., 2017). DNA bending is also considered to be an important consequence of the action of those small molecules inserted into the DNA duplexes (Hou et al., 2002; Hall et al., 2011; Hall et al., 2014). Significantly, many structural features of small-molecule–DNA complexes have also been found in DNA–protein complexes, which indicate that in some cases, they may share similar interaction mechanisms (Chen et al., 2018; Da and Yu, 2018).

The non–B-DNA secondary structures known as G-quadruplex (G4), formed by alternative GG Hoogsteen mismatches at physiological temperature and potassium concentration, found in oncogene promoters and telomeres are often used as antitumor and antibacterial targets (Musumeci et al., 2016; Hansel-Hertsch et al., 2017; Hansel-Hertsch et al., 2018; Punt et al., 2020). The appealing possibility to treat cancers without impairing normal cells stimulated the synthesis of large libraries of putative selective G-quadruplex

targeted ligands. For example, naphthalene diimides (NDIs) have a remarkable potential as anticancer drugs because of their well-proven ability to strongly interact with G-quadruplex (Salvati et al., 2016; Pirota et al., 2019; Platella et al., 2020a; Platella et al., 2020b). Encouraged by these results, many scientists use various optical methods (Gómez-González et al., 2018; Zhang and Wang, 2019; Lim and Hohng, 2020; Chen et al., 2021) and DFT theoretical calculations (Wu et al., 2012; Yao et al., 2013; Shi et al., 2015; Wang et al., 2019) to undertake an in-depth research on the interaction of intercalators and G-quadruplex, to reveal the structural details of this strong and specific binding. As we know, the visualization of these "host–guest" interactions based on X-ray crystallography will help understand the details of interactions between functional intercalations and targets, as well as the nucleotide conformational polymorphism changes. Although some related researches have been reported by single-crystal XRD (Monestier et al., 2017; Chu et al., 2019; Geng et al., 2019; Satange et al., 2019; Mao et al., 2020), the well-defined structure of "host–guest" interaction about intercalator-mismatched DNA remains as a fundamental and challenging issue for comprehensive understanding of the biological processes in genomic DNA. A proper design and synthesis of molecular building blocks is an effective methodological strategy to obtain innovative functional materials, which is an ultimate target in supramolecular chemistry. Based on the research of nucleotide–metal complexes, the diversities of coordination and supramolecular self-assembly inspired us to design and investigate the materials with programmable functions, by taking advantage of their unique properties including specific recognition ability, tunable conformations, and biocompatibility.

In the current study, $2'$–deoxyguanosine–$5'$–monophosphate (dGMP) fragment was used to simulate the interaction between small-molecule intercalators and mismatched DNA in a local hydrophobic microenvironment, in order to understand its structural consequences for DNA duplexes. We use bipyridine bridged ligands as a mild stabilizer in order to stabilize and enable crystallization of the GG mismatch containing complexes. Five complexes of dGMP with transition metals (**Scheme 1**), [Co(HdGMP)$_2$(H$_2$O)$_4$]·(4,4$'$-bipy)·3H$_2$O (1), [Co(HdGMP)$_2$(H$_2$O)$_4$]·(bpe)·4H$_2$O (2), [Co(HdGMP)$_2$(H$_2$O)$_4$]·(bpa)·4H$_2$O (3), and {[Zn (bpda) (H$_2$O)$_4$]·(HdGMP)·4H$_2$O}$_n$ (4), [Mn (dGMP) (H$_2$O)$_5$]·3H$_2$O (5), [4,4$'$–bipy = 4,4$'$–bipyridine, bpe = 1,2-bis(4-pyridyl)ethene, bpa = 1,2–bis(4-pyridyl)ethane, and bpda = 1,4-bis(4-pyridy)–2,3-diaza-1,3-butadiene]

TABLE 1 | Crystallographic data for complexes 1–5. Bold values are CCDC number of Crystals.

Complex	1	2	3	4	5
Formula	$C_{30}H_{50}CoN_{12}O_{22}P_2$	$C_{32}H_{52}CoN_{12}O_{22}P_2$	$C_{32}H_{54}CoN_{12}O_{22}P_2$	$C_{32}H_{52}N_{14}O_{22}P_2Zn$	$C_{10}H_{28}MnN_5O_{15}P$
Mr	1,051.69	1,077.72	1,079.74	1,112.18	544.28
Crystal system	Orthorhombic	Monoclinic	Monoclinic	Orthorhombic	Monoclinic
Space group	$P2_12_12$	$P2_1$	$P2_1$	$P2_12_12$	$C2$
a (Å)	15.2094(9)	6.9901(7)	7.0917(2)	15.7257 (5)	27.735 (2)
b (Å)	20.6549(12)	20.7406(19)	20.6519(7)	21.0314 (7)	11.2485 (11)
c (Å)	7.0696(4)	15.2603(14)	15.2533(5)	6.9203 (2)	6.7722 (6)
α (°)	90	90	90	90	90
β (°)	90	92.454(3)	92.7700(10)	90	92.021 (8)
γ (°)	90	90	90	90	90
V (Å³)	2,220.9(2)	2,210.4(4)	2,231.34(12)	2,288.78 (12)	2,111.4 (3)
Z	2	2	2	2	4
F (000)	1,094.0	1,122.0	1,126.0	1,156.0	1,132.0
Reflections collected	24,804	30,266	21,882	22,389	8,544
Independent reflections	4,711	12,673	7,887	4,037	3,994
Goodness–of–fit on F^2	1.093	0.976	1.024	1.052	1.027
Completeness to 2θ	53.46,100.0%	60.08,99.9%	50.04,99.9%	50.03, 99.9%	53.46, 99.5%
R_{int}	0.0341	0.0564	0.0263	0.0270	0.0461
R_1 [$I > 2\sigma(I)$]	0.0760	0.0516	0.0319	0.0813	0.0379
wR_2 [$I > 2\sigma(I)$]	0.2264	0.0865	0.0799	0.2224	0.0806
R_1 (all data)	0.0855	0.1052	0.0371	0.0903	0.0450
wR_2 (all data)	0.2372	0.1029	0.0826	0.2319	0.0844
Flack parameter	0.02(5)	0.012(18)	0.011(15)	0.015 (7)	–0.02 (2)
CCDC Number	**2,064,323**	**2,064,324**	**2,064,325**	**2,064,326**	**2,064,327**

were successfully designed and obtained *via* the process of self-assembly. We use X-ray crystallography to observe the supramolecular interactions between small guest molecules and isolated mismatched base pair. A novel guanine–guanine base mismatch pattern with unusual (*high anti*)—(*high anti*) type of arrangement around the glycosidic angle conformations was successfully constructed. This base pair is different from GG Hoogsteen base pairs and reverse Watson–Crick GG mismatched base pairing (Mondal et al., 2016)[7], but is similar to hemiprotonated CC+ and AA base pairs in i–motif and A–motif, respectively. So, we named it g–motif in this work. Precise structures indicate that the shorter auxiliary ligands produce the g–motif structure in which guanine is involved in the coordination at N7 site due to their smaller space; the longer bridging ligand provides a bigger hydrophobic microenvironment for guanine bases; thus, a perfect g–motif structure is presented. Certainly, the g–motif is not produced in the absence of auxiliary ligand. These results will be meaningful for revealing the genetic instability, and provide insights on intercalator–mismatch DNA interactions and a rationale. Obviously, it also provides a certain theoretical basis for the development of targeted therapeutic drugs.

RESULTS AND DISCUSSION

Design and Synthesis

In biological systems, short nucleotide fragments (such as single nucleotides and dinucleotides) usually cannot form stable hydrogen-bonded base pairs or duplexes in aqueous environments until higher order oligomers are used (Philp and Stoddart, 1996), because water molecules are constant competitors. Hence, a majority of studies involve hydrogen bonds, which

typically exploit additional weak interactions [aromatic stacking (Kato et al., 1995; Westover et al., 2004; Korostelev et al., 2006) or the hydrophobic effect (Jourdan et al., 1999; Hirschberg et al., 2000)] or employ noncompetitive organic solvents to shield from the competing water molecules.

In our strategy, the bipyridyl-type bridging ligands with different sizes were chosen as a multifunctional auxiliary ligand; on the one hand, they can precisely adjust the orientation of purine bases through stacking interactions; on the other hand, they can provide an ideal flat, hydrophobic microenvironment with different interplanar distances for the binding of single planar aromatic molecules (nucleobase or nucleotide). Additionally, they can prevent the nonenzymatic hydrolysis of nucleotide phosphate groups and increase the crystallization of nucleotide complexes, because the bridging ligands would coordinate to metal ions by competing with dGMP as a structure modifier. As a result, under the co-control of auxiliary ligands and solvent based on the above design idea, we successfully synthesized and obtained 1–4 in water–ethanol solution (the ratio is 2:1) and 5 in water solvent.

Crystal Structure and G–motif

All of the complexes were obtained at a slightly acidic condition and studied by the X-ray single crystal diffraction method. Complexes 1–3 and 5 are mononuclear nucleotide complexes, but 4 is a 1D coordination polymer. The nucleotides in 1–3 are coordinated with metal ions, and the auxiliary ligands exist as guest molecules. However, 4 is opposite to 1–3, which is a 1D coordination polymer linked by the auxiliary ligand as a bridge ligand and the nucleotide is uncoordinated. Complex 5 is a binary
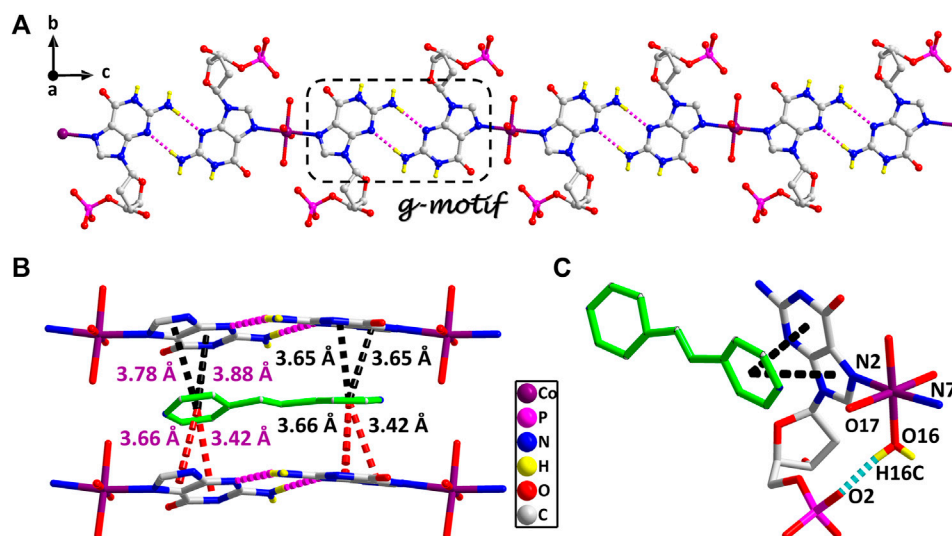
FIGURE 1 | (A) The 1D supramolecular structure of two viewed from *a* axis. **(B)** The π–π stacking interactions in the 2D structure of two. **(A)** Various noncovalent interactions in high *trans* conformation (O16–H16C···O2, 0.84 Å, 1.90 Å, 2.70 Å, 159°). Partially shaded area of **(A)** is the g–motif structure (N5–H5A···N9, 0.86 Å, 2.11 Å, 2.96 Å, 171°; N10–H10 A···N4, 0.86 Å, 2.13 Å, 2.99 Å, 175°) (cobalt: violet, carbon: gray, hydrogen: yellow, oxygen: red, nitrogen: blue, and phosphorus: pink).

complex without the participation of auxiliary ligands. The protonated nucleotide HdGMP can be determined by the length of the longer uncoordinated P–O bond *via* X-ray diffraction at a good accuracy. The crystallographic data for complexes 1–5 are summarized in **Table 1**. Interestingly, ternary nucleotide complexes (1–4) with the auxiliary ligand can be obtained only in organic solvents, while binary nucleotide complex (5) can be obtained just in pure water environment. Clearly, the solvent effect also plays an important and effective role to control the formation of nucleotide complexes.

Complexes 1–3 are essentially isomorphous, except for the size of the bridging ligand (**Supplementary Figure S3**). Since the size of the auxiliary ligand in 2 (bpe = 9.4 Å) is greater than that of 1 (bipy = 7.1 Å) and the stiffness is stronger than that of 3, we take 2 as an example for structural analysis. In addition, the molecular structure diagrams and related hydrogen bond information of 1 and 3 are given for comparison (**Supplementary Figures S4–S8**). The single crystal X-ray diffraction analysis reveals that Co(II) central in 2 is six-coordinated, showing a N_2O_4 octahedral coordination mode with two imidazole N atoms (N2 and N7) from HdGMP at the axial positions and four oxygen atoms from water molecules at the equatorial positions (**Supplementary Figure S1**). Another four water molecules and one bpe molecule exist as guest molecules and play an important role in the geometry and conformation of the nucleoside moiety. The terminal P–O bond lengths are 1.565(4) Å for *p* (1)–O (4) and 1.561(4) Å for *p* (2)–O (10) in 2, whereas the mean value of P–O is 1.517(3) Å for nonprotonated nucleotides (**Supplementary Tables S3, S6**), so the longer bond length indicates that only those oxygen atoms (O4 and O10) are protonated.

The stereochemistry around the glycosidic bond C (1′)–N bond angle χ for the purine bases in two is unusual. They are measured by the C (8)–N (1)–C (5)–O (5) and C (18)–N (6)–C

(15)–O (12) (χ) torsion angle, which is –76 (1)° for the N (1)–bound Co(II) central and –82 (1)°for the N (6)–bound Co(II) central, respectively. This special conformation can be described as high *anti*, –*sc* (Cini and Pifferi, 1999; Asami et al., 2012) for the coordinated nucleotide (**Supplementary Figure S2**). To the best of our knowledge, this extreme position described as high *anti* is not frequent for nucleoside and has never been found before for the solid-state structures of dGMP nucleotides. Intriguingly, upon studying the H-bonding of 2, we found that the complex has a novel guanine–guanine base mismatch pattern (**Figure 1A**). Because of very limited examples in the GG mismatch base pairs with the structural details and in order to specify the mismatch base pair study as well, the g–motif has been named for the first time in this manuscript. Compared with the hydrogen bonds of G–quadruplex, the g–motif base pair of two has a slightly longer bond length and a larger angle except for the absence of N–H···O-type hydrogen bonds (Complex 2: N–H···N, 2.96–2.99 Å, 171°–175°; G–quadruplex: N–H···N, 2.88–2.91 Å, 166–170°, N–H···O, 2.86–2.92 Å, 159–165°). Simultaneously, this kind of H-bonding can expand the structure of this complex from 0D into a 1D linear chain (**Figure 1A**).

These observations lead us to suspect that bridging ligands play a key role in relating the stereochemistry of the base with respect to the sugar and the formation of the g–motif structure. Further studies indicated that the deviations of the Co(II) central from the plane of the purine bases are obviously smaller (0.18 Å and 0.18 Å) in 2, and the N(2)–Co–N(7) angle is close to 180° (172°). However, compared with other complexes (Poojary and Manohar, 1988), the coordination geometry and mode of metal central are the same as that of 2, except for the guest molecule, which forms a sharp contrast with 2. In those complexes, the Co(II) central is significantly out of the plane of the purine rings, and the deviations were 0.67–0.68 Å. Even though the N–Co–N angles are about 82.3–84.5°, the dihedral angle between the two
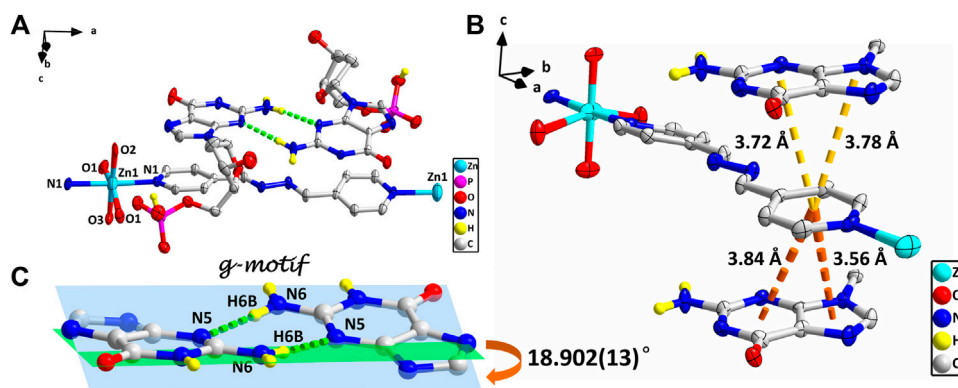
FIGURE 2 | (A) Molecular structure of four. The uncoordinated water molecules and part of hydrogen atoms are omitted for clarity. **(B)** The π–π stacking interactions in four. **(C)** g–motif and dihedral angle in four (N6–H6A⋯N5, 0.86 Å, 2.18 Å, 3.04 Å, 177°). The protonation of phosphate is highlighted by yellow hydrogen atoms. (zinc: turquoise, carbon: gray, hydrogen: yellow, oxygen: red, nitrogen: blue, and phosphorus: pink).

purine bases is only 40–50°. Therefore, the noncovalent interactions between purine bases and auxiliary ligands in 2 can fix and stabilize this extreme conformation of purine bases, and further induce it to form an almost perfect plane along *a* axis (**Figure 1A**). This hypothesis was confirmed by a crystal structure analysis, in which multiple π–π stacking interaction was formed between the auxiliary ligands and the nucleobases (**Figure 1B**; **Supplementary Figure S4**). Another reason is the strong intramolecular hydrogen bonds among the coordinated water molecules (O15 and O16) with the phosphate oxygen atoms (O2 and O9) and carbonyl oxygen atoms of the purine base (O7 and O14), which can also limit the flexible conformation of guanine nucleotides (**Figure 1C**). It is worth noting that this extreme conformation high *anti* is caused by the cooperation of those above noncovalent interactions.

Furthermore, the 1D linear chains are combined into a 2D supramolecular sheet *via* N–H⋯O hydrogen bonds between pyrimidine nitrogen atoms (N3 and N8) and the phosphate oxygen atoms (O3 and O11) in the adjacent chains (**Supplementary Figure S6**). Based on hydrogen bonds formed by the hydroxy group of the pentose ring with carbonyl oxygen atom of the base, these 2D structures can be further assembled into a 3D sandwiched framework (**Supplementary Figure S7**). Although the bridging ligand bpe does not participate in the coordination, it plays a decisive role in the formation of the g–motif structure. As a Lewis base, bpe can not only act as a buffer regulator of solution pH but also induce the formation of g–motif through stacking interaction. The shorter bridging ligand 4,4'-bipy and the more flexible auxiliary ligand bpa can also still induce the formation of the g–motif structure. The structural details of their g–motif can be seen in **Supplementary Figure S5**. Due to the narrow hydrophobic microenvironment of 4,4'-bipy in 1, the π–π stacking interaction between the pyridine ring and the purine base is significantly weakened. So the corresponding hydrogen bond interaction in 1 is slightly weaker than that in 2. The length of bpa is close to bpe, so the hydrogen bond strength of g–motif in 2 and 3 is almost the same. However, the dihedral

angle of g–motif is less than that of 2 for the flexibility of bpa, which makes it more adaptable to the orientation of purine bases.

However, studies have shown that due to blockage of N7 of the purine ring, the same hydrogen bonding patterns occur on the minor groove binding face in this nucleobase (Sigel et al., 2002). To further demonstrate the universality of this strategy, we chose bpda (11.2 Å) with larger molecular length as the bridging ligand, and fortunately obtained the single crystal structure of 4. X-ray diffraction shows that 4 is made up of 1D linear [Zn (bpda) $(H_2O)_4]^+$ cationic chains, uncoordinated partially protonated [HdGMP]⁻ anions, and guest water molecules. The protonated nucleotide [HdGMP]⁻ can still be determined by the relatively longer uncoordinated P–O bond length (**Supplementary Table S5**; **Supplementary Figure S9**). The coordination geometry of the Zn(II) central in the 1D Zn (bpda) $(H_2O)_4{}^{2+}$ chain is presently a deformed octahedral geometry with two nitrogen atoms from two different bridging molecules at the axial positions and four coordinated water molecules in the equatorial sites (**Supplementary Figure S9**). It is remarkable that the guest partial protonation [HdGMP]⁻ anions also have g–motifs, and the dihedral angle of the base rings is 18.9 (2)° (**Figures 2A,C**). Compared with 1–3, the N7 site in 4 does not coordinate with the metal ion, but still produced the same base-pair mismatch, which well demonstrated the effectiveness of our strategy. There are multiple π–π stacking interactions between the coordinated bridging ligand bpda and the guest [HdGMP]⁻ anions (**Figure 2B**). The Zn⋯Zn distance of four bridged by the bpda is 15.702 (1) Å. Each pyridine ring of bpda is basically directly opposite to the purine base part of [HdGMP]⁻ (**Figure 2B**), and the distance of the –C=N–N=C– part of bpda exactly matches the space required to form a guanine–guanine base pair, so that the prospective g–motif structure has been obtained. If the bpda ligands are ignored, these dimers, which were connected by g–motif, obtain a 2D H-bonding layer through hydrogen bonds between the base and the phosphate oxygen (**Supplementary Figure S10**). Then, the same layers are further linked into the 3D supramolecular structure *via* the
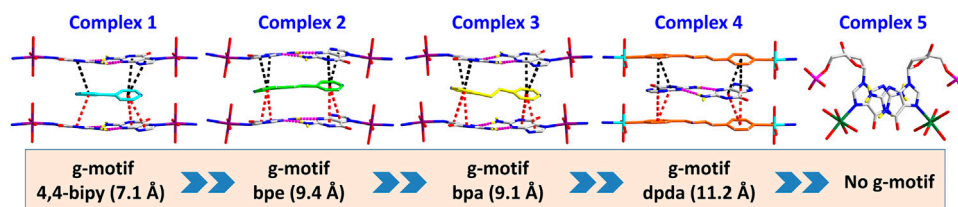
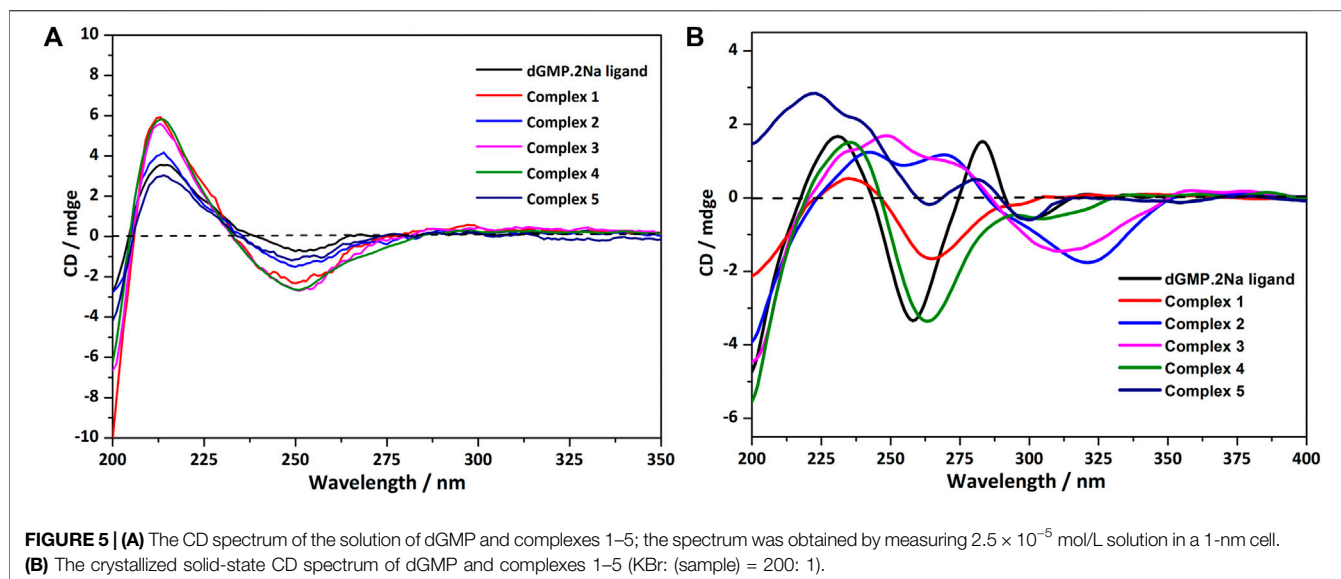**FIGURE 3 |** Summary of crystal structures presenting g–motif and π–π stacking interaction in complexes 1–5.
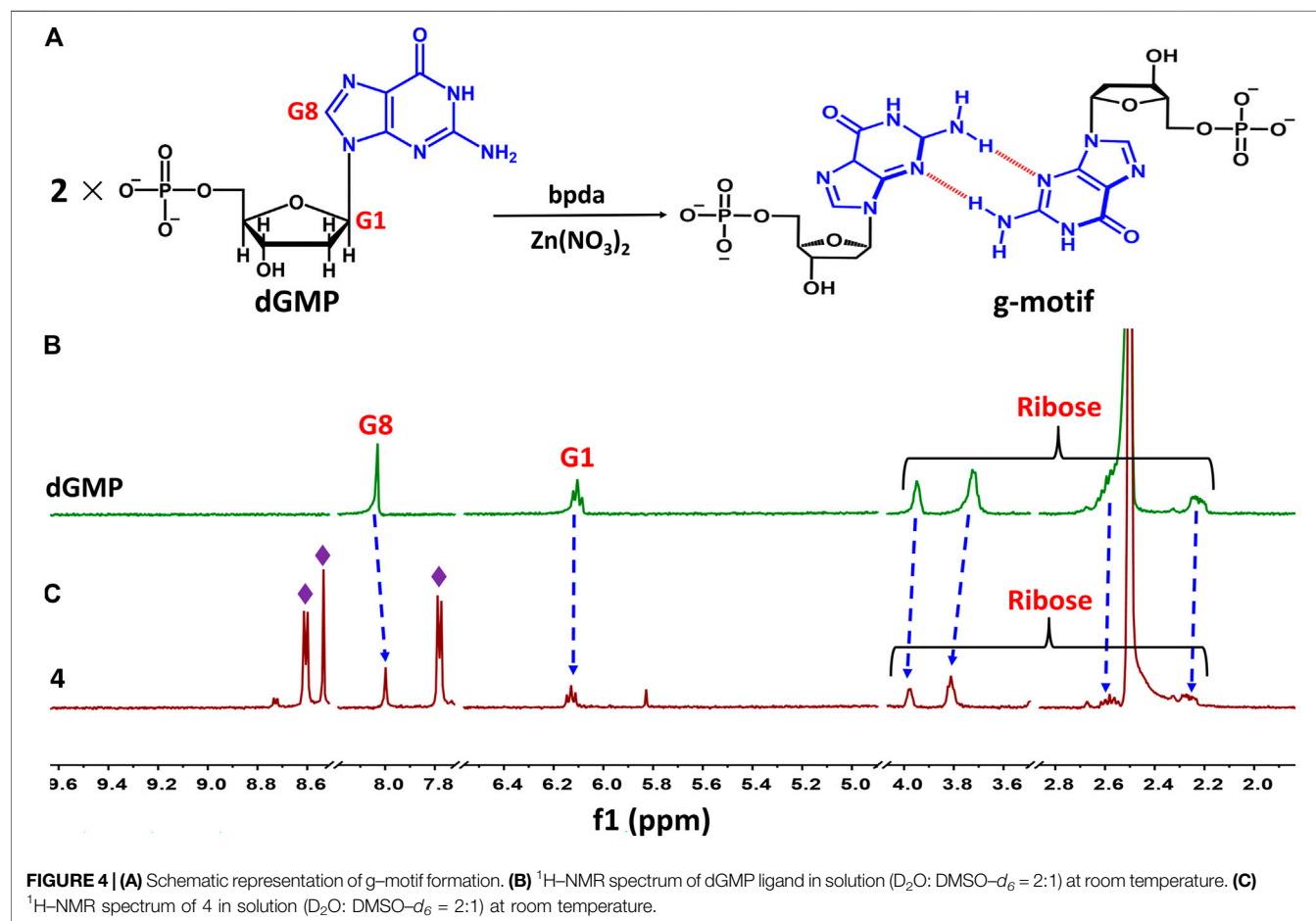
FIGURE 4 | (A) Schematic representation of g–motif formation. **(B)** ^{1}H–NMR spectrum of dGMP ligand in solution (D$_2$O: DMSO–d_6 = 2:1) at room temperature. **(C)** ^{1}H–NMR spectrum of 4 in solution (D$_2$O: DMSO–d_6 = 2:1) at room temperature.

hydrogen bonds between the sugar ring hydroxyl and the carbonyl group on the base (**Supplementary Figure S11A**). While there are electrostatic interaction and hydrogen bonds between the 1D [Zn (bpda) (H$_2$O)$_4$]$^+$ cationic chain and the nucleotide anion in this 3D structure (**Supplementary Figure S11B**). It is worth noting that the value of the glycosyl torsion angles χ C (4)–N (9)–C (1′)–O (1′) is –83.4°, which was also corresponding to the high *anti* conformation. This discovery proves the importance of the conformation of nucleoside moiety once again.

Complex 5 was obtained in pure water, and the Mn(II) center is also present as a slightly distorted octahedral geometry with five

coordinated water molecules and one dGMP^{2-} ligand by oxygen atoms and imidazole N atoms, respectively (**Figure 3**; **Supplementary Figure S12**). The mean value of bond length Mn–O$_{water}$ is 2.201 (2) Å, which is in accordance with that in the previous reports (Lin et al., 2018). In this complex, the symmetry-related nucleotides coordinate in the *cis* position. Although the central metal Mn(II) is significantly in the plane of the purine rings, no base pairing was found in its crystal structure. Why? Compared with 1–4, this may be attributed to the lack of participation and induction of auxiliary ligands, thus lacking the local environment of the hydrophobic required for base pairing. Additionally, the value of the glycosyl torsion angles χ

FIGURE 5 | (A) The CD spectrum of the solution of dGMP and complexes 1–5; the spectrum was obtained by measuring 2.5×10^{-5} mol/L solution in a 1-nm cell. **(B)** The crystallized solid-state CD spectrum of dGMP and complexes 1–5 (KBr: (sample) = 200: 1).

is −163° corresponding to *anti* conformation. This counterexample also confirms the key role of the high *trans* conformation in the formation of g–motif.

Studies of G–Motif in Solution

Taking 4 as an example, we illustrate the formation of the g–motif structure in a solution. Stirring an aqueous solution of 2′-deoxyguanosine-5′-monophosphate (dGMP, 0.05 mmol) and $Zn(NO_3)_2$ (0.05 mmol) in the presence of bpda bridging ligand (0.05 mmol) resulted in the formation of four, as evidenced by ^{1}H–NMR spectroscopy (**Figure 4A**). In order to increase the solubility of the complex, we mixed a small amount of DMSO organic solvent with a ratio of 2:1.

The nucleobase protons were shifted upfield and downfield ($\Delta\delta$ = 8.03→8.00 ppm and 6.11→6.13 ppm) for guanosine H8 and H1 of dGMP (**Figures 4B,C; Supplementary Figure S23**), respectively. The ribose protons signal around 2.24–3.94 ppm shift slightly, indicating the existence of little changes in the environment. The ratio of peak area of four indicates that the molecular number ratio of dGMP to bpda is 2:1 (**Supplementary Figure S24**). These observations may suggest that the nucleobase moieties are located on the inner side of the bpda *via* stacking interaction, and that the ribose part also undergoes conformational changes. The three aromatic signals derived from bpda (8.75, 8.70, and 7.83 ppm, **Supplementary Figure S23**) are much sharper, presumably owing to fast formation processes of the g–motif structure in 4 (Sawada et al., 2009; Sawada and Fujita, 2010). Additionally, we successfully captured g–motif structural fragments in ESI-MS spectrometry (**Supplementary Figure S25**), which further proved that g–motif can form in a solution.

In order to study the interactions of bridging ligands (4,4′–bipy, bpe, bpa, bpda) with M–dGMP (M = Co^{2+}, Zn^{2+}) in an aqueous medium, UV titrations were carried out by adding an auxiliary ligand to the solution of M-dGMP. UV absorbance was measured as a function of concentration of bridging ligands.

The measurement results are shown in **Supplementary Figure S21**. Isosbestic points were not found in all titration curves, indicating that the auxiliary ligand does not directly interact with the M-dGMP system. The high-quality crystal data of the complexes show that only the host–guest interaction existed between the auxiliary ligand and dGMP. With increased auxiliary ligand concentration, the apparent intensity increased at 250–300 nm and broadened the main absorption at 265 nm. Those changes come from the strong π–π* transition induced by the intermolecular interaction between auxiliary ligands and dGMP based on UV-*vis* absorption spectra of individual dGMP, bridging ligands and complexes (5×10^{-5} mol/L, **Supplementary Figure S20**), rather than a simple superposition of the auxiliary ligand and the absorption spectrum of M-dGMP, and the intermolecular interaction can also be proved by the single crystal structure of the complexes.

Circular Dichroism Spectroscopy

The Flack absolute parameters clearly indicate that all these coordination complexes exhibit homochirality. There are two kinds of chirality sources: 1) the intrinsic chirality of the pentose ring of nucleotides and 2) supramolecular helical chirality formed by noncovalent bonds (H-bonding and π–π stacking). All the chiral sources of these complexes were investigated in detail based on their crystal structures and circular dichroic spectrums.

In an aqueous solution, the negative CD signal near 250 nm and the positive Cotton effect at 220 nm for dGMP ligand (**Figure 5A**) correspond to the pentose ring and base n–σ*, n–π* transition absorption, and π–π* transition (Brunner and Maestre, 1975; Holm et al., 2007) between adjacent bases, respectively, which are consistent with its UV absorption spectrum (**Supplementary Figure S19**). Compared with the dGMP ligand, the UV-*vis* spectra of 5 is basically consistent with the ligand, but the UV-*vis* spectra intensity of 1–4 is significantly increased and obviously broadening, which may be attributed to the formation of conjugate structures between

the bridging ligand and the nucleotide. In the CD spectrum, the signal peaks of the complexes and the ligand are almost the same, indicating that the chirality of the complexes depends on the inherent chirality of the ligand (**Figure 5A**). The negative Cotton effect of 1–5 is slightly enhanced at 250 nm, which is due to the mutarotation of the dGMP molecule in aqueous solution, resulting in α–– and β-type enantiomers, and the coordination of metal ions enhances the advantage of the β-type enantiomer (Ingwall, 1972).

The solid CD spectra of the dGMP ligand and complexes are shown in **Figure 5B**, and the relevant summary is shown in **Supplementary Figure S15**. Among them, 1 and 4, and 2 and 3 are similar, which may depend on the same space group (**Supplementary Table S1**). Complex 5 almost maintains the chiral signals of the ligand. Based on our research on the solid-state CD spectrums and crystal structures of the dGMP and GMP ligands, the chiral signals at 281 nm (–) and 301 nm (+) may be attributed to the pentose ring envelope (**E**) conformation (**Supplementary Figures S14–18**; **Supplementary Tables S13, S14**). The Cotton effects centered at 260 nm (–) have a slight redshift, and the signal is almost reversed, which is caused by the widespread π–π stacking interactions and supramolecular helical structure along b axis, respectively. Complexes 1 and 4 generally have a slight redshift at the absorption peak at 235 nm (+) relative to the dGMP ligand, which can be explained by the formation of the g–motif. Crystal analysis shows that the formation of N–H···N hydrogen bonds between the purine bases reduces the energy of the system, so n–π* transition does not need to absorb higher energy. On the contrary, due to the lack of the g–motif structure, this absorption peak blue shifted to 222 nm (+) in 5. The negative Cotton effect about 263/264 nm (+) was also redshifted relative to the ligand in 1 and 4, which was related to the extensive and very strong π–π stacking interaction. Curiously, the chiral signals of 2 and 3 at Cotton effect 258 nm (–) changed, and new peaks are generated at 312–318 nm. This may be attributed to the supramolecular helical structure constructed by hydrogen bonds, which, as a new source of chirality, changes the symmetry of electronic transitions, causing the chiral signal to reverse (Maeda et al., 2006). The new peaks may be attributed to the supramolecular helix chirality of the complexes. Further crystallographic research shows that the 3D supramolecular structure of 2 and 3 contains a quadruple helical structure constructed by hydrogen bonds (O6–H6···O7, 1.91 Å, 2.71 Å, 169°; O13–H13···O14, 2.01 Å, 2.81 Å, 168°, and N3–H3···O3, 1.84 Å, 2.70 Å, 173°; N8–H8···O11, 1.87 Å, 2.73 Å, 176°). The chiral conformation of the quadruple helical in 2 and 3 exhibits *P*-chirality because the dGMP ligand wraps around the b axis in a clockwise manner (**Supplementary Figure S8**). Compared with 3, complex 2 has stronger H-bonding, so a slight redshift occurs (312→318 nm).

CONCLUSION

In summary, a rational design and construction of the GG mismatch base pairing has been achieved by dGMP with pyridine derivatives to simulate a local hydrophobic microenvironment in DNA, which was named as the g–motif for the first time, in order to specify the mismatch base pairs. There are fully characterized g–motif both in solution and the crystallized solid state. Especially, single crystal structural analysis for the g–motif in the five nucleotide coordination complexes provides the structural details of the GG mismatch base pairing. In this work, the interaction mode of the g–motif shows an unusual (*high anti*)–(*high anti*) pattern. The shorter auxiliary ligands with different sizes produce a suitable space for the formation of the g–motif, in which guanine is involved in the coordination of N7 donor. However, the g–motif does not appear in the coordination complex without auxiliary ligand. The co-assembly of these DNA intercalators and nucleotides produces supramolecular crystals arranged through a combination of π–π stacking and hydrogen-bond interactions, which overcomes the inherent limitations of self-assembly leading to materials with unprecedented properties. Our research critically expands the breadth of programmable and functional materials attainable by self-assembly. In solution, the g–motif also exists and is confirmed by ^{1}H–NMR and ESI–MS spectrum. In addition, the strong π–π stacking interaction between the auxiliary ligand and dGMP can be detected by the UV–*vis* titration. The chirality of the coordination complexes has been studied by the method of solid-state CD spectra combining with X-ray crystal diffraction analysis which has been developed in our laboratory, which is an effective way to help us to understand the g–motif comprehensively, both the structure and the properties. Primarily, the g–motif can be identified in a crystallized state CD spectrum by the redshift coming from the hydrogen bond in g–motif. Additionally, some small-molecule ligands, such as rhodium and platinum metalloinsertors, have been reported to target mismatch DNA, with important applications in the therapy and diagnosis of cancer. However, many of these metalloinsertors are generally highly cytotoxic with many different side effects. The understanding of the structure interaction in current research that can be regarded as a chemical tool for interrogating and detecting mismatch-related diseases is expected to be helpful to guide the development of future generations of more selective targeted drugs.

EXPERIMENTAL SECTION

Materials and Instrumentation

All chemical reagents were commercially available and used without further purification. $Co(NO_3)_2 \cdot 6H_2O$, $Zn(NO_3)_2 \cdot 6H_2O$, $Mn(NO3)2 \cdot 4H2O$, and 4,4′-bipyridine (bipy) were purchased from Adamas, 1,2-bis (4-pyridyl)ethane (bpe) and 1,2-bis (4-pyridyl)ethane (bpa) were purchased from Tci, and 2′-deoxyguanosine-5′-monophosphate disodium salt hydrate (dGMP) was purchased from Alfa Aesar.

Elemental analyses (C, H, and N) were determined on an EA3000 elemental analyzer. FT-IR spectra were recorded on a Nicolet Nexus FT-IR spectrometer using the KBr pellet in the range of 4,000–400 cm^{-1}. UV-*vis* spectra were obtained from a TU-1950 spectrophotometer. X-ray powder diffraction studies

were performed by a Bruker D8 Advance X-ray diffractometer. The X-ray single crystal data collections were performed on a Bruker APEX-II CCD and Rigaku Saturn724+ (2 × 2 bin mode) diffractometer with graphite monochromatized MoKα radiation ($\lambda = 0.71073$ Å). CD measurements were carried out under a constant flow of nitrogen on a JASCO J–810 spectropolarimeter. Thermogravimetric analyses (TGA) were carried out using a DTG-60H thermal analyzer under nitrogen atmosphere from room temperature to 800°C with a heating rate of 5 C/min. The pH of the sample solution was measured using a PHS-3C meter.

Synthesis and Structural Characterization

The synthesis method of all complexes is that an aqueous solution (5 ml) of 2′-deoxyguanosine-5′-monophosphate disodium salt (dGMP) was added into an aqueous solution (5 ml) of $M(NO_3)_2$ (M = Mn^{2+}, Co^{2+}, and Zn^{2+}). After the mixture was stirred for 10–15 min, a solution of bridging ligand (4,4-bipy, bpe, bpa, bpda) that dissolved in distilled water or ethanol (5 ml) was added. The suspension acidity was adjusted by HNO_3 (1 M) until the solution became clear. The resulting solution was stirred at room temperature for 20–30 min and then filtered. Single crystals suitable for X-ray diffraction analysis can be obtained by slow evaporation under room temperature. It should be noted that except for 5, all other complexes were obtained in water–ethanol mixed solvent.

Powder X-ray diffraction (PXRD) patterns of polycrystalline samples of the ligands and complexes were all coincident with their theoretical ones (**Supplementary Figure S25**), confirming the phase purity of the bulk samples and their isostructurality with the crystals selected for single-crystal X-ray diffraction. The water contents of the complexes and thermal stability were estimated by thermogravimetric analysis (TGA) (**Supplementary Figure S27**). Elemental analysis (C, H, and N) further confirmed the chemical identity of the complexes

determined by single-crystal X-ray diffraction. The types of metal–nucleotide interactions have been identified by the FT-IR (**Supplementary Figure S26**).

DATA AVAILABILITY STATEMENT

The original contributions presented in the study are included in the article/**Supplementary Material**; further inquiries can be directed to the corresponding author.

AUTHOR CONTRIBUTIONS

YZ is the main contributor for this manuscript and has prepared the coordination polymers, and performed the structural characterization and CD spectrum; ZL and PW are the project participants. HM and Q-MQ did some measurements and data analysis; HL is the project leader and the corresponding author of this manuscript.

FUNDING

SUPPLEMENTARY MATERIAL

The Supplementary Material for this article can be found online at: https://www.frontiersin.org/articles/10.3389/fchem.2021.709777/full#supplementary-material

REFERENCES

Afek, A., Shi, H., Rangadurai, A., Sahay, H., Senitzki, A., Xhani, S., et al. (2020). DNA Mismatches Reveal Conformational Penalties in Protein-DNA Recognition. *Nature* 587, 291–296. doi:10.1038/s41586-020-2843-2

Asami, H., Urashima, S.-h., Tsukamoto, M., Motoda, A., Hayakawa, Y., and Saigusa, H. (2012). Controlling Glycosyl Bond Conformation of Guanine Nucleosides: Stabilization of the Anti Conformer in 5′-O-Ethylguanosine. *J. Phys. Chem. Lett.* 3, 571–575. doi:10.1021/jz300081e

Brovarets', O. h. O., Oliynyk, T. A., and Hovorun, D. M. (2019). Novel Tautomerisation Mechanisms of the Biologically Important Conformers of the Reverse Löwdin, Hoogsteen, and Reverse Hoogsteen G*·C* DNA Base Pairs via Proton Transfer: A Quantum-Mechanical Survey. *Front. Chem.* 7, 597. doi:10.3389/fchem.2019.00597

Brovarets', O. h. O., Tsiupa, K. S., and Hovorun, D. M. (2018). Surprising Conformers of the Biologically Important A·T DNA Base Pairs: QM/QTAIM Proofs. *Front. Chem.* 6, 8. doi:10.3389/fchem.2018.00008

Brunner, W. C., and Maestre, M. F. (1975). Circular Dichroism of Some Mononucleosides. *Biopolymers* 14, 555–565. doi:10.1002/bip.1975.360140310

Chen, J., Hickey, B. L., Wang, L., Lee, J., Gill, A. D., Favero, A., et al. (2021). Selective Discrimination and Classification of G-Quadruplex Structures with a Host-Guest Sensing Array. *Nat. Chem.* 13, 488–495. doi:10.1038/s41557-021-00647-9

Chen, Y.-W., Satange, R., Wu, P.-C., Jhan, C.-R., Chang, C.-k., Chung, K.-R., et al. (2018). CoII(Chromomycin)2 Complex Induces a Conformational Change of CCG Repeats from I-Motif to Base-Extruded DNA Duplex. *Ijms* 19, 2796. doi:10.3390/ijms19092796

Chu, B., Zhang, D., and Paukstelis, P. J. (2019). A DNA G-Quadruplex/i-Motif Hybrid. *Nucleic Acids Res.* 47, 11921–11930. doi:10.1093/nar/gkz1008

Cini, R., and Pifferi, C. (1999). Supramolecular Networks via Hydrogen Bonding and Stacking Interactions for Adenosine 5′-diphosphate. Synthesis and crystal Structure of diaqua(2,2′:6′,2″-terpyridine)Copper(II) [adenosine 5′-diphosphato(3−)](2,2′:6′,2″-terpyridine)Cuprate(II) Adenosine 5′-diphosphate(1−) Hexadecahydrate and Density Functional Geometry Optimization Analysis of Copper(II)- and Zinc(II)-pyrophosphate Complexes. *J. Chem. Soc. Dalton Trans.*, 699–710. doi:10.1039/A807793B

Da, L.-T., and Yu, J. (2018). Base-flipping Dynamics from an Intrahelical to an Extrahelical State Exerted by Thymine DNA Glycosylase during DNA Repair Process. *Nucleic Acids Res.* 46, 5410–5425. doi:10.1093/nar/gky386

DeJesus-Hernandez, M., Mackenzie, I. R., Boeve, B. F., Boxer, A. L., Baker, M., Rutherford, N. J., et al. (2011). Expanded GGGGCC Hexanucleotide Repeat in Noncoding Region of C9ORF72 Causes Chromosome 9p-Linked FTD and ALS. *Neuron* 72, 245–256. doi:10.1016/j.neuron.2011.09.011

Faibis, V., Cognet, J. A. H., Boulard, Y., Sowers, L. C., and Fazakerley, G. V. (1996). Solution Structure of Two Mismatches G·G and I·I in the K-rasGene Context by Nuclear Magnetic Resonance and Molecular Dynamics†. *Biochemistry* 35, 14452–14464. doi:10.1021/BI960871E

Geng, Y., Liu, C., Zhou, B., Cai, Q., Miao, H., Shi, X., et al. (2019). The crystal Structure of an Antiparallel Chair-type G-Quadruplex Formed by Bromo-Substituted Human Telomeric DNA. *Nucleic Acids Res.* 47, 5395–5404. doi:10.1093/nar/gkz221

Ghosh, A., Kar, R. K., Krishnamoorthy, J., Chatterjee, S., and Bhunia, A. (2014). Double GC:GC Mismatch in dsDNA Enhances Local Dynamics Retaining the DNA Footprint: a High-Resolution NMR Study. *Chemmedchem* 9, 2059–2064. doi:10.1002/cmdc.201402238

Gómez-González, J., Peña, D. G., Barka, G., Sciortino, G., Maréchal, J.-D., Vázquez López, M., et al. (2018). Directed Self-Assembly of Trimeric DNA-Bindingchiral Miniprotein Helicates. *Front. Chem.* 6, 520. doi:10.3389/fchem.2018.00520

Granzhan, A., Kotera, N., and Teulade-Fichou, M.-P. (2014). Finding needles in a Basestack: Recognition of Mismatched Base Pairs in DNA by Small Molecules. *Chem. Soc. Rev.* 43, 3630–3665. doi:10.1039/c3cs60455a

Hall, J. P., O'Sullivan, K., Naseer, A., Smith, J. A., Kelly, J. M., and Cardin, C. J. (2011). Structure Determination of an Intercalating Ruthenium Dipyridophenazine Complex Which Kinks DNA by Semiintercalation of a Tetraazaphenanthrene Ligand. *Proc. Natl. Acad. Sci.* 108, 17610–17614. doi:10.1073/pnas.1108685108

Hall, J. P., Sanchez-Weatherby, J., Alberti, C., Quimper, C. H., O'Sullivan, K., Brazier, J. A., et al. (2014). Controlled Dehydration of a Ruthenium Complex-DNA crystal Induces Reversible DNA Kinking. *J. Am. Chem. Soc.* 136, 17505–17512. doi:10.1021/ja508745x

Hänsel-Hertsch, R., Di Antonio, M., and Balasubramanian, S. (2017). DNA G-Quadruplexes in the Human Genome: Detection, Functions and Therapeutic Potential. *Nat. Rev. Mol. Cel Biol.* 18, 279–284. doi:10.1038/nrm.2017.3

Hänsel-Hertsch, R., Spiegel, J., Marsico, G., Tannahill, D., and Balasubramanian, S. (2018). Genome-wide Mapping of Endogenous G-Quadruplex DNA Structures by Chromatin Immunoprecipitation and High-Throughput Sequencing. *Nat. Protoc.* 13, 551–564. doi:10.1038/nprot.2017.150

Hirschberg, J. H. K. K., Brunsveld, L., Ramzi, A., Vekemans, J. A. J. M., Sijbesma, R. P., and Meijer, E. W. (2000). Helical Self-Assembled Polymers from Cooperative Stacking of Hydrogen-Bonded Pairs. *Nature* 407, 167–170. doi:10.1038/35025027

Holm, A. I. S., Worm, E. S., Chakraborty, T., Babu, B. R., Wengel, J., Hoffmann, S. V., et al. (2007). On the Influence of Conformational Locking of Sugar Moieties on the Absorption and Circular Dichroism of Nucleosides from Synchrotron Radiation Experiments. *J. Photochem. Photobiol. A: Chem.* 187, 293–298. doi:10.1016/j.jphotochem.2006.10.025

Hou, M.-H., Robinson, H., Gao, Y. G., and Wang, A. H. (2002). Crystal Structure of Actinomycin D Bound to the CTG Triplet Repeat Sequences Linked to Neurological Diseases. *Nucleic Acids Res.* 30, 4910–4917. doi:10.1093/nar/gkf619

Ingwall, J. S. (1972). Cicular Dichroism of Nucleosides. I. Anomeric Pairs of the D-Pentofuranosides of Adenine. *J. Am. Chem. Soc.* 94, 5487–5495. doi:10.1021/ja00770a054

Iyer, R. R., Pluciennik, A., Burdett, V., and Modrich, P. L. (2006). DNA Mismatch Repair: Functions and Mechanisms. *Chem. Rev.* 106, 302–323. doi:10.1021/cr0404784

Jourdan, M., Garcia, J., Lhomme, J., Teulade-Fichou, M.-P., Vigneron, J.-P., and Lehn, J.-M. (1999). Threading Bis-Intercalation of a Macrocyclic Bisacridine at Abasic Sites in DNA: Nuclear Magnetic Resonance and Molecular Modeling Study†. *Biochemistry* 38, 14205–14213. doi:10.1021/bi991111h

Jourdan, M., Granzhan, A., Guillot, R., Dumy, P., and Teulade-Fichou, M.-P. (2012). Double Threading through DNA: NMR Structural Study of a Bis-Naphthalene Macrocycle Bound to a Thymine-Thymine Mismatch. *Nucleic Acids Res.* 40, 5115–5128. doi:10.1093/nar/gks067

Kato, Y., Conn, M. M., and Rebek, J., Jr. (1995). Hydrogen Bonding in Water Using Synthetic Receptors. *Proc. Natl. Acad. Sci.* 92, 1208–1212. doi:10.1073/pnas.92.4.1208

Korostelev, A., Trakhanov, S., Laurberg, M., and Noller, H. F. (2006). Crystal Structure of a 70S Ribosome-tRNA Complex Reveals Functional Interactions and Rearrangements. *Cell* 126, 1065–1077. doi:10.1016/j.cell.2006.08.032

Li, X., Pei, Y., Zhang, Y., Liu, Y., Fu, W., Li, J., et al. (2020). Single-Molecule Mechanical Unfolding of AT-Rich Chromosomal Fragile Site DNA Hairpins: Resolving the Thermodynamic and Kinetic Effects of a Single G-T Mismatch. *J. Phys. Chem. B* 124, 9365–9370. doi:10.1021/acs.jpcb.0c06954

Lim, G., and Hohng, S. (2020). Single-molecule Fluorescence Studies on Cotranscriptional G-Quadruplex Formation Coupled with R-Loop Formation. *Nucleic Acids Res.* 48, 9195–9203. doi:10.1093/nar/gkaa695

Lin, C. G., Zhou, W., Xiong, X. T., Xuan, W., Kitson, P. J., Long, D. L., et al. (2018). Digital Control of Multistep Hydrothermal Synthesis by Using 3D Printed Reactionware for the Synthesis of Metal-Organic Frameworks. *Angew. Chem. Int. Ed.* 57, 16716–16720. doi:10.1002/anie.201810095

Maeda, K., Mochizuki, H., Watanabe, M., and Yashima, E. (2006). Switching of Macromolecular Helicity of Optically Active Poly(phenylacetylene)s Bearing Cyclodextrin Pendants Induced by Various External Stimuli. *J. Am. Chem. Soc.* 128, 7639–7650. doi:10.1021/ja060858+

Maity, A., Winnerdy, F. R., Chen, G., and Phan, A. T. (2021). Duplexes Formed by G4C2 Repeats Contain Alternate Slow- and Fast-Flipping G·G Base Pairs. *Biochemistry* 60, 1097–1107. doi:10.1021/acs.biochem.0c00916

Mao, S., Sekula, B., Ruszkowski, M., Ranganathan, S. V., Haruehanroengra, P., Wu, Y., et al. (2020). Base Pairing, Structural and Functional Insights into N4-Methylcytidine (m4C) and N4,N4-Dimethylcytidine (m42C) Modified RNA. *Nucleic Acids Res.* 48, 10087–10100. doi:10.1093/nar/gkaa737

Mondal, S., Bhat, J., Jana, J., Mukherjee, M., and Chatterjee, S. (2016). Reverse Watson-Crick G-G Base Pair in G-Quadruplex Formation. *Mol. Biosyst.* 12, 18–22. doi:10.1039/C5MB00611B

Monestier, A., Aleksandrov, A., Coureux, P.-D., Panvert, M., Mechulam, Y., and Schmitt, E. (2017). The Structure of an *E. coli* tRNAfMet A1-U72 Variant Shows an Unusual Conformation of the A1-U72 Base Pair. *RNA* 23, 673–682. doi:10.1261/rna.057877.116

Musumeci, D., Platella, C., Riccardi, C., Merlino, A., Marzo, T., Massai, L., et al. (2016). A First-In-Class and a Fished Out Anticancer Platinum Compound: cis-[PtCl2(NH3)2] and cis-[PtI2(NH3)2] Compared for Their Reactivity towards DNA Model Systems. *Dalton Trans.* 45, 8587–8600. doi:10.1039/C6DT00294C

Pages, B. J., Gurung, S. P., Mcquaid, K., Hall, J. P., Cardin, C. J., and Brazier, J. A. (2019). Stabilization of Long-Looped I-Motif DNA by Polypyridyl Ruthenium Complexes. *Front. Chem.* 7, 744. doi:10.3389/fchem.2019.00744

Philp, D., and Stoddart, J. F. (1996). Self-Assembly in Natural and Unnatural Systems. *Angew. Chem. Int. Ed. Engl.* 35, 1154–1196. doi:10.1002/anie.199611541

Pirota, V., Nadai, M., Doria, F., and Richter, S. (2019). Naphthalene Diimides as Multimodal G-Quadruplex-Selective Ligands. *Molecules* 24, 426. doi:10.3390/molecules24030426

Platella, C., Pirota, V., Musumeci, D., Rizzi, F., Iachettini, S., Zizza, P., et al. (2020a). Trifunctionalized Naphthalene Diimides and Dimeric Analogues as G-Quadruplex-Targeting Anticancer Agents Selected by Affinity Chromatography. *Ijms* 21, 1964. doi:10.3390/ijms21061964

Platella, C., Trajkovski, M., Doria, F., Freccero, M., Plavec, J., and Montesarchio, D. (2020b). On the Interaction of an Anticancer Trisubstituted Naphthalene Diimide with G-Quadruplexes of Different Topologies: a Structural Insight. *Nucleic Acids Res.* 48, 12380–12393. doi:10.1093/nar/gkaa1001

Poojary, M. D., and Manohar, H. (1988). Interaction of Metal Ions with 6-oxopurine Nucleotides. Part 1. X-Ray Structures of Ternary Cobalt(III) Complexes with Inosine 5′-monophosphate or Guanosine 5′-monophosphate. *J. Chem. Soc. Dalton Trans.*, 1297–1302. doi:10.1039/DT9880001297

Punt, P. M., Stratmann, L. M., Sevim, S., Knauer, L., Strohmann, C., and Clever, G. H. (2020). Heteroleptic Coordination Environments in Metal-Mediated DNA G-Quadruplexes. *Front. Chem.* 8, 26. doi:10.3389/fchem.2020.00026

Salvati, E., Doria, F., Manoli, F., D'Angelo, C., Biroccio, A., Freccero, M., et al. (2016). A Bimodal Fluorescent and Photocytotoxic Naphthalene Diimide for Theranostic Applications. *Org. Biomol. Chem.* 14, 7238–7249. doi:10.1039/C6OB00987E

Satange, R., Chang, C.-k., and Hou, M.-H. (2018). A Survey of Recent Unusual High-Resolution DNA Structures Provoked by Mismatches, Repeats and Ligand Binding. *Nucleic Acids Res.* 46, 6416–6434. doi:10.1093/nar/gky561

Satange, R., Chuang, C.-Y., Neidle, S., and Hou, M.-H. (2019). Polymorphic G:G Mismatches Act as Hotspots for Inducing Right-Handed Z DNA by DNA Intercalation. *Nucleic Acids Res.* 47, 8899–8912. doi:10.1093/nar/gkz653

Sawada, T., and Fujita, M. (2010). A Single Watson−Crick G·C Base Pair in Water: Aqueous Hydrogen Bonds in Hydrophobic Cavities. *J. Am. Chem. Soc.* 132, 7194–7201. doi:10.1021/ja101718c

Sawada, T., Yoshizawa, M., Sato, S., and Fujita, M. (2009). Minimal Nucleotide Duplex Formation in Water through Enclathration in Self-Assembled Hosts. *Nat. Chem* 1, 53–56. doi:10.1038/nchem.100

Shi, S., Gao, X., Huang, H., Zhao, J., and Yao, T. (2015). Effect of the Ancillary Ligands on the Spectral Properties and G-Quadruplexes DNA Binding Behavior: A Combined Experimental and Theoretical Study. *Chem. Eur. J.* 21, 13390–13400. doi:10.1002/chem.201501830

Sigel, R. K. O., Freisinger, E., Abbate, M., and Lippert, B. (2002). Hydrogen Bonding Patterns of 7,9-dimethylguanine and its Transplatinum(II) Complexes. *Inorg. Chim. Acta* 339, 355–365. doi:10.1016/S0020-1693(02)00962-3

Tseng, W.-H., Chang, C.-k., Wu, P.-C., Hu, N.-J., Lee, G.-H., Tzeng, C.-C., et al. (2017). Induced-Fit Recognition of CCG Trinucleotide Repeats by a Nickel-Chromomycin Complex Resulting in Large-Scale DNA Deformation. *Angew. Chem. Int. Ed.* 56, 8761–8765. doi:10.1002/anie.201703989

Varani, G., and McClain, W. H. (2000). The G·U Wobble Base Pair. *EMBO Rep.* 1, 18–23. doi:10.1093/embo-reports/kvd001

Wang, S., Zhao, J., Lu, S., Sun, J., and Yang, X. (2019). A Duplex Connection Can Further Illuminate G-Quadruplex/crystal Violet Complex. *Chem. Commun.* 55, 1911–1914. doi:10.1039/C8CC09940E

Watson, J. D., and Crick, F. H. C. (1953). Molecular Structure of Nucleic Acids: A Structure for Deoxyribose Nucleic Acid. *Nature* 171, 737–738. doi:10.1038/171737a0

Westover, K. D., Bushnell, D. A., and Kornberg, R. D. (2004). Structural Basis of Transcription. *Cell* 119, 481–489. doi:10.1016/j.cell.2004.10.016

Wu, J., Fu, Y., He, Z., Han, Y., Zheng, L., Zhang, J., et al. (2012). Growth Mechanisms of Fluorescent Silver Clusters Regulated by Polymorphic DNA Templates: a DFT Study. *J. Phys. Chem. B* 116, 1655–1665. doi:10.1021/jp206251v

Xiong, X., Xiao, M., Lai, W., Li, L., Fan, C., and Pei, H. (2021). Optochemical Control of DNA-Switching Circuits for Logic and Probabilistic Computation. *Angew. Chem. Int. Ed.* 60, 3397–3401. doi:10.1002/anie.202013883

Yao, J.-L., Gao, X., Sun, W., Shi, S., and Yao, T.-M. (2013). [Ru(bpy)2dppz-idzo]2+: a Colorimetric Molecular "light Switch" and Powerful Stabilizer for G-Quadruplex DNA. *Dalton Trans.* 42, 5661–5672. doi:10.1039/c3dt32640c

Zhang, D., and Wang, H. (2019). Fluorescence Anisotropy Reduction of an Allosteric G-Rich Oligonucleotide for Specific Silver Ion and Cysteine Detection Based on the G-Ag+-G Base Pair. *Anal. Chem.* 91, 14538–14544. doi:10.1021/acs.analchem.9b03556

A Multifunctional 3D Supermolecular Co Coordination Polymer With Potential for CO_2 Adsorption, Antibacterial Activity, and Selective Sensing of Fe^{3+}/Cr^{3+} Ions and TNP

Xiaojing Zhou, Lili Liu, Hang Kou, Shimei Zheng, Mingjun Song, Jitao Lu* and Xishi Tai*

School of Chemical and Chemical Engineering and Environmental Engineering, Weifang University, Weifang, China

A 3D supermolecular structure [Co$_3$(L)$_2$ (2,2′-bipy)$_2$](DMF)$_3$(H$_2$O)$_3$ 1) (H$_3$L = 4,4′,4″-nitrilotribenzoic acid) has been constructed based on H$_3$L, and 2,2′-bipy ligands under solvothermal conditions. Compound **1** can be described as a (3, 6)-connected kgd topology with a Schläfli symbol $(4^3)_2(4^6.6^6.8^3)$ formed by [Co$_3$(CO$_2$)$_6$] secondary building units. The adsorption properties of the activated sample 1a has been studied; the result shows that 1a has a high adsorption ability: the CO_2 uptakes were 74 $cm^3 \cdot g^{-1}$ at 273 K, 50 $cm^3 \cdot g^{-1}$ at 298 K, the isosteric heat of adsorption (Q$_{st}$) is 25.5 kJ mol^{-1} at zero loading, and the N_2 adsorption at 77 K, 1 bar is 307 cm^3 g^{-1}. Magnetic measurements showed the existence of an antiferromagnetic exchange interaction in compound **1**, besides compound **1** exhibits effective luminescent performance for Fe^{3+}/Cr^{3+} and TNP.

Keywords: sensing, Fe^{3+}/Cr^{3+}, TNP, antibacterial, CO_2 adsorption, magnetism, coordination polymer

INTRODUCTION

Nowadays, the rapid detection of toxic organic and heavy metal ion pollutants has attracted more and more attention due to their harmful effects on the environment and human life (Rasheed and Nabeel, 2019; Haldar et al., 2020). For instance, nitroaromatic explosives (NACs), which include nitrobenzene, 2,4,6-trinitrophenol (TNP), 2-nitrotoluene, 2,4-dinitrotoluene, nitrobenzene, 4-nitrotoluene and 3-nitrotoluene, have many application in the chemical industry and can cause terrorism and environmental issues. Among NACs, TNP is highly toxic, it harms the microorganisms and the human body (Wollin and Dieter, 2005). Likewise, heavy metal pollutants are not degradable and tend to accumulate in ecosystems, imposing a threat to human beings because of their toxicity and carcinogenicity (Jia et al., 2017; Peng et al., 2018; Ashraf et al., 2019; Cai et al., 2019). Fe^{3+} is an abundant and essential transition metal for biological organisms, and plays an important role in biological processes, such as enzymatic reactions, nitrogen fixation in nitrogenases, and oxygen transport. It is also well known that inadequate or excess iron concentration can induce serious health problems including anemia, Alzheimer's disease, liver and kidney damage, diabetes and heart disease, mitochondrial DNA damage (Harigae, 2018; VanderMeulen and Sholzberg, 2018; Wallace et al., 2018; Sahoo and Crisponi, 2019; Fan et al., 2020). Similarly, Cr^{3+} has mutagenicity and cytogenetic toxicity, the scarcity or excess uptake of Cr^{3+} results in cardiovascular diseases and diabetes, mutations or malignant cells (Paul et al., 2015; Zhang et al., 2015; Dong et al., 2016; Rasheed and Nabeel, 2019), so it is urgent and necessary to detect metal ion pollutants in solution for the human security and environmental protection.

Various techniques have been developed to detect Fe^{3+}/Cr^{3+} and TNP (Chen et al., 2018; Pavlačka et al., 2016; Sadak et al., 2017; Tian et al., 2017; Goswami et al., 2013; Wen et al., 2002); among them, fluorescence analysis has been very popular due to its simplicity, sensitivity, fast response, economical way, low interference (Carter et al., 2014; Guo et al., 2014). Therefore the development of excellent fluorescence sensors for the sensitivity of Fe^{3+}/Cr^{3+} and TNP has become a focus. The use of coordination polymers for fluorescence analysis has been explored extensively (Zhang et al., 2018; Hu et al., 2014; Yi et al., 2016). The coordination polymers, built up from organic ligands and metal ions or clusters, are porous materials suitable for various applications including luminescence, magnetism, gas adsorption and separation, as well as catalysis, drug delivery, and proton conduction (Kurmoo, 2009; Huxford et al., 2010; Sun et al., 2013; Yamada et al., 2013; Li et al., 2014; Liu et al., 2014; Zhou. and Kitagawa, 2014; Chughtai et al., 2015; Lustig et al., 2017; Espallargas and Coronado, 2018).

Over the past few years, many luminescent coordiantion polymers have been synthesized to detect metal ions, anions, pH value, small molecules, gases and vapors (Kurmoo, 2009; Lan et al., 2009; Li et al., 2013; Ma et al., 2013; Zhang et al., 2015; Yu et al., 2017; Mi et al., 2019; Tang et al., 2020), in this contribution, we select a tricarboxytriphenylamine (H_3L) as a ligand to construct a new Co coordiantion polymer is mainly based on the following considerations: 1) The conjugated and photoactive triphenylamine moiety makes the MOFs highly fluorogenic; 2) Lewis base N sites on the internal surface of the framework can improve the sensing of ions and adsorption of CO_2; 3) The carboxylate groups have multiple coordination modes to coordinate the metal ions, and the uncoordinated O atoms can provide interaction sites for the metal ions and NACs (specifically, TNP containing three NO_2 groups). Meanwhile, among the MOF sensors, highly economical and abundant Co. ions with magnetic properties have rarely been studied as sensors, mainly because the non-d^{10} electronic structures have low emission performance owing to d–d transitions (Mishra et al., 2014; Chen et al., 2017; Zhang et al., 2018; Zhao et al., 2018).

For the recent years, significant progress has been expended on the development of materials for CO_2 capture, because CO_2 is responsible for the global warming. Utilizing the activated carbon, zeolites or amine solutions for absorbing CO_2 are considered the most adequate adsorbents, though the insufficient uptake capacity and high expense prevent these materials mass production (Zhang et al., 2014).

Many human diseases and infections are caused by unsafe drinking water and food containing bacteria such as *Escherichia coli*, *Staphylococcus aureus*. As to the low molecular weight antibacterial materials, they have many disadvantages, such as toxicity to the environment, short-term antibacterial activity. Hence, there is an urgent need for the development of effective antibacterial materials (Haendel et al., 2014; Kaur et al., 2020; Saira et al., 2020).

Taking the luminescence properties, CO_2 adsorption and antibacterial activity into consideration, we used the coordination polymer as the multifunctional material for sensitivity as well as CO_2 adsorption and antibacterial activity.

FIGURE 1 | The coordination mode of Co atoms in compound **1** (C: Gray, N: Blue, Co:Purple, O: Red).
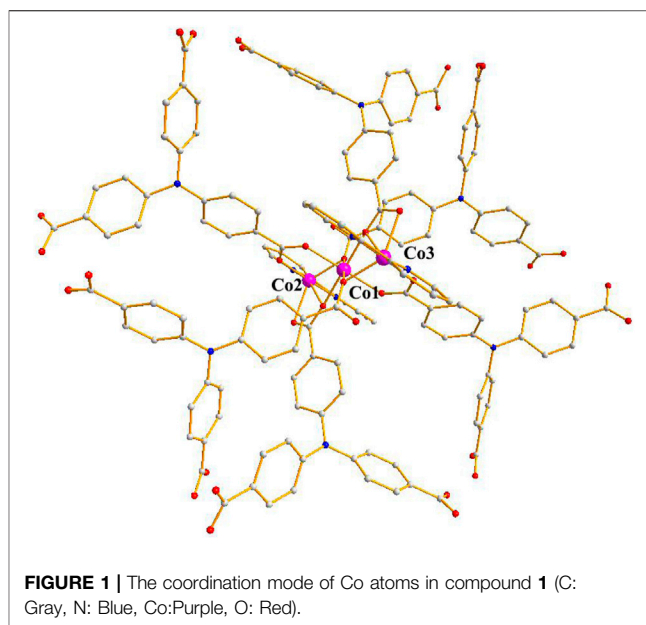
In the manuscript, we obtained a Co. based coordiantion polymer $[Co_3(L)_2 \ (2,2'\text{-bipy})_2](DMF)_3(H_2O)_3$ (denoted as compound **1**) under solvothermal conditions which has been utilized as a multifunctional MOF with preferential CO_2 adsorption, antibacterial activity, selective sensing of metal ions (Fe^{3+}, Cr^{3+}) and TNP, meanwhile, magnetic measurements show that there exists an antiferromagnetic exchange interaction in compound **1**.

MATERIALS AND METHODS

Synthesis of Compound 1

Co.$(NO_3)_2 \bullet 6H_2O$ (29.1 mg), H_3L (18.8 mg), and 2,2′-bipy (15.6 mg), *N,N*-dimethylformamide (3 ml), distilled water (1 ml), and ethanol (1 ml) were mixed in a 15 ml Teflon-lined stainless steel autoclave and heated at 100 °C for 72 h. Upon cooling at room temperature, purple crystals were prepared, which were washed with DMF and dried at 60°C for 6 h. Yield 38% (based on H_3L), IR (KBr 4000–400 cm^{-1}) 3463 (w), 3082 (w), 2,793 (w), 2,496 (w), 1,593 (s), 1,388 (s), 1,191 (w), 1,036 (w), 803 (m), 768 (m), 704 (m), 636 (w), 485 (m). Elemental analysis (%): Calcd for: $C_{71}H_{67}Co_3N_9O_{18}$: C 56.39, H 4.43, N 8.34; Found: C 56.41, H 4.29, N 8.37.

RESULTS AND DISCUSSION

Crystal Structure of Compound 1

The single-crystal X-ray data were collected using the X-ray diffraction technique and the results showed that crystallization of compound 1 in the monoclinic space group $C2/c$ and the presence of two independent Co. atoms, one 2,2′-bipy molecule, and one linker (L^{3-}) in the asymmetric unit of 1 (**Supplementary Figure S1**). The Co1 atom is involved in

FIGURE 2 | The 2D framework of compound **1** (Co:Purple, O: Red, N: Blue, C: Gray).
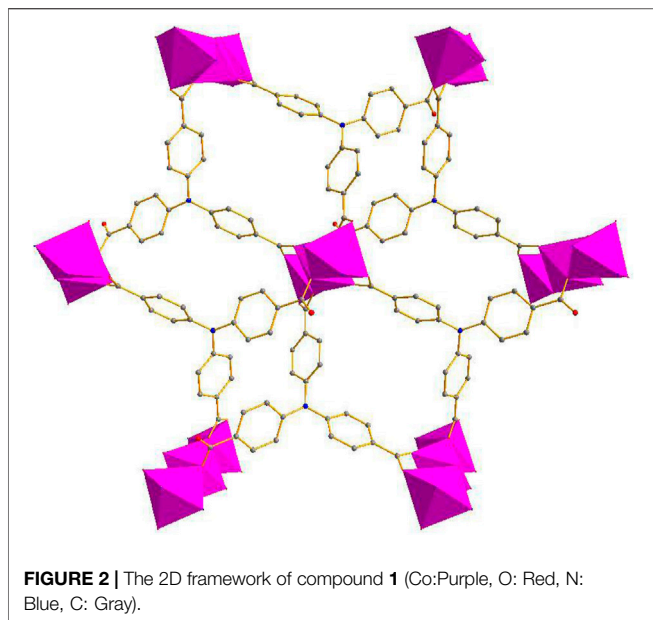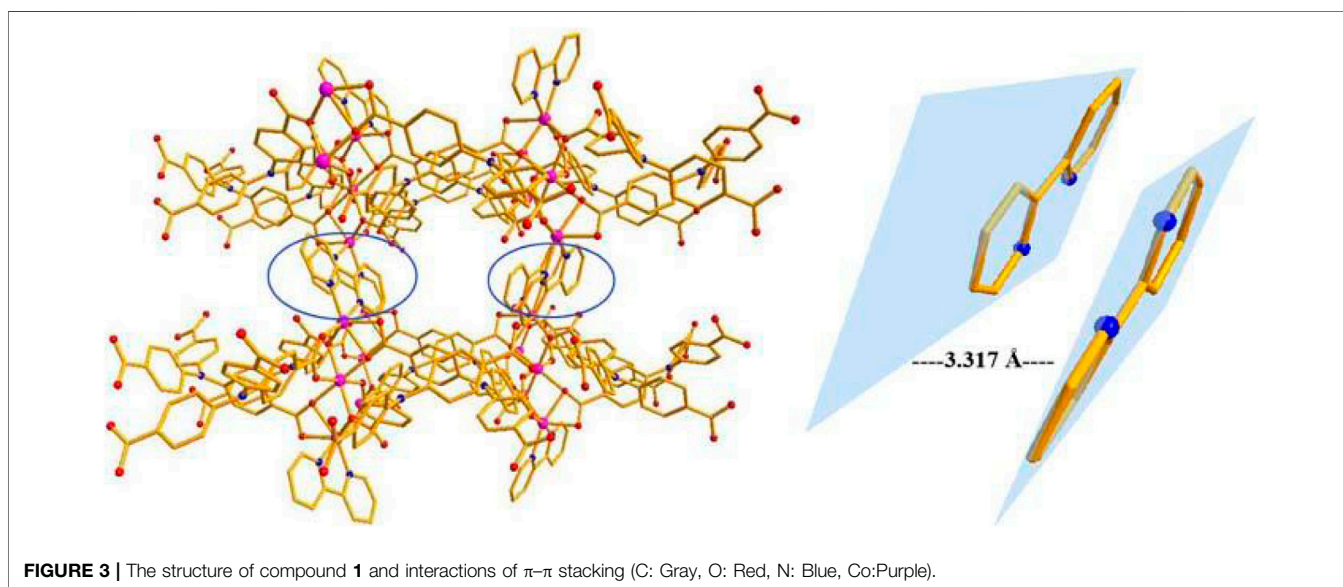
coordination with six O atoms of the carboxylates of $6\,L^{3-}$ ligands, showing an octahedral configuration (Co–O = 2.053–2.108 Å), the six-coordinated Co2 or its symmetry-related Co3 atom displays a distorted octahedral configuration, which is bonded with four carboxylate O atoms from $3\,L^{3-}$ ligands, and 2 N atoms from one 2,2′-bipy molecule, Co2–O and Co2–N or Co3–O and Co3–N are in the range of 2.007–2.183 Å and 2.085–2.115 Å, respectively (**Figure 1**) (Mistri et al., 2017; Zhou et al., 2019), the bonding mode of the carboxylate toward the six Co^{2+} ions is μ^{6}-η^{1}:η^{2}:η^{1}:η^{1}:η^{2}:η^{0} (**Supplementary Scheme 1** in the Supplementary Information), the adjacent Co1–Co3 atoms (Co···Co. separation, 3.168–6.337 Å) are united together by six carboxylates to form
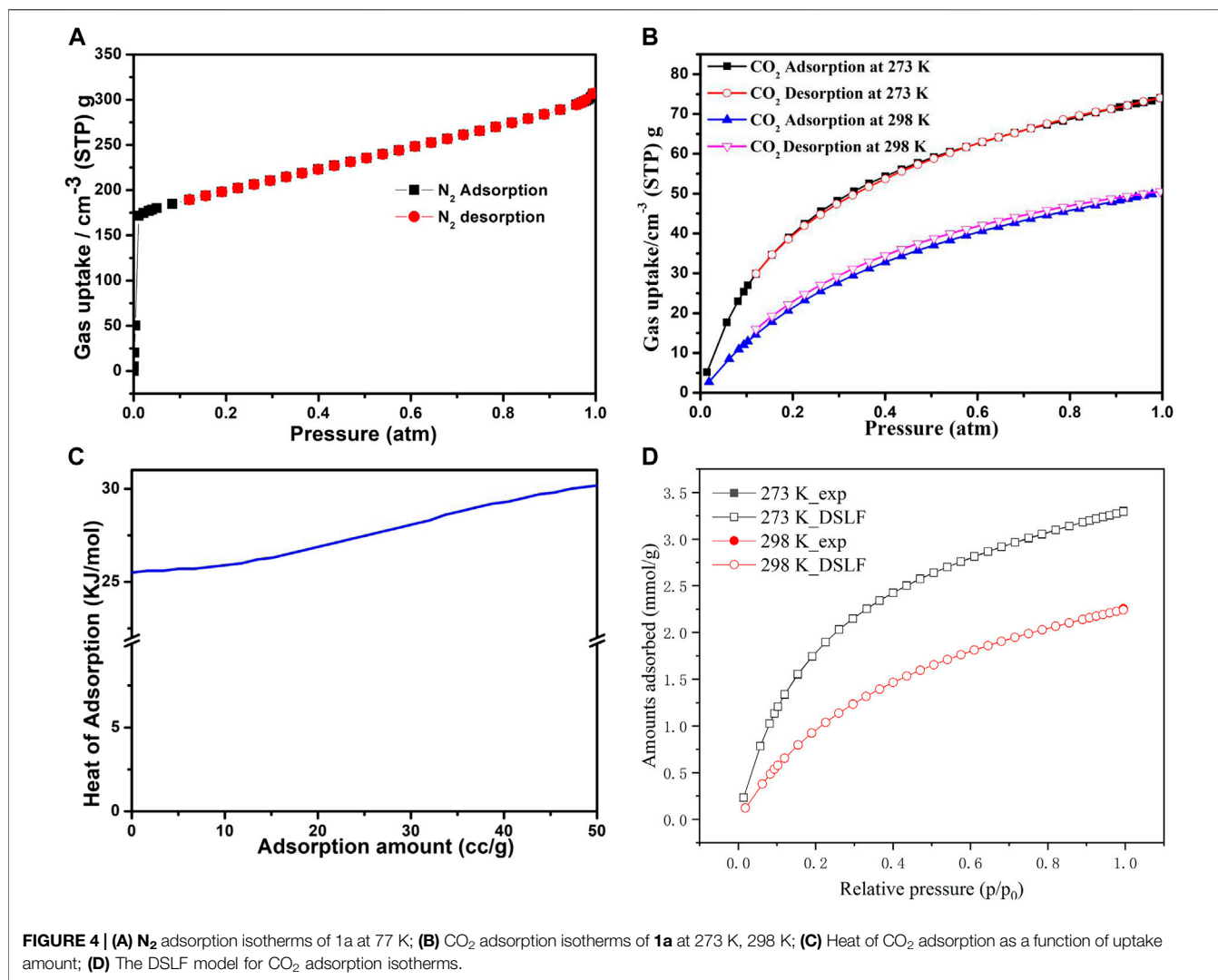
trinuclear Co.(II) clusters, each cluster can be connected to the adjacent ones to evolve a unique bylayer 2D framework, which contains quadrangle grids with a size of 7.0 Å × 6.4 Å running along the b-axis (atom-to-atom distance) (**Figure 2**). The 2D layers are then further converted into a 3D (supramolecular) structure via interactions of π–π stacking with the distance of 3.317 Å (**Figure 3**). The solvent-accessible volume in compound 1 was found to be 28.8 % (calculated using the PLATON software.12 after removal of solvent molecules).

If the L^{3-} ligands are defined as three-connected nodes, and the trinuclear Co.(II) cluster as six-connected nodes, the entire structure of Co. coordiantion polymer can be denoted as a (3, 6)-connected two-nodal net with a point symbol of $\{4^{3}\}_{2}\{4^{6}.6^{6}.8^{3}\}$, displaying the kgd topology (**Supplementary Figure S2**) (Kim et al., 2012; Wang et al., 2014).

Gas Sorption Experiment

The as-synthesized compound **1** was subjected to stirring with methanol at ambient temperature for 24 h to remove the solvent in the pores, followed by filtration of the compound and keeping at 60°C for 6 h in an oven. The compound was then heated for 24 h at 100°C under a vacuum to obtain the activated sample, 1a. The N_2 adsorption isotherm was acquired at 77 K, the result indicates that 1a displays a reversible type-I adsorption isotherm with the Brunauer–Emmett–Teller (BET) surface area of 658 $m^2 \cdot g^{-1}$, and the N_2 uptake (1 atm) reached 307 $cm^3 \cdot g^{-1}$ (**Figure 4A**). Meanwhile, the CO_2 adsorption isotherms for 1a were measured at 273 and 298 K; at 273 K (1 atm), and 298 K (1 atm) the CO_2 uptakes reached a maximum of 74 $cm^3 \cdot g^{-1}$ and 50 $cm^3 \cdot g^{-1}$, respectively (**Figure 4B**). The PXRD pattern of compound 1a remained stable after the adsorption of N_2 and CO_2 (**Supplementary Figure S11**). Considering the adsorption isotherm at 298 K, the observed CO_2 adsorption capacity of 1a is better than the metal-organic frameworks including

FIGURE 3 | The structure of compound **1** and interactions of π–π stacking (C: Gray, O: Red, N: Blue, Co:Purple).

FIGURE 4 | (A) N_2 adsorption isotherms of 1a at 77 K; **(B)** CO_2 adsorption isotherms of **1a** at 273 K, 298 K; **(C)** Heat of CO_2 adsorption as a function of uptake amount; **(D)** The DSLF model for CO_2 adsorption isotherms.

[Zn(BPTC)$_{0.5}$ (Tz)]•DMF•CH$_3$OH, JUC-MOF56, {[Cd$_2$ (tdz)$_2$ (4,4'-bpy)$_2$]•6.5H$_2$O}n, [Zn$_2$ (TCA) (BIB)$_{2.5}$]•(NO$_3$), ([Zr$_6$O$_4$(OH)$_8$(H$_2$O)$_4$(BTEB)$_2$]), and {[Cd$_4$ (hbhdpy)$_2$ (bdc-NH$_2$)$_3$ (DMA)$_2$]•(H$_2$O)$_4$}n that are summarized in **Supplementary Table S3** (Hong et al., 2017; Kong et al., 2018; Yao et al., 2018; Zhou et al., 2018; Liu et al., 2019). The adsorption isotherms show typical type-I sorption isotherm with fast kinetics and good reversibility, further indicating its microporosity.
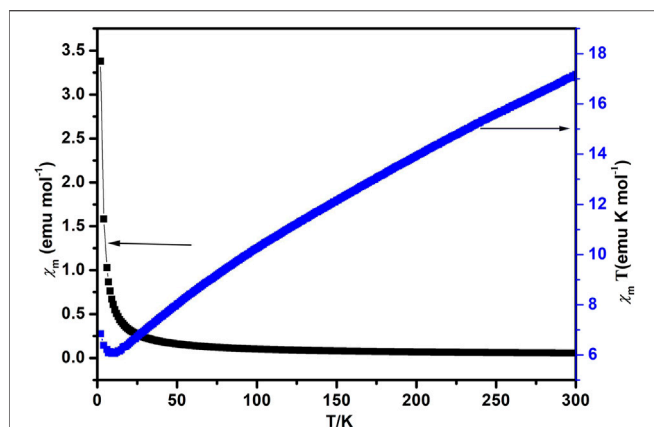
To understand better the CO_2 adsorption, we calculated the Q$_{st}$ (isosteric heat) for 1a using the CO_2 adsorption data, which were recorded at 273 and 298 K using the virial coefficient method. As depicted in **Figure 4C**, the Q$_{st}$ value reached 25.5 kJ mol^{-1} at zero loading, showing the good interactions of framewok–CO_2 in compound **1**, which can be ascribed to the uncoordinated O sites, N-donor of the H$_3$L, and the unique microporous channels. The dual-site Langmuir-Freundlich (DSLF) model was also utilized to fit the absolute adsorption isotherms of CO_2 from molecular simulations (**Figure 4D**). The result shows that the simulated

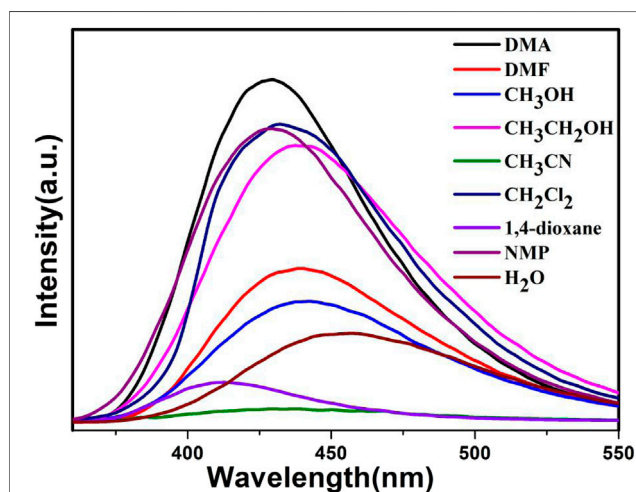CO_2 adsorption isotherms are in accordance with the experimental datas.

Magnetic Properties

Compound **1** was subjected to magnetic susceptibility measurements in the range 2–300 K at 1,000 Oe field, plots of the variable temperature magnetic susceptibility for compound **1** in the form of χ_mT vs T are presented in **Figure 5**. Compound **1** showed a higher χ_mT of about 17.17 emuK·mol^{-1} for a Co$_3$ unit at 300 K than the calculated spin-only value for three isolated Co^{2+} ions (5.75 emuK mol^{-1} and S = 3/2), and lies well in the range identified for octahedral Co^{2+} ions in the ^{4}T$_{2g}$ state, which is due to the significant contribution of orbitals belonging to Co^{2+} ion in the octahedral surroundings. Upon cooling, the χ_mT value decreases sharply until the temperature descends to 11 K, then it starts to increase rapidly, attaining a minimum value of 6.84 emuK·mol^{-1} at 2 K. The behavior is consistent with antiferromagnetic phenomenon between 11–300 K. The magnetic susceptibility fits the Curie–Weiss law well above 130 K, giving C = 20.95 emuK·mol^{-1} and θ = −185.5 K,

FIGURE 5 | Magnetic susceptibility of compound **1** plotted as χ_m vs. T (black) and χ_mT vs. T curves (blue).
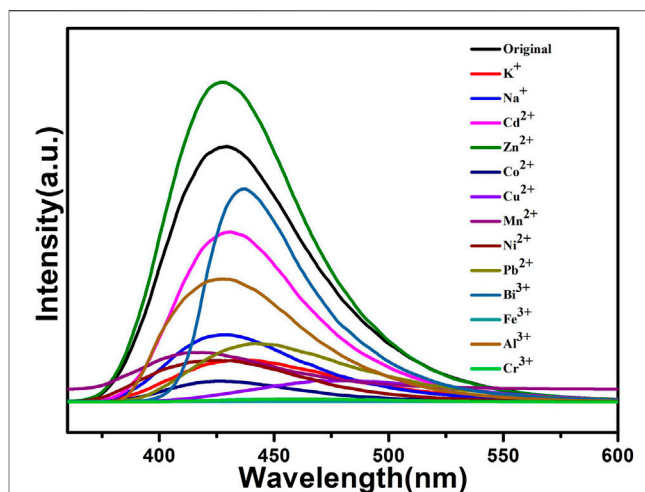

FIGURE 7 | Fluorescent analysis of 1a toward various metal ions (10^{-2} M) in DMA solution.

FIGURE 6 | Fluorescent spectra of compound **1a** in different solvents.

FIGURE 8 | Fluorescence of 1a in DMA containing different volumes of Fe^{3+} (1×10^{-3} M).

indicating an antiferromagnetic interaction between the Co_3 units.
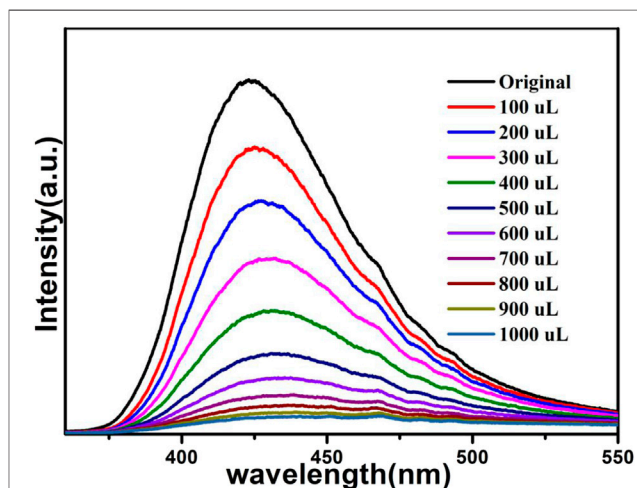
Luminescent Emission

The solid-state emission spectra of compound **1** and H_3L ligand are depicted in **Supplementary Figure S3**. The free ligand H_3L displayed emission at 448 nm when it is excited at 330 nm. Meanwhile, compound **1** showed an emission peak at 420 nm under excitation at 345 nm, there is a blue shift of 28 nm in comparison with the H_3L ligand. The fluorescence emission of compound **1** can be associated with the corresponding intraligand transitions ($\pi^\star \to \pi$ and $\pi^\star \to n$) (Zhang et al., 2018).

We select compound **1a** as a representative example to study its sensing sensitivity. Dispersions of compound **1a** (3 mg) in different solvents, namely DMA, DMF, methanol, ethanol, acetonitrile, dichloromethane, 1,4-dioxane, NMP (N-methyl-2-pyrrolidone), and H_2O (3 ml) were prepared, and the emission spectra were measured. As shown in **Figure 6**, the luminescence intensity was affected by the solvent, especially for DMA.

The above fluorescence performance prompted us to explore their potential sensing of metal ions. Samples of grounded 1a were dispersed in $M(NO_3)_x$ DMA solution separately (3 mg each sample in 3 ml, 0.01 M, $M(NO_3)_x$) (M = K^+, Cd^{2+}, Na^+, Zn^{2+}, Co^{2+}, Cu^{2+}, Mn^{2+}, Ni^{2+}, Pb^{2+}, Bi^{3+}, Fe^{3+}, Al^{3+}, Cr^{3+}), followed by ultrasonication for 1 h to obtain the uniform suspensions, the luminescence intensities of the suspensions were measured. The different emission peaks are shown in **Figure 7**, the metal ions exhibited different influence on the luminescence intensity, and the result showed that Fe^{3+} and Cr^{3+} exhibited a remarkable effect to quench the luminescence of **1a,** which indicate the high sensitivity performance of 1a towards Fe^{3+} and Cr^{3+}, the PXRD of compound 1a were measured after sensing the metal ions which remained their structural integrity (**Supplementary**

FIGURE 9 | Fluorescence of 1a in DMA containing different volumes of Cr^{3+} (5×10^{-3} M).

FIGURE 10 | Fluorescence of 1a in NACs solutions (10^{-3} M).

TABLE 1 | Inhibition zone diameters of compound **1** (A), H$_3$L (B) and 2,2′-bipy (C).

Diameters	A	B	C
Samples of inhibition zone (mm)			
Escherichia coli	5	0	0
Staphylococcus aureus	0	0	0

FIGURE 11 | Fluorescence of 1a in DMA containing different volumes of TNP (10^{-3} M).

[M], where I_0 and I are the fluorescence intensities before and after the addition of Fe^{3+} or Cr^{3+}, K_{sv} and [M] are the quenching constant and the concentration of Fe^{3+} or Cr^{3+}, the Stern–Volmer analysis of quenching effect on Fe^{3+} and Cr^{3+} ions show that the values of K_{sv} for Fe^{3+} and Cr^{3+} ions are 5.4×10^4 M^{-1}, 7.83×10^3 M^{-1}, and the limit detection of Fe^{3+} and Cr^{3+} are 0.278 mM, 1.91 mM respectively (Figs. S4 and S5).

The results indicate that compound 1a has the potential to act as a luminescence sensor toward Fe^{3+}, Cr^{3+}.

The NACs are explosive and environmentally deleterious. They have been used a lot in the chemical industry, so it is necessary to develop effective and quick detection of NACs. As presented in **Figure 10**, the luminescent intensity of 1a is completely quenched at 425 nm in the presence of TNP, while no obvious luminescent changes of 1a can be observed in other NACs, confirming that TNP has a pronounced emission quenching of compound **1a**, while other NACs showed less pronounced quenching.

To investigate further the sensitivity of 1a for TNP, a fluorescence titration study of TNP was conducted (**Figure 11**), the results showed that with increased incorporation of TNP solution (10^{-3} M), the luminescent intensity drastically decreased. Moreover, For the emission band of 1a, there is a large bathochromic shift of 39 nm, which is due to the energy transfer between TNP and compound **1a** (Gogia and Mandal, 2019). The quenching
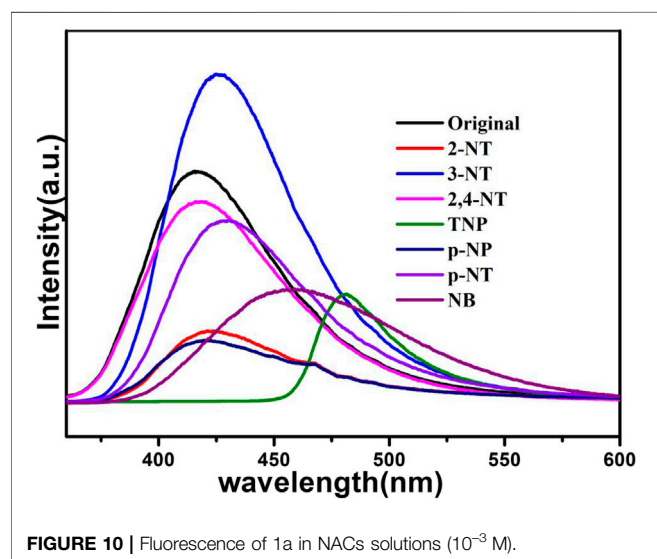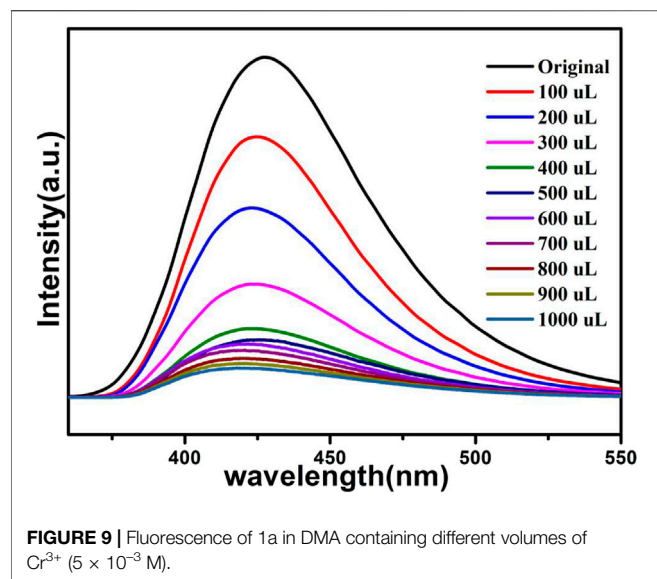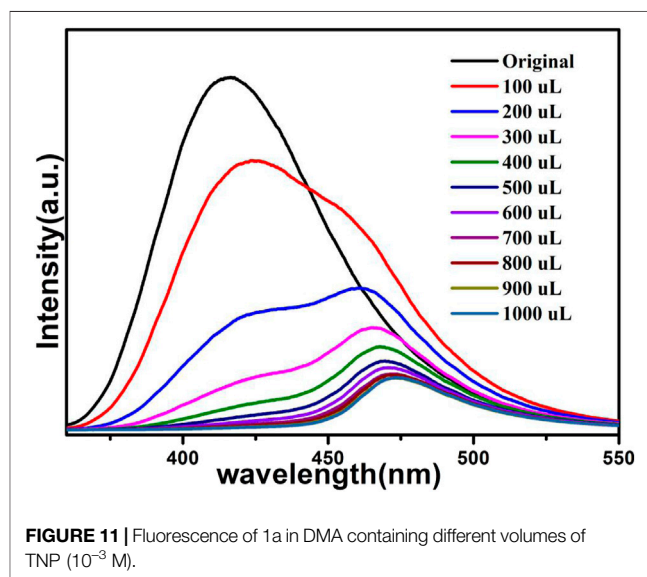
Figure S12). Furthermore, the anti-interference experiments were performed and the results indicated that the presence of other metal ions would not disturb the selective sensing of Fe^{3+} or Cr^{3+} (**Supplementary Figure S7**). Meanwhile, 3 mg samples of 1a were ground and immersed in DMA solution, sonicated for 1 h, the well-dispersed original suspensions were obtained, the Fe^{3+} or Cr^{3+} have been prepared in 1×10^{-3} M or 5×10^{-3} M DMA solution. The emission intensity decreased by gradually increasing the volume of Fe^{3+} and Cr^{3+} (**Figures 8**, **9**). Compound 1a was centrifuged and washed by DMA solvent after sensing Fe^{3+} or Cr^{3+}, the framework of the regenerated samples retained their stability, and reused for three cycles, the PXRD pattern of compound 1a is consistent with the recovered samples after three cycles (**Supplementary Figure S13**).

The fluorescence quenching efficiency can be discussed though the linear Stern–Volmer (S–V) equation: $I_0/I = 1 + K_{sv}$

effect of TNP on compound **1** can also be explained by the Stern-Volmer equation, and the details are provided in the SI. The S–V plot shows that the concentration of TNP and I_0/I possess a direct relationship over the added TNP volume range (100–1000 μL), with a linear fit coefficient value of 0.982. It is commendable that the K_{sv} value of sensing TNP reaches $3.99 \times 10^5 \, M^{-1}$ (**Supplementary Figure S6**), which is one of the highest reported values for TNP sensing, and the limit detection of TNP is 0.0376 mM (Hong et al., 2017; Hua et al., 2018; Gogia and Mandal, 2019; Ghorai et al., 2019; Wang et al., 2019).

In addition, the Fe^{3+}, Cr^{3+} and TNP solutions exhibit an absorption in the 260–500 nm range, which has overlaps with the excitation of compound 1a (Figs. S8 and S9). This shows the energy of excited light is taken by Fe^{3+}, Cr^{3+} or TNP, so the transfer of energy from L^{3-} to Co^{2+} is blocked, resulting the quenching effect on compound 1a. The sensing mechanism for metal ions can be attributed to the suppression of luminescence resonance energy transfer and the enhancement of intermolecular electron transfer (Chen et al., 2018).

Antibacterial Activity

The antibacterial activities of compound **1** against *Staphylococcus aureus* and *Escherichia coli* were measured using the transparent ring method. Compound **1**, the organic linker of TCA, and 2,2′-bipy were dissolved in distilled water with a concentration of 2 mg/ml. All the cultures were incubated for 18 h at 37 °C.

The results of the inhibition zone (ZOI) are shown in **Table 1** which reveals the antibacterial potential of compound **1** against *E. Coli*, whereas compound **1** does not have antibacterial activity against *S. aureus* (**Supplemetary Figure S16**). Therefore, compound **1** has potential applications as an antibacterial agent.

CONCLUSIONS

A new fluorescent 3D supramolecular Co. coordination polymer that contains uncoordinated O atoms in the channels was synthesized and characterized. The activated 1a exhibits a strong affinity toward CO_2 molecules, with the adsorption of $74 \, cm^3 \cdot g^{-1}$ (273 K, 1 atm). Magnetic measurements show that an antiferromagnetic exchange interaction exists in compound **1**. Moreover, compound 1 shows luminescence quenching with Fe^{3+}/Cr^{3+} metal ions, further studies on detection of NACs showed high performance for sensing TNP. These results may contribute to the design of more multifunctional coordiantion polymers.

DATA AVAILABILITY STATEMENT

The datasets presented in this study can be found in online repositories. The names of the repository/repositories and accession number(s) can be found below: Cambridge Crystallographic Data Centre (CCDC, https://www.ccdc.cam.ac.uk/), identification number 1961577

AUTHOR CONTRIBUTIONS

The experiments were conceived and designed by XZ; XZ, and HK. carried out the experimental work; Data were analyzed by LL, SZ, and MS; Supervision for this work was carried out by JL, and XT. All the authors contributed to the revision of manuscript.

FUNDING

SUPPLEMENTARY MATERIAL

The Supplementary Material for this article can be found online at: https://www.frontiersin.org/articles/10.3389/fchem.2021.678993/full#supplementary-material

REFERENCES

Ashraf, S., Ali, Q., Zahir, Z. A., Ashraf, S., and Asghar, H. N. (2019). Phytoremediation: Environmentally Sustainable Way for Reclamation of Heavy Metal Polluted Soils. *Ecotoxicology Environ. Saf.* 174, 714–727. doi:10.1016/j.ecoenv.2019.02.068

Cai, C., Zhao, M., Yu, Z., Rong, H., and Zhang, C. (2019). Utilization of Nanomaterials for *In-Situ* Remediation of Heavy Metal(loid) Contaminated Sediments: A Review. *Sci. Total Environ.* 662, 205–217. doi:10.1016/j.scitotenv.2019.01.180

Carter, K. P., Young, A. M., and Palmer, A. E. (2014). Fluorescent Sensors for Measuring Metal Ions in Living Systems. *Chem. Rev.* 114, 4564–4601. doi:10.1021/cr400546e

Chen, C.-H., Wang, X.-S., Li, L., Huang, Y.-B., and Cao, R. (2018). Highly Selective Sensing of Fe3+ by an Anionic Metal-Organic Framework Containing Uncoordinated Nitrogen and Carboxylate Oxygen Sites. *Dalton Trans.* 47, 3452–3458. doi:10.1039/c8dt00088c

Chen, L., Ma, N., Park, Y., Jin, S., Hwang, H., Jiang, D., et al. (2018). Highly Sensitive Determination of Iron (III) Ion Based on Phenanthroline Probe: Surface-Enhanced Raman Spectroscopy Methods. *Spectrochimica Acta A: Mol. Biomol. Spectrosc.* 197, 43–46. doi:10.1016/j.saa.2017.12.043

Chen, W.-M., Meng, X.-L., Zhuang, G.-L., Wang, Z., Kurmoo, M., Zhao, Q.-Q., et al. (2017). A superior Fluorescent Sensor for Al3+ and UO22+ Based on a Co(ii) Metal-Organic Framework with Exposed Pyrimidyl Lewis Base Sites. *J. Mater. Chem. A.* 5, 13079–13085. doi:10.1039/c7ta01546a

Chughtai, A. H., Ahmad, N., Younus, H. A., Laypkov, A., and Verpoort, F. (2015). Metal-organic Frameworks: Versatile Heterogeneous Catalysts for Efficient Catalytic Organic Transformations. *Chem. Soc. Rev.* 44, 6804–6849. doi:10.1039/c4cs00395k

Dong, C., Wu, G., Wang, Z., Ren, W., Zhang, Y., Shen, Z., et al. (2016). Selective Colorimetric Detection of Cr(III) and Cr(VI) Using Gallic Acid Capped Gold Nanoparticles. *Dalton Trans.* 45, 8347–8354. doi:10.1039/c5dt04099j

Espallargas, G. M., and Coronado, E. (2018). Magnetic Functionalities in MOFs: from the Framework to the Pore. *Chem. Soc. Rev.* 47, 533–557. doi:10.1039/C7CS00653E

Fan, J., Zhang, S., Xu, Y., Wei, N., Wan, B., Qian, L., et al. (2020). A Polyethylenimine/salicylaldehyde Modified Cellulose Schiff Base for Selective and Sensitive Fe3+ Detection. *Carbohydr. Polym.* 228, 115379. doi:10.1016/j.carbpol.2019.115379

Ghorai, P., Dey, A., Hazra, A., Dutta, A., Dutta, B., Brandão, P., et al. (2019). Cd(II) Based Coordination Polymer Series: Fascinating Structures, Efficient Semiconductors, and Promising Nitro Aromatic Sensing. *Cryst. Growth Des.*, 19, 6431–6447. doi:10.1021/acs.cgd.9b00891

Gogia, A., and Mandal, S. K. (2019). A Rational Design and green Synthesis of 3D Metal Organic Frameworks Containing a Rigid Heterocyclic Nitrogen-Rich Dicarboxylate: Structural Diversity, CO2 Sorption and Selective Sensing of 2,4,6-TNP in Water. *Dalton Trans.* 48, 2388–2398. doi:10.1039/c8dt04474k

Goswami, S., Aich, K., Das, A. K., Manna, A., and Das, S. (2013). A Naphthalimide-Quinoline Based Probe for Selective, Fluorescence Ratiometric Sensing of Trivalent Ions. *RSC Adv.* 3, 2412–2416. doi:10.1039/c2ra22624c

Guo, Z., Park, S., Yoon, J., and Shin, I. (2014). Recent Progress in the Development of Near-Infrared Fluorescent Probes for Bioimaging Applications. *Chem. Soc. Rev.* 43, 16–29. doi:10.1039/c3cs60271k

Haendel, S. R., Juan, P. H., Cristian, O. P., Cesar, A. S., and Carlos, Y. S. (2014). Antibacterial Activity against *Escherichia coli* of Cu-BTC (MOF-199) Metal-Organic Framework Immobilized onto Cellulosic Fibers. *J. Appl. Polym. Sci.* 131, 40815. doi:10.1002/app.40815

Haldar, R., Bhattacharyya, S., and Maji, T. K. (2020). Luminescent Metal-Organic Frameworks and Their Potential Applications. *J. Chem. Sci.* 132, 99. doi:10.1007/s12039-020-01797-y

Harigae, H. (2018). Iron Metabolism and Related Diseases: an Overview. *Int. J. Hematol.* 107, 5–6. doi:10.1007/s12185-017-2384-0

Hong, X.-J., Wei, Q., Cai, Y.-P., Zheng, S.-R., Yu, Y., Fan, Y.-Z., et al. (2017). 2-Fold Interpenetrating Bifunctional Cd-Metal-Organic Frameworks: Highly Selective Adsorption for CO2 and Sensitive Luminescent Sensing of Nitro Aromatic 2,4,6-Trinitrophenol. *ACS Appl. Mater. Inter.* 9, 4701–4708. doi:10.1021/acsami.6b14051

Hua, J. S., Cheng, T. T., Dong, S. J., Zhou, C. H., Huang, X. H., and Zhang, N. (2018). Multifunctional Luminescent Cd (II)-based Metal-Organic Framework Material for Highly Selective and Sensitive Sensing 2,4,6-trinitrophenol (TNP) and Fe3+ Cation. *Micropor. Mesopor. Mater.* 272, 177–183. doi:10.1016/j.micromeso.2018.06.013

Hu, Z., Deibert, B. J., and Li, j. (2014). Luminescent Metal-Organic Frameworks for Chemical Sensing and Explosive Detection. *Chem. Soc. Rev.* 43, 5815–5840. doi:10.1039/c4cs00010b

Huxford, R. C., Della Rocca, J., and Lin, W. (2010). Metal-Organic Frameworks as Potential Drug Carriers. *Curr. Opin. Chem. Biol.* 14, 262–268. doi:10.1016/j.cbpa.2009.12.012

Jia, X.-X., Yao, R.-X., Zhang, F.-Q., and Zhang, X.-M. (2017). A Fluorescent Anionic MOF with Zn4(trz)2 Chain for Highly Selective Visual Sensing of Contaminants: Cr(III) Ion and TNP. *Inorg. Chem.* 56, 2690–2696. doi:10.1021/acs.inorgchem.6b02872

Kaur, N., Tiwari, P., Kapoor, K. S., Saini, A. K., Sharma, V., and Mobin, S. M. (2020). Metal-organic Framework Based Antibiotic Release and Antimicrobial Response: an Overview. *CrystEngComm* 22, 7513–7527. doi:10.1039/d0ce01215g

Kim, D., Song, X., Yoon, J. H., and Lah, M. S. (2012). 3,6-Connected Metal-Organic Frameworks Based on Triscarboxylate as a 3-Connected Organic Node and a Linear Trinuclear Co3(COO)6 Secondary Building Unit as a 6-Connected Node. *Cryst. Growth Des.*, 12, 4186–4193. doi:10.1021/cg300686n

Kong, X.-J., Zhang, Y.-Z., He, T., Wu, X.-Q., Xu, M.-M., Wang, S.-N., et al. (2018). Two Interpenetrated Metal-Organic Frameworks with a Slim Ethynyl-Based Ligand: Designed for Selective Gas Adsorption and Structural Tuning. *CrystEngComm* 20, 6018–6025. doi:10.1039/c8ce00779a

Kurmoo, M. (2009). Magnetic Metal-Organic Frameworks. *Chem. Soc. Rev.* 38, 1353–1379. doi:10.1039/b804757j

Lan, A., Li, K., Wu, H., Olson, D. H., Emge, T. J., Ki, W., et al. (2009). A Luminescent Microporous Metal-Organic Framework for the Fast and Reversible Detection of High Explosives. *Angew. Chem. Int. Edition* 48, 2334–2338. doi:10.1002/anie.200804853

Li, B., Wen, H.-M., Zhou, W., and Chen, B. (2014). Porous Metal-Organic Frameworks for Gas Storage and Separation: what, How, and Why? *J. Phys. Chem. Lett.* 5, 3468–3479. doi:10.1021/jz501586e

Li, Y., Zhang, S., and Song, D. (2013). A Luminescent Metal-Organic Framework as a Turn-On Sensor for DMF Vapor. *Angew. Chem. Int. Ed.* 52, 710–713. doi:10.1002/anie.201207610

Liu, J., Chen, L., Cui, H., Zhang, J., Zhang, L., and Su, C.-Y. (2014). Applications of Metal-Organic Frameworks in Heterogeneous Supramolecular Catalysis. *Chem. Soc. Rev.* 43, 6011–6061. doi:10.1039/c4cs00094c

Liu, S., Yao, S., Liu, B., Sun, X., Yuan, Y., Li, G., et al. (2019). Two Ultramicroporous Metal-Organic Frameworks Assembled from Binuclear Secondary Building Units for Highly Selective CO2/N2 Separation. *Dalton Trans.* 48, 1680–1685. doi:10.1039/c8dt04424d

Lustig, W. P., Mukherjee, S., Rudd, N. D., Desai, A. V., Li, J., and Ghosh, S. K. (2017). Metal-organic Frameworks: Functional Luminescent and Photonic Materials for Sensing Applications. *Chem. Soc. Rev.* 46, 3242–3285. doi:10.1039/c6cs00930a

Ma, D., Li, B., Zhou, X., Zhou, Q., Liu, K., Zeng, G., et al. (2013). A Dual Functional MOF as a Luminescent Sensor for Quantitatively Detecting the Concentration of Nitrobenzene and Temperature. *Chem. Commun.* 49, 8964–8966. doi:10.1039/c3cc44546a

Mi, X., Sheng, D., Yu, Y. e., Wang, Y., Zhao, L., Lu, J., et al. (2019). Tunable Light Emission and Multiresponsive Luminescent Sensitivities in Aqueous Solutions of Two Series of Lanthanide Metal-Organic Frameworks Based on Structurally Related Ligands. *ACS Appl. Mater. Inter.* 11, 7914–7926. doi:10.1021/acsami.8b18320

Mishra, A., Jo, J.-H., Kim, H., Woo, S., and Chi, K.-W. (2014). A Discrete Cobalt Complex Obtained from a 1 D Coordination Polymer for Highly Selective Sensing of the Mercury(II) Ion. *ChemPlusChem* 79, 925–928. doi:10.1002/cplu.201402059

Mistri, S., Zangrando, E., Vojtíšek, P., and Manna, S. C. (2017). 1D, 2D, and 2D Parallel Interpenetrated Dicarboxylato Bridged Co(II) Metal Organic Frameworks: Synthesis, Crystal Structure, Fluorescence Sensing and Band Gap Calculation. *ChemistrySelect* 2, 2634–2642. doi:10.1002/slct.201700237

Paul, S., Manna, A., and Goswami, S. (2015). A Differentially Selective Molecular Probe for Detection of Trivalent Ions (Al3+, Cr3+and Fe3+) upon Single Excitation in Mixed Aqueous Medium. *Dalton Trans.* 44, 11805–11810. doi:10.1039/c5dt01314c

Pavlačka, M., Bajerová, P., Kortánková, K., Bláha, J., Zástěra, M., Mázl, R., et al. (2016). Analysis of Explosives Using Differential Mobility Spectrometry. *Int. J. Ion Mobil. Spec.* 19, 31–39. doi:10.1007/s12127-016-0190-7

Peng, Y. G., Zhang, Y. X., Kang, C. F., Chen, S. M., Song, L., Liu, D. H., et al. (2018). A Versatile MOF-Based Trap for Heavy Metal Ion Capture and Dispersion. *Nat. Comm.* 9, 187. doi:10.1038/s41467-017-02600-2

Rasheed, T., and Nabeel, F. (2019). Luminescent Metal-Organic Frameworks as Potential Sensory Materials for Various Environmental Toxic Agents. *Coord. Chem. Rev.* 401, 1–22. doi:10.1016/j.ccr.2019.213065

Rasheed, T., and Nabeel, F. (2019). Luminescent Metal-Organic Frameworks as Potential Sensory Materials for Various Environmental Toxic Agents. *Coord. Chem. Rev.* 401, 213065. doi:10.1016/j.ccr.2019.213065

Sadak, O., Sundramoorthy, A. K., and Gunasekaran, S. (2017). Highly Selective Colorimetric and Electrochemical Sensing of Iron (III) Using Nile Red Functionalized Graphene Film. *Biosens. Bioelectron.* 89, 430–436. doi:10.1016/j.bios.2016.04.073

Sahoo, S. K., and Crisponi, G. (2019). Recent Advances on Iron(III) Selective Fluorescent Probes with Possible Applications in Bioimaging. *Molecules* 24, 3267. doi:10.3390/molecules24183267

Saira, S., Waqas, A., Amjad, H. M., Sumaira, S., Yun, W., Yuan, Q. P., et al. (2020). Cu/H3BTC MOF as a Potential Antibacterial Therapeutic Agent against *Staphylococcus aureus* and *Escherichia coli*. *New J. Chem.* 44, 17671–17678. doi:10.1039/D0NJ04120C

Sun, C.-Y., Qin, C., Wang, X.-L., and Su, Z.-M. (2013). Metal-organic Frameworks as Potential Drug Delivery Systems. *Expert Opin. Drug Deliv.* 10, 89–101. doi:10.1517/17425247.2013.741583

Tang, Y., Chen, J., Wu, H., Yu, J., Jia, J., Xu, W., et al. (2020). A Highly Fluorescent post-modified Metal Organic Framework Probe for Selective, Reversible and Rapid Carbon Dioxide Detection. *Dyes Pigm.* 172, 107798. doi:10.1016/j.dyepig.2019.107798

Tian, C., Yin, J., Zhao, Z., Zhang, Y., and Duan, Y. (2017). Rapid Identification and Desorption Mechanisms of Nitrogen-Based Explosives by Ambient Micro-fabricated Glow Discharge Plasma Desorption/ionization (MFGDP) Mass Spectrometry. *Talanta* 167, 75–85. doi:10.1016/j.talanta.2017.02.011

VanderMeulen, H., and Sholzberg, M. (2018). Iron Deficiency and Anemia in Patients with Inherited Bleeding Disorders. *Transfus. Apher. Sci.* 57, 735–738. doi:10.1016/j.transci.2018.10.015

Wallace, K. J., Johnson, A. D. G., Jones, W. S., and Manandhar, E. (2018). Chemodosimeters and Chemoreactands for Sensing Ferric Ions. *Supramolecular Chem.* 30, 353–383. doi:10.1080/10610278.2017.1415434

Wang, J., Wu, J., Lu, L., Xu, H. J., Trivedi, M., Kumar, A., et al. (2019). A New 3D 10-Connected Cd(II) Based MOF with Mixed Ligands: A Dual Photoluminescent Sensor for Nitroaroamatics and Ferric Ion. *Front. Chem.* 7, 244. doi:10.3389/fchem.2019.00244

Wang, R., Wang, Z., Xu, Y., Dai, F., Zhang, L., and Sun, D. (2014). Porous Zirconium Metal-Organic Framework Constructed from 2D → 3D Interpenetration Based on a 3,6-Connected Kgd Net. *Inorg. Chem.* 53, 7086–7088. doi:10.1021/ic5012764

Wen, B., Shan, X. Q., and Lian, J. (2002). Separation of Cr(III) and Cr(VI) in River and Reservoir Water with 8-hydroxyquinoline Immobilized Polyacrylonitrile Fiber for Determination by Inductively Coupled Plasma Mass Spectrometry. *Talanta* 56, 681–687. doi:10.1016/s0039-9140(01)00632-4

Wollin, K. M., and Dieter, H. H. (2005). Toxicological Guidelines for Monocyclic Nitro-, Amino- and Aminonitroaromatics, Nitramines, and Nitrate Esters in Drinking Water. *Arch. Environ. Contam. Toxicol.* 49, 18–26. doi:10.1007/s00244-004-0112-2

Yamada, T., Otsubo, K., Makiura, R., and Kitagawa, H. (2013). Designer Coordination Polymers: Dimensional Crossover Architectures and Proton Conduction. *Chem. Soc. Rev.* 42, 6655–6669. doi:10.1039/c3cs60028a

Yao, C., Zhou, S., Kang, X., Zhao, Y., Yan, R., Zhang, Y., et al. (2018). A Cationic Zinc-Organic Framework with Lewis Acidic and Basic Bifunctional Sites as an Efficient Solvent-free Catalyst: CO2 Fixation and Knoevenagel Condensation Reaction. *Inorg. Chem.* 57, 11157–11164. doi:10.1021/acs.inorgchem.8b01713

Yi, F.-Y., Chen, D., Wu, M.-K., Han, L., and Jiang, H.-L. (2016). Chemical Sensors Based on Metal-Organic Frameworks. *ChemPlusChem* 81, 675–690. doi:10.1002/cplu.201600137

Yu, M.-H., Hu, T.-L., and Bu, X.-H. (2017). A Metal-Organic Framework as a "turn on" Fluorescent Sensor for Aluminum Ions. *Inorg. Chem. Front.* 4, 256–260. doi:10.1039/c6qi00362a

Zhang, J., O. Y, J., Ouyang, Y., Li, Z., Lin, Q., Chen, T., et al. (2018). Mixed-Valence Cobalt(II/III) Metal-Organic Framework for Ammonia Sensing with Naked-Eye Color Switching. *ACS Appl. Mater. Inter.* 10, 27465–27471. doi:10.1021/acsami.8b07770

Zhang, S.-R., Li, J., Du, D.-Y., Qin, J.-S., Li, S.-L., He, W.-W., et al. (2015). A Multifunctional Microporous Anionic Metal-Organic Framework for Column-Chromatographic Dye Separation and Selective Detection and Adsorption of Cr3+. *J. Mater. Chem. A.* 3, 23426–23434. doi:10.1039/c5ta07427d

Zhang, Y., Yuan, S., Day, G., Wang, X., Yang, X., and Zhou, H.-C. (2018). Luminescent Sensors Based on Metal-Organic Frameworks. *Coord. Chem. Rev.* 354, 28–45. doi:10.1016/j.ccr.2017.06.007

Zhang, Z., Yao, Z.-Z., Xiang, S., and Chen, B. (2014). Perspective of Microporous Metal-Organic Frameworks for CO2capture and Separation. *Energy Environ. Sci.* 7, 2868–2899. doi:10.1039/c4ee00143e

Zhao, X.-X., Qin, Z.-B., Li, Y.-H., and Cui, G.-H. (2018). Two Luminescent Cobalt(II) Coordination Polymers for Selective Sensing of MnO4− in Water. *Transit. Met. Chem.* 43, 597–604. doi:10.1007/s11243-018-0248-y

Zhou, E.-L., Qin, C., Tian, D., Wang, X.-L., Yang, B.-X., Huang, L., et al. (2018). A Difunctional Metal-Organic Framework with Lewis Basic Sites Demonstrating Turn-Off Sensing of Cu2+ and Sensitization of Ln3+. *J. Mater. Chem. C* 6, 7874–7879. doi:10.1039/c8tc02425a

Zhou, H.-C. J., and Kitagawa, S. (2014). Metal-Organic Frameworks (MOFs). *Chem. Soc. Rev.* 43, 5415–5418. doi:10.1039/c4cs90059f

Zhou, X. J., Guo, X. L., Liu, L. L., Shi, Z., Pang, Y., and Tai, X. S. (2019). Synthesis, Crystal Structures, and Magnetic Properties of Three Cobalt(II) Coordination Polymers Constructed from 3,5-Pyridinedicarboxylic Acid or 3,4-Pyridinedicarboxylic Acid Ligands. *Crystals* 9 (166), 1–10. doi:10.3390/cryst9030166

Host-Guest Interactions Between Metal–Organic Frameworks and Air-Sensitive Complexes at High Temperature

Bo Huang[1,2]* and Zhe Tan[1]

[1]Institute of Chemical Engineering and Technology, Xi'an Jiaotong University, Xi'an, China, [2]State Key Laboratory of Structural Chemistry, Fujian Institute of Research on the Structure of Matter, Chinese Academy of Sciences, Fuzhou, China

The host-guest chemistry of metal–organic frameworks (MOFs) has been attracting increasing attention owing to the outstanding properties derived from MOFs-guests combinations. However, there are large difficulties involved in the syntheses of the host-guest MOF systems with air-sensitive metal complexes. In addition, the behaviors on host-guest interactions in the above systems at high temperature are not clear. This study reported the synthetic methods for host-guest systems of metal–organic framework and air-sensitive metal complexes via a developed chemical vapor infiltration process. With the synchrotron X-ray powder diffraction (XRPD) measurements and Fourier Transform infrared spectroscopy (FTIR), the successful loadings of $Fe(CO)_5$ in HKUST-1 and NH_2-MIL-101(Al) have been confirmed. At high temperatures, the structural and chemical componental changes were investigated in detail by XRPD and FTIR measurements. HKUST-1 was proven to have strong interaction with $Fe(CO)_5$ and resulted in a heavy loading amount of 63.1 wt%, but too strong an interaction led to deformation of HKUST-1 sub-unit under heating conditions. NH_2-MIL-101(Al), meanwhile, has a weaker interaction and is chemically inert to $Fe(CO)_5$ at high temperatures.

INTRODUCTION

Metal–organic frameworks (MOFs) or porous coordination polymers (PCPs) have attracted much attention in the past several decades (Zhang et al., 2020; Yuan et al., 2018). Benefiting from their high crystallinity, porosity, and designability, thousands of unique MOFs have been designed and synthesized, with potential applications in gas storage (Chen et al., 2020; Tian et al., 2018; Kalmutzki, Diercks, and Yaghi 2018; Alezi et al., 2015; Jiang et al., 2016), separation (Fu et al., 2016; Liu et al., 2018; Gao et al., 2020; Peng et al., 2017; Zhang et al., 2019), catalysis (Wang, An, and Lin 2019; Liang et al., 2018; Manna et al., 2015), and so on. On the other hand, metal complexes are one of the most developed research fields, with various properties such as magnetism (Guo, Bar, and Layfield 2019), superconductivity (Wang et al., 2019), and catalysis(Nicastri et al., 2020; Trammell, Rajabimoghadam, and Garcia-Bosch 2019). It would be useful to merge MOFs and metal complexes together and investigate their host-guest chemistry.

There have been several pioneering works in this field, but most research is focused on physical properties like electrical conductivity (Talin et al., 2014) and magnetism (Han et al., 2015). The interactions based on chemical properties between host MOFs and guest metal complexes are

relatively less researched (Nayak, Harms, and Dehnen 2011). The largest limitation on research of host-guest systems for MOFs and metal complexes is the difficulties in their syntheses, especially in air-sensitive systems. In chemical processes, the chemical components and structures of them may have complicated changes. The systematic investigation on the host-guest chemistry of MOF-metal complex systems with air-sensitive complexes has rarely been reported, although a few air-stable metal complexes have already been researched, such as $FeCp_2$ and Ru (cod) (cot) (Kalidindi, Yusenko, and Fischer 2011).

In this study, we reported a systematic research on MOF-metal complex systems of air-sensitive $Fe(CO)_5$ guest in HKUST-1 and NH_2-MIL-101(Al), consisting of syntheses, characterization, and investigation on host-guest interactions at high temperatures.

EXPERIMENTAL

Synthesis of HKUST-1

875 mg of $Cu(NO_3)_2 \cdot 3H_2O$ and 420 mg of benzene-1,3,5-tricarboxylic acid (BTC) were dissolved in 24 ml of H_2O and EtOH mixture solvent (1:1 vol. ratio). The solution was sealed in a solvothermal container and reacted at 120°C for 12 h. The solution was then cooled down to room temperature at a fixed rate for 6 h. The light blue solid was filtered and washed with EtOH. The washed HKUST-1 was dried at 60°C and activated at 100°C under vacuum. The activated sample was stored in a glovebox for further use.

Synthesis of NH_2-MIL-101(Al)

Aluminium chloride hexahydrate ($AlCl_3 \cdot 6H_2O$, 0.51 g), 2-amino terephthalic acid (0.56 g), and DMF (30 ml) were heated at 130°C over 3 days. The product was refluxed in methanol overnight and dried at 100°C under vacuum overnight. The activated sample was stored in a glovebox for further use.

X-Ray Powder Diffraction and Synchrotron X-Ray Powder Diffraction

The crystal structures of MOFs, $Fe(CO)_5$-loaded MOFs, and their thermal decomposition products were investigated by powder XRD analysis using a Bruker D8 Advance diffractometer (Cu $K\alpha$ radiation).

The crystal structures were investigated by capillary synchrotron XRPD analysis measured at the BL02B2 beamline, SPring-8. The XRPD patterns of the samples sealed in a glass capillary were measured *in situ* with a wavelength of 1.000 Å.

Fourier Transform Infrared Spectroscopy and Transmission Electron Microscopy

FTIR spectra of MOFs, $Fe(CO)_5$-loaded MOFs, and their thermal decomposition products were obtained to evaluate sample structures. All IR spectra were recorded inside a glovebox using a Bruker PLATINUM ATR FTIR spectrometer, accumulating 64 scans at a resolution of 4 cm^{-1}.

TEM images were captured using Talos F200X operated at 200 kV accelerating voltage.

RESULTS AND DISCUSSION

Chemical Vapor Infiltration of $Fe(CO)_5$ Into HKUST-1

$Fe(CO)_5$ is one of the most common metal complexes which are sensitive to air. The $Fe(CO)_5$ loading experiment in HKUST-1 was shown in the schematic image of **Figure 1A** via a chemical vapor infiltration (CVI) method. The HKUST-1 was synthesized and activated according to the reported method (Chui et al., 1999). The as-synthesized HKUST-1 was confirmed by capillary XRPD measurement; similar XRPD patterns with simulated HKUST-1 proved the successful synthesis of HKUST-1 (**Supplementary Figure S1**).

104.5 mg of activated HKUST-1 and 405.3 mg $Fe(CO)_5$ were sealed in CVI vessel inside a glovebox (**Figure 1B** left). The CVI vessel was transferred to autoclave and heated at 60°C for 2 h for $Fe(CO)_5$ loading; the obtained product was named $Fe(CO)_5@$ HKUST-1 (**Figure 1B** right). The mass of CVI product was weighed inside a glovebox as 270.3 mg, with 61.3 wt% loading amount.

To check the state of $Fe(CO)_5$ loading in HKUST-1, synchrotron XRPD measurements have been carried out with incident wavelengths of 1.000 Å. All samples were kept under inert conditions inside glass capillary during measurements. As shown in **Figure 2**, the activated HKUST-1 exhibits strong diffraction intensity. However, after loading with $Fe(CO)_5$, most of the diffraction peaks disappeared, with only remaining weak peaks below 10°. This phenomenon suggested the perturbation on the original crystalline structure of HKUST-1 by $Fe(CO)_5$ infiltration.

To further confirm the MOF structure after loading, FTIR measurements have been performed under inert conditions. As shown in **Supplementary Figure S2**, sharp IR peaks were observed in activated HKUST-1. After loading of $Fe(CO)_5$, all peaks originated from HKUST-1 remained, which strongly proved the stability of MOF structure before and after loading. In addition to those sharp peaks belonging to HKUST-1, a new typical carbonyl peak marked with asterisks has been found, confirming the successful loading of $Fe(CO)_5$. Furthermore, the red shift of HKUST-1 peak at 1,650 cm^{-1} suggested the obstruction of MOF ligand vibration from the loaded $Fe(CO)_5$ guest molecules, which gave further proof for successful loading of $Fe(CO)_5$ inside HKUST-1 pores.

High Temperature Behavior of $Fe(CO)_5@$ HKUST-1

In order to further understand the host-guest interactions between HKUST-1 and $Fe(CO)_5$, we performed high temperature experiments with different heating conditions inside a glovebox. As shown in **Supplementary Figure S3A**, the dark blue solid of $Fe(CO)_5@$HKUST-1 was heated at 140°C, and the color change to yellow was observed after 10 min heating
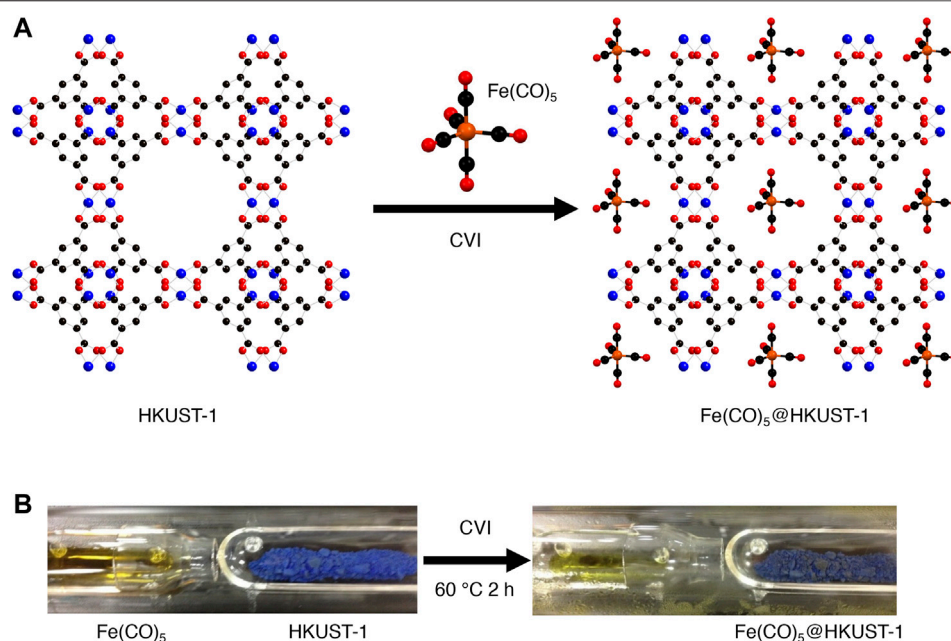
FIGURE 1 | **(A)** Schematic image and **(B)** experimental images for Fe(CO)₅ loading in HKUST-1 via a chemical vapor infiltration process.
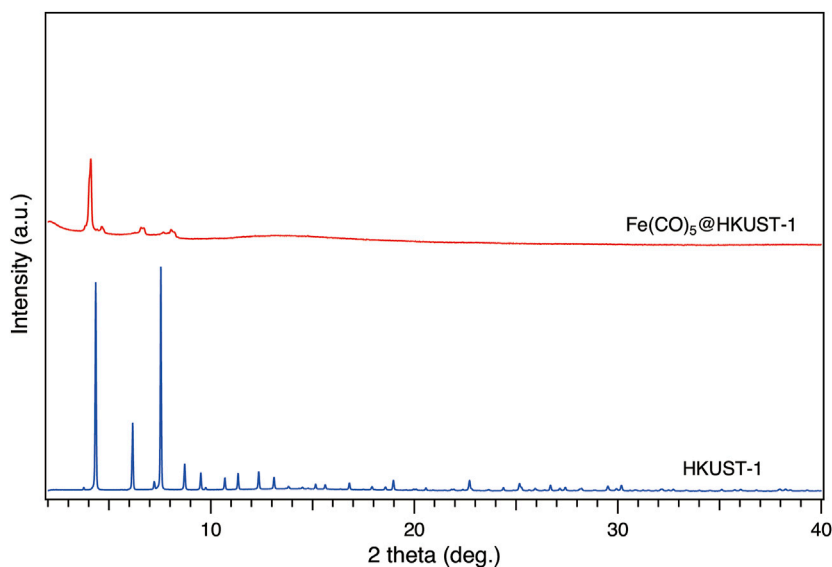
FIGURE 2 | Synchrotron XRPD patterns of activated HKUST-1 (blue) and CVI product of Fe(CO)₅@HKUST-1 (red) at 303 K. All samples were sealed in glass capillary in a glovebox under Ar atmosphere. The radiation wavelength was 1.000 Å.

(sample named **140–10**). We also tested other heating temperature of 170 and 200°C; similar color changes to yellow solid occurred within 1 min (**Supplementary Figure S3B**, samples named **170–1** and **200–1**, respectively). For longer heating times at 200°C, a gradual color change from yellow to purple was observed within 1.5 h (**Supplementary Figure S3B**, sample named **200–90**).

To explore the structural information of Fe(CO)₅@HKUST-1 under various heating conditions, we performed XRPD measurements under inert conditions by using an inert sample holder (**Supplementary Figure S4**). Before measurements, to avoid the samples being contaminated by air, the inert holder was tightly sealed inside a glovebox after sample setup. The measurement results are shown in **Figure 3**; after heat
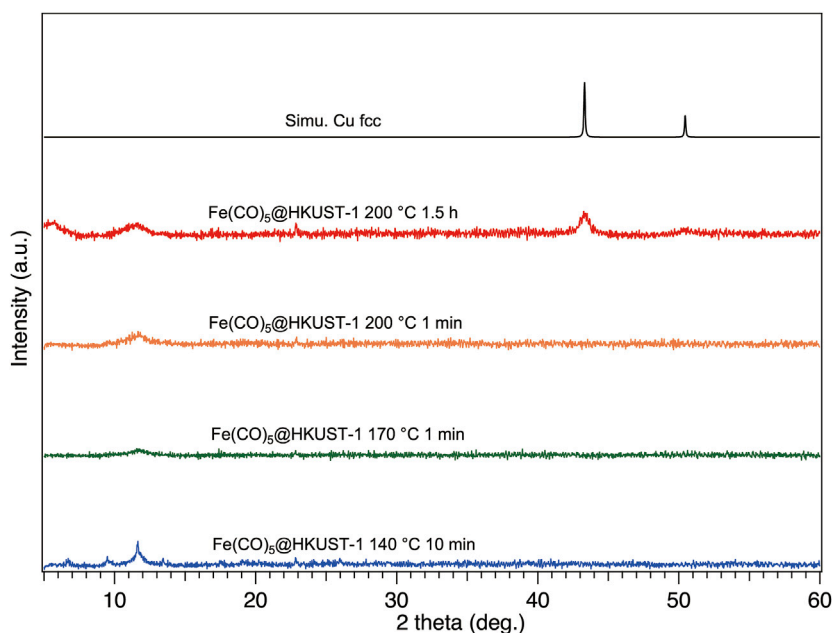
FIGURE 3 | XRPD patterns of Fe(CO)₅@HKUST-1 decomposed at different conditions: 140˚C-10 min (blue), 170˚C-1 min (green), 200˚C-1 min (orange), 200˚C-1.5 h (red), and simulated Cu (black). All samples were sealed inside a glovebox and measured under inert conditions. The background of XRPD patterns had been removed for clarity. The radiation wavelength was 1.5406 Å.

treatment at 140˚C for 10 min, the crystallinity of HKUST-1 was slightly damaged compared with XRPD pattern of Fe(CO)₅@ HKUST-1 in **Figure 2**, due to the thermal decomposition of Fe(CO)₅. In TEM image of **140–10**, a homogenous solid structure was observed (**Supplementary Figure S5**), the result is consistent with its XRPD pattern. For **170–1**, even the heating time was much shorter than **140–10**, and higher temperatures led to harsh damage on crystallinity, where only the (222) main peak at 11.8˚ of HKUST-1 remained, shown in **Figure 3**, owing to faster decomposition of Fe(CO)₅. The XRPD result of **200–1** was similar to that of **170–1** (**Figure 3**).

With the extension of heating time to 1.5 h (sample **200–90**), a crush of crystallinity was accompanied with the appearance of new broad diffraction peaks at 43.5 and 50.7˚, which are consistent with diffraction peaks of simulated face-centered cubic (fcc) Cu, proving the generation of Cu NPs. Actually, under vacuum conditions, after heating at 200˚C for 18 h, no Cu diffraction peak was detected (**Supplementary Figure S6**). Even with sufficient heating of HKUST-1 at 500˚C for 2 h (Lee et al., 2019), instead of the metallic state of Cu NPs, only semiconductor CuO NPs can be obtained. On the other hand, Cu NPs can be easily generated when the heating atmosphere is changed to 1 atm of H_2, at 200˚C for 1 h (**Supplementary Figure S7**). Under H_2 atmosphere, the decreasing on (222) peak of Cu^{2+} ion-rich plane in HKUST-1 and the increasing on (111) peak of Cu NPs demonstrate the migration of Cu elements from the square-planar coordinated Cu^{2+} ions in HKUST-1 to dodecahedral coordinated Cu atoms in fcc-Cu NPs. Therefore, in sample **200–90**, it may be suggested that the reduction reaction of Cu^{2+} to Cu atom was triggered by decomposition of Fe(CO)₅.

The existence of Cu NPs in **200–90** was also confirmed by TEM measurement (**Supplementary Figure S8**).

To understand more about the thermal decomposition processes of the Fe(CO)₅@HKUST-1 at various conditions, the FTIR spectroscopy has been measured inside a glovebox (**Figure 4**). Samples **140–10**, **170–1,** and **200–1** show almost identical IR spectra among each other. The incomplete decomposition of Fe(CO)₅ can be noticed from the remaining typical CO peaks in these three samples. The broadening of MOF peaks compared with the initial sharp peaks from HKUST-1 demonstrated the decomposition of MOFs sub-units under thermal decomposition of Fe(CO)₅ guest molecule, in addition to the collapse of HKUST-1 crystal structure confirmed by XRPD measurements in **Figure 3B**. In spectrum of **200–90**, CO peaks vanished because of the complete decomposition of Fe(CO)₅ with a longer heat treatment.

High Temperature Behavior of Fe(CO)₅@ MIL-101(Al)

The above results have shown the host-guest interactions in case of Fe(CO)₅@HKUST-1 at high temperatures, where the decomposition of Fe(CO)₅ broke the Cu_2O_8 clusters in HKUST-1. Other MOFs with different clusters may resist Fe(CO)₅ at high temperatures. Among potential candidate MOFs, we guessed that NH_2-MIL-101(Al) can be durable to Fe(CO)₅ at high temperaturse because of its relatively high thermal stability and chemical inertness. The NH_2-MIL-101(Al) was synthesized via a reported protocol (Serra-Crespo et al., 2011).
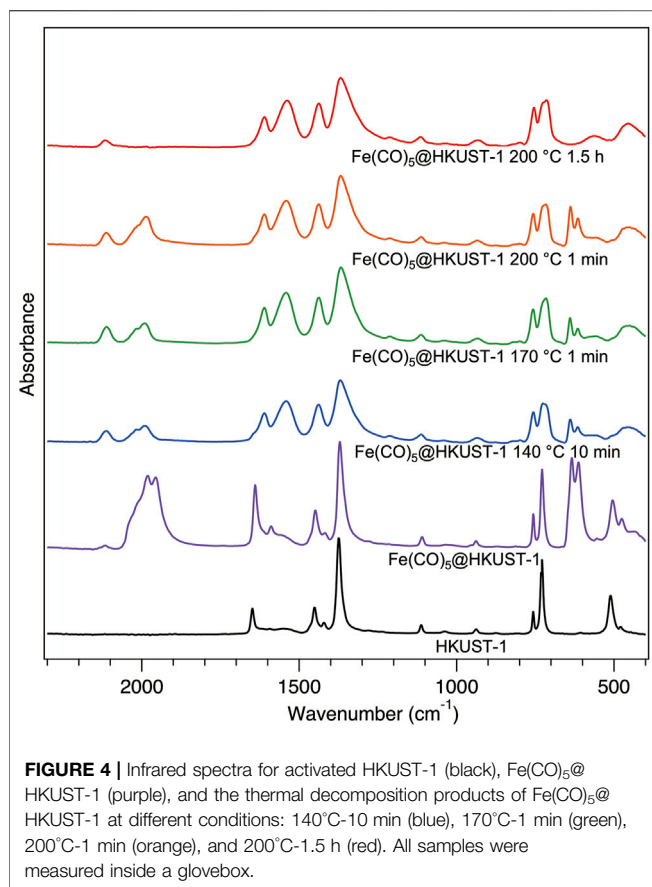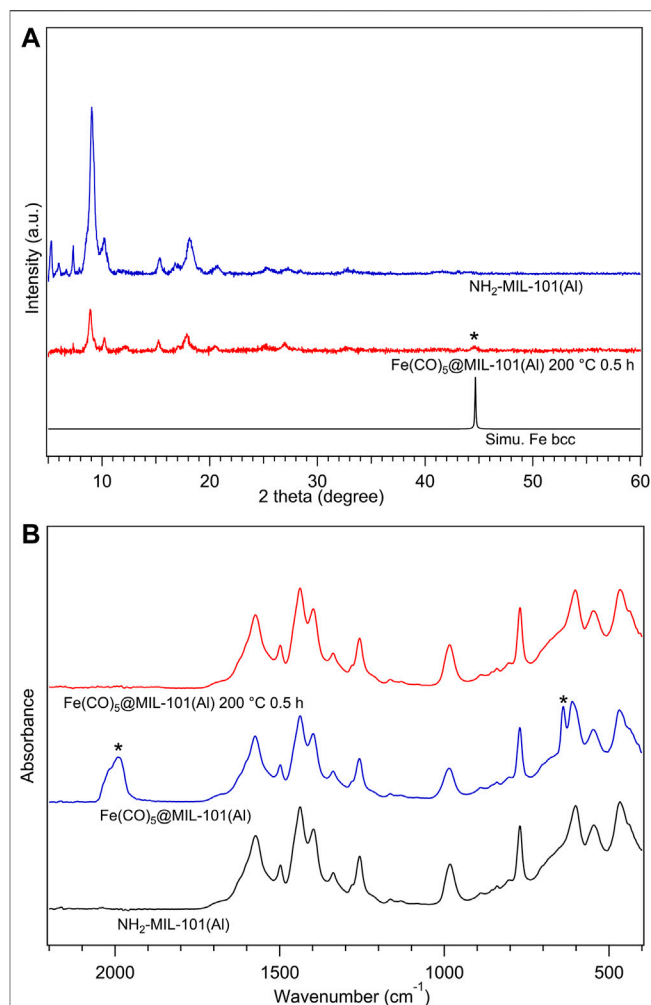
FIGURE 4 | Infrared spectra for activated HKUST-1 (black), Fe(CO)$_5$@ HKUST-1 (purple), and the thermal decomposition products of Fe(CO)$_5$@ HKUST-1 at different conditions: 140°C-10 min (blue), 170°C-1 min (green), 200°C-1 min (orange), and 200°C-1.5 h (red). All samples were measured inside a glovebox.

FIGURE 5 | (A) Infrared spectra for activated NH$_2$-MIL-101(Al) (black), Fe(CO)$_5$@MIL-101(Al) (blue), and Fe(CO)$_5$@MIL-101(Al) decomposed at 200°C/0.5 h (red), all samples were measured inside a glovebox. **(B)** XRPD patterns of NH$_2$-MIL-101(Al) (blue), Fe(CO)$_5$@MIL-101(Al) decomposed at 200°C/0.5 h (red), and simulated body-centred-cubic Fe (black), all samples were measured under inert conditions by capillary technique. The radiation wavelength was 1.5406 Å.

After activation of NH$_2$-MIL-101(Al), the gas phase loading of Fe(CO)$_5$ to NH$_2$-MIL-101(Al) was performed by CVI process under similar conditions. 101.7 mg of activated NH$_2$-MIL-101(Al) and 403.2 mg Fe(CO)$_5$ were kept at 60°C for 2 h under Ar atmosphere. The mass of loading product Fe(CO)$_5$@ MIL-101(Al) was 127.4 mg with 20.2 wt% loading amount. Lower loading amounts for NH$_2$-MIL-101(Al) than 61.3 wt% of HKUST-1 may be attributed to its weaker host-guest interaction as the lack of open metal site.

The CVI product Fe(CO)$_5$@MIL-101(Al) was investigated by FTIR measurements performed inside the glovebox. As shown in **Figure 5A**, there are typical carbonyl vibration peaks in the spectrum of Fe(CO)$_5$@MIL-101(Al) marked with asterisks, proving the existence of Fe(CO)$_5$ guest molecules in the product. Combined with the carbonyl peaks, the sustenance for the IR peaks of the MOF structure before and after CVI process suggested the successful loading of Fe(CO)$_5$ to NH$_2$-MIL-101(Al) without breaking the MOF structure.

The thermal stability of Fe(CO)$_5$@MIL-101(Al) was tested under inert conditions. Fe(CO)$_5$@MIL-101(Al) was heated to 200°C (same temperature as Fe(CO)$_5$@HKUST-1) for 0.5 h, referred to as **200–30**. In **Figure 5A**, with the comparison of the FTIR spectra of NH$_2$-MIL-101(Al), Fe(CO)$_5$@MIL-101(Al), and **200–30**, the complete decomposition of Fe(CO)$_5$ and the maintaining of MOF structure can be confirmed in **200–30**. On the other hand, in XRPD measurement results shown in

Figure 5B, the asterisk diffraction peak from the body-centred cubic (bcc) Fe NPs was detected in **200–30**, as solid evidence for Fe formation from Fe(CO)$_5$. The XRPD measurements also show the lower crystallinity in diffraction pattern of **200–30** compared with that of NH$_2$-MIL-101(Al), which may be considered as a perturbation of periodic structure by randomly dispersed guest molecules inside pores.

Finally, to elucidate the reasons for the different behaviors between Fe(CO)$_5$@HKUST-1 and Fe(CO)$_5$@MIL-101(Al), the possible reaction mechanisms in each case should be further discussed. Since the decomposition of Fe(CO)$_5$ below 150°C is negligible (Carlton and Oxley, 1965), the molecular Fe(CO)$_5$ reacting with HKUST-1 backbone in **140–10** can be considered as the redox reaction between penta-coordinated Fe (0) with tetra-coordinated Cu(II) open metal sites. At

higher temperatures of 170 and 200°C, the $Fe(CO)_5$ decompositions were significantly promoted, supplying atomic Fe and molecular CO to these systems. HKUST-1 backbone is stable with CO molecule to at least 210°C, (Stawowy et al., 2020), therefore, the rapid destruction of MOFs shown in **Figure 4** for **170–1** and **200–1** are mainly attributed to the strong reduction ability of atomic Fe. As the ligand reactivity difference between benzene-1,3,5-tricarboxylic acid in HKUST-1 and 2-amino terephthalic acid in NH_2-MIL-101(Al) is almost negligible, the main reason for the different behavior of $Fe(CO)_5$@HKUST-1 and $Fe(CO)_5$@MIL-101(Al) can be concluded as the different reactivity of metal ions. With the systematic investigations on loading and heating processes of $Fe(CO)_5$ guest to HKUST-1 and NH_2-MIL-101(Al), the interactions between host MOFs and guest molecules were clarified.

CONCLUSION

The host-guest systems of MOFs and air-sensitive metal complexes were synthesized, with $Fe(CO)_5$ loaded in HKUST-1 and NH_2-MIL-101(Al) via a chemical vapor infiltration process. With the XRPD and FTIR measurements under inert conditions, the successful loading of $Fe(CO)_5$ in HKUST-1 and NH_2-MIL-101(Al) has been confirmed. The interactions between MOFs and $Fe(CO)_5$ at different heating temperatures were investigated in detail. As a result, the $Fe(CO)_5$@HKUST-1 was not stable under thermal conditions. Under minor heating conditions, deconstructions of HKUST-1 sub-unit were observed from XRPD and FTIR results; under major heating conditions, Cu^{2+} ions in HKUST-1 were reduced to Cu NPs with the interaction to $Fe(CO)_5$. On the other hand, in $Fe(CO)_5$@MIL-101(Al), the decomposition of $Fe(CO)_5$ to Fe NPs was found and NH_2-MIL-101 (Al) was stable to $Fe(CO)_5$ as well as its decomposition products. The synthetic methods and the systematic investigation for the air-sensitive host-guest MOFs-metal complex systems in this report provide valuable experimental experience and insight between porous functional materials and

guest molecules. We envision that this method could be expanded to other metal precursors and porous materials on fabricating various functional nanocomposites and devices.

DATA AVAILABILITY STATEMENT

The original contributions presented in the study are included in the article/**Supplementary Material**, further inquiries can be directed to the corresponding author.

AUTHOR CONTRIBUTIONS

BH has designed the work and performed the experiments. BH and ZT cowrote the manuscript.

FUNDING

ACKNOWLEDGMENTS

SUPPLEMENTARY MATERIAL

The Supplementary Material for this article can be found online at: https://www.frontiersin.org/articles/10.3389/fchem.2021.706942/full#supplementary-material

REFERENCES

Alezi, D., Belmabkhout, Y., Suyetin, M., Bhatt, P. M., Weseliński, Ł. J., Solovyeva, V., et al. (2015). MOF Crystal Chemistry Paving the Way to Gas Storage Needs: Aluminum-Based Soc-MOF for CH4, O2, and CO2 Storage. *J. Am. Chem. Soc.* 137, 13308–13318. doi:10.1021/jacs.5b07053

Carlton, H. E., and Oxley, J. H. (1965). Kinetics of the Heterogeneous Decomposition of Iron Pentacarbonyl. *Aiche J.* 11, 79–84. doi:10.1002/aic.690110119

Chen, Z., Li, P., Anderson, R., Wang, X., Zhang, X., Robison, L., et al. (2020). Balancing Volumetric and Gravimetric Uptake in Highly Porous Materials for Clean Energy. *Science* 368, 297–303. doi:10.1126/science.aaz8881

Chui, S. S., Lo, S. M. F., Charmant, J. P. H., Orpen, A. G., and Williams, I. D. (1999). A Chemically Functionalizable Nanoporous Material [Cu3(TMA)2(H2O)3]n. *Science* 283, 1148–1150. doi:10.1126/science.283.5405.1148

Fu, J., Das, S., Xing, G., Ben, T., Valtchev, V., and Qiu, S. (2016). Fabrication of COF-MOF Composite Membranes and Their Highly Selective Separation of H2/CO2. *J. Am. Chem. Soc.* 138, 7673–7680. doi:10.1021/jacs.6b03348

Gao, J., Qian, X., Lin, R. B., Krishna, R., Wu, H., Zhou, W., et al. (2020). Mixed Metal-Organic Framework with Multiple Binding Sites for Efficient C 2 H 2/CO

2 Separation. *Angew. Chem. Int. Ed.* 59, 4396–4400. doi:10.1002/anie.202000323

Guo, F.-S., Bar, A. K., and Layfield, R. A. (2019). Main Group Chemistry at the Interface with Molecular Magnetism. *Chem. Rev.* 119, 8479–8505. doi:10.1021/acs.chemrev.9b00103

Han, S., Kim, H., Kim, J., and Jung, Y. (2015). Modulating the Magnetic Behavior of Fe(II)-MOF-74 by the High Electron Affinity of the Guest Molecule. *Phys. Chem. Chem. Phys.* 17, 16977–16982. doi:10.1039/c5cp01441g

Jiang, J., Furukawa, H., Zhang, Y.-B., and Yaghi, O. M. (2016). High Methane Storage Working Capacity in Metal-Organic Frameworks with Acrylate Links. *J. Am. Chem. Soc.* 138, 10244–10251. doi:10.1021/jacs.6b05261

Kalidindi, S. B., Yusenko, K., and Fischer, R. A. (2011). Metallocenes@COF-102: Organometallic Host-Guest Chemistry of Porous Crystalline Organic Frameworks. *Chem. Commun.* 47, 8506–8508. doi:10.1039/c1cc11450f

Kalmutzki, M. J., Diercks, C. S., and Yaghi, O. M. (2018). Metal-Organic Frameworks for Water Harvesting from Air. *Adv. Mater.* 30, 1704304. doi:10.1002/adma.201704304

Lee, J. E., Kim, D. Y., Lee, H.-K., Park, H. J., Ma, A., Choi, S.-Y., et al. (2019). Sonochemical Synthesis of HKUST-1-Based CuO Decorated with Pt Nanoparticles for Formaldehyde Gas-Sensor Applications. *Sensors Actuators B: Chem.* 292, 289–296. doi:10.1016/j.snb.2019.04.062

Liang, Z., Qu, C., Xia, D., Zou, R., and Xu, Q. (2018). Atomically Dispersed Metal Sites in MOF-Based Materials for Electrocatalytic and Photocatalytic Energy Conversion. *Angew. Chem. Int. Ed.* 57, 9604–9633. doi:10.1002/anie.201800269

Liu, G., Chernikova, V., Liu, Y., Zhang, K., Belmabkhout, Y., Shekhah, O., et al. (2018). Mixed Matrix Formulations with MOF Molecular Sieving for Key Energy-Intensive Separations. *Nat. Mater* 17, 283–289. doi:10.1038/s41563-017-0013-1

Manna, K., Zhang, T., Greene, F. X., and Lin, W. (2015). Bipyridine- and Phenanthroline-Based Metal-Organic Frameworks for Highly Efficient and Tandem Catalytic Organic Transformations via Directed C-H Activation. *J. Am. Chem. Soc.* 137, 2665–2673. doi:10.1021/ja512478y

Nayak, S., Harms, K., and Dehnen, S. (2011). New Three-Dimensional Metal−Organic Framework with Heterometallic [Fe-Ag] Building Units: Synthesis, Crystal Structure, and Functional Studies. *Inorg. Chem.* 50, 2714–2716. doi:10.1021/ic1019636

Nicastri, M. C., Lehnherr, D., Lam, Y.-h., Dirocco, D. A., and Rovis, T. (2020). Synthesis of Sterically Hindered Primary Amines by Concurrent Tandem Photoredox Catalysis. *J. Am. Chem. Soc.* 142, 987–998. doi:10.1021/jacs.9b10871

Peng, Y., Li, Y., Ban, Y., and Yang, W. (2017). Two-Dimensional Metal-Organic Framework Nanosheets for Membrane-Based Gas Separation. *Angew. Chem. Int. Ed.* 56, 9757–9761. doi:10.1002/anie.201703959

Serra-Crespo, P., Ramos-Fernandez, E. V., Gascon, J., and Kapteijn, F. (2011). Synthesis and Characterization of an Amino Functionalized MIL-101(Al): Separation and Catalytic Properties. *Chem. Mater.* 23, 2565–2572. doi:10.1021/cm103644b

Stawowy, M., Jagódka, P., Matus, K., Samojeden, B., Silvestre-Albero, J., Trawczyński, J., et al. (2020). HKUST-1-Supported Cerium Catalysts for CO Oxidation. *Catalysts* 10, 108. doi:10.3390/catal10010108

Talin, A. A., Centrone, A., Ford, A. C., Foster, M. E., Stavila, V., Haney, P., et al. (2014). Tunable Electrical Conductivity in Metal-Organic Framework Thin-Film Devices. *Science* 343, 66–69. doi:10.1126/science.1246738

Tian, T., Zeng, Z., Vulpe, D., Casco, M. E., Divitini, G., Midgley, P. A., et al. (2018). A Sol-Gel Monolithic Metal-Organic Framework with Enhanced Methane Uptake. *Nat. Mater.* 17, 174–179. doi:10.1038/NMAT5050

Trammell, R., Rajabimoghadam, K., and Garcia-Bosch, I. (2019). Copper-Promoted Functionalization of Organic Molecules: from Biologically Relevant Cu/O2Model Systems to Organometallic Transformations. *Chem. Rev.* 119, 2954–3031. doi:10.1021/acs.chemrev.8b00368

Wang, C., An, B., and Lin, W. (2019). Metal-Organic Frameworks in Solid-Gas Phase Catalysis. *ACS Catal.* 9, 130–146. doi:10.1021/acscatal.8b04055

Wang, R.-S., Chen, L.-C., Yang, H., Fu, M.-A., Cheng, J., Wu, X.-L., et al. (2019). Superconductivity in an Organometallic Compound. *Phys. Chem. Chem. Phys.* 21, 25976–25981. doi:10.1039/c9cp04227j

Yuan, S., Feng, L., Wang, K., Pang, J., Bosch, M., Lollar, C., et al. (2018). Stable Metal-Organic Frameworks: Design, Synthesis, and Applications. *Adv. Mater.* 30, 1704303. doi:10.1002/adma.201704303

Zhang, C., Wu, B.-H., Ma, M.-Q., Wang, Z., and Xu, Z.-K. (2019). Ultrathin Metal/Covalent-Organic Framework Membranes towards Ultimate Separation. *Chem. Soc. Rev.* 48, 3811–3841. doi:10.1039/c9cs00322c

Zhang, X., Chen, Z., Liu, X., Hanna, S. L., Wang, X., Taheri-Ledari, R., et al. (2020). A Historical Overview of the Activation and Porosity of Metal-Organic Frameworks. *Chem. Soc. Rev.* 49, 7406–7427. doi:10.1039/d0cs00997k

Experimental Investigation of Self-Assembled Particles on Profile Control in the Fuyu Oilfield

Lifei Dong[1,2]*, Miao Wang[1], Jie He[3], Mingchen Ding[4] and Hun Lin[5]

[1]Chongqing Three Gorges University, Chongqing, China, [2]Chongqing Engineering Research Center of Disaster Prevention & Control for Banks and Structures in Three Gorges Reservoir Area, Chongqing, China, [3]Southwest Petroleum University, Chengdu, China, [4]China University of Petroleum, Qingdao, China, [5]Chongqing University of Science and Technology, Chongqing, China

The particle system is one of the widely used profile control agents in many oilfields, and the matching relationship between the particle and the reservoir pore throat is significant for the profile control effect. In order to enhance oil recovery after water breakthrough in the Fuyu oilfield, a self-assembled particle with some branches on the surface, compounded by inverse emulsion polymerization and added, is introduced as the profile control agent in this paper. Then the permeabilities of the water channel and the oil remaining area in the Fuyu oilfield are achieved after the statistic analysis of 1,022 cores from the practical reservoir. Furthermore, the oil restarting pressure in the oil remaining area and the self-assembled particle plugging strength in the water channel are tested. Finally, the adaption of the self-assembled particle and effect of profile control in the Fuyu oilfield are evaluated by comparing the oil restarting pressure and the plugging strength. The results show that the self-assembled particles can be gathered together easily by the force of the ionic bond, which is good for water channel plugging. The permeability of the water channel in the Fuyu oilfield ranges from 1,000 mD to 1,500 mD. The oil restarting pressure increases with the decreasing of permeability, and the increasing rate grows rapidly when it drops below 50 mD. Comparing the oil restarting pressure with the plugging strength, a self-assembled particle with a diameter of 20–40 μm in the water channel with a permeability of 1,265.7 mD can provide sufficient plugging strength to restart the remaining oil in the oil remaining areas with a permeability over 3.38 mD. The matched window of the self-assembled particle is wider than a normal particle in the Fuyu oilfield.

Keywords: profile control, self-assembled particle, oil restarting pressure, plugging strength, fuyu oilfield

INTRODUCTION

High water cut and low oil recovery efficiency are common phenomena in most oilfields now after long-term water flooding (Feng, et al., 2013). The effective way to enhance oil recovery is to use a suitable profile control agent to plug the water channel, which exists in the high permeability areas of the reservoir. After the water channel is plugged by the agent, the subsequent injected fluid can be swept to the low permeability areas and avoid flowing along the water channel. Thus, the residual oil there can be displaced (Yadav and Mahto, 2014).

Many chemical particle systems, such as the preformed gel particle (PGP), microgels, and dispersed particle gels (DPG), are proposed by researchers as profile control agents, and the mechanism of the
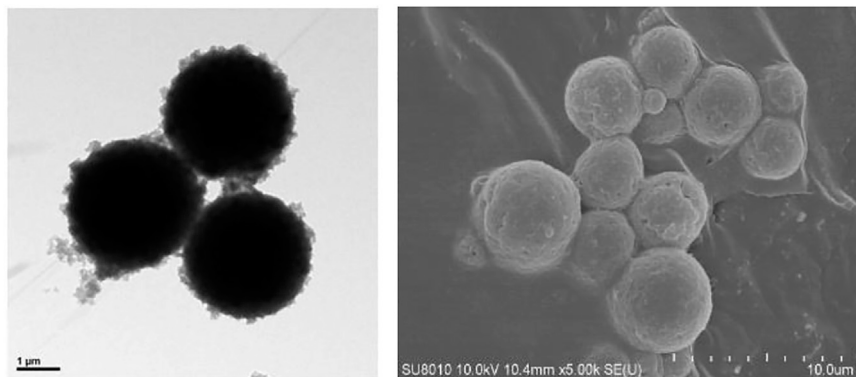
FIGURE 1 | The property of self-assembly in static and dynamic conditions.
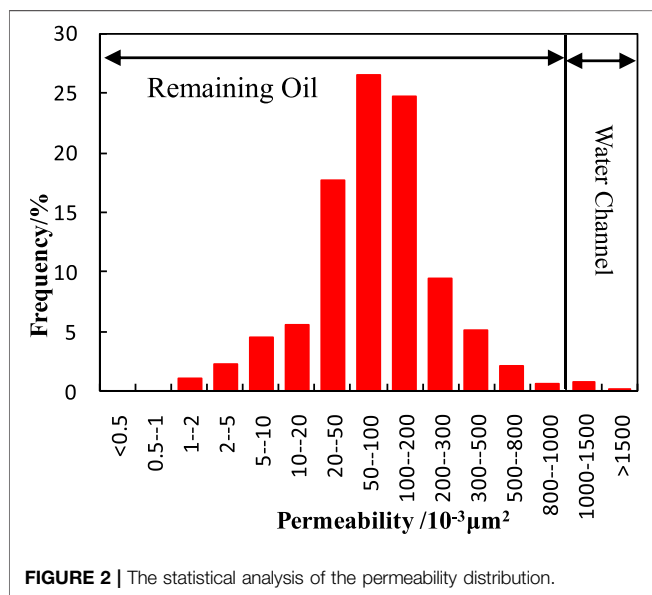
FIGURE 2 | The statistical analysis of the permeability distribution.

TABLE 1 | The component content of ions in experimental water.

Ions	$K^+ + Na^+$	Ca^{2+}	Mg^{2+}	Cl^-	SO_4^{2-}	HCO_3^-	CO_3^{2-}
Content (ppm)	1,070	20	27	1,152	228	763	0

plugging and profile control are studied (Dai, et al., 2012; Goudarzi, et al., 2013; You, et al., 2013; Zhou, et al., 2013; Yue, et al., 2006). Bai observed elastic deformability during the migration and plugging process of the preformed gel particle in visible etched-glass micromodels, and concluded profile control mechanism and sweep efficiency improvement in the reservoir (Bai, 2001; Bai et al., 2007a; Bai et al., 2007b). Iscan, A.G. and Civan, F. showed that particles with sizes comparable to pore throat sizes can reduce the permeability effectively in high permeability formations (Iscan and Civan, 2006; Iscan, et al., 2007; Tran, et al., 2009). Al-Ibadi, A. and Civan, F. explored the effects of flow rate, concentration, and size on the plugging ability when injecting the deformable gel particles in the

near-wellbore formation (Al-lbadi, et al., 2012; Al-lbadi and Civan, 2013). Zhao investigated the mechanisms of profile control and enhanced oil recovery of DPG particles with core flow tests and visual simulation experiments, and the deformation, retention, adsorption, trapping, and bridging during DPG particle migration in porous media were demonstrated (Zhao, et al., 2014).

These studies mentioned above all concentrated on the plugging ability and the matchable degree between the reservoir and the different particles. However, the restarting pressure of remaining oil in the lower permeability areas is little considered, which was exactly related to the final profile control effect and enhanced oil recovery.

As the water channel in the Fuyu oilfield has had long-term water flooding (Liu, et al., 2009), the measure of profile control should be taken urgently (Li, et al., 2010; Shu, et al., 2013).

In this work, the physical properties (permeability distribution) of 1,022 cores from the practical reservoir in the Fuyu oilfield are analyzed first. Then, a self-assembled particle with some branches on the surface is introduced as the profile control agent. The particle is compounded with the method of inverse emulsion polymerization. After that, two kind of experiments, the remaining oil restarting pressure test and particle plugging strength analysis, are designed and completed according to the theoretical foundation of profile control. Furthermore, the plugging ability of the self-assembled particle and the matchable degree between the particle and the water channel in the Fuyu oilfield is discussed. Finally, the adaption of the self-assembled particle for profile control in the Fuyu oilfield is evaluated by comparing the plugging strength with the remaining oil restarting pressure.

MATERIALS

Self-Assembled Particle

The profile control agent used in the reservoir is the self-assembled particle, which is made with the method of emulsion polymerization. The main synthesis materials of the particle are styrene (St), acrylamide (AAm), and N,N′-methylenebisacrylamide (MBA).

The self-assembled property of this particle is determined by its structure, which can be seen from the SEM tests in the continuous

FIGURE 3 | Water breakthrough and profile control.
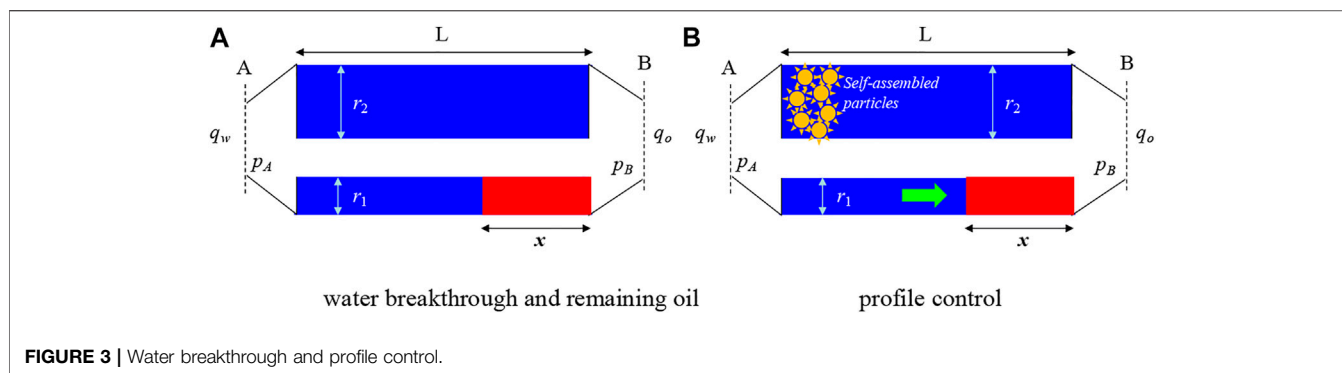
TABLE 2 | Basic parameters of experimental cores.

Number	Diameter/cm	Length/cm	Oil saturation/%	Permeability/mD
H1	2.50	30.00	60.26	0.38
H2	—	—	62.53	6.88
H3	—	—	64.02	35.66
H4	—	—	64.72	56.36
H5	—	—	65.15	104.25
H6	—	—	68.87	540.12
H7	—	—	70.88	1,265.70

TABLE 3 | Basic parameters of experimental cores.

Number	Diameter/cm	Length/cm	Permeability/mD	Porosity/%
ZR-1	2.50	30.00	1,265.70	33.40
ZR-2	2.50	30.00	3,014.70	38.10

medium or in the porous media (**Figure 1**). This property can make single particles gather together, which is good for plugging the water channel.

Experimental Cores

The experimental cores are selected and confirmed after the statistical analysis of the permeability from 1,022 natural cores in the Fuyu oilfield (**Figure 2**).

It can be seen that the distribution frequency of permeability is normal. As the water channel exists in high permeability reservoirs, the experimental cores with the permeability above 1,000 mD are selected in this paper according to the statistical analysis.

Experimental Fluids

The water used in the experiments is formation water, with a total salinity of 3260 mg/L. The component content of ions is shown in **Table 1**.

The oil is a mixture composed of gas-free crude oil and kerosene. Oil viscosity is 7.36 mPa·s at 32 °C.

EXPERIMENTS

Theoretical Foundation

The measure of profile control in the oilfield is taken for reducing water channeling and enhancing oil recovery. According to the

research of Dong et al., 2021, water breakthrough will happen if microheterogeneity exists in the reservoir, and the oil will remain local in the high permeability areas (**Figure 3A**). As seen from **Figure 2**, the heterogeneity of the reservoir in the Fuyu oilfield is common. Thus, water breakthrough is unavoidable. The oil saturation in the smaller size capillary (or lower permeability areas) is

$$S_o = \frac{\mu_o}{\mu_o - \mu_w} \left\{ \sqrt{1 - \left(\frac{r_1}{r_2}\right)^2 \left[1 - \left(\frac{\mu_w}{\mu_o}\right)^2\right]} - \left(\frac{\mu_w}{\mu_o}\right) \right\} \quad (1)$$

where S_o is oil saturation; μ_o, μ_w are the viscosity of oil and water; r_1, r_2 are the sizes of the smaller capillary (lower permeability areas) and the bigger capillary (higher permeability areas). The theoretical model can be found in **Appendix A**.

The self-assembled particle is used to plug the water channel (bigger-sized capillary), and the finally purpose is to restart the remaining oil in the smaller-sized capillary (low permeability areas). It means that the plugging strength of the particle in high permeability areas (P_{r2}) should be larger than the restart pressure of oil in the low permeability areas (P_{r1}).

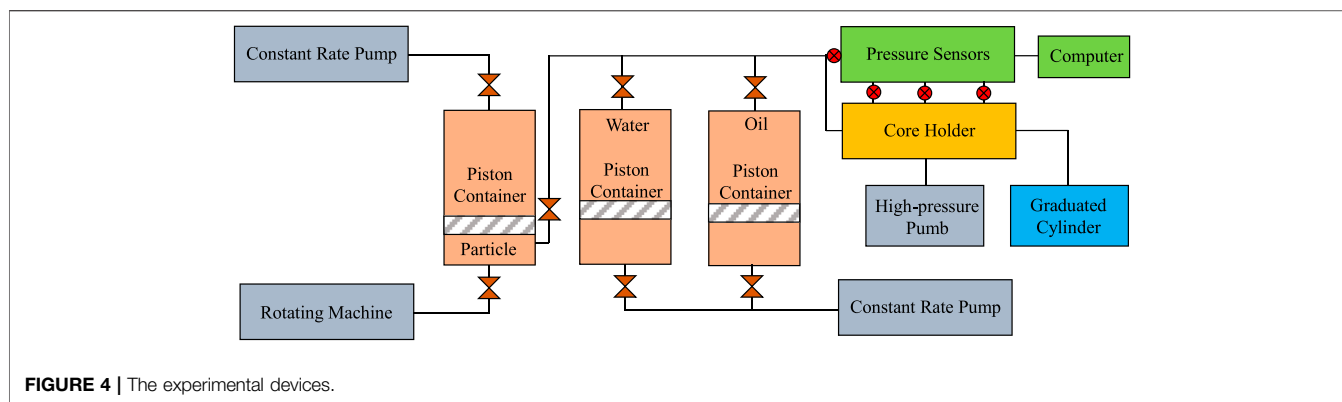As seen from **Figure 3B**, the condition below should be satisfied:

$$P_{r2} \geq P_{r1} \quad (2)$$

That is the theoretical foundation of profile control.

Experimental Scheme

Based on the theoretical analysis, two pressures should be achieved and compared before the adaptation evaluation. So two kind of experiments are designed.

FIGURE 4 | The experimental devices.

1) The oil restarting pressure experiment.

Seven different permeability cores saturated the oil are taken, and the water is injected in the cores to displace the oil. The injecting pressure is tested when the first oil drop flows out. This pressure can be represented as the oil restarting pressure. And the experimental temperature is 32°C. The basic parameters of experimental cores are shown in **Table 2**.

2) The plugging strength experiment of the self-assembled particle.

Two high permeability cores are used to inject the self-assembled particles. The particles will plug and migrate in the pore throat of the core, and the injecting pressure will remain stable when the plugging and migration is balanced. After that, the water injection follows. And the stable water injection pressure can be seen as the particle plugging strength.

As the particle plugging is formed in the water channel (high permeability areas), two cores with the permeability of 1,265.7 mD and 3,014.7 mD are used for the core experiments, and their basic parameters are listed in **Table 3**.

Thus, the effect of profile control in the Fuyu oilfield can be evaluated according to these two pressures. The devices of the experiments are shown below **Figure 4**.

RESULTS AND DISCUSSION

1) The oil restarting pressure in different permeability cores

The pressures (or pressure gradients) tested from the experiments of different permeability cores are shown in **Figure 5**.

It can be seen that the oil restarting pressure increases with the decreasing of permeability. And the increasing rate grows rapidly when the permeability drops below 50 mD. That means the oil remaining in the lower permeability areas needs more driving force for restarting.

2) The plugging strength of the self-assembled particle in high permeability cores

The self-assembled particle with the diameter of 20~40 μm is used for the experiments. The concentration of the particle solution is 1,000 ppm. The particle injection rate is 1 m/d. The dynamic behaviors of pressure gradients at different position of the cores are show in **Figure 6**.

It can be seen that the pressure gradient at different positions rises gradually with the increasing particle injection. That means the self-assembled particle can migrate to deep within the cores. Meanwhile, the pressure gradient remains stable after injecting the particle for a while. That is because the particle retention in the core reaches its maximum. The final pressure gradient of subsequent water flooding can be represented as the plugging strength of the self-assembled particle during the profile control measure.

According to the injection dynamics of Core ZR-1, the plugging strength at 0–5 cm is much higher than the one at other positions. That is because the particle retention in the entrance is higher than that at other places, which is called the entrance face effect. The plugging strength in the center of the cores can be represented as the actual particle plugging strength. Thus, the plugging strength of the self-assembled particle in Core ZR-1 is about 14.05 MPa/m, which is achieved from the average

$$y = 46.58x^{-0.893}$$

FIGURE 5 | The pressure gradient of oil restarting with different permeabilities.
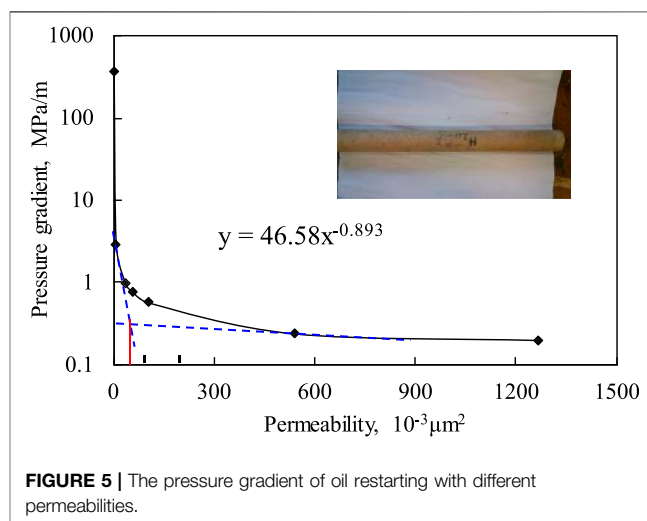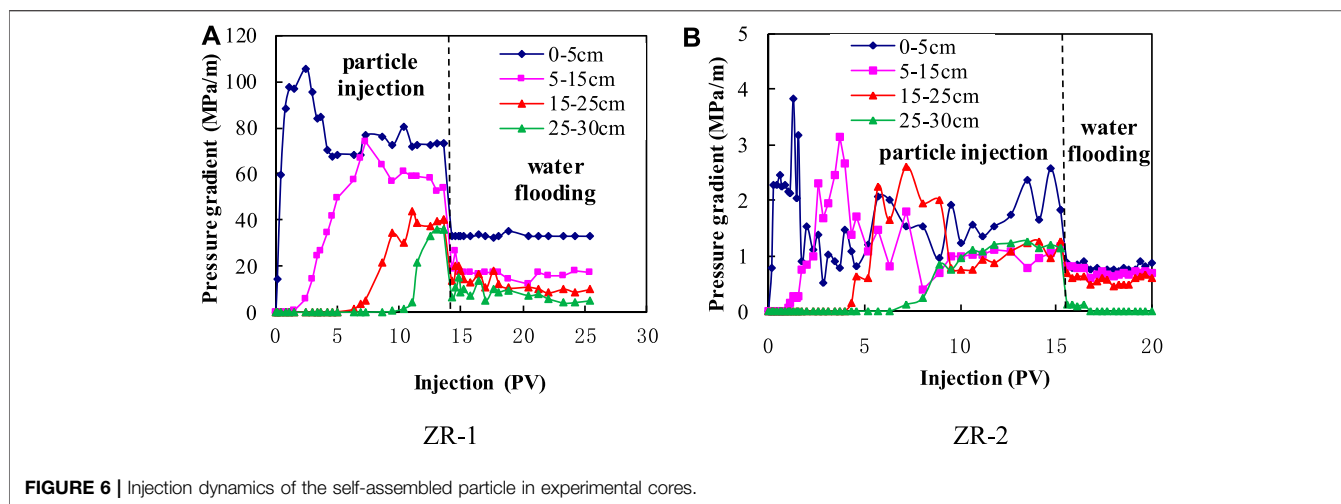
FIGURE 6 | Injection dynamics of the self-assembled particle in experimental cores.

TABLE 4 | Comparison of plugging strength and oil restarting pressure.

Pressure gradient MPa/m	Permeability/mD	
	Particle plugging	Oil restarting
14.05	1,265.70	3.83
0.64	3,014.70	121.65

TABLE 5 | Plugging strength of self-assembled particle and normal particle.

Permeability mD	Plugging strength/MPa/m	
	Self-assembled particle	Normal particle
3,014.70	0.64	0.40

value of point 5–15 cm and point 15–25 cm. Also, the plugging strength in Core ZR-2 is 0.64 MPa/m.

3) The evaluation of the self-assembled particle on profile control in the Fuyu oilfield

The permeability of where the oil can be forced to restart is achieved by comparing the plugging strength of the self-assembled particle with the oil restarting pressure in **Figure 5**. The results are shown below.

Seen from the table (**Table 4**), the plugging strength in the area with a permeability of 1,265.70 mD is equal to the oil restarting pressure in the area with a permeability of 3.38 mD. That means the oil in the reservoir with a permeability above 3.38 mD can be displaced completely by water if the water channel with a permeability of 1,265.70 mD is plugged by the particle. Thus, combined with the statistical analysis of the permeability in the Fuyu oilfield (**Figure 2**), most of the remaining oil can be displaced. Similarly, if the self-assembled particle plugs the water channel with a

permeability of 3,014.70 mD, the plugging strength can force the oil to be displaced in the areas with permeability over 121.65 mD. So the remaining oil where the permeability is below 121.65 mD cannot be exploited.

As the frequency of permeability over 1,500 mD is very low, the water channel in the Fuyu oilfield exists mostly in the areas with a permeability between 1,000 mD to 1,500 mD. Therefore, the self-assembled particle with a diameter of 20–40 μm is suitable for profile control in the Fuyu oilfield.

Furthermore, seen from the research of Dong et al., 2016, the plugging strength of a normal particle in the core with a permeability of 3014.70 mD is only 0.12 MPa/0.3 m (equals to 0.4 MPa/m), which is less than the plugging strength caused by the self-assembled particle injection in the same permeability core (**Table 5**). The property of self-assembly gives the particle a higher plugging ability and a larger matching window. To sum up, the self-assembled particle is more suitable for profile control than the normal particle.

CONCLUSIONS

1) The permeability in the Fuyu oilfield is normally distributed, and the water channel mostly exists at the areas with a permeability ranging from 1,000 mD to 1,500 mD.
2) The oil restarting pressure increases with the decreasing of permeability, and the increasing rate grows rapidly when the permeability drops below 50 mD.
3) The self-assembled particle with the diameter of 20–40 μm has a good plugging ability in the reservoir with a permeability of 1,265.7 mD, and it can make the remaining oil in the areas with a permeability over 3.38 mD displace by subsequent water flooding.
4) The property of self-assembly can provide the particle with a higher plugging ability and a larger matching window with the water channel than the normal particle. It is suitable for profile control in the Fuyu oilfield.

DATA AVAILABILITY STATEMENT

The original contributions presented in the study are included in the article/**Supplementary Material**, further inquiries can be directed to the corresponding author.

AUTHOR CONTRIBUTIONS

LD: Investigation, Experimental schemes design, Methodology, Results discussion, Writing- Reviewing and Editing. MW: Experimental datas analysis, Figures production. JH: Characterization of static properties of the microsphere. MD: Implementation of the core experiments. HL: Writing–Original draft preparation.

REFERENCES

Al-lbadi, A., and Civan, F. (2013). Experimental Investigation and Correlation of Treatment in Weak and High-Permeability Formations by Gel Particles. *SPE Prod. Operations* 28 (4), 387–401.

Al-lbadi, A., and Civan, F. (2012). Experimental Study of Gel Particles Transport through Porous media. *SPE Lat. Am. Caribb. Petro. Eng. Conf. Proc* 2, 1459–1485. doi:10.2118/153557-MS

Bai, B. J. (2001). "Fundamental Research on Usage of Pre-gel Particles' In-Depth Profile Controlling and Flooding," in *Doctoral Dissertation* (Beijin: China University of Geosciences).

Bai, B., Li, L., Liu, Y., Liu, H., Wang, Z., and You, C. (2007b). Preformed Particle Gel for Conformance Control: Factors Affecting its Properties and Applications. *SPE Reservoir Eval. Eng.* 10, 415–422. doi:10.2118/89389-pa

Bai, B., Liu, Y., Coste, J.-P., and Li, L. (2007a). Preformed Particle Gel for Conformance Control: Transport Mechanism through Porous media. *SPE Reserv. Eval. Eng* 10 (2), 176–184. doi:10.2118/89468-pa

Dai, C., Zhao, G., Zhao, M., and You, Q. (2012). Preparation of Dispersed Particle Gel (DPG) through a Simple High Speed Shearing Method. *Molecules* 17, 14484–14489. doi:10.3390/molecules171214484

Dong, L., Wang, M., Wang, W., Ding, M., and Lin, H. (2021). Analysis of Oil Displacement and Residue Distribution in Microheterogeneity Reservoir. *J. Dispersion Sci. Technology*, 1–7. doi:10.1080/01932691.2020.1848576

Dong, L., Yue, X. A., Su, Q., Qin, W., Song, W., Zhang, D., et al. (2016). Study on the Plugging Ability of Polymer Gel Particle for the Profile Control in Reservoir. *J. Dispersion Sci. Technology* 37, 34–40. doi:10.1080/01932691.2015.1022656

Feng, Q., Chen, X., and Zhang, G. (2013). Experimental and Numerical Study of Gel Particles Movement and Deposition in Porous media after Polymer Flooding. *Transp Porous Med.* 97, 67–85. doi:10.1007/s11242-012-0110-1

Goudarzi, A., Zhang, H., Varavei, A., Hu, Y., Delshad, M., Bai, B., et al. (2013). "Water Management in Mature Oil Fields Using Preformed Particle Gels," in SPE165356 Presented at the SPE Regional & AAPG Pacific Section Meeting *Held in Monterey* (USA: California). doi:10.2118/165356-ms

Iscan, A. G., and Civan, F. (2006). Correlation of Criteria for Perforation and Pore Plugging by Particles. *J. Por Media* 9 (6), 541–558. doi:10.1615/jpormedia.v9.i6.40

Iscan, A. G., Civan, F., and Kok, M. V. (2007). Alteration of Permeability by Drilling Fluid Invasion and Flow Reversal. *J. Pet. Sci. Eng.* 58 (1), 227–244. doi:10.1016/j.petrol.2007.01.002

Li, D. X., Hou, J. R., and Zhao, F. L. (2010). Research on Profile Control and Water Shut off Performance of Pre-crosslinked Gel Particles and Matching Relationship between Particle and Pore Size. *J. Petrochem. Univ.* 23 (2), 25–28.

Liu, P. L., Pan, Z. G., and Chen, G. X. (2009). Reservoir Waterflooding Characteristics and Water Plugging Technology in Fuyu Oilfield. *Fault-Block Oil &Gas Field* 16 (2), 103–105.

Shu, J. F., Zhang, L., and Chen, Y. (2013). Evaluation and Field Application of Gel Particle Profile Control Agent. *J. Adv. Fine Petrochem.* 14 (1), 15–18.

Tran, T. V., Civan, F., and Robb, I. D. (2009). Correlating Flowing Time and Condition for Perforation Plugging by Suspended Particles. *SPE Drill. Completion* 24 (3), 398–403. doi:10.2118/120847-pa

Yadav, U. S., and Mahto, V. (2014). *In Situ* Gelation Study of Organically Crosslinked Polymer Gel System for Profile Modification Jobs. *Arab J. Sci. Eng.* 39, 5229–5235. doi:10.1007/s13369-014-1014-x

You, Q., Dai, C. L., Tang, Y. C., Guan, P., Zhao, G., and Zhou, F. L. (2013). Study on Performance Evaluation of Dispersed Particle Gel for Improved Oil Recovery. *J. Energ. Resour. Technology* 135, 1–7. doi:10.1115/1.4024119

Yue, X. A., Hou, J. R., Qiu, M. J., and Zhang, H. F. (2006). Evaluation on Character of Profile Control by Polymer Gel Particle. *J. Pet. Geology. Recovery Efficency* 13 (2), 81–84.

Zhao, G., Dai, C. L., and Zhao, M. (2014). Investigation of the Profile Control Mechanisms of Dispersed Particle Gel. *Plos One* 9 (6), e100471. doi:10.1371/journal.pone.0100471

Zhou, W., Wang, Z., Delshad, M., Avaravei, A., Wang, X., and Zhang, W. (2013). "A Multi-Well Performance Particle Gel Injection Evaluation Using a Sophisticated Simulator," in IPTC16693 Presented at the International Petroleum Technology Conference, Beijing, China. doi:10.2523/IPTC-16693-Abstract

FUNDING

SUPPLEMENTARY MATERIAL

The Supplementary Material for this article can be found online at: https://www.frontiersin.org/articles/10.3389/fchem.2021.681846/full#supplementary-material

NOMENCLATURE

L Length of the parallel capillary, m

v Moving velocity of oil-water interface, m/d

x Distance between oil-water interface and entrance, m

r Radius of capillary, m

r_1 Radius of smaller-sized capillary, m

r_2 Radius of bigger-sized capillary, m

p_A Pressures at interface-A, MPa

p_B Pressures at interface-B, MPa

μ_w Viscosity of water, mPa.sViscosity of oil, mPa.s

μ_w Viscosity of water, mPa.sViscosity of oil, mPa.s

t Time of water flooding, s

x_1 Position of oil-water interface in the smaller size capillary when the oil-water interface in the bigger-sized capillary is arriving at Interface-B, m

L_R Length of remaining oil in the smaller-sized capillary, m

S_o Saturation of remaining oil in the smaller-sized capillary, %

An Active Catalyst System Based on Pd (0) and a Phosphine-Based Bulky Ligand for the Synthesis of Thiophene-Containing Conjugated Polymers

Meifang Liu[1]*, Li Liu[1], Zhihui Zhang[2], Meixiu Wan[3], Huanmei Guo[1]* and Dan Li[1]*

[1]*Department of Chemistry and Chemical Engineering, Weifang University, Weifang, China,* [2]*Department of Continuing Education, Weifang Nursing Vocational College, Weifang, China,* [3]*Institute of New Energy Technology, College of Information Science and Technology, Jinan University, Guangzhou, China*

To address the limitations of conventional Pd catalysts in the polymerization of thiophene-containing conjugated polymers, an active catalyst system based on Pd (0) and a phosphine-based bulky ligand, L1, is explored systematically in Suzuki–Miyaura polymerizations using thiophene boronic acid pinacol ester as one of the monomers. This active catalyst is found very efficient in synthesizing a series of thiophene-containing linear and hyperbranched conjugated polymers. First, as a model example, coupling reactions between electron-rich/moderately hindered aryl or thienyl halides and thiophene boronic acid pinacol ester give excellent yields with lower catalyst loading and can be completed in a shorter reaction time relative to Pd(PPh$_3$)$_4$. Notably, high molecular weight thiophene-containing polymers are successfully synthesized by Suzuki–Miyaura polycondensation of 2,5-thiophene bis(boronic acid) derivatives with different dibromo- and triple bromo-substituted aromatics in 5–15 min.

Keywords: cross-coupling, thiophene boronic acid pinacol ester, aryl halides, polymerization, hyperbranched polymers

INTRODUCTION

π-Conjugated polymers have received considerable interest for their potential in a variety of applications, such as optoelectronics, chemical sensors, and biological sensors (Ponder et al., 2018; Yue et al., 2019; Li and Pu, 2019; González et al., 2019; Ochieng, et al., 2020; Abdollahi and Zhao, 2020). In particular, conjugated polymers containing thiophene, tri-phenylamine, and benzo(lmn)(3,8) phenanthroline-1,3,6,8(2H,7H)-tetraone in the main or side chains have attracted much attention due to their unique optophysical properties, and they can be used as active components for light-emissive and charge carrier thin-film materials (Koyuncu, 2012; Ma et al., 2013; Ponder et al., 2018; Wu et al., 2018; Li and Pu, 2019; Jessop et al., 2020). Linear conjugated polymers usually have a rigid structure and are easy to form aggregation or crystallization in solvent and solid films. The aggregation of conjugated polymer chains in the film can greatly reduce the luminescence quantum efficiency and is detrimental to the device performance in light-emitting applications. Therefore, in recent years, hyperbranched conjugated polymers with a three-dimensional structure have attracted extensive interest. They mostly possess good solubility, processability, and adjustable photophysical and chemical properties, with effectively inhibited aggregation in the solid state (Xia et al., 2007; Okamoto et al., 2013; Wu et al., 2015; Jiang et al., 2019; Yen and Liou, 2019).
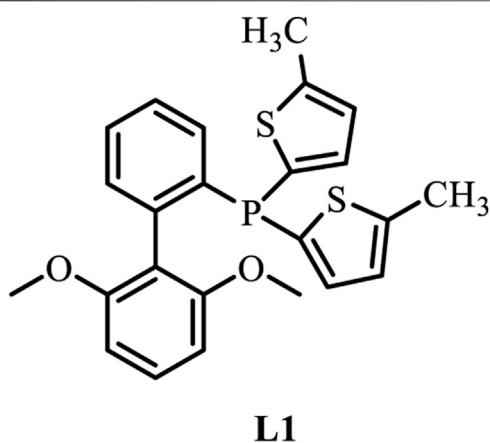
FIGURE 1 | The chemical structure of L1.

The palladium-catalyzed Suzuki–Miyaura cross-coupling is a mild and efficient reaction to construct the carbon–carbon bonds among aromatics (Bellina et al., 2004; Han, 2013; Paul et al., 2015; Qiu et al., 2018; Rizwan et al., 2018; Ayogu and Onoabedje, 2019; Zhang et al., 2019). This reaction is advantageous over alternative reactions, such as Kumada–Corriu (Clagg et al., 2019; Loewe et al., 1999), Negishi (Chen and Rieke, 1992; Pei et al., 2002; Abdiaj et al., 2018), and Stille (Zou et al., 2009; Rathod et al., 2017), with regard to the tolerance to many kinds of functional groups, the commercial availability of various boronic acids, the nontoxicity and the stability of the catalyst, and the easy separation of by-products (Shen, 1997; Buchwald et al., 1998). Great efforts on the development of catalyst systems for Suzuki–Miyaura cross-coupling reactions have been made over the past 2 decades by Buchwald (Littke and Fu, 2002; Altenhoff et al., 2004; Buchwald et al., 2004; Barder et al., 2005), Beller (Beller et al., 2004), Bedford (Bedford, 2003; Bedford et al., 2003a; Bedford et al., 2003b), Fu (Littke et al., 2000; Liu et al., 2001), Herrmann (Böhm et al., 2000), Norlan (Zhang et al., 1999; Grasa et al., 2002), etc. It should be noted that the catalyst system based on Pd (0) with the electron-rich and bulky phosphorus ligands showed high activity even with existing hindered and electron-rich aryl chloride substrates, and the synthesis of thiophene-containing polymers by Suzuki polymerization is performed successfully by using aryl boronic acids and thiophene halides as starting materials (Littke and Fu, 2002; Altenhoff et al., 2004; Buchwald et al., 2004; Barder et al., 2005; Zou et al., 2009). Because of deboronation of thiophene boronic acid pinacol ester at high temperature, it is difficult to obtain the thiophene-containing products with excellent yields and high molecular weights from electron-rich thiophene boronic acid pinacol ester by Suzuki polymerization. Only few groups reported that high molecular weight polymers were obtained by Suzuki polymerization based on 2,5-thiophenebis (boronic acid pinacol ester)s using Pd(PPh$_3$)$_4$ as the catalyst precursor (Lu et al., 2008; Liu et al., 2013; Nguyen et al., 2014).

A palladium complex containing a bulky electron-rich ligand facilitates the oxidative addition of the aryl halide (Grushin and Alper, 1994; Farina et al., 1997). The chemical structure of L1 is shown in **Figure 1**. The alkoxy groups attached to the second phenyl ring stabilize the Pd center and prevent cyclometalation, and the

thienyl groups on the phosphorus core increase interactions with the Pd center and enhance the electron density of the phosphine-based ligand backbone. These features are beneficial to the activity and lifetime of the catalyst (Ryabov, 1990; Buchwald et al., 2004). The catalyst system consisting of Pd (0) and L1 shows high efficiency for the Suzuki–Miyaura cross-coupling of thiophene-2-boronic ester and aryl halide (Liu et al., 2013). The main drawbacks of the catalytic system Pd (0)/L1 might involve a long reaction time and poor turnover numbers (TONs) and turnover frequencies (TOFs) (Gautam and Bhanage, 2015). Despite the high performance of L1, there is still room to optimize the catalyst system toward a wider scope, higher reactivity, lower catalyst loading, and a shorter reaction time. In this report, L1 was studied as the ligand with zero-valent palladium as the catalyst precursor for Suzuki–Miyaura cross-coupling reaction of benzyl bromide and thiophene boronic acid pinacol ester by changing various reaction conditions including reaction times and the quantities of the catalyst together with the different ratios to ligand L1, and optimized conditions can be obtained. In addition, Suzuki–Miyaura cross-coupling reactions were completed with low levels of catalyst loading and short reaction times for a broad range of substrates. Compared with the traditional palladium source Pd(PPh$_3$)$_4$, the catalyst Pd$_2$(dba)$_3$/L1 showed higher performance in generating TON and TOF. Furthermore, this catalyst system can be conducted for Suzuki polycondensation of polymers based on 2,5-thiophenebis (boronic acid pinacol ester), and high molar mass polymers can be easily gained within 15 min.

EXPERIMENTAL SECTION
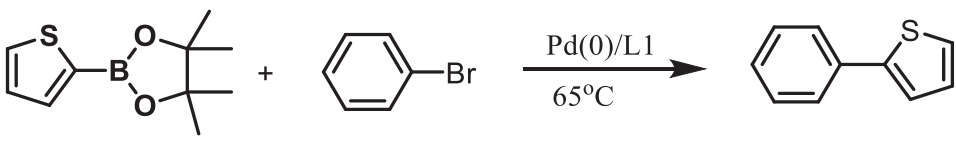
Materials and Measurements

All chemicals were obtained from commercial suppliers and applied without purification. Solvents were disposed according to the standard process. 5-Bromothiophene-2-carbaldehyde and L1 were gained according to a previous literature procedure (Li et al., 2008; Liu et al., 2013). The catalyst precursor Pd(PPh$_3$)$_4$ was prepared according to the literature (Coulson, 1972). All reactions proceeded under N$_2$ and monitored by thin-layer chromatography. Column chromatography was conducted on silica gel (200–300 mesh). ^{1}H NMR was performed in CDCl$_3$ on a Bruker DM 300, AV 400, or AV 600 spectrometer. The gel permeation chromatography (GPC) measurements were performed on a Waters chromatography system connected to a Shimadzu LC-20AD differential refractometer with THF as an eluent or at 150°C with 1,2,4-trichlorobenzene as an eluent and calibration with polystyrene standards.

METHODS

Pd-catalyzed (Pd$_2$(dba)$_3$ + L1) Suzuki–Miyaura Coupling of Aryl Bromide or Thienyl Bromide With Thiophene Boronic Ester

A mixture of aryl halides or thienyl halides, thiophene boronic ester, THF (5 L mol^{-1} halide), water, the base (5 equiv), Pd$_2$(dba)$_3$, and L1 was mixed under nitrogen and refluxed. CH$_2$Cl$_2$ was then

TABLE 1 | Yields of the isolated products from Suzuki–Miyaura cross-coupling reactions of thiophene-2-boronic esters (a) and bromobenzene (b) under various reaction conditions.

	Reaction time (h)||base||Catalyst system			a: b	Yield [%]	TON	TOF (h^{-1})
1	48	NaHCO$_3$	1%Pd, Pd: L1 = 1:3	1:1	94	94	1.98
2	48	NaHCO$_3$	0.1%Pd, Pd: L1 = 1:3	1:1	89	890	18.6
3	0.25	NaHCO$_3$	0.1%Pd, Pd: L1 = 1:3	1:1	85	850	3,400
4	0.25	K$_2$CO$_3$	0.1%Pd, Pd: L1 = 1:3	1:1	95	950	3,800
5	0.25	K$_3$PO$_4$	0.1%Pd, Pd: L1 = 1:3	1:1	88	880	3,520
6	0.25	Cs$_2$CO$_3$	0.1%Pd, Pd: L1 = 1:3	1:1	94	940	3,760
7	0.25	Et$_3$N	0.1%Pd, Pd: L1 = 1:3	1:1	85	850	3,400
8	0.25	NaHCO$_3$	0.01%Pd, Pd: L1 = 1:5	2:1	73	7,300	29,200
9	0.25	K$_2$CO$_3$	0.01%Pd, Pd: L1 = 1:5	2:1	89	8,900	35,600
10	0.25	K$_3$PO$_4$	0.01%Pd, Pd: L1 = 1:5	2:1	74	7,400	29,600
11	0.25	Cs$_2$CO$_3$	0.01%Pd, Pd: L1 = 1:5	2:1	86	8,600	34,400
12	0.25	Et$_3$N	0.01%Pd, Pd: L1 = 1:5	2:1	62	6,200	24,800

Reaction conditions: bromobenzene, thiophene-2-boronic acid pinacol ester, 5 equiv. of the base, THF, H$_2$O, Pd$_2$(dba)$_3$ + L1, reflux.

poured into the mixture, and the organic layer was separated and dried with MgSO$_4$. The crude product was purified on silica gel eluting with petroleum ether (60–90°C)/acetate ester to provide the title compound.

Pd-Catalyzed (Pd$_2$(dba)$_3$ + L1) Suzuki Polycondensation of Aryl Bromide or Thienyl Bromide With Thiophene Boronic Ester

A mixture of aryl halides or thienyl halides, thiophene boronic ester, THF (5 L mol^{-1} halide), water, the base (5 equiv), Pd$_2$(dba)$_3$, and L1 was mixed under nitrogen and refluxed. Water was then added, and the organic layer was separated and precipitated into methanol. The crude product was purified to provide the polymers.
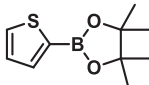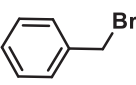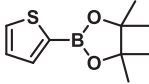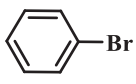
RESULTS AND DISCUSSION
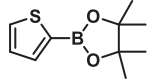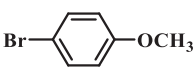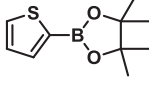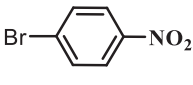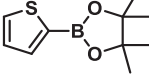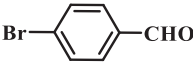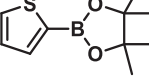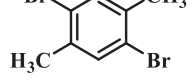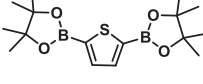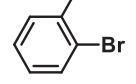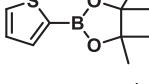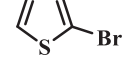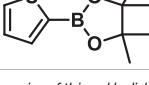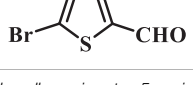
Suzuki–Miyaura Cross-Coupling Reaction of Aryl or Thienyl Halide and Thiophene-2-Boronic Acid Pinacol Ester

The Suzuki–Miyaura cross-coupling reactions of thiophene-2-boronic acid pinacol ester and aryl bromide using Pd (0)/L1 have been screened in **Table 1**. Yields of the isolated product were obtained under various reaction conditions (**Table 1**). First, decreasing the catalyst loading to 0.1% Pd for reaction of thiophene-2-boronic acid pinacol ester and aryl bromide, the coupling product was obtained in a good yield of 89% after 48 h at 65°C. Interestingly, when the reaction time was shortened to 15 min, there was little effect on the yield of the reaction, and the product was gained in good yields of 85–95% under similar conditions with an increase in the values of TON and TOF (especially by shortening the reaction time to 15 min, the value of TOF increased

to 10^3 h^{-1}) (**Table 1**, entries 3–7). Besides, by further decreasing the Pd loading to 0.01% Pd and using the L1: Pd ratio of 5:1, the process was carried out at 65°C after 0.5 h in yields of 62–89%, and a value of TOF of 2.5–3.6 × 10^4 h^{-1} could be generated (**Table 1**, entries 8–12). Among the bases offered in Suzuki–Miyaura cross-coupling reactions, the base K$_2$CO$_3$ was proved to be the best choice, and the desired products were obtained with the highest yields under the above conditions (**Table 1**) (Buchwald et al., 2004). According to the results, this catalyst system showed efficient activity for the cross-coupling reactions of aryl bromide and thiophene-2-boronic acid pinacol ester.

To test the performance of our ligand L1 with low levels of catalyst loading and short reaction times, we chose nine substrates under the conditions of K$_2$CO$_3$ as the case with 0.1% Pd (0)/L1 (1: 3) within 30 min as a test case (**Table 2**). The isolated yields of the corresponding product are depicted in **Table 2**. Compared with the catalyst Pd(PPh$_3$)$_4$, ligand L1 gave better yields in reactions of aryl halide and 2-thiopheneboronic ester under the above conditions. For example, the coupling reaction of bromobenzene or benzyl bromide and aromatic boronic acid pinacol ester with 0.1% Pd (0) (Pd: L1 = 1:3) within 15 min gave excellent isolated yields of the corresponding products, wherein TOFs of 3,840 h^{-1} and 3,800 h^{-1} were obtained, respectively (**Table 2**, entries 1–2; **Supplementary Table S2**, entries 1–2). The reaction of electron-rich 1-bromo-4-methoxybenzene and electron-deficient aryl bromide with thiophene-2-boronic acid pinacol ester (ratio 1:1) resulted in the excellent yields of 92–97% with 0.1% Pd (0) (Pd: L1 = 1:3) (**Table 2**, entries 3–5; **Supplementary Table S2**, entries 3–5). The above results showed that the presence of electron-rich or electron-deficient groups of aryl bromide had little effect on the yield and TOF of these reactions. In addition, the Suzuki cross-coupling reactions of substrates such as moderately hindered 1,4-dibromo-2,5-dimethylbenzene with thiophene-2-boronic ester could be completed at 0.1% Pd (0) (Pd: L1 = 1:3) to give an 88% yield with a decreased TOF of 880 h^{-1} within 30 min (**Table 2**, entry 6;

TABLE 2 | Yields of the isolated products from Suzuki–Miyaura cross-coupling reactions of thiophene-2-boronic esters and aryl halides with different catalysts.

	Thiophene-2-boronic esters	Aryl halides	Time (min)	Yield (%)	
				Pd$_2$(dba)$_3$/L1	Pd(PPh$_3$)$_4$
1	thiophene-2-boronic acid pinacol ester	benzyl bromide	15	96	83
2	thiophene-2-boronic acid pinacol ester	bromobenzene	15	95	76
3	thiophene-2-boronic acid pinacol ester	Br–C$_6$H$_4$–OCH$_3$	15	92	72
4	thiophene-2-boronic acid pinacol ester	Br–C$_6$H$_4$–NO$_2$	15	93	81
5	thiophene-2-boronic acid pinacol ester	Br–C$_6$H$_4$–CHO	15	97	81
6	thiophene-2-boronic acid pinacol ester	1,4-dibromo-2,5-dimethylbenzene	30	88	24
7	2,5-thiophenebis(boronic acid pinacol ester)	2-bromobenzaldehyde	30	90	18
8	thiophene-2-boronic acid pinacol ester	2-bromothiophene	30	90	31
9	thiophene-2-boronic acid pinacol ester	5-bromothiophene-2-carbaldehyde	30	91	48

Reaction conditions: 1 equiv. of thienyl halide, 1 or 2 equiv. of thiophenylboronic ester, 5 equiv. of K$_2$CO$_3$, THF (5 L mol^{-1}), H$_2$O, 0.1 mol% Pd$_2$(dba)$_3$ + L1, reflux, within 15–30 min, 1 mol% Pd(PPh$_3$)$_4$, reflux, within 2 h.

Supplementary Table S2, entry 6). Under the similar conditions, Pd(PPh$_3$)$_4$ furnished the target products with a 24% isolated yield and only a 6 h^{-1} TOF after 2 h. Notably, the Suzuki cross-coupling reactions of 2,5-thiophenebis (boronic ester)s and ortho-substituted bromobenzene Pd (0)/L1 provided the target products in an isolated yield of 90% with a value of TOF of 900 within 30 min, whereas under the similar conditions, Pd(PPh$_3$)$_4$ gained the isolated yield of 18% with only a 4.5 h^{-1} TOF after 2 h (**Table 2**, entry 7; **Supplementary Table S2**, entry 7). Besides, the process worked well on the coupling of electron-rich thienyl bromide and thiophenylboronic ester, and the coupling reactions could be carried out at 0.1% Pd (0) (Pd: L1 = 1:3) to give 90 and 91% yields, with TOFs of 1,800 h^{-1} and 1,820 h^{-1} after 30 min, and Pd(PPh$_3$)$_4$ gained the isolated yields of 31% and 48%, with TOFs of 15.5 h^{-1} and 24 h^{-1} after 2 h, respectively (**Table 2**, entries 8–9; **Supplementary Table S2**, entries 8–9). These results suggest that the catalyst system is remarkably effective for the cross-coupling based thiophene-2-boronic ester with low levels of catalyst loading and short reaction times for a broad range of substrates. Compared with the traditional catalyst precursor Pd(PPh$_3$)$_4$, the catalyst system

Pd$_2$(dba)$_3$/L1 showed higher performance in yield and TOF. The general mechanism for the Pd-catalytic cross-coupling reaction is divided into three steps, including oxidative addition, transmetalation, and reductive elimination (Miyaura, N. and Suzuki, A. 1995). Oxidative addition is the rate-limiting step for Suzuki–Miyaura coupling reaction, which might be accelerated in the Pd (0)/L1 catalyst system. A high reaction rate can effectively reduce the undesired deboronation of thiophene-2-boronic acid pinacol ester that negatively affects Suzuki–Miyaura cross-coupling reactions under standard conditions (Jayakannan et al., 2001; Kinzel et al., 2010).

Suzuki Polycondensation Reaction Based on Thiophenylboronic Ester

To test the performance and wide scope of the catalyst precursor Pd (0)/L1, the catalytic system with ligand L1 and Pd$_2$(dba)$_3$ (Pd/L1 = 1/3) was tested for the synthesis of hyperbranched polymers based 2,5-thiophenebis (boronic acid pinacol ester)s (**Scheme 1**). For comparison, Pd$_2$(dba)$_3$ (Pd/L1 = 1/3) and Pd(PPh$_3$)$_4$ were
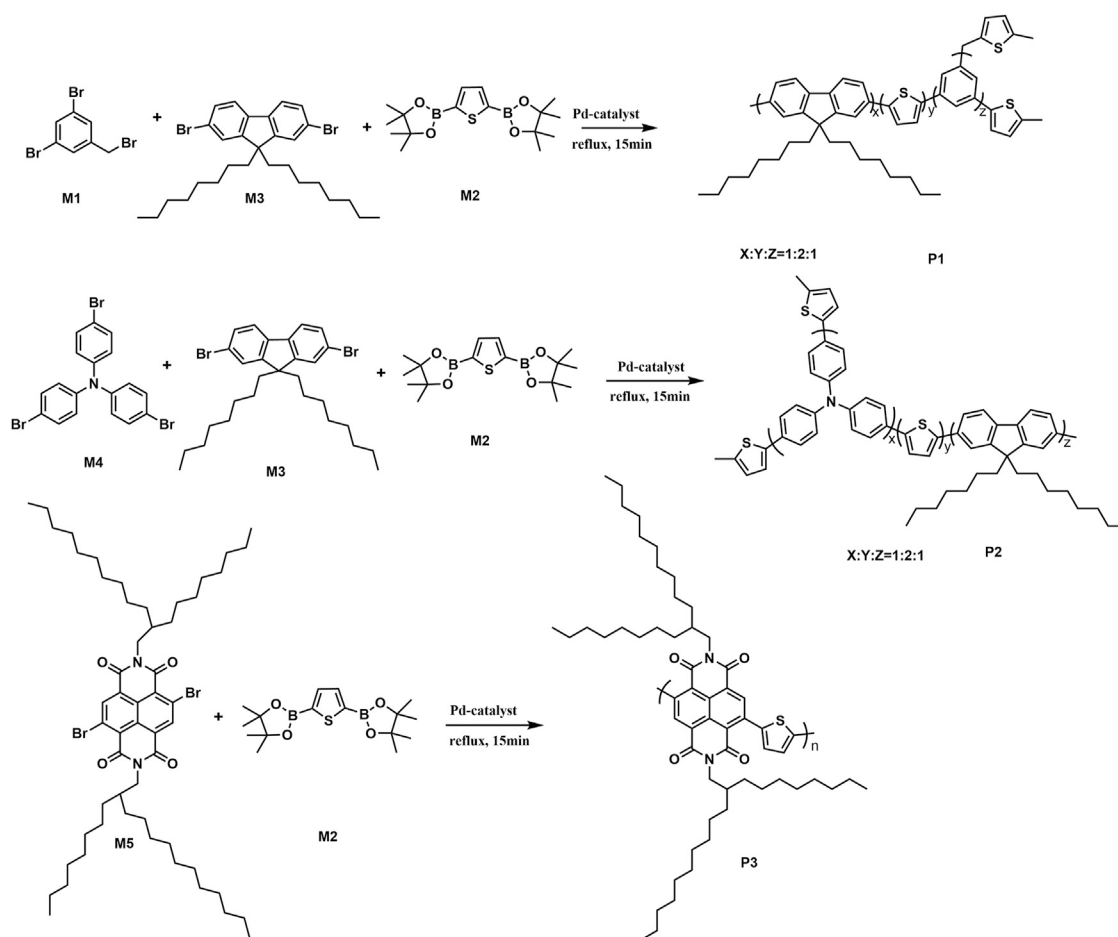
SCHEME 1 | Suzuki polycondensation based on 2,5-thiophenebis (boronic acid pinacol ester) with $Pd_2(dba)_3$ (Pd/L1 = 1/3) and $Pd(PPh_3)_4$ as catalyst precursors.

TABLE 3 | Catalyst precursor, yield, weight-average molecular weight (Mw), and polydispersity index (PDI).

Polymers	Catalyst precursor	Yield (%)	Mw^a (g mol^{-1})	PD
P1	$Pd_2(dba)_3$/L1	95	24,800^b	1.7
P1	$Pd(PPh_3)_4$	93	3,000	3.2
P2	$Pd_2(dba)_3$/L1	97	7,900^b	1.4
P2	$Pd(PPh_3)_4$	89	2000	1.5
P3	$Pd_2(dba)_3$/L1	92	112,000	3.5
P3	$Pd(PPh_3)_4$	82	8,400	1.1

^{a}Molecular weight determined by GPC with THF as the eluent, calibrated with polystyrene standards.
^{b}Molecular weight determined by GPC at 150°C with 1,2,4-trichlorobenzene as the eluent, calibrated with polystyrene standards.

also applied for the same polymerization as catalyst precursors. Suzuki polycondensation of 2,5-thiophenebis (boronic acid pinacolester)s (M2) with tris(4-bromophenyl)amine (M1) or tris(4-bromophenyl)amine (M4) and 2,7-dibromo-9,9-dioctyl-9H-fluorene (M3) was carried out in a biphasic mixture of THF and aqueous K_2CO_3 with freshly prepared $Pd_2(dba)_3$/L1 or $Pd(PPh_3)_4$ as the

catalyst precursor in 15 min. The results of polymerization are displayed in **Table 3**. When using $Pd_2(dba)_3$/L1 as the catalyst precursor, the polycondensation proceeded very rapidly, and large amounts of precipitation were observed in the reaction flask after 5 min. Polymers were not soluble in common reagents such as $CHCl_3$ or THF even at the refluxed temperature, but little were soluble in 150°C 1,2,4-trichlorobenzene. The molecule molar masses of P1 and P2 were determined by GPC at 150°C with 1,2,4-trichlorobenzene as the eluent and calibration with polystyrene standards. The soluble fractions of polymers P1 and P2 had molecular weights Mw of 24,800 g mol^{-1} and 7,900 g mol^{-1}, respectively. Using the representative palladium catalyst $Pd(PPh_3)_4$, Suzuki polycondensation of monomers (M1 or M4) and monomer M3 with 2,5-thiophenebis (boronic acid pinacolester)s (M2) provided only low molecule molar mass oligomers with an Mw less than 3,000 g mol^{-1}.

To test the performance and obtain fully soluble polymers in the reaction solvents, we chose 4,9-dibromo-2,7-bis(2-octyldodecyl) benzo(lmn)(3,8)phenanthroline-1,3,6,8(2H, 7H)-tetraone (M5) and 2,5-thiophenebis (boronic acid pinacolester)s (M2) as monomers. Using $Pd_2(dba)_3$/L1 as the catalyst precursor,
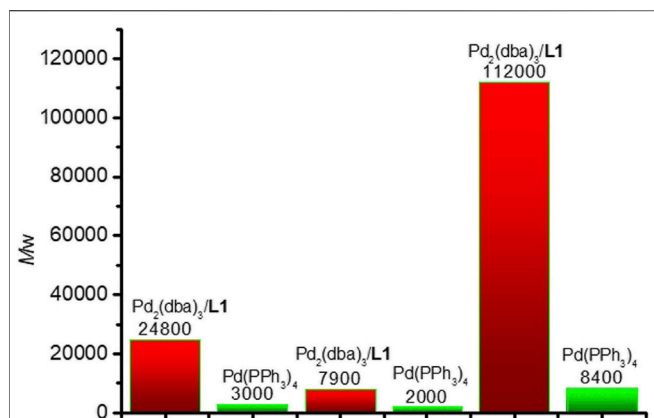
FIGURE 2 | The molecular weight Mw of P1, P2 and P3 with different catalysts.

polymer P3 was synthesized, which was completely soluble in THF at room temperature in 15 min. The GPC elution curve of P3 showed narrow molecular weight distribution. The number-average molecular weight and weight-average molecular weight of P3 were 32,000 g mol^{-1} and 11,2000 g mol^{-1}, respectively (**Figure 2**). The polycondensation of M2 and M5 was also tested using Pd(PPh$_3$)$_4$ as the catalyst precursor. GPC data showed that polymer P3 was gained with a molecular weight Mw 8,400 g mol^{-1}. The results are also displayed in **Table 3**.

CONCLUSIONS

In conclusion, the catalyst system based on Pd (0)/L1 was studied for the Suzuki–Miyaura cross-coupling reactions of thiophene-2-boronic ester with aryl bromides and unactivated thienyl bromides. The catalytic system is efficient in good to excellent yields and high

TOFs with low catalyst loadings or shorter reaction times. In addition, relative to Pd(PPh$_3$)$_4$, this catalyst system also demonstrates higher activity in the Suzuki polymerization of aryl halide and 2,5-thiophenebis (boronic acid pinacol ester)s, resulting in various thiophene-containing conjugated polymers with good yields and high molecular weights within 15 min.

DATA AVAILABILITY STATEMENT

The original contributions presented in the study are included in the article/**Supplementary Material**, and further inquiries can be directed to the corresponding authors.

AUTHOR CONTRIBUTIONS

Conceptualization, ML and HG; investigation, LL; resources, LL and ZZ; data curation, LL and ML; writing—original draft and writing—review, ML and MW; supervision, ML, HG, and DL; funding acquisition, ML and MW. All authors have read and agreed to the published version of the manuscript.

FUNDING

SUPPLEMENTARY MATERIAL

The Supplementary Material for this article can be found online at: https://www.frontiersin.org/articles/10.3389/fchem.2021.743091/full#supplementary-material

REFERENCES

Abdiaj, I., Huck, L., Mateo, J., Hoz, A., Gomez, M., Ortiz, A., et al. (2018). Photoinduced Palladium-Catalyzed Negishi Cross-Couplings Enabled by the Visible-Light Absorption of Palladium–Zinc Complexes. *Angew. Chem. Int. Ed.* 57, 13231–13236. doi:10.1002/anie.201808654

Altenhoff, G., Goddard, R., Lehmann, C. W., and Glorius, F. (2004). Sterically Demanding, Bioxazoline-Derived N-Heterocyclic Carbene Ligands with Restricted Flexibility for Catalysis. *J. Am. Chem. Soc.* 126, 15195–15201. doi:10.1021/ja045349r

Ayogu, J. I., and Onoabedje, E. A. (2019). Recent Advances in Transition Metal-Catalysed Cross-Coupling of (Hetero)aryl Halides and Analogues under Ligand-free Conditions. *Catal. Sci. Technol.* 9, 5233–5255. doi:10.1039/C9CY01331H

Barder, T. E., Walker, S. D., Martinelli, J. R., and Buchwald, S. L. (2005). Catalysts for Suzuki-Miyaura Coupling Processes: Scope and Studies of the Effect of Ligand Structure. *J. Am. Chem. Soc.* 127, 4685–4696. doi:10.1021/ja042491j

Bedford, R. B. (2003). Palladacyclic Catalysts in C-C and C-Heteroatom Bond-Forming Reactions. *Chem. Commun.* 1787–1796. doi:10.1039/B211298C

Bedford, R. B., Blake, M. E., Butts, C. P., and Holder, D. (2003a). The Suzuki Coupling of Aryl Chlorides in TBAB—Water Mixtures. *Chem. Commun.* 21, 466-467. doi:10.1039/b211329e

Bedford, R. B., Cazin, C. S. J., Coles, S. J., Gelbrich, T., Horton, P. N., Hursthouse, M. B., et al. (2003b). High-Activity Catalysts for Suzuki Coupling and Amination Reactions with Deactivated Aryl Chloride Substrates: Importance of the Palladium Source. *Organometallics* 22, 987–999. doi:10.1021/om020841+

Beller, M., Zapf, A., JackstellMonsees, R. A., Rataboul, F., Riermeier, T., Monsees, A., et al. (2004). Practical Synthesis of New and Highly Efficient Ligands for the Suzuki Reaction of Aryl Chlorides. *Chem. Commun.* 7, 38-39. doi:10.1039/B311268N

Bellina, F., Carpita, A., and Rossi, R. (2004). Palladium Catalysts for the Suzuki Cross-Coupling Reaction: an Overview of Recent Advances. *Synthesis* 15, 2419–2440. doi:10.1055/s-2004-831223

Böhm, V. P. W., Gstöttmayr, C. W. K., Weskamp, T., and Herrmann, W. A. (2000). Synthesis, Structure and Catalytic Application of Palladium(II) Complexes Bearing N-Heterocyclic Carbenes and Phosphines. *J. Organomet. Chem.* 595, 186–190. doi:10.1016/S0022-328X(00)00722-110.1016/s0022-328x(99)00590-2

Borges-González, J., Kousseff, C. J., and Nielsen, C. B. (2019). Organic Semiconductors for Biological Sensing. *J. Mater. Chem. C* 7, 1111–1130. doi:10.1039/C8TC05900D

Buchwald, S. L., Old, D. W., and Wolfe, J. P. (1998). A Highly Active Catalyst for Palladium-Catalyzed Cross-Coupling Reactions: Room-Temperature Suzuki Couplings and Amination of Unactivated Aryl Chlorides. *J. Am. Chem. Soc.* 120, 9722–9723. doi:10.1021/ja982250+

Buchwald, S. L., Walker, S. D., Barder, T. E., and Martinelli, J. R. (2004). A Rationally Designed Universal Catalyst for Suzuki–Miyaura Coupling Processes. *Angew. Chem. Int. Ed.* 43, 1871–1876. doi:10.1002/anie.200353615

Chen, T. A., and Rieke, R. D. (1992). The First Regioregular Head-To-Tail Poly(3-Hexylthiophene-2,5-Diyl) and a Regiorandom Isopolymer: Nickel versus Palladium Catalysis of 2(5)-Bromo-5(2)-(bromozincio)-3-Hexylthiophene Polymerization. *J. Am. Chem. Soc.* 114, 10087–10088. doi:10.1021/ja00051a066

Clagg, K., Holda, S., Kumar, A., Koeniga, S., and Angelaud, R. (2019). A Telescoped Knochel-Hauser/Kumada-Corriu Coupling Strategy to Functionalized Aromatic Heterocycles. *Tetra. Lett.* 60, 5–7. doi:10.1016/j.tetlet.2018.11.014

Coulson, D. R. (1972). Tetrakis(triphenylphosphine)palladium(0). *Inorg. Synth.* 13, 121–124. doi:10.1002/9780470132449.ch23

F. Abdollahi, M., and Zhao, Y. (2020). Recent Advances in Dithiafulvenyl-Functionalized Organic Conjugated Materials. *New J. Chem.* 44, 4681–4693. doi:10.1039/C9NJ06430C

Farina, V., Krishnamurthy, V., and Scott, W. J. (1997). The Stille Reaction. *Org. React.* 50, 1–652. doi:10.1002/0471264180.or050.01

Gautam, P., and Bhanage, B. M. (2015). Palladacycle Catalyzed Carbonylative Suzuki–Miyaura Coupling with High Turnover Number and Turnover Frequency. *J. Org. Chem.* 80, 7810–7815. doi:10.1021/acs.joc.5b01160

Grasa, G. A., Viciu, M. S., Huang, J., Zhang, C., Trudell, M. L., and Nolan, S. P. (2002). Suzuki—Miyaura Cross-Coupling Reactions Mediated by Palladium/Imidazolium Salt Systems. *Organometallics* 21, 2866–2873. doi:10.1021/om020178p

Grushin, V. V., and Alper, H. (1994). Transformations of Chloroarenes, Catalyzed by Transition-Metal Complexes. *Chem. Rev.* 94, 1047–1062. doi:10.1021/cr00028a008

Han, F. S. (2013). Transition-metal-catalyzed Suzuki–Miyaura Cross-Coupling Reactions: a Remarkable advance from Palladium to Nickel Catalysts. *Chem. Soc. Rev.* 42, 5270–5298. doi:10.1039/C3CS35521G

Jayakannan, M., van Dongen, J., and Janssen, R. (2001). Mechanistic Aspects of the Suzuki Polycondensation of Thiophenebisboronic Derivatives and Diiodobenzenes Analyzed by MALDI-TOF Mass Spectrometry. *Macromolecules* 34, 5386–5393. doi:10.1021/ma0100403

Jessop, I. A., Chong, A., Graffo, L., Camarada, M. B., Espinoza, C., Angel, F. A., et al. (2020). Synthesis and Characterization of a 2,3-Dialkoxynaphthalene-Based Conjugated Copolymer via Direct Arylation Polymerization (DAP) for Organic Electronics. *Polymers* 12, 1377–1392. doi:10.3390/polym12061377

Jiang, K., Luo, S., Pang, C., Wang, B., Wu, H., and Wang, Z. (2019). A Functionalized Fluorochrome Based on Quinoline-Benzimidazole Conjugate: From Facile Design to Highly Sensitive and Selective Sensing for Picric Acid. *Dyes Pigm.* 162, 367–376. doi:10.1016/j.dyepig.2018.10.041

Kinzel, T., Zhang, Y., and Buchwald, S. L. (2010). A New Palladium Precatalyst Allows for the Fast Suzuki—Miyaura Coupling Reactions of Unstable Polyfluorophenyl and 2-Heteroaryl Boronic Acids. *J. Am. Chem. Soc.* 132, 14073–14075. doi:10.1021/ja1073799

Koyuncu, F. B. (2012). An Ambipolar Electrochromic Polymer Based on Carbazole and Naphthalene Bisimide: Synthesis and Electro-Optical Properties. *Electrochimica Acta* 68, 184–191. doi:10.1016/j.electacta.2012.02.048

Li, J., and Pu, K. (2019). Development of Organic Semiconducting Materials for Deep-Tissue Optical Imaging, Phototherapy and Photoactivation. *Chem. Soc. Rev.* 48, 38–71. doi:10.1039/C8CS00001H

Li, W. W., Han, Y., Li, B. S., Liu, C., and Bo, Z. S. (2008). Tris[tri(2-thienyl)phosphine]palladium as the Catalyst Precursor for Thiophene-Based Suzuki-Miyaura Cross-Coupling and Polycondensation. *J. Polym. Sci. Part A: Polym. Chem.* 46, 4556–4563. doi:10.1002/pola.22792

Littke, A. F., Dai, C. Y., and Fu, G. C. (2000). Versatile Catalysts for the Suzuki Cross-Coupling of Arylboronic Acids with Aryl and Vinyl Halides and Triflates under Mild Conditions. *J. Am. Chem. Soc.* 122, 4020–4028. doi:10.1021/ja0002058

Littke, A. F., and Fu, G. C. (2002). Palladium-Catalyzed Coupling Reactions of Aryl Chlorides. *Angew. Chem. Int. Ed.* 41, 4176–4211. doi:10.1002/1521-3773(20021115)41:22<4176::AID-ANIE4176>3.0.CO;2-U

Liu, M., Chen, Y., Zhang, C., Li, C., Li, W., and Bo, Z. (2013). Synthesis of Thiophene-Containing Conjugated Polymers from 2,5-thiophenebis(boronic

Ester)s by Suzuki Polycondensation. *Polym. Chem.* 4, 895–899. doi:10.1039/C2PY21070C

Liu, S. Y., Choi, M. J., and Fu, G. C. (2001). A Surprisingly Mild and Versatile Method for Palladium-Catalyzed Suzuki Cross-Couplings of Aryl Chlorides in the Presence of a Triarylphosphine. *Chem. Commun.* 2408–2409. doi:10.1039/B107888G

Lu, G., Usta, H., Risko, C., Wang, L., Facchetti, A., Ratner, M. A., et al. (2008). Synthesis, Characterization, and Transistor Response of Semiconducting Silole Polymers with Substantial Hole Mobility and Air Stability. Experiment and Theory. *J. Am. Chem. Soc.* 130, 7670–7685. doi:10.1021/ja800424m

Ma, F., Shi, W., Mi, H., Luo, J., Lei, Y., and Tian, Y. (2013). Triphenylaminebased Conjugated polymer/I−complex as Turn-On Optical Probe for Mercury (II) Ion. *Sensors Actuators B Chem.* 182, 782–788. doi:10.1016/j.snb.2013.03.096

Miyaura, N., and Suzuki, A. (1995). Palladium-catalyzed Cross-Coupling Reactions of Organoboron Compounds. *Chem. Rev.* 95, 2457–2483. doi:10.1021/cr00039a007

Nguyen, H., Nguyen, L., Nguyen, T., Luu, A., and Le, T. (2014). Synthesis of Hyperbranched Conjugated Polymers Based on 3-hexylthiophene, Triphenylamine and Benzo [c] [1,2,5] Thiadiazole Moieties: Convenient Synthesis through Suzuki Polymerization and Impact of Structures on Optical Properties. *J. Polym. Res.* 21, 552–563. doi:10.1007/s10965-014-0552-y

Ochieng, M. A., Ponder, J. F., and Reynolds, J. R. (2020). Effects of Linear and Branched Side Chains on the Redox and Optoelectronic Properties of 3,4-dialkoxythiophene Polymers. *Polym. Chem.* 11, 2173–2181. doi:10.1039/C9PY01720H

Okamoto, K., Housekeeper, J. B., Michael, F. E., and Luscombe, C. K. (2013). Thiophene Based Hyperbranched Polymers with Tunable Branchingusing Direct Arylation Methods. *Polym. Chem.* 4, 3499–3506. doi:10.1039/C3PY00412K

Paul, S., Islamc, M. M., and Islam, S. M. (2015). Suzuki–Miyaura Reaction by Heterogeneously Supported Pd in Water: Recent Studies. *RSC Adv.* 5, 42193–42221. doi:10.1039/C4RA17308B

Pei, J., Ni, J., Zhou, X. H., Cao, X. Y., and Lai, Y. H. (2002). Head-to-Tail Regioregular Oligothiophene-Functionalized 9,9'-Spirobifluorene Derivatives. 1. Synthesis. *J. Org. Chem.* 67, 4924–4936. doi:10.1021/jo011146z

Ponder, J. F., Schmatz, B., Hernandez, J. L., ReynoldsMcQuade, J. R. D. T., Pullen, A. E., and Swager, T. M. (2018). Soluble Phenylenedioxythiophene Copolymers via Direct (Hetero)arylation Polymerization: a Revived Monomer for Organic Electronics. *J. Mater. Chem. C* 6, 1064–1070. doi:10.1039/C7TC05293F

Qiu, L., Caffrey, R., Jin, Y., Gong, Y., Hu, Y., Sun, H., et al. (2018). Cage-templated Synthesis of Highly Stable Palladium Nanoparticles and Their Catalytic Activities in Suzuki–Miyaura Coupling. *Chem. Sci.* 9, 676–680. doi:10.1039/C7SC03148C

Rathod, J., Sharma, P., Pandey, P., Singh, A., and Kumar, P. (2017). Highly Active Recyclable SBA-15-EDTA-Pd Catalyst for Mizoroki-Heck, Stille and Kumada C–C Coupling Reactions. *J. Porous Mat* 24, 837–846. doi:10.1007/s10934-016-0323-8

Rizwan, K., Zubair, M., Rasool, N., Mahmood, T., Ayub, K., Alitheen, N., et al. (2018). Palladium(0) Catalyzed Suzuki Cross-Coupling Reaction of 2,5-Dibromo-3-Methylthiophene: Selectivity, Characterization, DFT Studies and Their Biological Evaluations. *Chem. Cent. J.* 12, 49. doi:10.1186/s13065-018-0404-7

Ryabov, A. D. (1990). Mechanisms of Intramolecular Activation of Carbon-Hydrogen Bonds in Transition-Metal Complexes. *Chem. Rev.* 90, 403–424. doi:10.1021/cr00100a004

Shen, W. (1997). Palladium Catalyzed Coupling of Aryl Chlorides with Arylboronic Acids. *Tetrahedron Lett.* 38, 5575–5578. doi:10.1016/S0040-4039(97)01261-6

Wu, W., Tang, R., Li, Q., and Li, Z. (2015). Functional Hyperbranched Polymers with Advanced Optical, Electrical and Magnetic Properties. *Chem. Soc. Rev.* 44, 3997. doi:10.1039/C4CS00224E

Wu, Y., An, C., Shi, L., Yang, L., Qin, Y., and Liang, N. (2018). The Crucial Role of Chlorinated Thiophene Orientation in Conjugated Polymers for Photovoltaic Devices. *Angew. Chem. Int. Ed.* 57, 12911–12915. doi:10.1002/anie.201807865

Xia, H., He, J., Peng, P., Zhou, Y., Li, Y., and Tian, W. (2007). Synthesis and Photophysical Properties of Triphenylamine-Based Dendrimers with 1,3,5-triphenylbenzene Cores. *Tetrahedron Lett.* 48, 5877. doi:10.1016/j.tetlet.2007.06.052

Yen, H. J., and Liou, G. S. (2019). Design and Preparation of Triphenylamine-Based Polymeric Materials towards Emergent Optoelectronic Applications. *Prog. Polym. Sci.* 89, 250–287. doi:10.1016/j.progpolymsci.2018.12.001

Yue, H., Kong, L., Wang, B., Yuan, Q., Zhang, Y., Du, H., et al. (2019). Synthesis and Characterization of Novel D-A Type Neutral Blue Electrochromic Polymers Containing Pyrrole[3-c]Pyrrole-1,4-Diketone as the Acceptor Units and the Aromatics Donor Units with Different Planar Structures. *Polymers* 11, 2023. doi:10.3390/polym11122023

Zhang, C., Huang, J., Trudell, M. L., and Nolan, S. P. (1999). Palladium—Imidazol-2-ylidene Complexes as Catalysts for Facile and Efficient Suzuki Cross-Coupling Reactions of Aryl Chlorides with Arylboronic Acids. *J. Org. Chem.* 64, 3804–3805. doi:10.1021/jo990554o

Zhang, C., Ogawa, K., Tu, S., Zu, C., Ringer, J., Derstine, C., et al. (2019). Highly Active Monoligated Arylpalladacyles for Cross-Coupling Reactions. *Org. Process. Res. Dev.* 23, 2181–2190. doi:10.1021/acs.oprd.9b00234

Zou, Y. P., Gendron, D., Plesu, R. N., and Leclerc, M. (2009). Synthesis and Characterization of New Low-Bandgap Diketopyrrolopyrrole-Based Copolymers. *Macromolecules* 42, 6361–6365. doi:10.1021/ma901114j

Tannic Acid as a Natural Crosslinker for Catalyst-Free Silicone Elastomers From Hydrogen Bonding to Covalent Bonding

Sen Kong[1], Rui Wang[1], Shengyu Feng[1,2] and Dengxu Wang[1,2]*

[1]National Engineering Research Center for Colloidal Materials and Key Laboratory of Special Functional Aggregated Materials, Ministry of Education, School of Chemistry and Chemical Engineering, Shandong University, Jinan, China, [2]Shandong Key Laboratory of Advanced Organosilicon Materials and Technologies and State Key Laboratory of Fluorinated Functional Membrane Materials, Zibo, China

The construction of silicone elastomers crosslinked by a natural crosslinker under a catalyst-free method is highly desirable. Herein we present catalyst-free silicone elastomers (SEs) by simply introducing tannic acid (TA) as a natural crosslinker when using poly (aminopropylmethylsiloxane-*co*-dimethylsiloxane) (PAPMS) as the base polymer. The crosslinked bonding of these SEs can be easily changed from hydrogen bonding to covalent bonding by altering the curing reaction from room temperature to heating condition. The formability and mechanical properties of the SEs can be tuned by altering various factors, including processing technique, the amount of TA and aminopropyl-terminated polydimethylsiloxane, the molecular weight and -NH$_2$ content of PAPMS, and the amount of reinforcing filler. The hydrogen bonding was proved by the reversible crosslinking of the elastomers, which can be gradually dissolved in tetrahydrofuran and re-formed after removing the solvent. The covalent bonding was proved by a model reaction of catechol and *n*-decylamine and occurred through a combination of hydroxylamine reaction and Michael addition reaction. These elastomers exhibit good thermal stability and excellent hydrophobic property and can bond iron sheets to hold the weight of 500 g, indicating their promising as adhesives. These results reveal that TA as a natural product is a suitable "green" crosslinker for the construction of catalyst-free silicone elastomers by a simple crosslinking strategy. Under this strategy, TA and more natural polyphenols could be certainly utilized as crosslinkers to fabricate more organic elastomers by selecting amine-containing polymers and further explore their extensive applications in adhesives, sealants, insulators, sensors, and so forth.

Keywords: silicone elastomers, tannic acid, catalyst-free, polysiloxane, green chemistry, natural crosslinkers

INTRODUCTION

In the past decades, silicone elastomers (SEs) have gained significant attention for extensive applications in aerospace, electronics, protective coating, wearable devices, medical systems, and bio-materials, by virtue of their unique properties, such as high/low temperature resistance, low surface energy, electrical insulation, aging resistance, and biocompatibility (Yilgör and Yilgör, 2014; Rücker and Kümmerer, 2015; Rus and Tolley, 2015; Eduok et al., 2017; Liu et al., 2020). SEs are typically constructed by linking the linear silicone polymers with small molecules or polymers containing two or more linkable sites, which are called crosslinkers, to form three-dimensional (3D) networks. Traditional silicone crosslinking technologies, involving free-radical, condensation and hydrosilylation reactions, have been widely utilized in laboratory and industry (Troegel and Stohrer, 2011; Picard et al., 2015). However, in these processes, catalysts are generally indispensable to accomplish the crosslinking and have brought cost (e.g., platinum catalysts in hydrosilylation) or environmental concerns (e.g., toxic tin catalysts in condensation) (Wang et al., 2017). More importantly, the catalysts that may have an undesirable toxicological effect cannot meet the requirement of green chemistry. Therefore, it is highly desirable to develop a catalyst-free crosslinking strategy.

In recent years, some novel crosslinking strategies, such as azide-alkyne cycloaddition (Rambarran et al., 2012), dynamic covalent bonding (e.g., imine (Bui and Brook, 2020) and boroxine (Lai et al., 2016)), and coordination bonding (Rao et al., 2016; Lai et al., 2018), have been developed to construct silicone elastomers without a catalyst. The key factor in these strategies is to rationally choose a suitable polysiloxane having applicable functional groups as the base polymer. Amine-functionalized polysiloxanes have been verified as a good choice because of their commercial availability and high reactivity, which can be readily crosslinked through versatile catalyst-free reactions, such as aza-Michael reactions (Feng et al., 2016), ureas from reaction with isocyanates (Yang et al., 2020), and imine bonding through reaction with aldehydes (Bui and Brook, 2020). However, in these reactions, the selected crosslinkers are normally synthetic molecules or polymers, thus making it difficult to meet the current requirements of silicone elastomers in terms of green chemistry. Actually, this situation exists in most of silicone materials. Thus it would be of great significance to develop green crosslinkers for silicone elastomers.

Natural polyphenols, featuring more than one phenolic groups, are ubiquitous in nature, such as in fruits, vegetables, grains, tea, coffees, wines, and chocolates, have played a crucial role in defending UV radiation and pathogenic invasion for plants (Xu R. et al., 2018). They not only possess intriguing biological activities (e.g., antioxidant, antiallergic, and antitumor), but also exhibit attractive chemical properties (Xu, et al., 2018a). The abundant phenolic hydroxyl groups in polyphenols can act as donors in the formation of hydrogen bonding. Polyphenols can be easily oxidized to the quinone forms, which can undergo reactions with various functional groups, such as amine and thiol through Michael addition or Schiff base reaction (Wu et al., 2015). The aromatic rings or hydroxyls can also interact with other molecules by hydrophobic or electrostatic interactions. By virtue of these features, natural

polyphenols can serve as versatile platforms for material engineering and surface functionalization (Xu L. Q. et al., 2018). In particular, they can be efficiently utilized to link linear polymers together to build crosslinked polymeric materials (Niu et al., 2020), especially high-strength hydrogels (Xu R. et al., 2018; Fan et al., 2018; López and Pich, 2018; Jiménez et al., 2019), and can be recognized as a class of ideal natural and green crosslinkers. However, polyphenols haven't been utilized as crosslinkers for the construction of elastomers, especially silicone elastomers.

Herein, a typical polyphenol, tannic acid (TA), is chosen as a green and natural crosslinker to fabricate catalyst-free silicone elastomers from amine-functionalized polysiloxanes. By taking the advantage of the feature of hydrogen bond donor from the phenolic hydroxyl group in TA, the elastomers can be readily crosslinked through non-covalent bonds, i.e., hydrogen bond at ambient temperature. It is interesting that the hydrogen bonding can be converted into covalent bonding by improving the crosslinking temperature, thus making TA as a covalent crosslinker for silicone elastomers. Various factors that influence the mechanical properties of these elastomers are systematically investigated. The covalent crosslinking mechanism is explored by designing a model reaction. In addition, the elastomers applied as adhesives were also explored.

EXPERIMENTAL

Materials

Tannic acid (TA), catechol, and n-decylamine were purchased from Energy Chemical Company of China. Aminopropyl-terminated polydimethylsiloxane (DP-1, $M_w = 10,000 \text{ g mol}^{-1}$) were purchased from Tangui Co., China. All other reagents were purchased from Fuyu Company of China.

Synthesis of poly (aminopropylmethylsiloxane-*co*-dimethylsiloxane) (PAPMS)

A series of poly (aminopropylmethylsiloxane-*co*-dimethylsiloxane) (PAPMS) were prepared as our previous report (Lu and Feng, 2017). The structure of PAPMS was shown in **Figure 1** and the obtained PAPMS were named as P-X (X represents b/(a+b)× 100, that is, the molar content of–NH_2 in the main chain), and P-2.2, P-2.5, P-4.8, P-5.8 and P-7.5 were obtained. The molecular weight (M_n) of these polymers were 1,63,305, 64,000, 45,000, 70,300, and 46,217 g mol^{-1} for P-2.2, P-2.5, P-4.8, P-5.8 and P-7.5, respectively, which were determined by gel permeation chromatography (GPC).

Preparation of Silicone Elastomers Crosslinked by Hydrogen Bond

In a typical procedure, an aqueous solution of TA was prepared by dissolving TA (30 mg) in water (0.2 ml), while a n-hexane solution of amino-containing polysiloxane was prepared by dissolving P-2.5 (1.6 g) and aminopropyl-terminated polysiloxane (DP-1) (0.6 g) in n-hexane (15 ml). Then the

FIGURE 1 | Preparation of silicone elastomers crosslinked by hydrogen bonding or covalent bonding. (i) H_2O/solvent, room temperature; (ii) H_2O/solvent, room temperature; 150°C, 1 h.
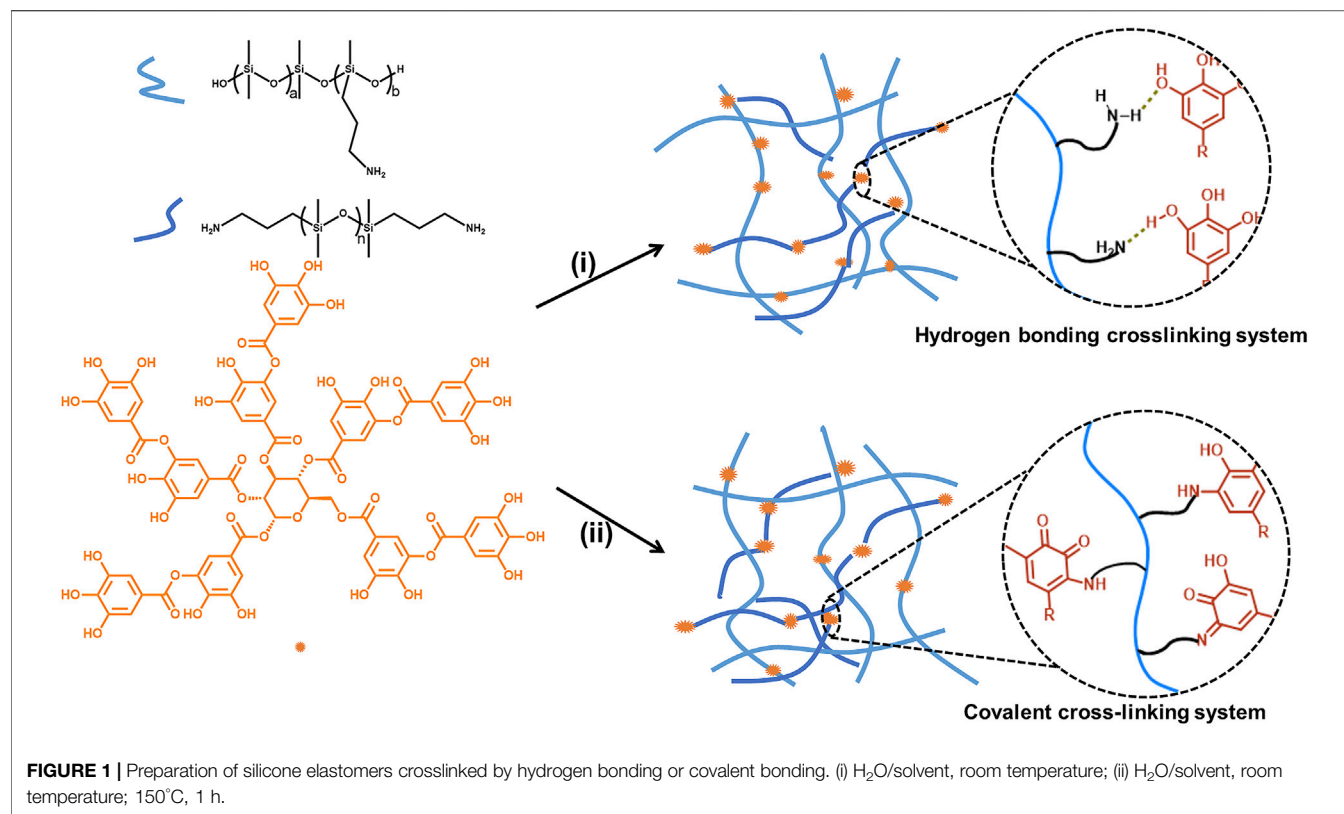
TABLE 1 | Data of hydrogen bond cross-linked silicone elastomers.

Entry	PAPMS (g)	DP-1 (g)	TA (mg)	Solvents/H_2O (ml)[a]	Sample description
Solvent Type					
H-1	P-2.5 (1.6)	0.6	30	TOL (15/0.2)	Formable
H-2	P-2.5 (1.6)	0.6	30	HEX (15/0.2)	Formable
H-3	P-2.5 (1.6)	0.6	30	THF (15/0.2)	TA aggregation
H-4	P-2.5 (1.6)	0.6	30	DCM (15/0.2)	×
H-5	P-2.5 (1.6)	0.6	30	TCM(15/0.2)	×
DP-1 dosage/-NH$_2$ molar content					
H-6	P-2.5 (1.6)	0	60	HEX (15/0.3)	Formable
H-7	P-2.5 (1.6)	0.6	60	HEX (15/0.3)	Formable
H-8	P-2.5 (1.6)	0.9	60	HEX (15/0.3)	×
H-9	P-5.8 (1.6)	0.6	60	HEX (15/0.3)	Formable
TA dosage					
H-10	P-2.5 (1.6)	0.6	8	HEX (15/0.2)	×
H-11	P-2.5 (1.6)	0.6	30	HEX (15/0.2)	Formable
H-12	P-2.5 (1.6)	0.6	50	HEX (15/0.3)	Formable
H-13	P-2.5 (1.6)	0.6	60	HEX (15/0.3)	Formable
H-14	P-2.5 (1.6)	0.6	90	HEX (15/0.4)	×
Molecular weight change (P-2.2: M_n = 1,63,305 g mol^{-1}, P-2.5: M_n = 64,000 g mol^{-1})					
H-15	P-2.2 (1.6)	0.6	50	HEX (20/0.3)	Formable
H-16	P-2.5 (1.6)	0.6	50	HEX (20/0.3)	Formable

[a]THF, tetrahydrofuran; DCM, dichloromethane; TCM, trichloromethane; HEX, n-hexane; TOL, toluene.

organic solution and TA aqueous solution were mixed evenly and poured into a Teflon mold. After 24 h, a transparent and dark yellow silicone elastomer was obtained. **Table 1** summarizes the variables for the synthesis of SEs (H-1 to H-16) crosslinked by hydrogen bond.

To improve the mechanical properties of the hydrogen bonding SEs, the reinforcing filler was added. Taking H-17 as an example, 0.22 g of fumed silica H2000 was added to DP-1 (0.6 g) and P-2.5 (1.6 g) in *n*-hexane solution, and then TA in aqueous solution (30 mg of TA in 0.2 ml of water) was added and

mixed with the organic solution. Finally, the mixture was poured into the Teflon mold and remained at room temperature. After 24 h, a transparent silicone elastomer was obtained. **Supplementary Table S2** summarizes the formulation data for hydrogen-bonding elastomers after the reinforcement.

Preparation of Silicone Elastomers Crosslinked by Covalent Bond

In a typical procedure, TA (30 mg) was dissolved in 0.3 ml of water, forming an aqueous solution of TA, while DP-1 (0.6 g) and P-5.8 (1.6 g) were dissolved in *n*-hexane. Then the TA solution and hexane solution were mixed evenly. The resulting mixture was poured into a Teflon mold. After evaporating the solvents at room temperature (~24 h), the resultant film was heated at 150°C for 1 h and a transparent and brown silicone elastomer was obtained. **Supplementary Table S1** summarizes the variables for the synthesis of SEs (C-1 to C-17) crosslinked by covalent bond.

The reinforcing filler was also added to improve the mechanical property. Taking C-18 as an example (Supplementary Table S2), fumed silica H2000 (0.22 g) was added into *n*-hexane solution containing (DP-1) (0.6 g) and P-2.5 (1.6 g). Then TA in aqueous solution was added to mixture and stirred rapidly for ca. 15–20 min. The resultant mixture was poured into a Teflon mold and remained at room temperature to remove the solvents (ca. 24 h), affording a film. The film was heated at 150°C for 1 h and the final silicone elastomer was obtained. **Supplementary Table S2** summarizes the formulation data for covalently bonding elastomers after the reinforcement.

Measurement of Crosslinking Density

The average molecular weight (M_c) between the crosslinking points is usually used to indicate the crosslinking density of silicone elastomers. It is generally measured using an equilibrium swelling method in toluene (Lu and Feng, 2017). The silicone elastomers were dried before measurement and weighed as mass m_1. Then the silicone elastomer was immersed in toluene at room temperature (ca. 3 days). The swollen gel was taken out from the liquid when the weight of the gel (m_2) kept constant (excess solvent was removed from the surface). The volume fraction Φ of the silicone elastomer dissolved in toluene was calculated by **Eq. 1**.

$$\Phi = \frac{\frac{m_1}{\rho_2}}{\frac{m_2 - m_1}{\rho_1} + \frac{m_1}{\rho_2}} \qquad (1)$$

m_1 and m_2 represent the masses of silicone elastomers before and after swollen in toluene, respectively. ρ_1 and ρ_2 represent the densities of toluene and silicone elastomers, respectively. M_c was calculated by Flory and French's **Eq. 2**. V_1 and χ represent the molar volume of toluene and the Flory-Huggins interaction parameter of polysiloxane and toluene (0.465).

$$M_c = -\frac{\rho_2 V_1 \Phi^{\frac{1}{3}}}{\ln(1 - \Phi) + \Phi + \chi \Phi^2} \qquad (2)$$
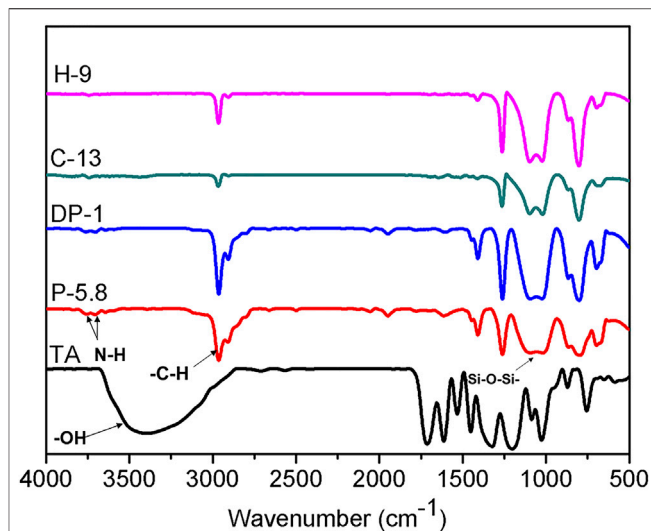
FIGURE 2 | FT-IR spectra of TA, P-5.8, DP-1, C-13, and H-9.

The crosslink density ν can be calculated by **Eq. 3**.

$$\nu = \frac{\rho_1}{M_c} \qquad (3)$$

Model Reaction of Catechol and *n*-decylamine

In a flask, catechol (0.5515 g, 5 mmol) and *n*-decylamine (1.5729 g, 10 mmol) were added and mixed. The mixture was heated at 150°C for 1 h under stirring. After the reaction finished, the product was afforded as a brown liquid.

Application as Adhesives for Bonding Iron Sheets

Taking B-3 as an example, TA (15 mg) and PAMPMS (0.4 g) was mixed in *n*-hexane (5 ml). The mixture was coated evenly on two 2 × 6 cm iron sheets and the bonding method is the lap joint. The application method and test method are performed in accordance with the national standard (GB 7124–2008). With the adhesive crosslinked by hydrogen bond, the bonded iron sheets were placed at room temperature to remove the solvent (24 h) before testing. With the adhesives crosslinked by covalent bond, the bonded iron sheets were heated at 150°C for 1 h before testing. **Supplementary Table S4** summarizes the formulation of adhesives.

RESULTS AND DISCUSSION

Synthesis and Characterization

Novel silicone elastomers were prepared using aminopropyl functionalized polysiloxanes as the base polymers and TA as the crosslinker at different conditions (**Figure 1**). At room

temperature, the silicone elastomers, H-1 to H-16, were crosslinked by hydrogen bond between amine groups from the polysiloxanes and phenolic groups from TA. After heating the hydrogen bonding elastomers at 150°C for 1 h, the silicone elastomers, C-1 to C-17, crosslinked by covalent bond were obtained.

The formed silicone elastomers were characterized by FT-IR technique. **Figure 2** shows the IR spectra of raw materials (P-5.8, DP-1 and TA) and elastomers (H-9 and C-13 as examples). The characteristic absorption of phenolic groups are observed at 3,450 cm^{-1} in TA, while the characteristic absorption peak of -N-H bond in amine groups from DP-1 and P-5.8 are observed at 3,700 cm^{-1} and 3,650 cm^{-1}. After crosslinking, these peaks nearly disappear in the elastomers (H-9 and C-13), thereby indicating that the interaction or a reaction between phenolic and amine groups occurred. In addition, the strong absorption peaks in the range of 1,022–1,094 cm^{-1} in P-5.8, DP-1, and C-13 are attributed to the characteristic Si-O-Si stretching vibration.

## Effect of Variables on the Properties of Hydrogen Bond Crosslinked SEs

As mentioned above, by virtue of the abundant phenolic groups in TA, it is expected to crosslink amino-functionalized polysiloxanes *via* the hydrogen bonding between phenolic hydroxyl and amine groups (**Figure 1**). To fabricate a high-value SE, it is indispensable to investigate the various effects on the formability and mechanical properties of the SEs. **Table 1** summarizes the variables that were examined to evaluate the formability of silicone elastomers based on hydrogen bonding.

The first factor is the processing technique. It is known that polysiloxanes containing low content of aminopropyl groups are insoluble in water, while TA is merely soluble in water. This feature makes TA difficult to be evenly dispersed in the polysiloxane system. Thus the crosslinking process was performed in a mixed solvent. In other word, the crosslinking proceeded by adding the aqueous solution of TA into the organic solution of aminopropyl polysiloxane. It is found that when the organic solvent was dichloromethane (H-4) or trichloromethane (H-5), the elastomers could not be formed. This finding can be explained by the phenomenon that dichloromethane and trichloromethane evaporate too quickly, resulting in the inability of tannic acid and PMPMS to form an effective contact. Although the crosslinking can occur in tetrahydrofuran (H-3), TA aggregated in the formed film. It is delighted that the SEs can be well-formable when using toluene (H-1) or *n*-hexane (H-2) as the solvent. Considering the toxicity of toluene, *n*-hexane was chosen as the organic solvent for the preparation of SEs. In addition, we found that if the solvent is insufficient, the formation of hydrogen bond in the system led to an increase of the viscosity, which made the elastomers be formed with some defects, *i.e.*, some bubbles in the elastomers. Thus, more solvent is required during the crosslinking process to reduce the viscosity of the system. It was found that the suitable volumes of solvent and water are 15 and 0.2 ml while the selected parameters include 1.6 g of P-2.5, 0.6 g of DP-1, and 30 mg of TA.

It is known that the addition of a base polymer with terminated functional group can enhance the break elongation of elastomers. Thus, amino-terminated polysiloxane DP-1 was added to study this effect. When the elastomer was cross-linked by hydrogen bond, we added no DP-1 in H-6 and 0.6 g of DP-1 in H-7. It was found that the tensile strength of the SEs decreased from 1,023 kPa (H-6) to 580 kPa (H-7) (**Figure 3A**). However, the elongation at break increased from 26% (H-6) to 66% (H-7). This phenomenon suggests that the addition of DP-1 can slightly increase the elongation at break of the elastomers. However, the Young's modulus and cross-link density decreased in a certain. This finding may be attributed to the low reactivity of DP-1, which can hinder the crosslinking.

The mechanical properties of hydrogen bond cross-linked elastomers are also affected by the -NH$_2$ content in PAPMS. As shown in **Figure 3A**, when the molar content of -NH$_2$ in PAPMS was increased from 2.5% (H-7) to 5.8% (H-9), the tensile strength increased from 580 kPa (H-7) to 632 kPa (H-9), but the elongation at break decreased from 66% (H-7) to 32% (H-9). This finding is apparently due to the enhancement of crosslinking density (0.16–0.32 mol/L) and Young's modulus (1.4–2.5 MPa), which was led by the increased -NH$_2$ contents (**Table 2**). The amount of the crosslinker TA undoubtedly influences the mechanical properties of SEs. As expected, too many or too few amounts of TA is detrimental to the formation of elastomers. For example, if the amount of TA is 8 mg (H-10), the elastomer cannot be formed due to too few crosslinking sites (The other parameters include 1.6 g of P-2.5, 0.6 g of DP-1, and 15/0.2 ml of hexane/water). When the amount of TA is too high, such as 90 mg (H-14), the cross-linking rate is too fast, resulting in significant defects in the elastomer. It was found that the TA dosages from 30 to 60 mg are suitable and the elastomers (H-11, H-12, and H-13) were obtained with good formability. As shown in **Figure 3B**, with an increment of TA dosages, the tensile strength was enhanced from 283 kPa (H-11) to 580 kPa (H-13), and the elongation at break and Young's modulus also increased from 38% (H-11) to 66% (H-13) and from 1.0 MPa (H-11) to 1.4 MPa (H-13), respectively (**Table 2**). This finding indicates an increase in the material's ability to resist deformation with increasing the amount of TA. In addition, the colors of the resultant elastomers turned from pale yellow to brownish-yellow (H-11 and H-13 in **Figure 3D**).

The molecular weights of PAPMS can also determine the properties of the elastomers. Two PAPMS with M$_n$ of 163,305 g mol^{-1} (P-2.2) and 64,000 g mol^{-1} (P-2.5) acted as the base polymers when the other parameters include 0.6 g of DP-1 and 20/0.4 ml of hexane/water (*Note*: it is difficult to precisely control the molecular weight and the–NH$_2$ content of the PAPMS). Due to the large molecular weight of P-2.2, 50 mg of tannic acid was added at room temperature for effective crosslinking. The results reveal that PAPMS with higher molecular weight can give the elastomers with higher elongation at break (**Figure 3C**), but lower tensile strength (H-15 and H-16). This result can be explained by the different crosslinking density. Although a higher molecular weight can lead to a better ductility of the cross-linked network, but higher molecular weight of PAPMS at the same mass means a lower
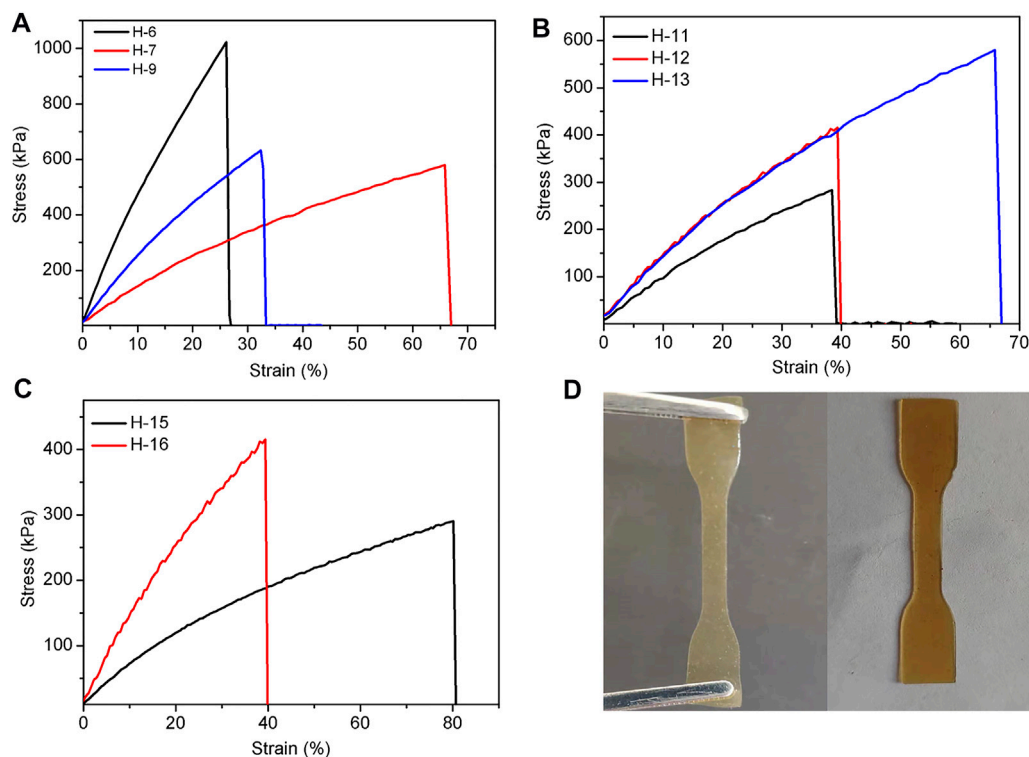
FIGURE 3 | (A–C) Tensile curves of hydrogen bond cross-linked silicone elastomers affected by amino content of PAPMS and the usage of DP-1 **(A)**, TA dosage **(B)**, and molecular weight of PAPMS **(C)**; **(D)** The images of H-11 **(left)** and H-13 **(right)**.

TABLE 2 | Mechanical properties of hydrogen bond cross-linked SEs.

Entry	Tensile strength (kPa)	Elongation at break (%)	Hardness (shore A)	Young's modulus (MPa)	Crosslink density (mol/L)
H-6	1,023	26	34.0	5.1	0.25
H-7	580	66	33.1	1.4	0.16
H-9	632	32	31.0	2.5	0.32
H-11	283	38	24.0	1.0	0.16
H-12	415	39	31.8	1.4	0.16
H-13	580	66	33.1	1.4	0.16
H-15	290	80	30.5	0.6	0.14
H-16	415	39	31.8	1.4	0.16

amount of amino groups, that is, fewer crosslinking sites, thereby leading to a lower degree of cross-linking density. This result was also evidenced by the Young's modulus (**Table 2**).

Effect of Variables on the Properties of Covalent Bond Crosslinked Silicone Elastomers

As mentioned above, the covalently crosslinked SEs can be readily prepared by heating the hydrogen bonding SEs at 150°C. The effect of various factors on the formability and mechanical properties of elastomers were also investigated and were summarized in **Supplementary Table S1** and

Table 3. The first variable is the heating time. When the selected parameters include 1.6 g of P-4.8, 0.6 g of DP-1, 30 mg of TA, and 15/0.2 ml of hexane/water, with an increment of heating time from 1 to 3 h, the tensile strength of the elastomer increased from 458 kPa (C-1) to 614 kPa (C-3), and the elongation at break increased from 36% (C-1) to 43% (C-3) (**Figure 4A**). This phenomenon suggests that the mechanical properties of elastomers can be enhanced by prolonging the heating time. Meanwhile, Young's modulus increased from 1.6 to 1.9 MPa and crosslink density increased from 0.22 to 0.44 mol/L (**Table 3**). However, as the heating time continued to increase to 4 h, a decrease of the mechanical property of the elastomer (C-4) was found. This

TABLE 3 | Mechanical properties of covalent cross-linked silicone elastomers.

Entry	Tensile strength (kPa)	Elongation at break (%)	Hardness (shore A)	Young's modulus (MPa)	Crosslink density (mol/L)
C-1	458	36	26.4	1.6	0.22
C-2	489	41	22.0	1.6	0.36
C-3	614	43	22.4	1.9	0.44
C-4	336	21	×	1.7	0.32
C-5	468	30	31.8	1.9	0.42
C-7	579	58	47.4	1.4	0.15
C-8	700	42	30.0	2.2	0.47
C-9	528	15	20.2	3.8	0.68
C-11	425	54	25.4	1.1	0.28
C-12	503	72	27.7	1.0	0.35
C-13	700	42	30.0	2.2	0.47
C-14	848	42	38.3	2.6	0.80
C-16	249	27	28.3	1.1	0.15
C-17	199	67	×	0.4	0.12

× means the sample is not available for the test.
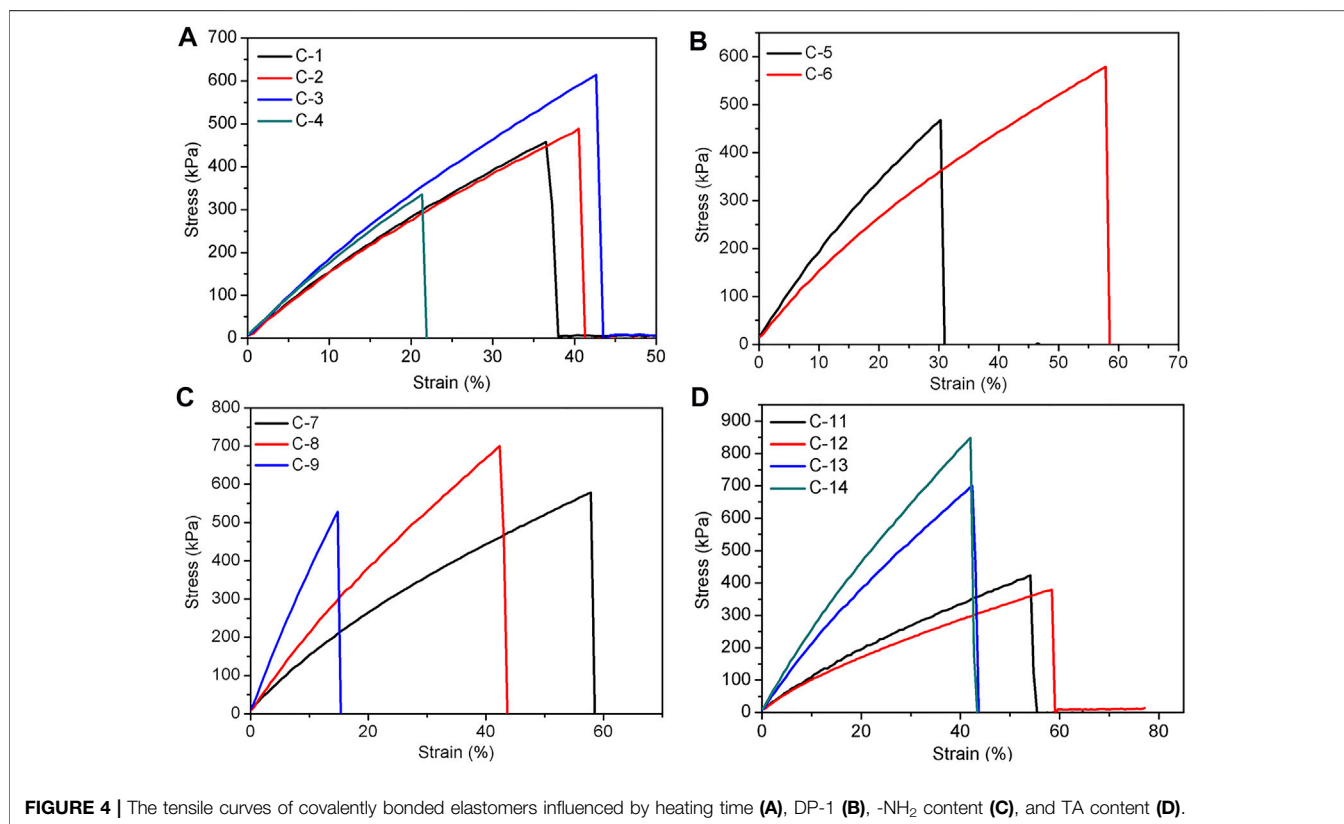
FIGURE 4 | The tensile curves of covalently bonded elastomers influenced by heating time (A), DP-1 (B), -NH$_2$ content (C), and TA content (D).

finding may be due to the fact that excessive cross-linking occurs within the networks due to prolonged heating.

Amino-terminated polysiloxane DP-1 was used as a chain extender for the cross-linking of elastomers. The results showed that the elastomer (C-5) had a tensile strength of 468 kPa and an elongation at break of 30% without the addition of DP-1 (**Figure 4B**). When 0.6 g of DP-1 was added, the tensile strength of the elastomer (C-7) was 579 kPa and the elongation at break was 58% (**Figure 3C**). It can be seen that

the addition of DP-1 can improve the mechanical properties of the elastomers. At the same time, excessive DP-1 is not conducive to the formation of cross-linked networks, and this phenomenon is similar to that of hydrogen bonding system. The Young's modulus and crosslink density of the elastomer underwent a decrease due to the addition of DP-1 (**Table 3**). In addition, the effect of -NH$_2$ content in PAPMS is similar to that of hydrogen bond cross-linked system (**Figure 4C**). As the -NH$_2$ content increases from 2.5 to 5.8 mol%, the tensile strength increases from
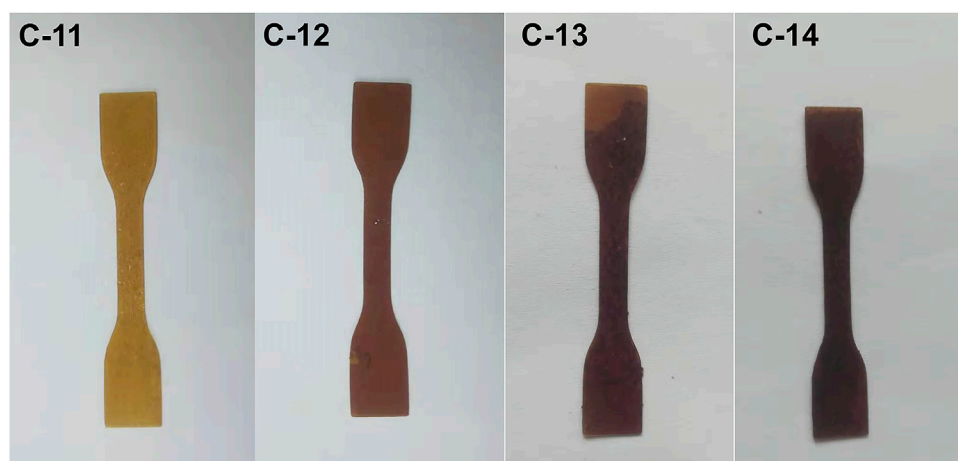
FIGURE 5 | Images of covalent bond crosslinked elastomers by altering the dosage of TA.

579 kPa (C-7) to 700 kPa (C-8) and the elongation at break largely decreases from 58% (C-7) to 42% (C-8) (**Figure 4C**) (**Table 3**). This finding can be explained as follows. As the amino content of PAPMS increases, the cross-linking degree of the elastomers increases and their mechanical properties are improved. This explanation can be also evidenced by the Young's modulus and crosslink density (**Table 3**). However, as the amino content continues to increase, the elastomer (C-9) becomes excessively cross-linked and thus leads to a decrease in tensile strength and elongation at break.

Based on the abovementioned results, the elastomers with the best elastomeric properties were prepared from P-5.8. Thus it was utilized as the base polymer to study the effect of TA dosage on the elastomer properties. As expected, if the amount of TA is too low (e.g., 8 mg for C-10 when the other parameters include 1.6 g of P-5.8, 0.6 g of DP-1, and 15/0.2 ml of hexane/water), the elastomer can not be formed due to the low crosslinking density. If the amount of TA is too high (e.g., 120 mg for C-15), the elastomer can be formed, but appeared as a film with apparent defect on the bottom because of too fast crosslinking rate. It was found that suitable amounts of TA are in the range of 10–90 mg. With an increment of TA dosage, the tensile strength increases from 425 kPa (C-11) to 848 kPa (C-14), while the elongation at break of the elastomers slightly decreases from 54% (C-11) to 42% (C-14) (**Figure 4D**). This finding is apparently due to the improved crosslinking density from 0.28 mol/L (C-11) to 0.80 mol/L (C-14) and Young's modulus increased from 1.1 MPa (C-11) to 2.6 MPa (C-14) as increasing the TA dosage (**Table 3**). This result indicates that the increase of TA dosage can improve the mechanical properties of the elastomers. Meanwhile, the hardness also increased from 25.4 Shore A (C-11) to 38.4 Shore A (C-14) (**Table 3**). It can be seen that in the covalent bonding cross-linking system, the increase of TA dosage can increase the hardness of the elastomers and has a reinforcing effect (Zhang et al., 2015). In addition, the increment of TA dosage makes the colors of products darken from deep yellow to nearly black (**Figure 5**).

The effect of molecular weight of PAPMS on the mechanical properties of silicone elastomers is similar to that found in hydrogen bond crosslinked SEs. P-2.2 (M_n = 163,305) and P-2.5 (M_n = 64,000) were chosen as the base polymers to investigate the effect of molecular weight (other parameter include 0.6 g of DP-1, 30 mg of TA, and 15/0.3 ml of hexane/water). As shown in **Supplementary Figure S1**, the elongation at break of the elastomers decreases from 249 kPa (C-16) to 199 kPa (C-17) with increasing the molecular weight, and the elongation at break increases from 27% (C-16) to 67.4% (C-17). Meanwhile, Young's modulus and crosslinking density decrease to some degree (**Table 3**). This result can be explained by the fact that higher molecular weight of the base polymer means less crosslinking sites and thus the crosslinking degree is low, but the elongation at break of the elastomer can increase.

The Performance Enhancement of SEs by Adding Reinforcing Fillers

Based on the abovementioned results, the mechanical properties of these elastomers crosslinked either by hydrogen bond or by covalent bond are not satisfied. To improve elastomer properties, the reinforcing filler was added and the fumed silica H2000 was used as an example. The formability and mechanical data of the resultant SEs are summarized in **Supplementary Tables S2, S3**. As expected, the mechanical properties of the elastomers, H-17 to H-20, were gradually improved as the amount of H2000 increased. In the hydrogen bond crosslinked system, the maximum tensile strength is 1.9 MPa (H-20), while the elongation at break of this elastomer is 111% (**Figure 6A**, the parameters include 1.6 g of P-2.5, 0.6 g of DP-1, and 15/0.2 ml of hexane/water). When the amount of H2000 continues to increase, the mechanical properties of the elastomer (H-21) will decline because too much H2000 hinders the formation of the cross-linked network. These hydrogen bond cross-linked elastomers (H-17 to H-20) were further heated at 150°C for 1 h to yield covalently cross-linked elastomers, C-18 to C-21. As shown in **Figure 6B**, the tensile strength was further increased to 3.0 MPa at a dosage of 0.88 g of H2000 (C-21). Compared to the analogous hydrogen bond crosslinked elastomer H-20, the tensile strength
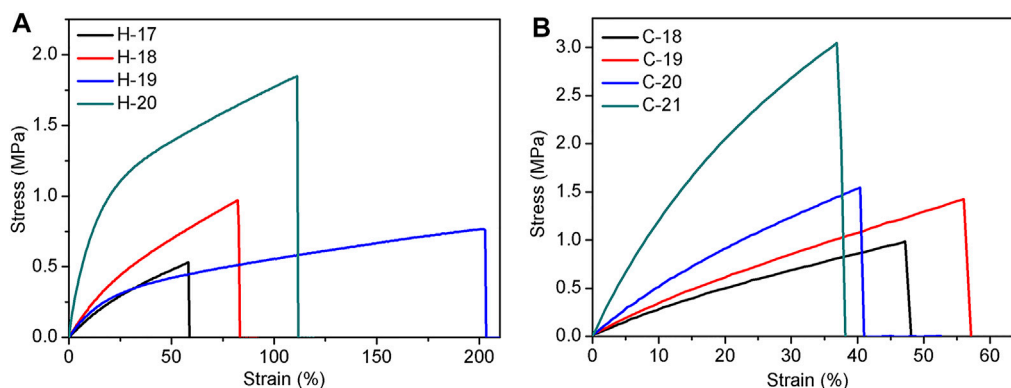
FIGURE 6 | The tensile curves of hydrogen bond cross-linked silicone elastomers, H-17 to H-20 **(A)** and covalent bond crosslinked silicone elastomers, C-18 to C-21 **(B)**, after adding the reinforcing filler.
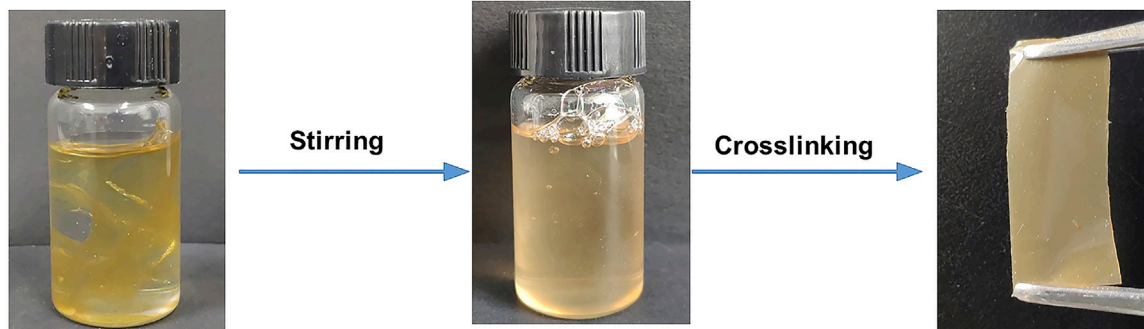
FIGURE 7 | The reversible film formation by hydrogen bonding crosslinking.

was increased by 50%. This finding can be explained by the increased cross-linking density (e.g., 0.45 mol/L for H-20 to 1.23 mol/L for C-21) after the transformation from hydrogen bond crosslinking to covalent crosslinking. In addition, the Young's modulus increased with the amount of H2000 in both the hydrogen bonding and covalent bonding cross-linking systems. In other word, the crosslinking density of the elastomer formed by the covalent system is greater than that of the elastomer formed by the hydrogen bonding system under the same formulation (**Supplementary Table S3**).

Cross-Linking Mechanism

The hydrogen bond crosslinking mechanism was investigated by immersing the elastomers in tetrahydrofuran (THF), which can serve as a hydrogen bond acceptor and thus interrupt the hydrogen bond crosslinking. It was found that the elastomers can be gradually soluble in THF under stirring and re-formed after removing the solvent (**Figure 7**). This reversible crosslinking feature accords with the characteristic of hydrogen bond, indicating the networks are formed by hydrogen bond crosslinking.

The cross-linking mechanism by covalent bond between TA and PAPMS was investigated by a model reaction between catechol and *n*-decylamine (**Supplementary Figure S2**). The reaction condition

was 1 h at 150°C, resulting in the products MC. The products were characterized by FT-IR, ^{1}H NMR and high resolution mass spectrometry. In FT-IR spectrum of catechol and the products, the broad characteristic peaks of–OH from catechol was observed at 3,500 cm^{-1} and 3,300 cm^{-1} and disappeared in MC (**Figure 8A**). This finding indicates the successful occurrence of some reactions, for example, hydroxylamine reaction, between catechol and *n*-decylamine. The ^{1}H NMR spectra also proves this result (**Figure 8B**). The proton peak from the phenolic hydroxyl group in catechol was observed at 8.8 ppm, while this peak disappeared in the product MC, indicating the reaction of the phenolic hydroxyl group. In addition, the protons from the benzene rings shift from 6.72 to 6.61 ppm in catechol to around 6.68–6.57 ppm in MC, further indicating that phenol was not fully oxidized and the hydroxylamine reaction occurred. The HR-MS results can prove the structure of the products. As shown in **Supplementary Figure S3**, the found weights of 250.2112, 406.3686, and 558.5202 g/mol are associated with the products by the hydroxylamine reaction of amino and–OH groups in TA and Michael addition reaction of amine and the quinone groups after the oxidation of TA, respectively, consistent with previous results (Liang et al., 2016). In addition, by comparing the ^{1}H NMR of the mixture of catechol and *n*-decylamine before the reaction and MC, ca. 70% of catechol
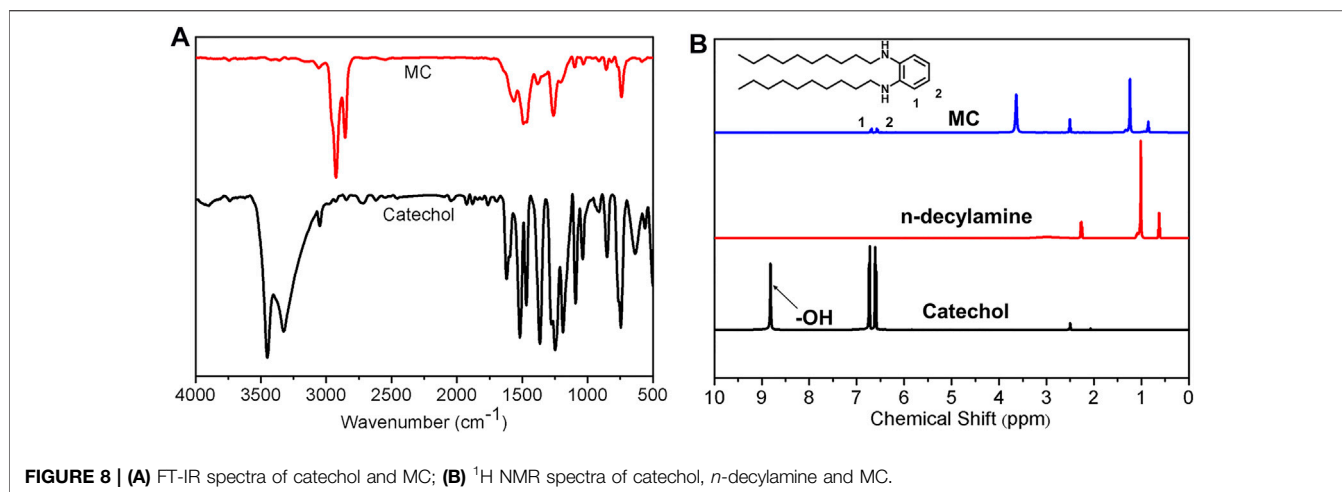
FIGURE 8 | (A) FT-IR spectra of catechol and MC; **(B)** ^{1}H NMR spectra of catechol, *n*-decylamine and MC.
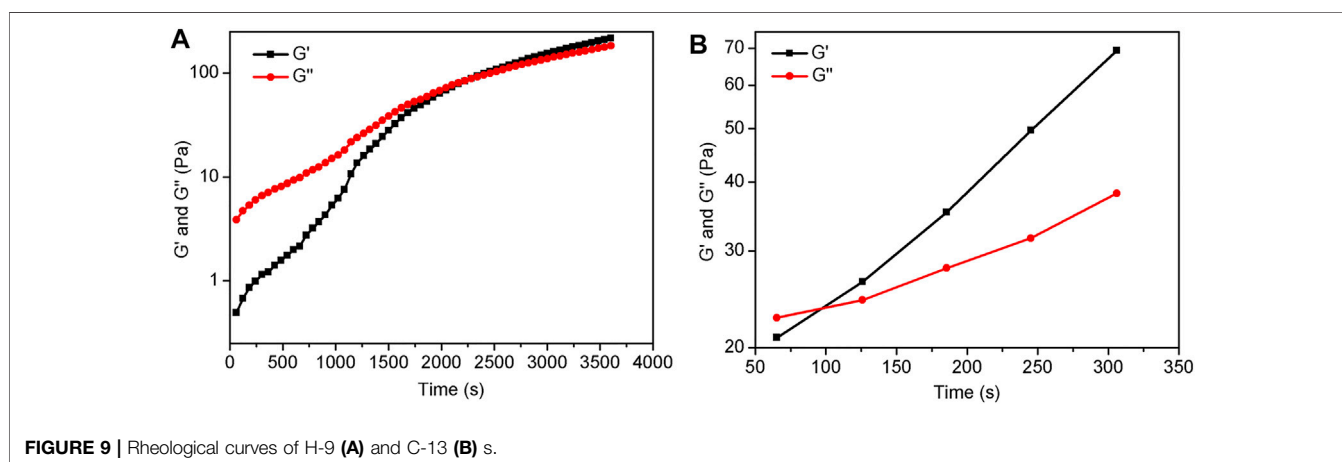
FIGURE 9 | Rheological curves of H-9 **(A)** and C-13 **(B)** s.

underwent a hydroxylamine reaction and the rest proceeded by the oxidation reaction of phenolic group and subsequent Michael addition reaction, which was calculated on the basis of integration ratio of the alkyl protons from *n*-decylamine and the phenyl protons from catechol (**Supplementary Figure S4**). These results reveal that the covalent crosslinking of SEs is determined by the combined contribution of the hydroxylamine reaction and Michael addition reaction, while the former is the main contributor.

Elastomer Curing Time Analysis

To investigate the specific crosslinking time between TA and aminopropyl polysiloxane, the rheometer was used to analyze the curing time of these two cross-linked systems. The hydrogen bond crosslinking system was studied using H-9 as an example. A representative parameters include P-5.8 (1.6 g), DP-1 (0.6 g), TA (60 mg), and *n*-hexane/water (15/0.3 ml). **Figure 9A** shows the curves of loss modulus (G″) and energy storage modulus (G′) of the hydrogen bond crosslinking system with curing time. It was found that G″ is larger than G′ before 37 min, indicating that the system did not cure. The intersection point of G″ and G′ is the gel-solution transition point. As the time increases, G′ becomes larger and the system becomes a gel. The curing behavior of

covalent bond cross-linking system was investigated using C-13 as an example, which was tested at 150°C. It was found that the G″ and G′ crossover point is about 90 s (**Figure 9B**). The difference in time between these two crosslinking systems is clearly related to the reaction conditions. The hydrogen bonding crosslinking and the covalent bonding crosslinking occurs at room temperature and at 150°C, respectively. Obviously, higher temperature resulted in higher reactivity, and thus in faster curing time.

Micromorphology and Hydrophobic Properties of Silicone Elastomers

The micromorphology of these SEs were observed by SEM technique. H-9 and C-13 were selected as examples. It was found that they display uniform surface morphology (**Figures 10A,B**), confirming that the hydrogen bond crosslinking and covalent bond crosslinking have occurred and the system is not a simple physical mixture. The hydrophobic properties of these elastomers were estimated by measuring the static contact angles. As shown in **Figure 10C**, these elastomers exhibit similar hydrophobicity compared to traditional SEs. The maximum contact angle of hydrogen bond crosslinked SEs is about 118°
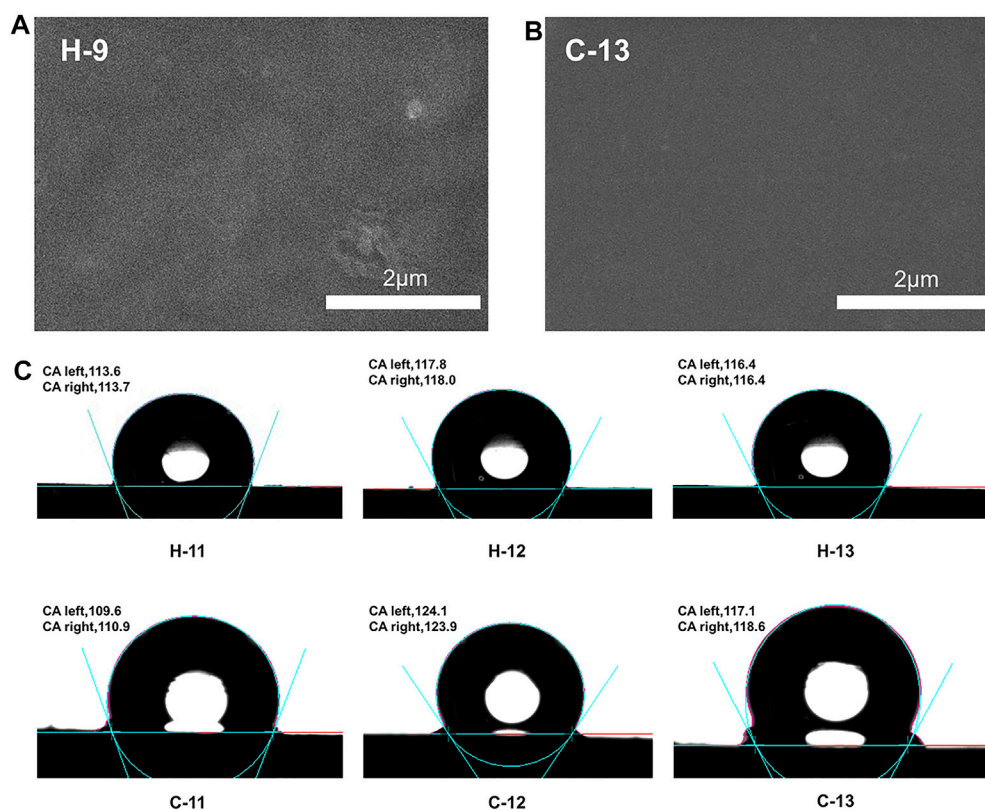
FIGURE 10 | **(A)** SEM image of H-9; **(B)** SEM image of C-13; **(C)** the contact angles of silicone elastomers, H-11 to H-13 and C-11 to C-13.
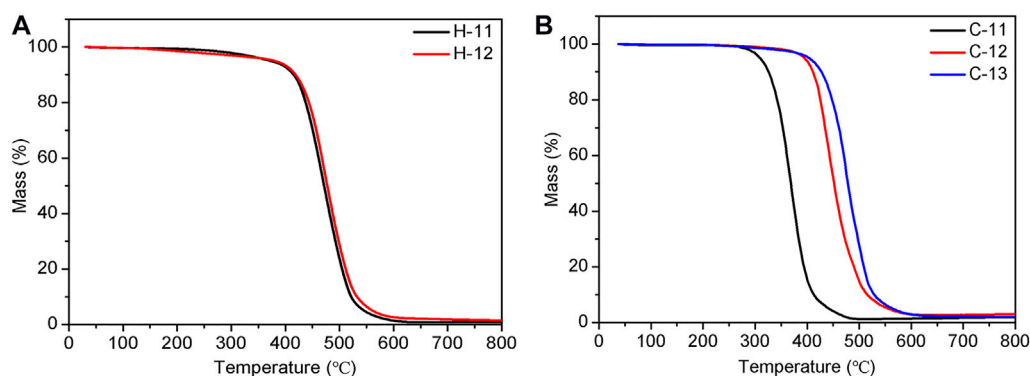
FIGURE 11 | TGA curves of hydrogen bond crosslinked SEs, H-11 and H-12 **(A)**, and covalent bond crosslinked SEs, C-11 to C-13 **(B)**.

(H-11 to H-13 as examples), while that of covalent bond crosslinked SEs is about 124° (C-11 to C-13 as examples). These results indicate the good hydrophobicity of these elastomers.

Thermal Stability

The thermal stability of these elastomers was also investigated by thermogravimetric analysis (TGA) because the decomposition temperature influences their applications. The experiments were conducted at a heating rate of 10 K/min under the atmosphere of

nitrogen. **Figure 11** depicts the TGA curves of two types of crosslinked SEs (H-11, H-12, and C-11 to C-13 as examples). The results reveal that the TA dosage for the hydrogen bond crosslinked does not have a significant effect on thermal stability and the SEs exhibit a high thermal stability with the $T_{d, 5\%}$ (5% weight loss temperature) at 372.5°C (**Figure 11A**). This finding can be explained by the reversible feature of hydrogen bonding, while the thermal stability is mainly contributed by the polysiloxane chains. In comparison, the increment of TA dosage
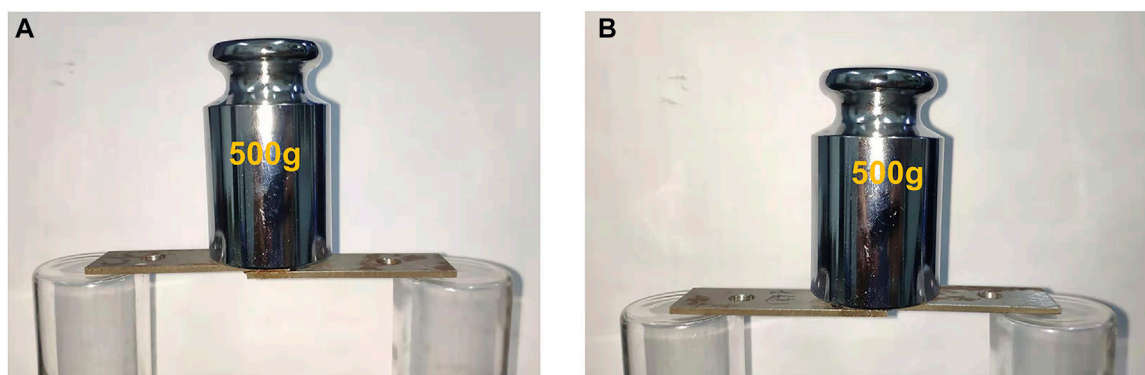
FIGURE 12 | Images of adhesive performance test bonding by hydrogen bonding SEs **(A)** and covalent bonding SEs **(B)**.

leads to a higher thermal stability for the covalent bond crosslinked SEs with the $T_{d,\ 5\%}$ from 308.6°C (C-11) to 401.8°C (C-13) (**Figure 11B**). This finding could be attributed to improved crosslinked density with an increment of TA dosage.

Application as Adhesives

To explore the potential applications of these materials, the elastomers were used as adhesives. The adhesive property was conducted by bonding two iron sheet together with a lap joint. The formulations for bonding are summarized in **Supplementary Table S4**. The results revealed that the prepared specimens are fully capable of carrying 500 g of weight for both hydrogen bond crosslinking and covalent bond crosslinking (**Figure 12**). In addition, the effect of amino content on the adhesive property was also investigated. It was found that the shear strength of both hydrogen bond crosslinking and covalent bond crosslinking increase with an increment of amino content, and the highest shear strength is 0.40 MPa (**Supplementary Table S5**).

CONCLUSION

Novel silicone elastomers have been prepared using amino-containing polysiloxanes as the base polymers and tannic acid as a natural crosslinker under a catalyst-free method. By altering the reaction conditions, the silicone elastomers have been successfully crosslinked by hydrogen bond and covalent bond. The formability and mechanical properties of these silicone elastomers can be tuned by processing technique, the amount of TA and aminopropyl-terminated polydimethylsiloxane, the molecular weight and -NH$_2$ content of PAPMS, and the amount of reinforcing filler. The hydrogen bonding mechanism can be proved by the reversible crosslinking feature of the elastomers, which can be gradually dissolved in THF and re-formed after removing THF. The covalent bond crosslinking contains the simultaneous occurrence of hydroxylamine reaction and Michael addition reaction, evidenced by a model reaction of catechol and *n*-decylamine. These elastomers exhibit good thermal stability and excellent hydrophobic property and can be applied as adhesives for bonding iron sheets to hold the weight of 500 g. To our best of knowledge, this report provides the

first example of silicone elastomers crosslinked by tannic acid under a catalyst-free method. In contrast to conventional silicone crosslinking technologies, the present strategy does not require any catalyst and the crosslinker is from nature, which can meet the requirement of green chemistry. By virtue of large database and low-cost of natural polyphenols, more organic elastomers and other crosslinked materials can be readily prepared by selecting amine-containing polymers and using the present tannic acid and other polyphenols as natural crosslinkers and thus their extensive applications could be promisingly explored.

DATA AVAILABILITY STATEMENT

The original contributions presented in the study are included in the article/**Supplementary Material**, further inquiries can be directed to the corresponding author.

AUTHOR CONTRIBUTIONS

SK and DW conceived the idea, designed the experiments, analyzed data, managed the project and drafted the manuscript. SK and RW supplemented the experimental data. SK, SF, and DW discussed the results and reviewed the manuscript.

FUNDING

SUPPLEMENTARY MATERIAL

The Supplementary Material for this article can be found online at: https://www.frontiersin.org/articles/10.3389/fchem.2021.778896/full#supplementary-material

REFERENCES

Bui, R., and Brook, M. A. (2020). Catalyst Free Silicone Sealants that Cure Underwater. *Adv. Funct. Mater.* 30, 2000737. doi:10.1002/adfm.202000737

Eduok, U., Faye, O., and Szpunar, J. (2017). Recent Developments and Applications of Protective Silicone Coatings: A Review of PDMS Functional Materials. *Prog. Org. Coat.* 111, 124–163. doi:10.1016/j.porgcoat.2017.05.012

Fan, H., Wang, J., and Jin, Z. (2018). Tough, Swelling-Resistant, Self-Healing, and Adhesive Dual-Cross-Linked Hydrogels Based on Polymer-Tannic Acid Multiple Hydrogen Bonds. *Macromolecules* 51, 1696–1705. doi:10.1021/acs.macromol.7b02653

Feng, L., Zhou, L., and Feng, S. (2016). Preparation and Characterization of Silicone Rubber Cured via Catalyst-free Aza-Michael Reaction. *RSC Adv.* 6, 111648–111656. doi:10.1039/C6RA23016D

Jiménez, N., Ballard, N., and Asua, J. M. (2019). Hydrogen Bond-Directed Formation of Stiff Polymer Films Using Naturally Occurring Polyphenols. *Macromolecules* 52, 9724–9734. doi:10.1021/acs.macromol.9b01694

López, C. M., and Pich, A. (2018). Supramolecular Stimuli-Responsive Microgels Crosslinked by Tannic Acid. *Macromol. Rapid Commun.* 39, 1700808. doi:10.1002/marc.201700808

Lai, J.-C., Li, L., Wang, D.-P., Zhang, M.-H., Mo, S.-R., Wang, X., et al. (2018). A Rigid and Healable Polymer Cross-Linked by Weak but Abundant Zn(II)-carboxylate Interactions. *Nat. Commun.* 9, 2725. doi:10.1038/s41467-018-05285-3

Lai, J.-C., Mei, J.-F., Jia, X.-Y., Li, C.-H., You, X.-Z., and Bao, Z. (2016). A Stiff and Healable Polymer Based on Dynamic-Covalent Boroxine Bonds. *Adv. Mater.* 28, 8277–8282. doi:10.1002/adma.201602332

Liang, H., Yao, Z., Ge, W., Qiao, Y., Zhang, L., Cao, Z., et al. (2016). Selective and Sensitive Detection of Picric Acid Based on a Water-Soluble Fluorescent Probe. *RSC Adv.* 6, 38328–38331. doi:10.1039/c6ra04080b

Liu, J., Yao, Y., Li, X., and Zhang, Z. (2021). Fabrication of Advanced Polydimethylsiloxane-Based Functional Materials: Bulk Modifications and Surface Functionalizations. *Chem. Eng. J.* 408, 127262. doi:10.1016/j.cej.2020.127262

Lu, H., and Feng, S. (2017). Supramolecular Silicone Elastomers with Healable and Hydrophobic Properties Crosslinked by "Salt-Forming Vulcanization". *J. Polym. Sci. Part A: Polym. Chem.* 55, 903–911. doi:10.1002/pola.28450

Niu, W., Zhu, Y., Wang, R., Lu, Z., Liu, X., and Sun, J. (2020). Remalleable, Healable, and Highly Sustainable Supramolecular Polymeric Materials Combining Superhigh Strength and Ultrahigh Toughness. *ACS Appl. Mater. Inter.* 12, 30805–30814. doi:10.1021/acsami.0c06995

Picard, L., Phalip, P., Fleury, E., and Ganachaud, F. (2015). Chemical Adhesion of Silicone Elastomers on Primed Metal Surfaces: A Comprehensive Survey of Open and Patent Literatures. *Prog. Org. Coat.* 80, 120–141. doi:10.1016/j.porgcoat.2014.11.022

Rambarran, T., Gonzaga, F., and Brook, M. A. (2012). Generic, Metal-free Cross-Linking and Modification of Silicone Elastomers Using Click Ligation. *Macromolecules* 45, 2276–2285. doi:10.1021/ma202785x

Rao, Y.-L., Chortos, A., Pfattner, R., Lissel, F., Chiu, Y.-C., Feig, V., et al. (2016). Stretchable Self-Healing Polymeric Dielectrics Cross-Linked through Metal-Ligand Coordination. *J. Am. Chem. Soc.* 138, 6020–6027. doi:10.1021/jacs.6b02428

Rücker, C., and Kümmerer, K. (2015). Environmental Chemistry of Organosiloxanes. *Chem. Rev.* 115, 466–524. doi:10.1021/cr500319v

Rus, D., and Tolley, M. T. (2015). Design, Fabrication and Control of Soft Robots. *Nature* 521, 467–475. doi:10.1038/nature14543

Troegel, D., and Stohrer, J. (2011). Recent Advances and Actual Challenges in Late Transition Metal Catalyzed Hydrosilylation of Olefins from an Industrial point of View. *Coord. Chem. Rev.* 255, 1440–1459. doi:10.1016/j.ccr.2010.12.025

Wang, D., Klein, J., and Mejía, E. (2017). Catalytic Systems for the Cross-Linking of Organosilicon Polymers. *Chem. Asian J.* 12, 1180–1197. doi:10.1002/asia.201700304

Wu, J., Wang, Z., Yan, W., Wang, Y., Wang, J., and Wang, S. (2015). Improving the Hydrophilicity and Fouling Resistance of RO Membranes by Surface Immobilization of PVP Based on a Metal-Polyphenol Precursor Layer. *J. Membr. Sci.* 496, 58–69. doi:10.1016/j.memsci.2015.08.044

Xu, L. Q., Neoh, K.-G., and Kang, E.-T. (2018a). Natural Polyphenols as Versatile Platforms for Material Engineering and Surface Functionalization. *Prog. Polym. Sci.* 87, 165–196. doi:10.1016/j.progpolymsci.2018.08.005

Xu, R., Ma, S., Lin, P., Yu, B., Zhou, F., and Liu, W. (2018b). High Strength Astringent Hydrogels Using Protein as the Building Block for Physically Cross-Linked Multi-Network. *ACS Appl. Mater. Inter.* 10, 7593–7601. doi:10.1021/acsami.7b04290

Yang, Z., Li, H., Zhang, L., Lai, X., and Zeng, X. (2020). Highly Stretchable, Transparent and Room-Temperature Self-Healable Polydimethylsiloxane Elastomer for Bending Sensor. *J. Colloid Interf. Sci.* 570, 1–10. doi:10.1016/j.jcis.2020.02.107

Yilgör, E., and Yilgör, I. (2014). Silicone Containing Copolymers: Synthesis, Properties and Applications. *Prog. Polym. Sci.* 39, 1165–1195. doi:10.1016/j.progpolymsci.2013.11.003

Zhang, J., Chen, Y., Sewell, P., and Brook, M. A. (2015). Utilization of Softwood Lignin as Both Crosslinker and Reinforcing Agent in Silicone Elastomers. *Green. Chem.* 17, 1811–1819. doi:10.1039/C4GC02409E

A Novel Calix[4]Crown-Based 1,3,4-Oxadiazole as a Fluorescent Chemosensor for Copper(II) Ion Detection

Chun Sun, Siyi Du, Tianze Zhang and Jie Han *

Key Laboratory of Advanced Energy Materials Chemistry (Ministry of Energy), College of Chemistry, Nankai University, Tianjin, China

The synthesis and characterization of a novel florescent chemosensor **1** with two different types of cationic binding sites have been reported in this work, which is a calix[4]crown derivative in 1,3-alternate conformation bearing two 2-phenyl-5-(4-dimethylaminopyenyl)-1,3,4-oxadiazole units. The recognition behaviors of **1** in dichloromethane/acetonitrile solution to alkali metal ions (Na^+ and K^+), alkaline earth metal ions (Mg^{2+} and Ca^{2+}), and transition metal ions (Co^{2+}, Ni^{2+}, Zn^{2+}, Cd^{2+}, Cu^{2+}, Mn^{2+}, and Ag^+) have been investigated by UV-Vis and fluorescence spectra. The fluorescence of **1** might be quenched selectively by Cu^{2+} due to the photo-induced electron transfer mechanism, and the quenched emission from **1** could be partly revived by the addition of Ca^{2+} or Mg^{2+}; thus, the receptor **1** might be worked as an on–off switchable fluorescent chemosensor triggered by metal ion exchange.

Keywords: calix[4]crown, 1,3-alternate conformation, 1,3,4-oxadiazole, copper (II) detection, fluorescent chemosensor

INTRODUCTION

As the third most abundant transition metal ion after zinc and iron in the human body, copper is required by many living organisms for normal physiological processes (Turski and Thiele, 2009; Cotruvo Jr et al., 2015). Maintaining optimal concentration of Cu^{2+} ion for living cells is an essential factor to keep the normal functioning of enzymes and intracellular metabolic balance. Thus, the development of new fluorescent chemosensors for Cu^{2+} ion has drawn continuous interest during the past decades. The main progress in this area has been well reviewed (Cao et al., 2019; Sivaraman et al., 2018; Udhayakumari et al., 2017; Liu et al., 2017), and many fluorescent chemosensors for Cu^{2+} ion based on various fluorophores such as coumarin (Zhang et al., 2019), Bodipy (Ömeroğlu et al., 2021), rhodamine (Fernandes and Raimundo, 2021), Schiff base (Singh et al., 2020), pyrene (Kowser et al., 2021), and 1,3,4-oxadiazole (Wang, et al., 2018) have been reported by different research groups. Among these fluorescent chemosensors, the 1,3,4-oxadiazoles have drawn special interest due to their electron-deficient nature, high photoluminescence quantum yield, and excellent chemical stability, and have found practical applications in the fields of organic light-emitting diodes (Meng et al., 2020) and liquid crystals (Han et al., 2013; Han et al., 2015; Han et al., 2018). In addition, the nitrogen and oxygen atoms of the 1,3,4-oxadiazole unit can provide potential coordination sites with metal ions, which makes it usable as a signaling component in fluorescent chemosensors.

Calixarenes, as one kind of the most important super-molecules, have been widely used in design of fluorescent chemosensors for ions and neutral molecules due to their outstanding
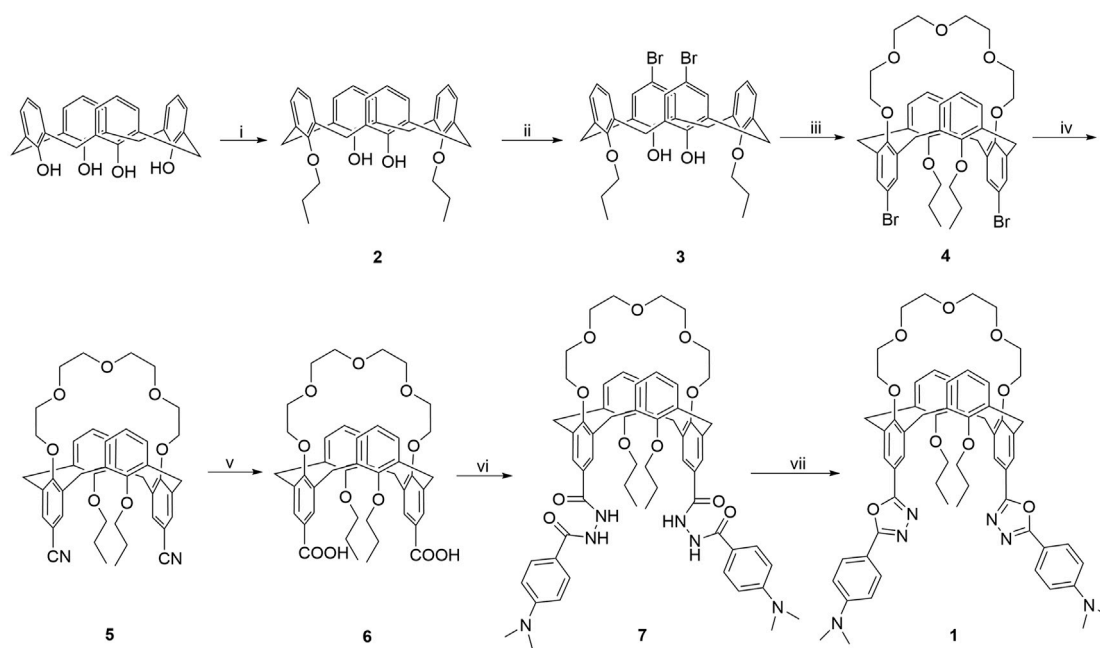
SCHEME 1 | Synthetic route for **1**, reagents, and conditions: (i) 1-iodopropane, K_2CO_3, CH_3CN, reflux, 24 h; (ii) Br_2, 0°C, 3 h; (iii) tetraethylene glycol ditosylate, Cs_2CO_3, CH_3CN, reflux, 72 h; (iv) (1) CuCN, NMP, 180°C, 5 h; (2) $FeCl_3$, 2 M HCl, 100°C, 1 h; (v) KOH, ethanol, reflux, 24 h; (vi) (1) $SOCl_2$, toluene, reflux, 5 h; (2) 4-(dimethylamino)benzohydrazide, pyridine, r. t., 12 h; (vii) $POCl_3$, reflux, 12 h.

features such as preorganized binding sites, easy derivatization, and flexible three-dimensional structures (Kim et al., 2012; An et al., 2019; Miranda et al., 2019; Noruzi et al., 2019; Chen et al., 2020). Many calixarene-based fluorescent chemosensors for transition metal ions have been reported in recent years (Ma et al., 2015). However, the fluorescent switchable chemosensors triggered by different ions are quite few (Chung et al., 2007), which remains a challenge in the field of supramolecular chemistry. Herein, as part of our continuous research in the design and synthesis of new fluorescent chemosensors (Liu et al., 2021; Xie et al., 2016; Han et al., 2012), we utilize the 1,3-alternate calix[4]crown scaffold to construct an on–off switchable fluorescent chemosensor **1** in this work. The synthetic route for **1** is shown in **Scheme 1**. There are quite a number of chemosensors based on various macrocycles for copper detection reported in literatures (Lvova, et al., 2018; Doumani, et al., Kamei, et al., 2021), in which the macrocyles often only worked as receptors for Cu^{2+} ions. In contrast, the chemosensor **1** in this work is special in that it has two kinds of macrocycles: one is from the 1,3-alternate calixarene, which provides a three-dimensional scaffold with two appending 1,3,4-oxadiazole units as both signaling component and fluorophore; the other is from the calix[4]crown, which can bind the Mg^{2+} or Ca^{2+} ions and has an allosteric effect on the 1,3,4-oxadiazole units on opposite rings. The selective binding of 1,3,4-oxadiazole with Cu^{2+} ions results in the fluorescence quenching, while the binding of calix[4]crown with Mg^{2+} or Ca^{2+} ions can partly revive the fluorescence consequently. Thus, the compound **1** might work as a new type of switchable off–on fluorescent chemosensor.

MATERIALS AND METHODS

25,27-Dihydroxy-26,28-dipropoxycalix[4]arene **2** and 5,17-dibromo-25,27-dihydroxy-26,28-dipropoxycalix[4]arene **3** were synthesized according to the literature procedures (Hobzova, 2010). Dichloromethane and acetonitrile used for photophysical studies were of spectrometric grade. All the other chemicals and solvents were of analytical grade and used as received from commercial sources. The solutions of metal ions were all prepared from their perchlorate salts. Column chromatography was performed on silica gel (200–300 mesh).

Solution ^{1}H NMR (Proton Nuclear Magnetic Resonance) and ^{13}C NMR (Carbon-13 Nuclear Magnetic Resonance) spectra were recorded on a Bruker AV400 spectrometer and the chemical shifts are quoted in parts per million (ppm) relative to tetramethylsilane (TMS) as an internal standard. ESI-HRMS (Electrospray Ionization-High Resolution Mass Spectrometry) data were obtained with a FTICR-MS mass spectrometer. Melting points were determined with an X-4 melting point apparatus, and the thermometer was uncorrected. Data for single x-ray structure were collected on a SMART1000 CCD-X diffractometer with graphite-monochromatized MoKα x-ray radiation ($\lambda = 0.71073$ Å) and Saturn CCD area detector. The x-ray crystal structure of 4 was solved by direct method and expanded using Fourier synthesis technique. No absorption correction was done. The non-hydrogen atoms were refined anisotropically. Hydrogen atoms were refined using riding model. Structural refinement based on full-matrix least-squares refinement on $|F|^2$ was performed by using Crystal Structure or SHELXL97 suite program (Sheldrick, 1997).

Synthesis of 4

A mixture of **3** (9.23 g, 13.9 mmol) and Cs_2CO_3 (11.30 g, 34.7 mmol) in MeCN (700 ml) under nitrogen was stirred at reflux for 30 min and then a solution of the tetraethylene glycol ditosylate (7.85 g, 15.6 mmol) in MeCN (40 ml) was added during an hour. The mixture was refluxed for 72 h and allowed to cool to room temperature. After evaporation of the solvent *in vacuo*, the residue was taken up in CH_2Cl_2 (30 ml × 3) and the resultant solution was washed with 1 mol/L HCl (30 ml) and brine (30 ml × 2). The organic layer was dried over $MgSO_4$ and evaporated *in vacuo*. Recrystallization of the residue from CH_2Cl_2/MeOH gave **4** a pale-yellow solid. Yield, 75%. Mp: 230–232 °C. ^{1}H NMR (400 MHz, CDCl$_3$) δ 7.17 (s, 4H), 7.08 (d, J = 8.0 Hz, 4H), 6.87 (t, J = 8.0 Hz, 2H), 3.78 (d, J = 4.0 Hz, 8H), 3.54 (s,8H), 3.45 (t, J = 8.0 Hz, 4H), 3.25–3.20 (m, 4H), 3.15 (m, 4H), 1.31 (m, 4H), 0.78 (t, J = 7.5 Hz, 6H). ^{13}C NMR (101 MHz, CDCl$_3$) δ 156.97, 155.14, 136.29, 133.81, 132.17, 129.70, 122.77, 115.15, 72.59, 72.09, 70.50, 70.13, 69.03, 37.89, 22.53, 10.23. HRMS-MALDI calculated for $C_{42}H_{48}Br_2O_7$ [M + Na] $^+$ 847.1639, found 847.1652.

Synthesis of 5

Under nitrogen, a mixture of **4** (10.17 g, 12.3 mmol) and cuprous cyanide (7.68 g, 86.4 mmol) in 20 ml of 1-methyl-2-pyrrolidinone was stirred at 180°C for 4 h. Then, the reaction mixture was cooled slowly to 100°C, and a solution of 23.23 g (86.4 mmol) of $FeCl_3 \cdot 6H_2O$ in 5 ml of concentrated hydrochloride and 25 ml of water was added to the reaction mixture. The reaction mixture was further stirred at 100°C for 1 h and cooled to room temperature. The solid was filtered off and recrystallized from chloroform/hexane yielding 5.5 g of compound **5** as yellow solid. Yield 62%. ^{1}H NMR (400 MHz, CDCl$_3$) δ 7.36 (s, 4H), 7.10 (d, J = 7.4 Hz, 4H), 6.90 (s, 2H), 3.82 (d, J = 5.5 Hz, 8H), 3.55 (s, 8H), 3.46 (t, J = 7.4 Hz, 4H), 3.30 (t, J = 6.1 Hz, 4H), 3.17 (t, J = 6.1 Hz, 4H), 1.24 (m, 4H), 0.74 (t, J = 7.5 Hz, 6H). ^{13}C NMR (101 MHz, CDCl$_3$) δ 159.98, 156.80, 135.72, 133.54, 133.05, 129.94, 123.05, 119.17, 106.08, 77.36, 72.52, 72.17, 70.56, 69.85, 69.13, 37.75, 22.81, 10.05; HRMS: calcd for $C_{44}H_{48}N_2O_7$ [M+NH$_4$]$^+$ 734.3800, found 734.3796.

Synthesis of 6

A solution of 5.18 g (9.2 mmol) of KOH in 100 ml of water was added to the suspension of 1.32 g (1.80 mmol) of **5** in 20 ml of ethanol. The reaction mixture was heated under reflux for 24 h. After cooling, the aqueous solution hydrogen chloride (10% w/w) was added dropwise until the solution became slightly acidic. The precipitate was filtered off, washed with water, and dried to yield a yellow solid product **6** (1.33 g, 96%). Mp: 296–298°C. ^{1}H NMR (400 MHz, CDCl$_3$) δ 12.52 (s, 2H), 7.81–7.77 (m, 8H), 6.98–6.94 (m, 2H), 3.93–3.80 (m, 12H), 3.62 (s, 16H), 1.42–1.31 (m, 4H), 0.69 (t, J = 7.5 Hz, 6H). ^{13}C NMR (101 MHz, DMSO-d_6) δ 167.03, 158.48, 156.72, 135.62, 133.71, 132.13, 130.41, 125.24, 122.05, 71.17, 70.07, 69.72, 40.15, 39.94, 39.73, 39.52, 39.31, 39.10, 38.89, 35.98, 21.74, 9.52. HRMS: calcd for $C_{44}H_{50}O_{11}$ [M-H]$^+$ 753.3280, found 753.3285.

Synthesis of 1

To a round-bottomed flask was added **6** (80 mg, 0.1 mmol), 10 ml of toluene, and 1 ml of thionyl chloride, and the mixture was refluxed for 5 h. After cooling, the solvent and the excess of thionyl chloride were removed at reduced pressure to give the benzoyl chloride, which was added to a solution of 4-(dimethylamino)benzohydrazide (39 mg, 0.22 mmol) in 10 ml of dichloromethane and 0.1 ml of pyridine. The reaction mixture was stirred for 12 h at ambient temperature and filtered. The precipitate was washed with ethanol to give the bishydrazide **7** as white solid, which was used to the next step reaction without further purification. The intermediate compound **7** was added to POCl$_3$ (5 ml), and the resultant solution was refluxed overnight under a nitrogen atmosphere. After the reaction mixture cooled to room temperature, it was poured into ice water and extracted with dichloromethane (3 × 10 ml). The combined organic layer was washed with water and brine, respectively. Then, the solvent was removed under reduced pressure, and the crude solid was purified by silica gel column chromatography using petroleum ether/ethyl acetate (1:1) as eluent affording the product **1** as white solids. Yield, 35%. Mp: 281–283°C. ^{1}H NMR (400 MHz, CDCl$_3$) δ 7.91 (d, J = 8.0 Hz, 4H), 7.81 (s, 4H), 7.15 (d, J = 8.0 Hz, 4H), 6.93 (s, 2H), 6.72 (d, J = 8.0 Hz, 4H), 3.93 (m, 8H), 3.59–3.53 (m, 12H), 3.31 (d, J = 5.2 Hz, 4H), 3.26 (d, J = 5.2 Hz, 4H), 3.05 (m, 12H), 1.25–1.19 (m, 4H), 0.60 (t, J = 7.4 Hz, 6H). ^{13}C NMR (101 MHz, CDCl$_3$) δ 164.80, 163.55, 158.76, 157.10, 152.20, 135.07, 133.83, 129.79, 128.32, 128.13, 122.75, 121.14, 118.35, 111.59, 111.27, 72.43, 72.24, 70.42, 70.14, 69.22, 40.11, 38.05, 22.43, 9.95. HRMS-ESI calculated for $C_{62}H_{69}N_6O_9$ [M + H] $^+$ 1,041.5120, found 1,041.5126. (**Supplementary Figure S5**, ESI).

General Procedures for the UV/Vis and Fluorescence Experiments

UV-vis spectra were recorded on a Cary 3,010 spectrophotometer, and the resolution was set at 1 nm. Steady-state emission spectra were recorded on a Varian Cary Eclipse spectrometer. For all measurements of fluorescence spectra, excitation was set at 334 nm for complexation, and the excitation and emission slit width was set to be 2.5 nm. Fluorescence titration experiments were performed with CH_2Cl_2 solutions of compound **1** and varying concentrations of metal perchlorate in CH_3CN solution. During all measurements, the temperature of the quartz sample cell and chamber was kept at 25°C.

RESULTS AND DISCUSSION

Synthesis and Structural Analysis

As shown in **Scheme 1**, calix[4]arene **3** was reacted with tetraethylene glycol ditosylate in the presence of Cs_2CO_3 to successfully afford the calix[4]crown **3** in 75% yield. The substitution reaction of **4** with CuCN gave **5** in 62% yield, which was refluxed with KOH in ethanol and treated with hydrochloric acid solution, readily providing the carboxylic

FIGURE 1 | X-ray molecular structure of **5**.

FIGURE 2 | UV-vis spectra of **1** (1×10^{-6} mol/L) upon addition of metal ions (10 equiv) in CH_2Cl_2/CH_3CN (1,000:1, v/v).
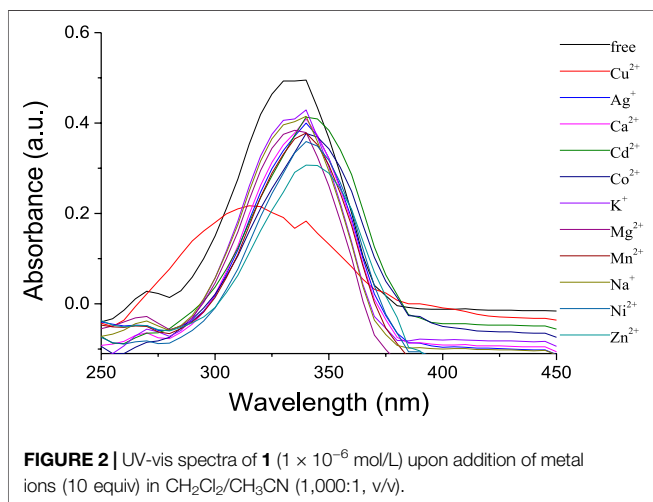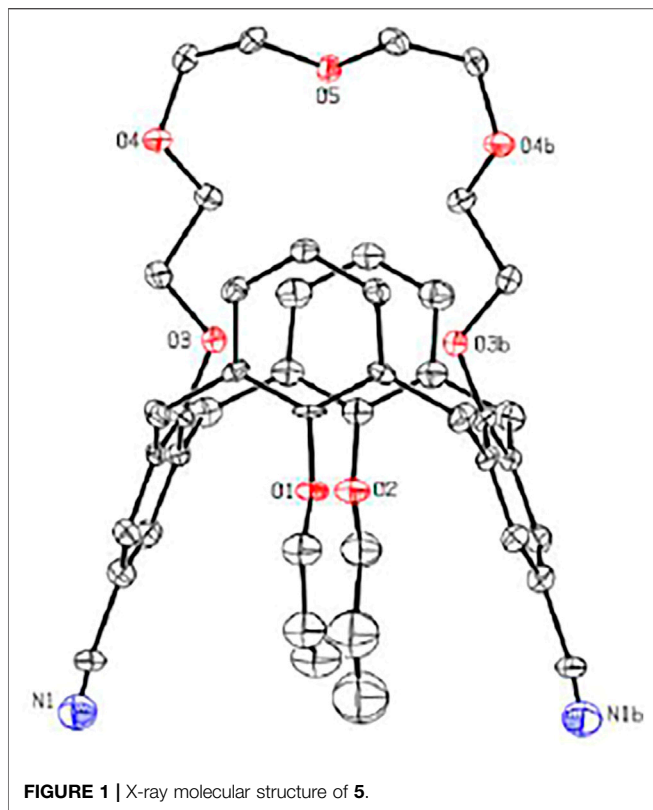
acid **6** in good yield. Then, the carboxylic acid **6** was reacted with thionyl chloride, and treated with benzyol hydrazine or 4-N,N′-dimethylaminobenzyol hydrazine to generate the intermediate bishydrazide **7**, which was used in the next step without purification and refluxed with phosphorus oxychloride to afford the target products **1**. Except for the calix[4]arene **3**, all of the intermediate calix[4]crowns **3–6** and the chemosensor **1** are in 1,3-alternate conformation, which were well established by ^{1}H NMR and ^{13}C NMR data (**Supplementary Figures S1–S4**,

FIGURE 3 | Fluorescence spectra (λ_{exc} = 334 nm, Slit = 2.5) of **1** (1×10^{-6} mol/L) upon addition of metal ions (10 equiv) in CH_2Cl_2/CH_3CN (1,000:1, v/v).

ESI). The 1,3-alternate conformation of **5** was further confirmed unambiguously by x-ray single crystal diffraction as shown in **Figure 1**. The x-ray crystallographic data are collected in **Supplementary Table S1**.

UV-Vis Absorption and Fluorescence Spectra Analysis

The selectivity of the receptor **1** toward different perchlorate salts, including Na^+, K^+, Mg^{2+}, Ca^{2+}, Co^{2+}, Ni^{2+}, Zn^{2+}, Cd^{2+}, Mn^{2+}, Ag^+, and Cu^{2+}, was first investigated by UV-Vis spectroscopy. The UV-Vis absorption spectra for free **1** in CH_2Cl_2 solution showed an intense and structureless absorption band ($\varepsilon = 4.94 \times 10^5$ L/mol·cm) peaking at 340 nm (**Figure 2**), which might have resulted from the spin-allowed π-π* transitions involving the phenyloxadiazole moiety (Han et al., 2006). The addition of Cu^{2+} ions in the solution of **1** resulted in a significant decrease in the absorbance with an appreciable hypochromic shift of 20 nm. In contrast, only a slight decrease was observed upon addition of other metal ions mentioned above, which suggested that the selectivity of **1** toward Cu^{2+} is much higher than the other metal ions.

Ion recognition ability of **1** was further studied by the fluorescence spectra. As shown in **Figure 3**, the receptor **1** exhibited a strong emission with λ_{max} at 405 nm in solution of CH_2Cl_2. Upon addition of Na^+, K^+, and Mg^{2+}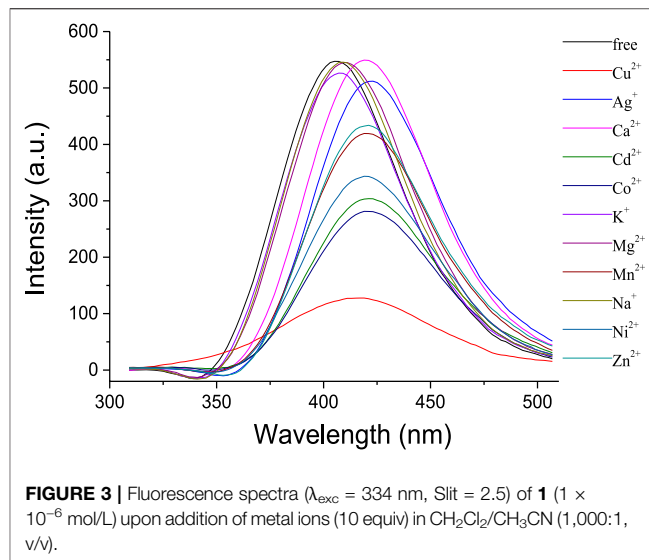, respectively, almost no changes were observed in the intensity and shape of the emission spectra of **1**. It is noted that the addition of Ca^{2+} might slightly increase the intensity with a bathochromic shift of ca. 15 nm, perhaps because the complexation between the Ca^{2+} and the crown ether moiety changed the space distance of the two phenyloxadiazole units and the fluorescence changed consequently. Apparently, the fluorescence response of **1** toward transition metal ions was found to be more pronounced, and the addition of Co^{2+}, Ni^{2+}, Zn^{2+}, and Ag^+ could quench the emission of **1** in a different extent, accompanied by a concomitant red shift of ca. 14–17 nm. In contrast, the addition of Cu^{2+} significantly quenched the

FIGURE 4 | Fluorescence spectra (λ_{exc} = 334 nm, Slit = 2.5) of **1** (1 × 10^{-6} mol/L) and Cu^{2+} (10 equiv) upon addition of other metal ions (10 equiv) in CH_2Cl_2/CH_3CN (1,000:1, v/v).
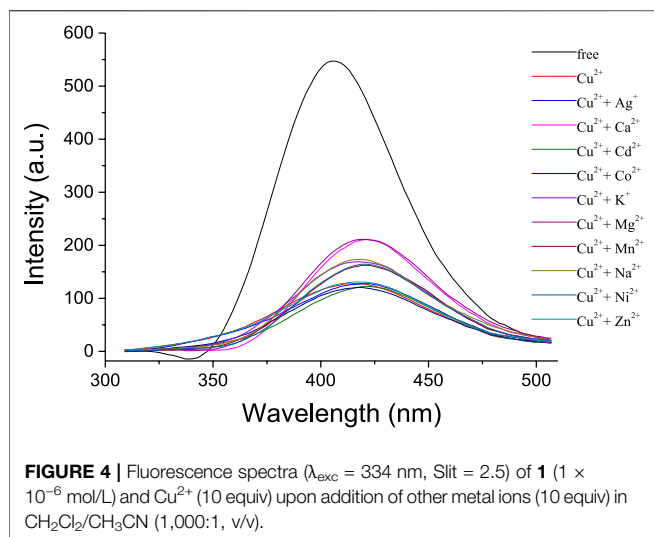
fluorescence of **1** under the same conditions as the aforementioned metal ions, suggesting that there is a strong interaction between 1,3,4-oxadiazole moieties of **1** and Cu^{2+} ion over the other metal ions.

The fluorescence emission properties of **1** in the presence of Cu^{2+} and a competitive metal ion were measured to investigate the selective recognition for Cu^{2+}. As shown in **Figure 4**, no apparent changes were observed in fluorescence intensity when 10 equivalent amounts of transition metal ions (Co^{2+}, Ni^{2+}, Zn^{2+}, Cd^{2+}, Mn^{2+}, and Ag^+) were added to the solution of **1** and Cu^{2+} (10 equiv). This suggested that the recognition for Cu^{2+} was not interrupted by the competitive

transition metal ions; thus, the receptor **1** might act as a selective fluorescent chemosensor for Cu^{2+}. The addition of alkali metal ions (Na^+ and K^+) to the solution of **1** and Cu^{2+} could increase the fluorescence intensity slightly, while the alkaline earth metal ions (Mg^{2+} and Ca^{2+}) could revive the emission significantly.

In order to elicit the binding property of the chemosensor **1** toward Cu^{2+} ion, fluorescence titration of **1** (1.0 × 10^{-5} mol/L) with Cu^{2+} ion (0–2 equiv) was carried out (**Supplementary Figure S6**). According to the fluorescence titration curves of **1** with Cu^{2+} ion at room temperatures, the association constant K_a was calculated as 1.6 × 10^{-4} L·mol^{-1} (R = 0.97526) for the **1**–Cu^{2+} complex by the Benesi–Hildebrand plot (Thordarson, 2011) (**Figure 5**). Moreover, the emission intensity of **1** is linearly proportional to the Cu^{2+} concentration in the range of 0–20 μM.

The fluorescence changes of **1** upon addition of Cu^{2+} and Mg^{2+} ions are displayed in **Figure 6**. The nitrogen atoms of the 1,3,4-oxadiazle units can bind with Cu^{2+} to form the complex **1**·Cu^{2+}, and the paramagnetic nature of Cu^{2+} ion could strongly quench the fluorescence of the 1,3,4-oxadiazole units through the electron transfer mechanism, which is consistent to the results reported in literature (Han et al., 2012). In contrast, the polyether ring (crown-5 moiety) and the oxygens from the two propoxyl groups could provide coordination sites with the alkaline earth metal ions to form the complex **1**·Mg^{2+}, which will change the molecular conformation as well as the space distance of the two 1,3,4-oxadiazole units. Consequently, the decomplexations between the 1,3,4-oxadiazoles and Cu^{2+} ions took place and resulted in the increase of the fluorescence. Thus, the receptor **1** might be acted as an on–off–on switchable fluorescent chemosensor triggered by the exchange of Cu^{2+} and Mg^{2+}.

FIGURE 5 | Plot of emission intensity versus the concentrations of Cu^{2+} ion (λ_{em} = 405 nm, λ_{ex} = 334 nm).
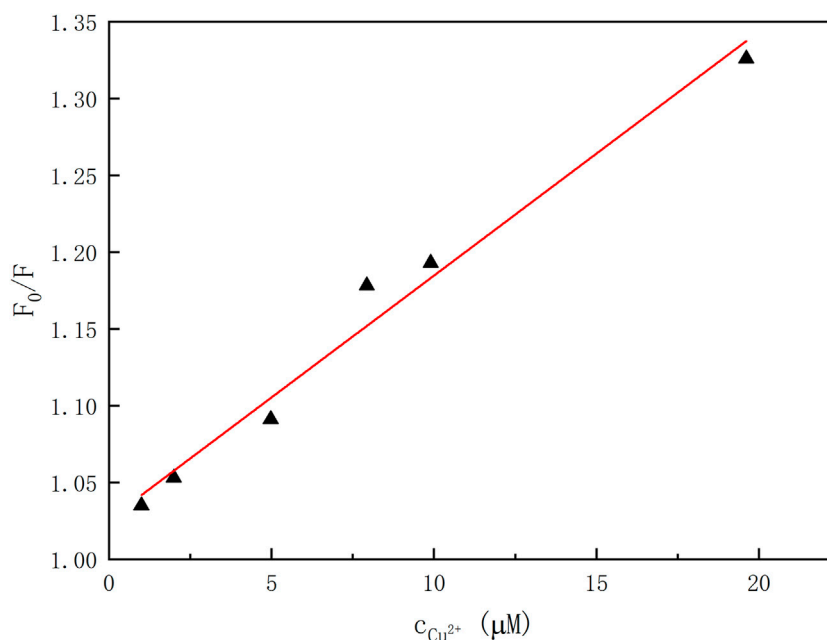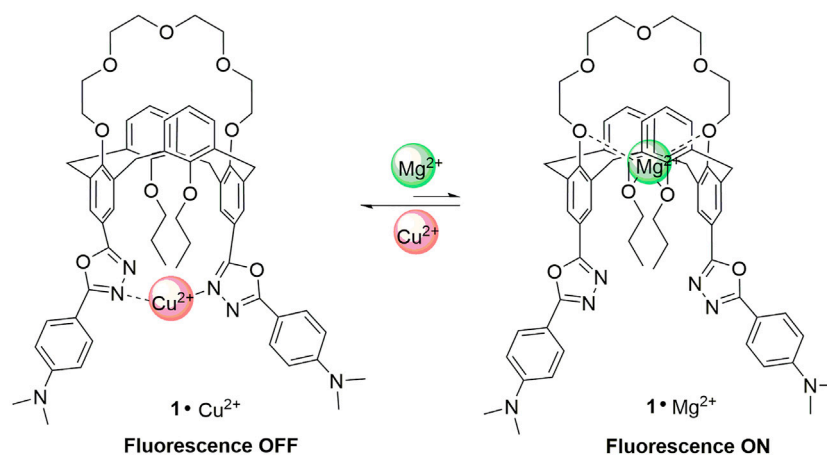
FIGURE 6 | The complexation of **1** with Cu^{2+} and Mg^{2+} ions.
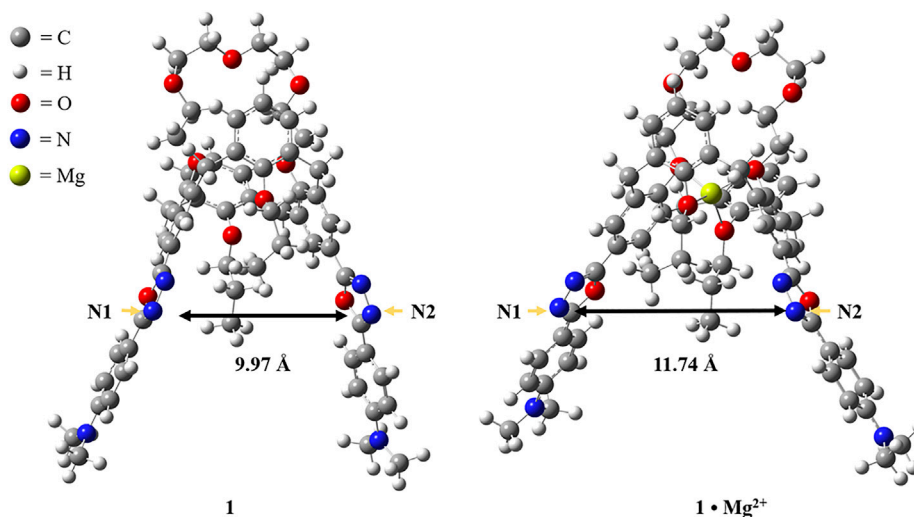
FIGURE 7 | Computational optimized molecular structures of **1** and **1·Mg²⁺**.

To gain a better understanding about the switchable fluorescence of the chemosensor **1**, DFT calculations with the GAUSSIAN 09 series of programs (Frisch et al., 2013) were carried out to analyze the molecular structures of **1** and **1·Mg²⁺**, and DFT method B3-LYP with 6-31G(d) basis set was used for geometry optimizations (A. D. Becke, 1993). As shown in **Figure 7**, the distance between N1 and N2 in the free receptor **1** is 9.97 Å, while the corresponding distance is 11.74 Å in the complex **1·Mg²⁺**, indicating that the molecular conformation changed simultaneously due to the allosteric effect (Kumar et al., 2012; Ni et al., 2013). The conformational change as well as the increase in distance makes it difficult for the chemosensor **1** to coordinate with Cu^{2+} ion to form the stable complex, which reasonably explains the fact that the addition of

Mg^{2+} ions to the solution of **1** and Cu^{2+} can trigger the revival of fluorescence.

CONCLUSION

In summary, we have designed a new type of fluorescent chemosensor based on a 1,3-alternate calix[4]crown with two different cationic binding sites. The 1,3,4-oxadiazole units could bind selectively with Cu^{2+} to form the complexation and resulted in the fluorescence quenching of the chemosensor. The presence of various transition metal ions does not interfere with the quenching process, while the alkaline earth metal ions Mg^{2+} might be entrapped by the crown-5 moiety and revive the fluorescence significantly due to the allosteric effect. As the

chemosensor in this work is not soluble in water, it is difficult to investigate the Cu^{2+} ions' detection under physiological conditions. Devising a water-soluble chemosensor for Cu^{2+} ions is in progress in our lab.

DATA AVAILABILITY STATEMENT

The original contributions presented in the study are included in the article/**Supplementary Material**, further inquiries can be directed to the corresponding author.

AUTHOR CONTRIBUTIONS

FUNDING

SUPPLEMENTARY MATERIAL

The Supplementary Material for this article can be found online at: https://www.frontiersin.org/articles/10.3389/fchem.2021.766442/full#supplementary-material

REFERENCES

An, L., Wang, C., Han, L., Liu, J., Huang, T., Zheng, Y., et al. (2019). Structural Design, Synthesis, and Preliminary Biological Evaluation of Novel Dihomooxacalix[4]arene-Based Anti-tumor Agent. *Front. Chem.* 7, 856. doi:10.3389/fchem.2019.00856

Becke, A. D. (1993). Density-functional Thermochemistry. III. The Role of Exact Exchange. *J. Chem. Phys.* 98, 5648. doi:10.1063/1.464913

Cao, X., Li, Y., Gao, A., Yu, Y., Zhou, Q., and Chang, X. (2019). Multifunctional Fluorescent Naphthalimide Self-Assembly System for the Detection of Cu^{2+} and K^+ and Continuous Sensing of Organic Amines and Gaseous Acids. *J. Mater. Chem. C* 7, 10589–10597. doi:10.1039/c9tc03243f

Chang, K.-C., Su, I.-H., Senthilvelan, A., and Chung, W.-S. (2007). Triazole-modified Calix[4]crown as Novel Fluorescent On-Off Switchable Chemosensor. *Org. Lett.* 9, 3363–3366. doi:10.1021/ol071337+

Chen, Y.-J., Chen, M.-Y., Lee, K.-T., Shen, L.-C., Hung, H.-C., Niu, H.-C., et al. (2020). 1,3-Alternate Calix[4]arene Functionalized with Pyrazole and Triazole Ligands as a Highly Selective Fluorescent Sensor for Hg^{2+} and Ag+ Ions. *Front. Chem.* 6, 593261. doi:10.3389/fchem.2019.59326110.3389/fchem.2020.593261

Cotruvo, Jr., J. A., Jr., Aron, A. T., Ramos-Torres, K. M., and Chang, C. J. (2015). Synthetic Fluorescent Probes for Studying Copper in Biological Systems. *Chem. Soc. Rev.* 44, 4400–4414. doi:10.1039/c4cs00346b

Doumani, N., Bou-Maroun, E., Maalouly, J., Tueni, M., Dubois, A., Bernhard, C., et al. (2019). A New pH-dependent Macrocyclic Rhodamine B-Based Fluorescent Probe for Copper Detection in white Wine. *Sensors* 19, 4514. doi:10.3390/s19204514

Fernandes, R. da. S., and Raimundo, I. M., Jr (2021). Development of a Reusable Fluorescent Nanosensor Based on Rhodamine B Immobilized in Stober Silica for Copper Ion Detection. *Anal. Methods* 13, 1970–1975. doi:10.1039/d1ay00168j

Frisch, M. J., Trucks, G. W., Schlegel, H. B., Scuseria, G. E., Robb, M. A., Cheeseman, J. R., et al. (2013). *Gaussian 09, Revision D.01*. Wallingford, CT: Gaussian, Inc.

Han, J. (2013). 1,3,4-Oxadiazole Based Liquid Crystals. *J. Mater. Chem. C* 1, 7779–7797. doi:10.1039/c3tc31458h

Han, J., Chui, S. S. Y., and Che, C. M. (2006). Thermotropic Liquid Crystals Based on Extended 2,5-Disubstituted-1,3,4-Oxadiazoles: Structure-Property Relationships, Variable-Temperature Powder X-ray Diffraction, and Small-Angel X-ray Scattering Studies. *Chem. Asian J.* 1, 814–825. doi:10.1002/asia.200600252

Han, J., Wang, F.-L., Liu, Y.-X., Zhang, F.-Y., Meng, J.-B., and He, Z.-J. (2012). Calix[4]arene-based 1,3,4-oxadiazole: Novel Fluorescent Chemosensors for Specific Recognition of Cu^{2+}. *ChemPlusChem* 77, 196–200. doi:10.1002/cplu.201200004

Han, J., Wang, Z.-Z., Wu, J., and Zhu, L.-R. (2015). A Room-Temperature Liquid Crystalline Polymer Based on Discotic 1,3,4-oxadiazole. *RSC Adv.* 5, 47579–47583. doi:10.1039/c5ra05983f

Han, J., Xi, Z., Wang, F., Bu, L., and Wang, Y. (2018). Synthesis, Liquid Crystalline and Photoluminscent Properties of 1,3,4-oxadiazole Derivatives: from Calamitic Monomers, H-Shaped Dimers to Calix[4]arene-Based Tetramers. *Dyes Pigm.* 154, 234–241. doi:10.1016/j.dyepig.2018.03.008

Hobzova, R., Sysel, P., and Duskova-Smrckova, M. (2010). Synthesis and Characterization of Calix[4]arene-Containing Polyimides. *Polym. Int.* 60, 405–413. doi:10.1002/pi.2962

Kamel, A. H., Amr, A. E.-G. E., Almehizia, A. A., Elsayed, E. A., and Moustafa, G. O. (2021). Low-cost Potentiometric Paper-Based Analytical Device Based on Newly Synthesized Macrocyclic Pyrido-Pentapeptide Derivatives as Novel Ionophores for point-of-care Copper(II) Determination. *RSC Adv.* 11, 27174–27182. doi:10.1039/d1ra04712d

Kim, H. J., Min Hee Lee, M. H., Mutihac, L., Vicens, J., and Kim, J. S. (2012). Host–guest Sensing by Calixarenes on the Surfaces. *Chem. Soc. Rev.* 41, 1173–1190. doi:10.1039/c1cs15169j

Kowser, Z., Rayhan, U., Akther, T., Redshaw, C., and Yamato, T. (2021). A Brief Review on Novel Pyrene Based Fluorometric and Colorimetric Chemosensors for the Detection of Cu^{2+}. *Mater. Chem. Front.* 5, 2173–2200. doi:10.1039/D0QM01008A

Kumar, M., Kumar, N., and Bhalla, V. (2012). Ratiometric Nanomolar Detection of Cu^{2+} Ions in Mixed Aqueous media: a Cu^{2+}/Li^+ Ions Switchable Allosteric System Based on Thiacalix[4]crown. *Dalton Trans.* 41, 10189–10193. doi:10.1039/c2dt31081c

Liu, S., Wang, Y.-M., and Han, J. (2017). Fluorescent Chemosensors for Copper(II) Ion: Structure, Mechanism and Application. *J. Photochem. Photobio. C.* 32, 78–103. doi:10.1016/j.jphotochemrev.2017.06.002

Liu, S., Wu, Q., Zhang, T., Zhang, H., and Han, J. (2021). Supramolecular brush Polymers Prepared from 1,3,4-oxadiazole and Cyanobutoxy Functionalized Pillar[5]arene for Detecting Cu^{2+}. *Org. Biomol. Chem.* 19, 1287–1291. doi:10.1039/d0ob02587a

Lvova, L., Caroleo, F., Garau, A., Lippolis, V., Giorgi, L., Fusi, V., et al. (2018). A Fluorescent Sensor Array Based on Heteroatomic Macrocyclic Fluorophores for the Detection of Polluting Species in Natural Water Samples. *Front. Chem.* 6, 258. doi:10.3389/fchem.2018.00258

Ma, J., Song, M., Boussouar, I., Tian, D., and Li, H. (2015). Recent Progress of Calixarene-Based Fluorescent Chemosensors towards Mercury Ions. *Supramole. Chem.* 27, 444–452. doi:10.1080/10610278.2014.988627

Meng, X., Wang, P., Bai, R., and He, L. (2020). Blue-green-emitting Cationic Iridium Complexes with Oxadiazole-type Counter-anions and Their Use for Highly Efficient Solution-Processed Organic Light-Emitting Diodes. *J. Mater. Chem. C* 8, 6236–6244. doi:10.1039/d0tc01054e

Miranda, A. S., Serbetci, D., Marcos, P. M., Ascenso, J. R., Berberan-Santos, M. N., Hickey, N., et al. (2019). Ditopic Receptors Based on Dihomooxacalix[4]arenes

Bearing Phenylurea Moieties with Electron-Withdrawing Groups for Anions and Organic Ion Pairs. *Front. Chem.* 7, 758. doi:10.3389/fchem.2019.00758

Ni, X.-L., Cong, H., Yoshizawa, A., Rahman, S., Tomiyasu, H., Rayhan, U., et al. (2013). Heteroditopic Thiacalix[4]arene Receptor Having Ester and Bipyridyl Moieties for Ions Binding with Positive/negative Allosteric Effect. *J. Mol. Struc.* 1046, 110–115. doi:10.1016/j.molstruc.2013.04.040

Noruzi, E. B., Kheirkhahi, M., Shaabani, B., Geremia, S., Hickey, N., Asaro, F., et al. (2019). Design of a Thiosemicarbazide-Functionalized Calix[4]arene Ligand and Related Transition Metal Complexes: Synthesis, Characterization, and Biological Studies. *Front. Chem.* 7, 663. doi:10.3389/fchem.2019.00663

Ömeroğlu, İ., Tümay, S. O., Makhseed, S., Husain, A., and Durmuş, M. (2021). A Highly Sensitive "ON–OFF–ON" Dual Optical Sensor for the Detection of Cu(II) Ion and Triazole Pesticides Based on Novel BODIPY-Substituted Cavitand. *Dalton Trans.* 50, 6437–6443. doi:10.1039/d1dt00792k

Sheldrick, G. M. (1997). *SHELXS-97 and SHELXL-97*. Gottingen: University of Gottingen.

Singh, G., Shilpy, Singh, A., Dikshaand, Pawan. (2020). Synthesis of Organosilocane Allied N-Heteroaryl Schiff Base Chemosensor for the Detection of Cu²⁺ Metal Ions and Their Biological Applications. *New J. Chem.* 44, 13542–13552. doi:10.1039/d0nj01774d

Sivaraman, G., Iniy, M., Anand, T., Kotla, N. G., Sunnapu, O., Singaravadivel, S., et al. (2018). Chemically Diverse Small Molecule Fluorescent Chemosensors for Copper Ion. *Coord. Chem. Rev.* 357, 50–104. doi:10.1016/j.ccr.2017.11.020

Thordarson, P. (2011). Determining Association Constants from Titration Experiments in Supramolecular Chemistry. *Chem. Soc. Rev.* 40, 1305–1323. doi:10.1039/c0cs00062k

Turski, M. L., and Thiele, D. J. (2009). New Roles for Copper Metabolism in Cell Proliferation, Signaling, and Disease. *J. Biol. Chem.* 284, 717–721. doi:10.1074/jbc.R800055200

Udhayakumari, D., Naha, S., and Velmathi, S. (2017). Colorimetric and Fluorescent Chemosensors for Cu²⁺. A Comprehensive Review from the Years 2013-15. *Anal. Methods* 9, 552–578. doi:10.1039/c6ay02416e

Wang, L., Gong, X., Bing, Q., and Wang, G. (2018). A New Oxadiazole-Based Dual-Mode Chemosensor: Colorimetric Detection of Co²⁺ and Fluorometric Detection of Cu²⁺ with High Selectivity and Sensitivity. *Microchem. J.* 142, 279–287. doi:10.1016/j.microc.2018.07.008

Xie, D.-H., Wang, X.-J., Sun, C., and Han, J. (2016). Calix[4]arene Based 1,3,4-oxadiazole as a Fluorescent Chemosensor for Copper(II) Ion Detection. *Tetrahedron Lett.* 57, 5834–5836. doi:10.1016/j.tetlet.2016.11.051

Zhang, Z., Liu, Y., and Wang, E. (2019). A Highly Selective "Turn-on" Fluorescent Probe for Detecting Cu²⁺ in Two Different Sensing Mechanisms. *Dyes Pigm.* 163, 533–537. doi:10.1016/j.dyepig.2018.12.039

Porphyrin Photoabsorption and Fluorescence Variation with Adsorptive Loading on Gold Nanoparticles

Akira Shinohara[1,2,3], Guang Shao[1], Takashi Nakanishi[3]* and Hideyuki Shinmori[2]*

[1]School of Chemistry, Sun Yat-sen University, Guangzhou, China, [2]Faculty of Life and Environmental Science, Graduate Faculty of Interdisciplinary Research, Department of Biotechnology, University of Yamanashi, Kofu, Japan, [3]International Center for Materials Nanoarchitectonics (WPI-MANA), National Institute for Materials Science (NIMS), Tsukuba, Japan

Here, we report the photophysical structure–property relationship of porphyrins adsorbed on gold nanoparticles. The number of porphyrin–alkanethiolate adsorbates per particle was adjusted by a post-synthetic thiol/thiolate exchange reaction on 1-dodecanethiolate–protected gold nanoparticles. Even with a low loading level of adsorbates (<10% of all thiolate sites on gold nanoparticles), the shoulder absorption at the Soret band was intensified, indicating the formation of aggregates of porphyrin adsorbates on the nanoparticles. Steady-state fluorescence quantum yields could be adjusted by the bulkiness of substituents at the *meso*-positions of the porphyrin or the methylene linker chain length, regardless of the porphyrin loading level and the nanoparticle diameter.

Keywords: porphyrin, gold nanoparticle, photoabsorption, fluorescence, adsorbate

1 INTRODUCTION

The design of dye molecules with specific photophysical properties is necessary for many applications including optoelectronics, photocatalysis, and bioimaging (Lu and Nakanishi, 2019; Watanabe et al., 2019; Sato, 2020; Han et al., 2021). Various approaches to customize the properties of such dyes have been explored, based on the thorough investigation of the photophysical structure–property relationship (Shin and Lee, 2002; Benniston et al., 2003; Kovaliov et al., 2014; Kulinich et al., 2016). Despite these efforts, fine-tuning the properties that are intrinsic to the electronic structure of dyes remains challenging because the molecular design approach enables only stepwise adjustments.

One of the alternative approaches to adjusting the photophysical properties is to conjugate dyes and metal nanoparticles (Dulkeith et al., 2002; Doering and Nie, 2003; Pan et al., 2006; Hasobe, 2021). Nanoparticles are usually defined as particles with a diameter between ~1 and ~100 nm (Kreibig and Vollmer, 1995). In this size range, the chemical, photophysical, and electrical properties differ dramatically in comparison with the bulk counterparts (Glotov et al., 2019). For practical applications, gold is one of the few appropriate candidates, due to its chemical inertness. Gold nanoparticles (AuNPs), often protected with alkanethiolate groups as developed by Brust *et al.*(Brust et al., 1994) in the past quarter of a century, are widely employed for this purpose because of their extraordinary redispersibility (Thomas and Kamat, 2003). The alkanethiolate adsorbates can readily be replaced with other thiolates by thiol/thiolate exchange reactions to obtain AuNPs modified by incoming adsorbates. Additional desired functional properties such as
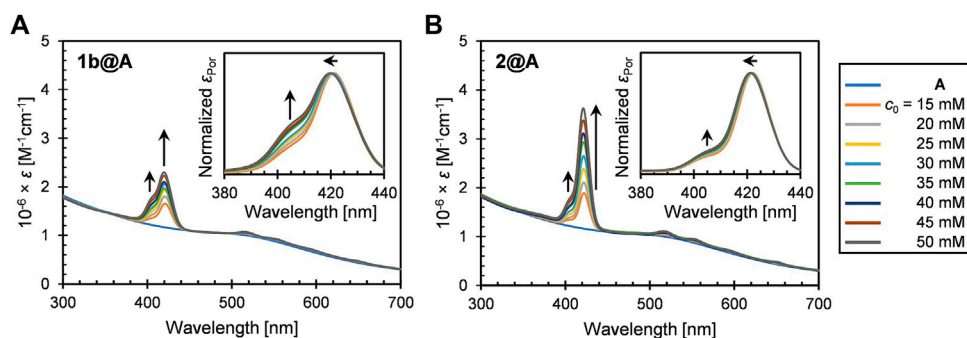
FIGURE 1 | UV-vis extinction spectra (in toluene) of **(A)** 1b@A and **(B)** 2@A prepared by post-synthetic modification of nanoparticle **A** with different initial concentrations of porphyrin–alkanethiols (c_0). Insets represent the normalized absorption spectra of porphyrin adsorbates.
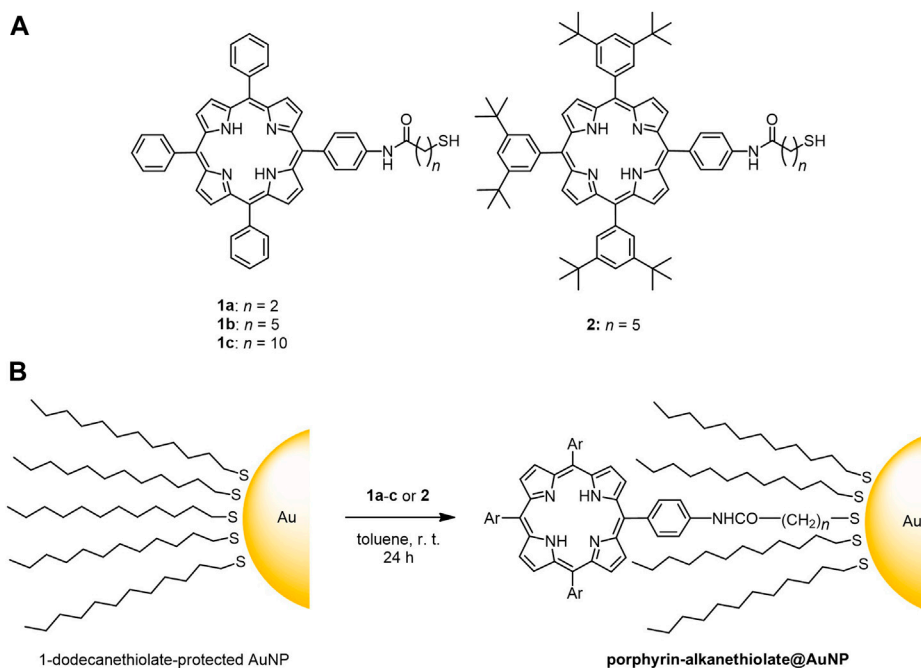
SCHEME 1 | **(A)** Chemical structure of porphyrin–alkanethiols 1a-c and 2; **(B)** post-synthetic loading of porphyrin–alkanethiols on 1-dodecanethiolate-protected AuNPs.

the solubility, charge, and affinity with other molecules can be added or amended by successive or coincident adsorbate exchange reactions to afford multifunctional nanoparticles (Ingram et al., 1997).

Porphyrins and their analogs have potential applications in many fields—sensing, catalysis, and photovoltaics, for example—so have attracted interest in their unique photophysics, including huge absorption coefficients of ~5 × $10^5 \, M^{-1} \, cm^{-1}$ (Kubo et al., 2003; Kinoshita et al., 2012; Barona–Castaño et al., 2016; Ghosh et al., 2019). Thorough investigations on the photophysics of porphyrin–AuNP conjugates have been conducted. For instance, Akiyama et al. reported photocurrent enhancement in porphyrin–AuNP

conjugates by a localized surface plasmon resonance (LSPR)–enhanced electromagnetic field (Akiyama et al., 2006). Imahori et al. reported the fluorescence lifetime of porphyrin adsorbates on AuNPs was significantly longer than those on a two-dimensional Au substrate (Imahori et al., 2001). The general strategy for the adjustment of photophysical properties of dye–AuNP conjugates involves altering the size and shape of the nanoparticles and the length of the linkers (Imahori et al., 1998; Dulkeith et al., 2005; Hong and Li, 2013; Do and Imae, 2021). However, less attention has been paid to the number of adsorbates loaded per particle, despite the strong influence on photophysical properties (Shinohara and Shinmori, 2016).
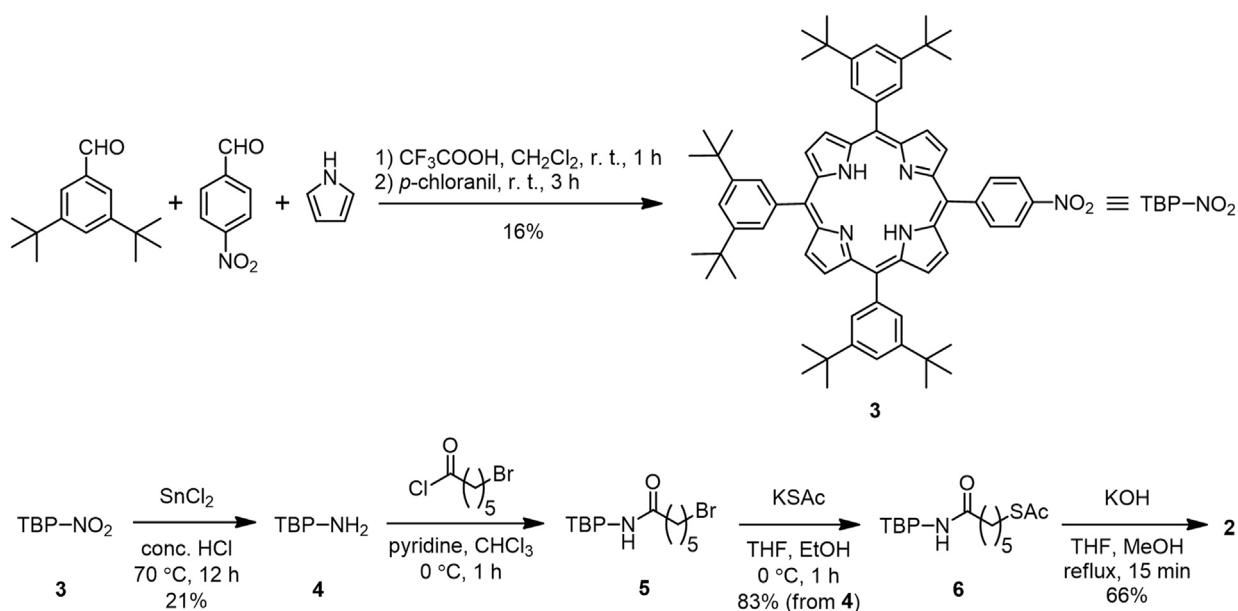
SCHEME 2 | Synthetic route to porphyrin–alkanethiol **2** with bulky *tert*-butyl substituents.

Here, we present the photophysical properties of porphyrin adsorbates on AuNPs having different loading levels, substituents on the *meso*-positions of porphyrin, lengths of alkanethiolate linkers, and nanoparticle diameters. Porphyrin–AuNP conjugates, with the adsorbate loading levels of up to 10% of all available thiolate sites, were obtained by post-synthetic thiol/thiolate exchange reactions employing 1-dodecanethiolate–protected AuNPs as the precursors. By characterizing conjugates with various loading levels, we have identified the factors that determine the photoabsorption and fluorescence properties of porphyrin adsorbates on the AuNPs.

FIGURE 2 | (A) Spectral deconvolution of the Soret band and shoulder into two Gaussian curves. **(B)** The relative shoulder intensity ($\varepsilon_{shoulder}/\varepsilon_{Soret}$) of porphyrin adsorbates with different numbers of porphyrin–alkanethiolate adsorbates per particle (N).

2 RESULTS AND DISCUSSION

2.1 Synthesis of Porphyrin–Gold Nanoparticle Conjugates

We employed three types of 1-dodecanethiolate–protected AuNPs A–C which have different diameters and distributions (A: 2.5 ± 0.5, B: 2.5 ± 0.9, and C: 5.6 ± 2.2 nm). The 2.5-nm species (A and B) showed weak LSPR around 510 nm (**Figure 1**), while the resonance was distinct for the 5.6-nm species C at 516 nm (Jin, 2010). Four porphyrin–alkanethiols, three with different methylene linker chain lengths (1a–c, n = 2, 5, and 10) and one with bulkier substituents at three *meso*-positions of porphyrin (**2**, n = 5) were chosen as adsorbates (**Scheme 1**). Compound **2** was synthesized using a route similar to those of 1a–c, as previously reported (**Scheme 2**) (Shinohara and Shinmori, 2016).

The post-synthetic modification of 1-dodecanethiolate–protected AuNPs, namely, thiol/thiolate exchange reaction, was performed by mixing with porphyrin–alkanethiols in toluene, followed by purification by gel permeation chromatography to remove unreacted porphyrin–alkanethiols. Hereafter, the porphyrin–AuNP conjugates are denoted as porphyrin–alkanethiolate@AuNPs. 1a–c@B and 1a–c@C that we previously prepared (Shinohara and Shinmori, 2016) were used for the photophysical characterization of the conjugates. The procedure of the thiol/thiolate exchange reaction was slightly modified for the synthesis of 1b@A and 2@A, where the initial concentrations of porphyrin–alkanethiols were adjusted (c_0 = 15–50 mM) under a constant concentration of the AuNPs, and the reaction time extended to obtain samples with different loading levels. The range of loaded porphyrin–alkanethiolate adsorbates per particle
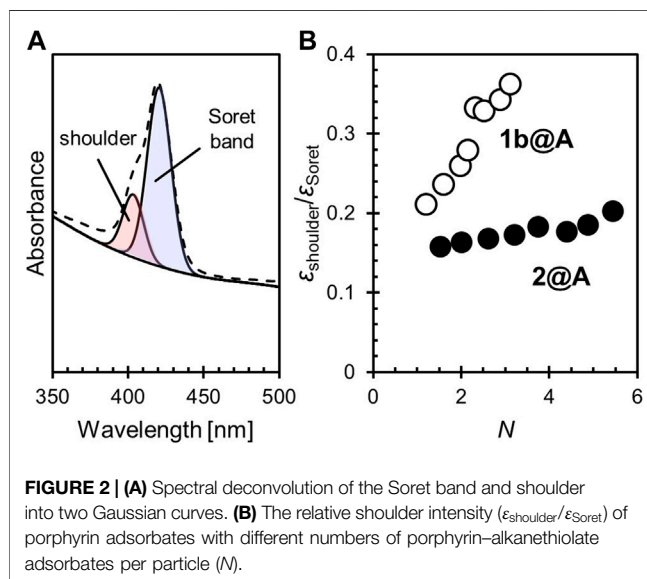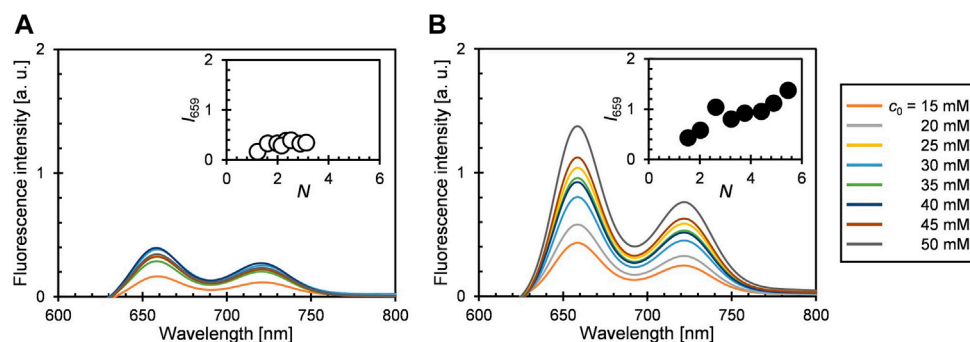
FIGURE 3 | Steady-state fluorescence spectra of **(A)** 1b@A and **(B)** 2@A in toluene (saturated with air at pO_2 = *ca.* 0.21 atm, λ_{ex} = 515 nm). Insets show fluorescence intensity at 659 nm (I_{659}, Q$_{(0-0)}$ band) versus N.
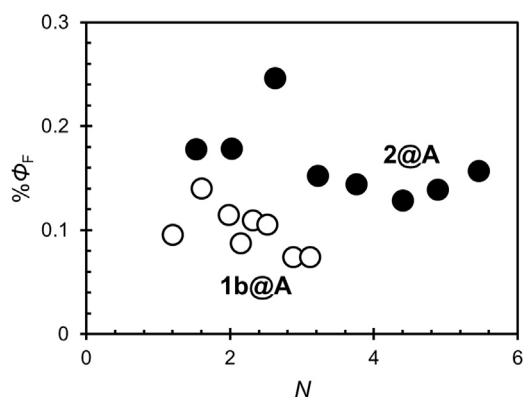
FIGURE 4 | Fluorescence quantum yields (Φ_F) of 1b@A and 2@A with different N.

(N) were determined to be 1.2–3.1 (1b@A) and 1.5–5.5 (2@A) of 126 total thiolate sites (Terrill et al., 1995), respectively. Detailed procedures for the synthesis of A, 2, 1b@A, and 2@A and the determination of N are given in the Experimental Section.

2.2 UV-Vis Extinction Spectra

The UV-vis extinction spectra of 1b@A and 2@A (n = 5, 2.5 ± 0.5 nm) in toluene are shown in **Figure 1**. Both the conjugates exhibit the weak LSPR band of the AuNPs around 510 nm, B band (Soret band) around 420 nm, and four Q bands in the range of 500–700 nm. The spectra indicate the successful loading of porphyrin–alkanethiolates on the AuNPs. The five absorption maxima of porphyrin adsorbates were red-shifted up to 4 nm (**Supplementary Tables S1**, **S2**) compared with those of the corresponding porphyrin–alkanethiols (1b and 2, **Supplementary Figure S1**). A similar bathochromic effect is also observed in other dye–nanoparticle conjugates (Prasanna et al., 2014; Ashjari et al., 2015).

While the extinction spectra of porphyrin–alkanethiols for 1b and 2 are almost identical (**Supplementary Figure S1**), the absorption features of porphyrin adsorbates on the AuNP show different trends. It should be noted that shoulder growth

on the shorter wavelength side of the Soret band around 405 nm was observed, which could be consistent with the blue-shifted absorption band arising from *H*-aggregate exciton formation (Eisfeld and Briggs, 2006). The vertical molecular orientation of the porphyrins on the AuNPs through Au–S covalent bonds allows face-to-face aggregations between neighboring porphyrin adsorbates. This is in contrast to the edge-to-edge *J*-aggregation of the porphyrin adsorbates on AuNPs using multivalent linking, where red-shifted shoulder growth is observed (Kanehara et al., 2008; Ohyama et al., 2009). No observable shoulder growth was found in the Q bands, as predicted by Kasha's theory that chromophores with a higher molar absorption coefficient show stronger exciton couplings (Kasha, 1976).

We qualified the aggregation of porphyrin adsorbates on AuNPs by the ratio of the molar absorption coefficients of the shoulder (~405 nm) to the Soret band (~420 nm), $\varepsilon_{shoulder}/\varepsilon_{Soret}$ (**Figure 2A**, **Supplementary Tables S3**, **S4**). The shoulder growth of 1b@A with increasing N strongly indicates the formation of face-to-face *H*-aggregates (**Figure 2B**). A significantly slower shoulder growth rate of 2@A likely results from the steric effect of the bulky aryl groups at *meso*-positions. The aryl groups that substitute the *meso*-positions of the porphyrin have a large dihedral angle (60–90°) from the porphyrin π plane (Rayati et al., 2008). Therefore, the introduction of the bulky *tert*-butyl groups at the 3 and 5 positions of the aryl groups increase their face-to-face distances in the *H*-aggregates and therefore weaken the exciton coupling (Imahori et al., 2004a).

In these conjugates, only a small fraction of the 1-dodecanethiolate sites were exchanged for porphyrin–alkanethiolate (see 2.1). It may seem strange that the porphyrin adsorbates form the aggregates on the AuNPs, despite their low loading level. It is known that the Au–S covalent adsorbates on the AuNPs dynamically migrate. This enables the self-assembly of adsorbates on the AuNPs when the formation of aggregates is thermodynamically favored (Werts et al., 2004; Tanaka et al., 2006). The aggregation tendency of porphyrins by π–π stacking may contribute to the self-assembly of porphyrins on the AuNPs. Also, the amide bond that links the porphyrin moiety is another functional group that can contribute to the aggregation *via* hydrogen bonds. Such an electrostatic interaction would provide a dominant cohesive force compared

TABLE 1 | Average fluorescence quantum yields (Φ_F) of porphyrin adsorbates on AuNPs with different diameters and size distributions.

Adsorbate	$\Phi_F{}^a$ on AuNP [%]		
	A^b (2.5 ± 0.5 nm)	B^c (2.5 ± 0.9 nm)	C^c (5.6 ± 2.2 nm)
1a	— — —	0.11 ± 0.04	0.14 ± 0.03
1b	0.10 ± 0.02	0.13 ± 0.02	0.15 ± 0.01
1c	— — —	0.20 ± 0.02	0.19 ± 0.01
2	0.15 ± 0.02 (0.17 ± 0.03^d)	— — —	— — —

^{a}In toluene, saturated with air at pO_2 = ca. 0.21 atm.
Sample count.
^{b}n = 8.
^{c}n = 5.
^{d}Value before the outlier point N = 2.6; %Φ_F, 0.25 was rejected.

with π–π stacking in the nonpolar environment (i.e., in toluene) (Pérez–Rentero et al., 2014) and so help one porphyrin adsorbate access an adjacent porphyrin adsorbate followed by aggregation (Sanz et al., 2012).

The broadening of the Soret band (i.e., the increase in the full width at half maximum (FWHM)) was also remarkable in 1b@A but not in 2@A. Interestingly, unlike the shoulder growth, which depends on N, the FWHM only shows a slight expansion according to the increase in N (1b: 12.2 nm, 2: 11.3 nm, 1b@A: 17.0–18.5 nm, and 2@A: 14.2–15.1 nm, **Supplementary Tables S3, S4**). It has been shown, in other systems, that the broadening of the absorption band, which is also observed in chromophores adsorbed on two-dimensional Au substrates, arises from interactions between chromophores and other molecules (e.g., other adsorbates or solvent) and is independent of exciton coupling (Leontidis et al., 1995). The porphyrin adsorbates can interact with not only the AuNPs and other porphyrins but also the remaining 1-dodecanethiolate adsorbates. Although the formation of porphyrin aggregates seems to result in this broadening, in the case of 1b@A, the effect of loading level (i.e., the number of possible porphyrin–porphyrin interactions) is much smaller (18.5–17.0 = 1.5 nm) than other effects (17.0–12.2 = 4.8 nm) associated with the porphyrin loading onto the AuNPs. The smaller broadening for 2@A (15.1–14.2 = 0.9 nm of the effect of a loading level, and 14.2–11.3 = 2.9 nm of other effects) indicates that the bulky *tert*-butyl substituents inhibit not only porphyrin–porphyrin interactions but also interactions with other molecules (e.g., 1-dodecanethiolate adsorbates).

2.3 Steady-State Fluorescence Spectra and Fluorescence Quantum Yields

The steady-state fluorescence spectra of 1b@A and 2@A with various N are shown in **Figure 3**. Two characteristic emission bands were observed at 658 nm and 721–722 nm, respectively (**Supplementary Tables S1, S2**) (Akimoto et al., 1999). Emission maxima (λ_{em}) were slightly red-shifted on loading (λ_{em}: 1b: 654 and 720 nm and 2: 655 and 721 nm) but not affected by N, which is similar to the tendency of the absorption spectra. The fluorescence of the porphyrin adsorbates on the AuNPs is almost quenched (fluorescence quantum yields Φ_F = 0.07–0.14% (1b@A), 0.13–0.25% (2@A), **Figure 4**) compared

to the absence of AuNPs (Φ_F = 11% (1b), 12% (2)). Such strong quenching of the fluorescence by the AuNPs is broadly found in various fluorophores such as pyrene, anthracene, and rhodamine 6G (Uznański et al., 2009; Kabb et al., 2015; Shaikh et al., 2015).

It is known that most fluorophores are non-fluorescent in *H*-aggregates, in contrast to *J*-aggregates which exhibit fluorescence (Liu et al., 2015). In present conjugates, excited porphyrin adsorbates can be quenched not only by the AuNPs but also by the adjacent porphyrin adsorbates. However, Φ_F is nearly independent of N (**Figure 4**), unlike the singlet oxygen quantum yields (Φ_Δ), which decreases exponentially as N increases (Shinohara and Shinmori, 2016). This fact indicates that the porphyrin–porphyrin energy transfer is not the dominant pathway for the quenching of fluorescence in the conjugates. Statistical analysis showed Φ_F of 2@A (0.15 ± 0.02) is higher than that of 1b@A (0.10 ± 0.02%) upon removing the outlier at N = 2.6 that fell more than two standard deviations (SD) above the mean (**Table 1**; the results of statistical rejection and significance tests are shown in **Supplementary Tables S5, S6**). Another potential factor that influences quench efficiency is the spatial freedom of the adsorbates. In this regard, bulky substituents inhibit aggregation and increase the spatial degree of freedom of porphyrin fluorophore, resulting in reduced energy transfer efficiency from porphyrin adsorbates to AuNPs (Best et al., 2007).

2.4 Effects of Linker Chain Length and Nanoparticle Size on Fluorescence

The porphyrin–AuNP conjugates 1a–c@B and 1a–c@C were synthesized as described and determined to have N ranges 3–15 (126 total thiolate sites) and 9–43 (632 total thiolate sites), respectively (spectral and statistical data are shown in **Supplementary Figures S3–S6** and **Supplementary Tables S6–S19**). The $\varepsilon_{shoulder}/\varepsilon_{Soret}$ increases with N on both nanoparticles but shows a non-monotonic trend with the length of the side chain (1b > 1c > 1a, **Supplementary Figure S4A,B**). As mentioned before, the space around the porphyrin becomes larger with the lengthening of the linker and smaller with the tendency of the adsorbate to aggregate. Based on this idea, the aggregation should be the strongest for 1a (n = 2), but it was not in the results. Steric repulsion between the adsorbents is

expected to be one of the factors that determine the aggregation formation in the successive adsorptive loading. One particular consideration in the adsorptive loading onto the nanoparticles to form three-dimensional monolayers is the curvature of the substrate surface. At the same curvature, the shorter linkers increase the porphyrin–porphyrin steric repulsion, which is thought to inhibit the formation of aggregates (Terrill et al., 1995) (**Supplementary Figure S7A,B**). The steric hindrance may also reduce the thiolate density on the gold surface, making such monolayers thermodynamically unfavorable (Ingram et al., 1997). The universal trend in the shoulder growth in adsorbates 1b ($n = 5$) and 1c ($n = 10$), which is independent of the particle size, was found (**Supplementary Figure S4C**). This fact supports our hypothesis: in the adsorptive loading, porphyrins are preferentially loaded next to the already introduced adsorbates and form aggregates. On the other hand, in 1a ($n = 2$), the universal trend was no longer held. This deviation suggests that the aggregation in 1a on the larger nanoparticles C, due to the π–π stacking and/or the hydrogen bonds between the amide groups, with a small curvature is thermodynamically unfavorable (**Supplementary Figure S7C,D**). Imahori et al.(Imahori et al., 2000) reported that for tetraarylporphyrin–amide–alkanethiolate (the same structure as the present system), the porphyrin plane is oriented perpendicular to the two-dimensional Au substrate surface when n is an odd number, which is preferable to form H-aggregates (**Supplementary Figure S8A**). When n is an even number, the porphyrin plane is tilted toward the substrate surface, resulting in weaker exciton coupling by H-aggregation (**Supplementary Figure S8B**). The competitive effects on the aggregation strength are considered to result in the non-monotonic tendency.

The average $\varPhi_F$ of the conjugates is shown in **Table 1**. In both series of conjugates, $\varPhi_F$ slightly increased with methylene linker chain length ($n = 2$, 5, and 10). Note that no significant difference was found between $n = 2$ and 5 (**Supplementary Table S6**), which is considered to be due to the large variance of $n = 2$ (SD = 0.03–0.04%). Strong aggregation at $n = 5$ (odd number) is likely to contribute to the reduction in the fluorescence quantum yield, however is not, as evidenced by the lack of dependence on N. This is consistent with previous reports of an increasing donor–acceptor distance reducing quenching efficiency (Rao and Mayor, 2005; Deng et al., 2019). In addition, similar to the effect of bulky substituents, lengthening of the linker chain increases the space around the end groups (i.e., porphyrin adsorbates) and may inhibit the quenching of fluorescence (Badia et al., 1996). There are numerous reports on LSPR-induced fluorescence enhancement, as well as the enhancement of photoabsorption, Raman scattering (Chung et al., 2011; Bauch et al., 2014; Zvyagina et al., 2018), and singlet oxygen generation (Shinohara and Shinmori, 2016); however, no statistically significant difference was found between the LSPR-silent (**1a–c@B**) and LSPR-active (**1a–c@C**) conjugates (**Supplementary Table S6**). This can be attributed to the fact that the quenching process, which depends on the porphyrin–nanoparticle distance, is dominant in the range of linker chain lengths ($n = 2$–10).

3 EXPERIMENTAL SECTION

3.1 General
All starting materials and reagents were purchased from commercial suppliers and used without further purification. Spectroscopic-grade toluene was saturated with air (partial pressure of oxygen $pO_2 = ca.$ 0.21 atm) before use.

3.2 Apparatus
UV–vis spectra were recorded on a Shimadzu UV-1800 spectrometer equipped with a Peltier temperature controller. Steady-state fluorescence spectra were recorded on a JASCO FP-5300 fluorospectrometer equipped with a temperature controller. Obtained spectra were corrected by referencing to a tungsten sub-reference lamp (JASCO). ^{1}H NMR spectra were recorded on a Bruker AVANCE DPX400 spectrometer (9.4 T) at ambient temperature in deuterated chloroform containing *ca.* 0.03% (v/v) tetramethylsilane as an internal standard ($\delta = 0.00$ ppm). TEM images were obtained using an FEI Tecnai Osiris field emission transmission electron microscope with an accelerating voltage of 200 kV.

3.3 Synthesis
3.3.1 Gold Nanoparticles A (2.5 ± 0.5 nm)
The title nanoparticles A were synthesized by one-phase method reported in the literature (Zheng et al., 2006). To a solution of chloro(triphenylphosphine)gold(I) (Braunstein et al., 2007) (250 mg, 0.505 mmol) and 1-dodecanethiol (250 mg, 1.24 mmol) in chloroform (12.5 ml), borane *tert*-butylamine complex (423 mg, 4.86 mmol) in chloroform/ethanol (12.5 ml/ 5 ml) was added. After 24 h of stirring at ambient temperature, the mixture was concentrated under reduced pressure, and ethanol (40 ml) was added. The precipitate was collected by centrifugation and repeatedly washed with ethanol under sonication to remove starting materials and other byproducts to obtain A as a black waxy solid (61 mg). The mean diameter and size distribution (a standard deviation) were determined to be 2.5 and 0.5 nm, respectively, by transmission electron microscopy (TEM) (**Supplementary Figure S2**).

3.3.2 5-(4-Nitrophenyl)-10,15,20-tris(3,5-di-*tert*-butylphenyl)porphyrin (3)
Pyrrole (2.19 ml, 30.0 mmol), 4-nitrobenzaldehyde (1.14 g, 7.5 mmol), and 3,5-di-*tert*-butylbenzaldehyde (Schuster et al., 2006) (4.92 g, 22.5 mmol) were dissolved in methylene chloride (3 L) and purged with nitrogen for 15 min. To the solution, trifluoroacetic acid (4.44 ml, 60.0 mmol) was added, and the mixture was stirred for 1 h in the dark before neutralization by the addition of triethylamine (14.4 ml, 22.8 mmol). To the mixture, *p*-chloranil (5.52 g, 22.8 mmol) was added, and the solution was stirred for 3 h at ambient temperature. After the removal of the solvent under reduced pressure, the residue was purified by column chromatography (silica gel, hexane:methylene chloride = 2:1), followed by recrystallization (methylene chloride/methanol) to obtain 3 as purple crystals (1.23 g, 16%). ^{1}H NMR (400 MHz, CDCl₃, SiMe₄,

294 K): δ/ppm −2.70 (2H, brs, inner NH), 1.51–1.55 (54H, m, CH₃), 7.80 (1H, t, J = 1.7 Hz, benzene), 7.81 (2H, t, J = 1.7 Hz, benzene), 8.08 (2H, d, J = 1.8 Hz, benzene), 8.08 (4H, d, J = 1.8 Hz, benzene), 8.43 (2H, d, J = 8.6 Hz, benzene), 8.64 (2H, d, J = 8.6 Hz, benzene), 8.74 (2H, d, J = 4.7 Hz, pyrrole), and 8.90–8.97 (6H, m, pyrrole).

3.3.3 5-(4-Aminophenyl)-10,15,20-tris(3,5-di-*tert*-butylphenyl)porphyrin (4)

To a dispersion of **3** (1.39 g, 1.40 mmol) in concentrated hydrochloric acid (50 ml), stannous chloride dihydrate (1.90 g, 8.40 mmol) was added, and the suspension was stirred for 12 h at 70°C. The mixture was neutralized by the addition of sodium carbonate and extracted with methylene chloride. The organic layer was washed with water and brine, dried over sodium sulfate, then concentrated under reduced pressure. The residue was purified by column chromatography (silica gel and dichloromethane) and then recrystallized from methylene chloride/methanol to obtain **4** as purple crystals (0.29 g, 21%). The majority of **3** was unreacted, apparently due to its low solubility. ¹H NMR (400 MHz, CDCl₃, SiMe₄, 296 K): δ/ppm −2.69, (2H, brs, inner NH), 1.50–1.55 (54H, m, CH₃), 4.02 (brs, 2H, NH₂), 7.06 (2H, d, J = 8.2 Hz, benzene), 7.78 (1H, t, J = 1.7 Hz, benzene), 7.79 (2H, t, J = 1.7 Hz, benzene), 8.01 (2H, d, J = 8.2 Hz, benzene), 8.07 (2H, d, J = 1.7 Hz, benzene) 8.09 (4H, d, J = 1.7 Hz, benzene), 8.82–8.92 (6H, m, pyrrole), and 8.94 (2H, d, J = 4.6 Hz, pyrrole).

3.3.4 6-Bromo-*N*-{4-[10,15,20-tris(3,5-di-*tert*-butylphenyl)porphyrin-5-yl]phenyl}hexanamide (5)

To a mixture of ε-bromocaproic acid (*ca.* 10 eq.) and *N,N*-dimethylformamide (1 drop) in toluene, excess thionyl chloride was added. After 1 h of stirring at ambient temperature, the mixture was concentrated under reduced pressure. The residue was redissolved in toluene and concentrated again to obtain ε-bromocaproyl chloride as yellow oil, which was subjected to the following reaction without purification.

An ice-cold mixture of **4** (50.0 mg, 0.0517 mmol) and dry pyridine (0.1 ml) in dry methylene chloride (5 ml), ε-bromocaproyl chloride (*ca.* 10 eq.) in dry methylene chloride was added dropwise. After 1 h of stirring, the mixture was concentrated under reduced pressure to obtain crude **5** as purple solid. This material was subjected to the following reaction without further purification.

3.3.5 6-Acetylthio-*N*-{4-[10,15,20-tris(3,5-di-*tert*-butylphenyl)porphyrin-5-yl]phenyl}hexanamide (6)

Crude **5** was dissolved in bench *N,N*-dimethylformamide, and potassium thioacetate (50 mg, 0.44 mmol) was added at 0°C. After 1 h of stirring at ambient temperature, the mixture was diluted with methylene chloride (40 ml) and washed with water. The organic layer was dried over sodium sulfate and concentrated under reduced pressure. The residue was purified by column chromatography (silica gel and methylene chloride) and subsequent reprecipitation from methylene chloride/methanol

to obtain **6** as purple solid. 49 mg (83% from **4**). ¹H NMR (400 MHz, CDCl₃, SiMe₄, 296 K): δ/ppm −2.71 (2H, brs, inner NH), 1.50–1.56 (54H, m, CH₃), 1.58 (2H, quint, J = 7.0 Hz, CH₂), 1.72 (2H, quint, J = 7.3 Hz, CH₂), 1.91 (2H, quint, J = 7.5 Hz, CH₂), 2.54 (2H, t, J = 7.5 Hz, NHCOCH₂), 2.96 (2H, t, J = 7.3 Hz, AcSCH₂), 7.56 (1H, brs, NHCO), 7.78 (1H, t, J = 1.6 Hz, benzene), 7.79 (2H, t, J = 1.6 Hz, benzene), 7.91 (2H, d, J = 8.2 Hz, benzene), 8.07 (2H, d, J = 1.7 Hz, benzene), 8.08 (4H, d, J = 1.7 Hz, benzene), 8.19 (2H, d, J = 8.3 Hz, benzene), 8.86 (2H, d, J = 4.6 Hz, pyrrole), and 8.87–8.92 (6H, m, pyrrole).

3.3.6 6-Mercapto-*N*-{4-[10,15,20-tris(3,5-di-tert-butylphenyl)porphyrin-5-yl]phenyl}hexanamide (2)

The title compound **2** was synthesized according to the method reported in the literature (Imahori et al., 2004b). To a solution of **6** (34.0 mg, 0.0299 mmol) in degassed tetrahydrofuran (1 ml), potassium hydroxide (30 mg, 0.53 mmol) was added in degassed methanol (1 ml) and the mixture refluxed for 15 min under nitrogen. The mixture was neutralized by the addition of acetic acid (0.1 ml) and then concentrated under reduced pressure. The residue was purified by column chromatography (silica gel and methylene chloride) and subsequent reprecipitation from methylene chloride/methanol to obtain **2** as purple solid. 22 mg (66%). ¹H NMR (400 MHz, CDCl₃, SiMe₄, and 296 K): δ/ppm −2.70 (2H, brs, inner NH), 1.41 (1H, t, J = 7.8 Hz, SH), 1.51–1.55 (54H, m, CH₃), 1.60 (2H, quint, J = 7.1 Hz, CH₂), 1.75 (2H, quint, J = 7.3 Hz, CH₂), 1.88 (2H, quint, J = 7.5 Hz, CH₂), 2.52 (2H, t, J = 7.4 Hz, NHCOCH₂), 2.62 (2H, q, J = 7.2 Hz, HSCH₂), 7.43 (1H, brs, NHCO), 7.78 (1H, t, J = 1.8 Hz, benzene), 7.79 (2H, t, J = 1.8 Hz, benzene), 7.90 (2H, d, J = 8.3 Hz, benzene), 8.07 (2H, d, J = 1.8 Hz, benzene), 8.08 (4H, d, J = 1.9 Hz, benzene), 8.15–8.19 (2H, d, 8.4 Hz, benzene), 8.85 (2H, d, J = 4.7 Hz, pyrrole), and 8.87–8.93 (6H, m, pyrrole).

3.3.7 Porphyrin–AuNP conjugates (1a@A and 2@A)

The solution of A (1 mg/ml = 9.6 μM, assuming the chemical formula of Au₄₀₀(C₁₂H₂₅S)₁₂₆ = 1.04 × 10⁵ Da (Terrill et al., 1995)) and porphyrin–alkanethiol (i.e., 1b or 2, 15–50 mM) in toluene (1 ml), was allowed to equilibrate for 24 h at ambient temperature. The mixture was concentrated under reduced pressure at ambient temperature using a centrifugal evaporator (EYELA CVE-2000 equipped with a common oil rotary vacuum pump). The residue was purified twice by size exclusion chromatography (BioBeads S-X1, toluene) to remove unreacted porphyrin–alkanethiol.

3.4 UV-Vis Extinction Spectra

Purified porphyrin–AuNP conjugates were dissolved in toluene to achieve an absorbance at 515 nm of 0.20 ± 0.01 [−], and extinction spectra were recorded. The same solution was subjected to fluorescence measurement (*vide infra*).

The molar extinction coefficients (ε) of AuNPs are related to their size and surface dielectric constant (Huang and El-Sayed, 2010). In the thiol/thiolate exchange reaction, no significant size change occurs, or even if it does occur, its effect is negligible (Hostetler et al., 1999). The surface dielectric constant mainly reflects the structure of the adsorbates, but since both the original

1-dodecanethiolate and the porphyrin–alkanethiolate are similar, the surface dielectric constants are unlikely to change. Assuming that the porphyrin–alkanethiolate adsorbates are also not affected by the AuNPs, the extinction spectrum of the porphyrin–AuNP conjugates can be considered as the sum of the extinction spectra of the 1-dodecanethiolate–protected AuNPs and the porphyrin–alkanethiol.

Based on this assumption, the extinction spectra of porphyrin–AuNP conjugates were deconvoluted using the following equation (Shinohara and Shinmori, 2016; Shinohara et al., 2020):

$$A(\lambda) = a \times \varepsilon_{Por}(\lambda) + b \times \varepsilon_{AuNP}(\lambda) + R(\lambda). \quad (1)$$

Here, $A(\lambda)$ is the actual extinction spectrum of porphyrin–AuNP conjugates. $\varepsilon_{Por}(\lambda)$ and $\varepsilon_{AuNP}(\lambda)$ are the separately measured molar absorption coefficients of porphyrin–alkanethiol (1a–c or 2) and 1-dodecanethiolate-protected AuNPs (A–C), respectively. The proportional coefficients a and b were determined by the non-linear least-squares method ($300 \leqq \lambda \leqq 800$ nm), and the residue $R(\lambda)$ was obtained. Finally, to obtain the number of porphyrin–alkanethiolate adsorbates per particle (N), as the quotient of the coefficients a and b, the following equation was used:

$$N = a/b. \quad (2)$$

To qualify the aggregation of porphyrin adsorbates on AuNPs, $\varepsilon_{Por}(\lambda)$ was further deconvoluted into two Gaussian functions, and the relative intensity of shoulder to the Soret band ($\varepsilon_{shoulder}/\varepsilon_{Soret}$) was obtained (**Supplementary Tables S3**, **S4**, **S13–S18**).

3.5 Fluorescence Spectra

Five milliliters of the solution of porphyrin–AuNP conjugates, used for the extinction spectra measurement (absorbance at 515 nm–0.2), was volumetrically diluted by toluene to make 50 ml. The absorbance of the solution was reduced to below 0.02 (>95% transmittance) in the measurement range, to ensure the elimination of reabsorption of fluorescence by the sample itself. Φ_F was determined by the following equation (Zhang et al., 2014):

$$\Phi_F = \Phi_{F,ref} \times \frac{A_{ref}}{A} \times \frac{S}{S_{ref}}, \quad (3)$$

where $\Phi_{F,ref}$ shows Φ_F of *meso*-tetraphenylporphyrin (10^{-8} M, $\Phi_{F,ref} = 0.11$ (Seybold and Gouterman, 1969)) as an external standard, and A and S show absorbance of porphyrin adsorbates at an excitation wavelength (515 nm) and the area of fluorescence spectra (600–800 nm), respectively.

4 CONCLUSION

In this work, a series of porphyrin–alkanethiols that have different linker chain lengths and substituents were loaded on the AuNPs by the post-synthetic thiol/thiolate exchange

reaction. The conditions of the reaction were optimized to obtain low loading levels of total thiolate sites on the AuNPs. The conjugates retain the unique photoabsorption features of porphyrin (the Soret band and Q band) after loading. Slight red-shift, shoulder growth, and broadening were observed in the Soret band but not in the Q bands. Interestingly, porphyrin adsorbates form *H*-aggregates soon after the onset of the thiol/thiolate exchange reaction. Fluorescence in the adsorbates was determined to be strongly quenched, due to intraparticle energy transfer from the excited adsorbates to the AuNPs. Contrary to our hypothesis, the aggregation contributes little to the fluorescence quenching. Fluorescence quantum yields are affected by linker chain length but neither by the loading level nor nanoparticle diameter, unlike our previous report on the singlet oxygen quantum yields. Thus, this work has advanced our understanding of the photophysical properties of dye adsorbates on AuNPs.

DATA AVAILABILITY STATEMENT

The raw data supporting the conclusion of this article will be made available by the authors, without undue reservation.

AUTHOR CONTRIBUTIONS

AS conducted the majority of experiments. AS and GS analyzed the data and wrote the manuscript. TN and HS are joint principal investigators; they conceived the work and designed the experiments. All authors discussed the results and commented on the manuscript.

FUNDING

ACKNOWLEDGMENTS

SUPPLEMENTARY MATERIAL

The Supplementary Material for this article can be found online at: https://www.frontiersin.org/articles/10.3389/fchem.2021.777041/full#supplementary-material

REFERENCES

Akimoto, S., Yamazaki, T., Yamazaki, I., and Osuka, A. (1999). Excitation Relaxation of Zinc and Free-Base Porphyrin Probed by Femtosecond Fluorescence Spectroscopy. *Chem. Phys. Lett.* 309, 177–182. doi:10.1016/S0009-2614(99)00688-0

Akiyama, T., Nakada, M., Terasaki, N., and Yamada, S. (2006). Photocurrent Enhancement in a Porphyrin-Gold Nanoparticle Nanostructure Assisted by Localized Plasmon Excitation. *Chem. Commun.*, 395–397. doi:10.1039/B511487J

Ashjari, M., Dehfuly, S., Fatehi, D., Shabani, R., and Koruji, M. (2015). Efficient Functionalization of Gold Nanoparticles Using Cysteine Conjugated Protoporphyrin IX for Singlet Oxygen Production *In Vitro*. *RSC Adv.* 5, 104621–104628. doi:10.1039/C5RA15862A

Badia, A., Singh, S., Demers, L., Cuccia, L., Brown, G. R., and Lennox, R. B. (1996). Self-Assembled Monolayers on Gold Nanoparticles. *Chem. Eur. J.* 2, 359–363. doi:10.1002/chem.19960020318

Barona-Castaño, J., Carmona-Vargas, C., Brocksom, T., and de Oliveira, K. (2016). Porphyrins as Catalysts in Scalable Organic Reactions. *Molecules* 21, 310. doi:10.3390/molecules21030310

Bauch, M., Toma, K., Toma, M., Zhang, Q., and Dostalek, J. (2014). Plasmon-Enhanced Fluorescence Biosensors: a Review. *Plasmonics* 9, 781–799. doi:10.1007/s11468-013-9660-5

Benniston, A. C., Davies, M., Harriman, A., and Sams, C. (2003). Photophysical Properties of a Supramolecular Interlocked Conjugate. *J. Phys. Chem. A.* 107, 4669–4675. doi:10.1021/jp034147z

Best, R. B., Merchant, K. A., Gopich, I. V., Schuler, B., Bax, A., and Eaton, W. A. (2007). Effect of Flexibility and Cis Residues in Single-Molecule FRET Studies of Polyproline. *Proc. Natl. Acad. Sci.* 104, 18964–18969. doi:10.1073/pnas.0709567104

Braunstein, P., Lehner, H., Matt, D., Burgess, K., and Ohlmeyer, M. J. (2007). A Platinum-Gold Cluster: Chloro-1κCl -Bis(Triethylphosphine-1κ P)Bis(Triphenyl- Phosphine)-2κ P, 3κP-Triangulo - Digold-Platinum(1 +) Trifluoromethanesulfonate. *Inorg. Synth.* 27, 218–221. doi:10.1002/9780470132586.ch42

Brust, M., Walker, M., Bethell, D., Schiffrin, D. J., and Whyman, R. (1994). Synthesis of Thiol-Derivatised Gold Nanoparticles in a Two-phase Liquid-Liquid System. *J. Chem. Soc. Chem. Commun.*, 801–802. doi:10.1039/C39940000801

Chung, T., Lee, S.-Y., Song, E. Y., Chun, H., and Lee, B. (2011). Plasmonic Nanostructures for Nano-Scale Bio-Sensing. *Sensors* 11, 10907–10929. doi:10.3390/s111110907

Deng, H., Ray, P. C., Ghann, W. E., Uddin, J., Samokhvalov, A., and Yu, H. (2019). Distance-dependent Fluorescence Quenching on a Silver Nanoparticle Surface. *Chem. Lett.* 48, 1504–1506. doi:10.1246/cl.190684

Do, T. T. A., and Imae, T. (2021). Photodynamic and Photothermal Effects of Carbon Dot-Coated Magnetite- and Porphyrin-Conjugated Confeito-like Gold Nanoparticles. *Bcsj* 94, 2079–2088. doi:10.1246/bcsj.20210192

Doering, W. E., and Nie, S. (2003). Spectroscopic Tags Using Dye-Embedded Nanoparticles and Surface-Enhanced Raman Scattering. *Anal. Chem.* 75, 6171–6176. doi:10.1021/ac034672u

Dulkeith, E., Morteani, A. C., Niedereichholz, T., Klar, T. A., Feldmann, J., Levi, S. A., et al. (2002). Fluorescence Quenching of Dye Molecules Near Gold Nanoparticles: Radiative and Nonradiative Effects. *Phys. Rev. Lett.* 89, 203002. doi:10.1103/PhysRevLett.89.203002

Dulkeith, E., Ringler, M., Klar, T. A., Feldmann, J., Muñoz Javier, A., and Parak, W. J. (2005). Gold Nanoparticles Quench Fluorescence by Phase Induced Radiative Rate Suppression. *Nano Lett.* 5, 585–589. doi:10.1021/nl0480969

Eisfeld, A., and Briggs, J. S. (2006). The J- and H-Bands of Organic Dye Aggregates. *Chem. Phys.* 324, 376–384. doi:10.1016/j.chemphys.2005.11.015

Ghosh, A., Yoshida, M., Suemori, K., Isago, H., Kobayashi, N., Mizutani, Y., et al. (2019). Soft Chromophore Featured Liquid Porphyrins and Their Utilization toward Liquid Electret Applications. *Nat. Commun.* 10, 4210. doi:10.1038/s41467-019-12249-8

Glotov, A., Stavitskaya, A., Chudakov, Y., Ivanov, E., Huang, W., Vinokurov, V., et al. (2019). Mesoporous Metal Catalysts Templated on Clay Nanotubes. *Bcsj* 92, 61–69. doi:10.1246/bcsj.20180207

Han, H.-H., Tian, H., Zang, Y., Sedgwick, A. C., Li, J., Sessler, J. L., et al. (2021). Small-molecule Fluorescence-Based Probes for Interrogating Major Organ Diseases. *Chem. Soc. Rev.* 50, 9391–9429. doi:10.1039/D0CS01183E

Hasobe, T. (2021). Organic-Inorganic Hybrid Molecular Architectures Utilizing Self-Assembled Monolayers for Singlet Fission and Light Energy Conversion. *Chem. Lett.* 50, 615–622. doi:10.1246/cl.200858

Hong, S., and Li, X. (2013). Optimal Size of Gold Nanoparticles for Surface-Enhanced Raman Spectroscopy under Different Conditions. *J. Nanomater.* 2013, 1–9. doi:10.1155/2013/790323

Hostetler, M. J., Templeton, A. C., and Murray, R. W. (1999). Dynamics of Place-Exchange Reactions on Monolayer-Protected Gold Cluster Molecules. *Langmuir* 15, 3782–3789. doi:10.1021/la981598f

Huang, X., and El-Sayed, M. A. (2010). Gold Nanoparticles: Optical Properties and Implementations in Cancer Diagnosis and Photothermal Therapy. *J. Adv. Res.* 1, 13–28. doi:10.1016/j.jare.2010.02.002

Imahori, H., Arimura, M., Hanada, T., Nishimura, Y., Yamazaki, I., Sakata, Y., et al. (2001). Photoactive Three-Dimensional Monolayers: Porphyrin−Alkanethiolate-Stabilized Gold Clusters. *J. Am. Chem. Soc.* 123, 335–336. doi:10.1021/ja002838s

Imahori, H., Hosomizu, K., Mori, Y., Sato, T., Ahn, T. K., Kim, S. K., et al. (2004a). Substituent Effects of Porphyrin Monolayers on the Structure and Photoelectrochemical Properties of Self-Assembled Monolayers of Porphyrin on Indium−Tin Oxide Electrode. *J. Phys. Chem. B* 108, 5018–5025. doi:10.1021/jp037625e

Imahori, H., Kashiwagi, Y., Endo, Y., Hanada, T., Nishimura, Y., Yamazaki, I., et al. (2004b). Structure and Photophysical Properties of Porphyrin-Modified Metal Nanoclusters with Different Chain Lengths. *Langmuir* 20, 73–81. doi:10.1021/la035435p

Imahori, H., Norieda, H., Nishimura, Y., Yamazaki, I., Higuchi, K., Kato, N., et al. (2000). Chain Length Effect on the Structure and Photoelectrochemical Properties of Self-Assembled Monolayers of Porphyrins on Gold Electrodes. *J. Phys. Chem. B* 104, 1253–1260. doi:10.1021/jp992768f

Imahori, H., Norieda, H., Ozawa, S., Ushida, K., Yamada, H., Azuma, T., et al. (1998). Chain Length Effect on Photocurrent from Polymethylene-Linked Porphyrins in Self-Assembled Monolayers. *Langmuir* 14, 5335–5338. doi:10.1021/la980351f

Ingram, R. S., Hostetler, M. J., and Murray, R. W. (1997). Poly-hetero-ω-functionalized Alkanethiolate-Stabilized Gold Cluster Compounds. *J. Am. Chem. Soc.* 119, 9175–9178. doi:10.1021/ja971734n

Jin, R. (2010). Quantum Sized, Thiolate-Protected Gold Nanoclusters. *Nanoscale* 2, 343–362. doi:10.1039/B9NR00160C

Kabb, C. P., Carmean, R. N., and Sumerlin, B. S. (2015). Probing the Surface-Localized Hyperthermia of Gold Nanoparticles in a Microwave Field Using Polymeric Thermometers. *Chem. Sci.* 6, 5662–5669. doi:10.1039/C5SC01535A

Kanehara, M., Takahashi, H., and Teranishi, T. (2008). Gold(0) Porphyrins on Gold Nanoparticles. *Angew. Chem. Int. Ed.* 47, 307–310. doi:10.1002/anie.200703943

Kasha, M. (1976). "Molecular Excitons in Small Aggregates," in *Spectroscopy of the Excited State* (Boston, MA: Springer US), 337–363. doi:10.1007/978-1-4684-2793-6_12

Kinoshita, T., Fujisawa, J.-i., Nakazaki, J., Uchida, S., Kubo, T., and Segawa, H. (2012). Visible to Near-Infrared Photoelectric Conversion in a Dye-Sensitized Solar Cell Using Ru(II) Porphyrin with Azopyridine Axial Ligands. *Jpn. J. Appl. Phys.* 51, 10NE02. doi:10.1143/jjap.51.10ne02

Kovaliov, M., Wachtel, C., Yavin, E., and Fischer, B. (2014). Synthesis and Evaluation of a Photoresponsive Quencher for Fluorescent Hybridization Probes. *Org. Biomol. Chem.* 12, 7844–7858. doi:10.1039/C4OB01185F

Kreibig, U., and Vollmer, M. (1995). *Optical Properties of Metal Clusters*. Berlin, Heidelberg: Springer. doi:10.1007/978-3-662-09109-8

Kubo, Y., Yamamoto, M., Ikeda, M., Takeuchi, M., Shinkai, S., Yamaguchi, S., et al. (2003). A Colorimetric and Ratiometric Fluorescent Chemosensor with Three Emission Changes: Fluoride Ion Sensing by a Triarylborane- Porphyrin Conjugate. *Angew. Chem. Int. Ed.* 42, 2036–2040. doi:10.1002/anie.200250788

Kulinich, A. V., Mikitenko, E. K., and Ishchenko, A. A. (2016). Scope of Negative Solvatochromism and Solvatofluorochromism of Merocyanines. *Phys. Chem. Chem. Phys.* 18, 3444–3453. doi:10.1039/C5CP06653K

Leontidis, E., Suter, U. W., Schuetz, M., Luethi, H.-P., Renn, A., and Wild, U. P. (1995). The Mechanism of Spectral Shift and Inhomogeneous Broadening of an

Aromatic Chromophore in a Polymer Glass. *J. Am. Chem. Soc.* 117, 7493–7507. doi:10.1021/ja00133a022

Liu, J., Zhang, H., Dong, H., Meng, L., Jiang, L., Jiang, L., et al. (2015). High Mobility Emissive Organic Semiconductor. *Nat. Commun.* 6, 10032. doi:10.1038/ncomms10032

Lu, F., and Nakanishi, T. (2019). Solvent-Free Luminous Molecular Liquids. *Adv. Opt. Mater.* 7, 1900176. doi:10.1002/adom.201900176

Ohyama, J., Hitomi, Y., Higuchi, Y., and Tanaka, T. (2009). Size Controlled Synthesis of Gold Nanoparticles by Porphyrin with Four Sulfur Atoms. *Top. Catal.* 52, 852–859. doi:10.1007/s11244-009-9229-x

Pan, S., Wang, Z., and Rothberg, L. J. (2006). Enhancement of Adsorbed Dye Monolayer Fluorescence by a Silver Nanoparticle Overlayer. *J. Phys. Chem. B* 110, 17383–17387. doi:10.1021/jp063191m

Pérez-Rentero, S., Grijalvo, S., Peñuelas, G., Fàbrega, C., and Eritja, R. (2014). Thioctic Acid Derivatives as Building Blocks to Incorporate DNA Oligonucleotides onto Gold Nanoparticles. *Molecules* 19, 10495–10523. doi:10.3390/molecules190710495

Prasanna, S. W., Poorani, G., Kumar, M. S., Aruna, P., and Ganesan, S. (2014). Photodynamic Efficacy of Rosebengal-Gold Nanoparticle Complex on Vero and HeLa Cell Lines. *mat express* 4, 359–366. doi:10.1166/mex.2014.1173

Rao, M., and Mayor, S. (2005). Use of Forster's Resonance Energy Transfer Microscopy to Study Lipid Rafts. *Biochim. Biophys. Acta (Bba) - Mol. Cel Res.* 1746, 221–233. doi:10.1016/j.bbamcr.2005.08.002

Rayati, S., Zakavi, S., Motlagh, S. H., Noroozi, V., Razmjoo, M., Wojtczak, A., et al. (2008). β-Tetra-brominated Meso-Tetraphenylporphyrin: A Conformational Study and Application to the Mn-Porphyrin Catalyzed Epoxidation of Olefins with Tetrabutylammonium Oxone. *Polyhedron* 27, 2285–2290. doi:10.1016/j.poly.2008.04.019

Sanz, V., Conde, J., Hernández, Y., Baptista, P. V., Ibarra, M. R., and de la Fuente, J. M. (2012). Effect of PEG Biofunctional Spacers and TAT Peptide on dsRNA Loading on Gold Nanoparticles. *J. Nanopart Res.* 14, 917. doi:10.1007/s11051-012-0917-2

Sato, Y. (2020). Design of Fluorescent Peptide Nucleic Acid Probes Carrying Cyanine Dyes for Targeting Double-Stranded RNAs for Analytical Applications. *Bcsj* 93, 406–413. doi:10.1246/bcsj.20190361

Schuster, D. I., MacMahon, S., Guldi, D. M., Echegoyen, L., and Braslavsky, S. E. (2006). Synthesis and Photophysics of Porphyrin-Fullerene Donor-Acceptor Dyads with Conformationally Flexible Linkers. *Tetrahedron* 62, 1928–1936. doi:10.1016/j.tet.2005.07.127

Seybold, P. G., and Gouterman, M. (1969). Porphyrins. *J. Mol. Spectrosc.* 31, 1–13. doi:10.1016/0022-2852(69)90335-X

Shaikh, A. J., Rabbani, F., Sherazi, T. A., Iqbal, Z., Mir, S., and Shahzad, S. A. (2015). Binding Strength of Porphyrin−Gold Nanoparticle Hybrids Based on Number and Type of Linker Moieties and a Simple Method to Calculate Inner Filter Effects of Gold Nanoparticles Using Fluorescence Spectroscopy. *J. Phys. Chem. A.* 119, 1108–1116. doi:10.1021/jp510924n

Shin, E.-J., and Lee, S.-H. (2002). Substituent Effect on Fluorescence and Photoisomerization of 1-(9-Anthryl)-2-(4-Pyridyl)ethenes. *Bull. Korean Chem. Soc.* 23, 1309–1338. doi:10.5012/bkcs.2002.23.9.1309

Shinohara, A., Pan, C., Wang, L., and Shinmori, H. (2020). Acid-base Controllable Singlet Oxygen Generation in Supramolecular Porphyrin-Gold Nanoparticle Composites Tethered by Rotaxane Linkers. *J. Porphyrins Phthalocyanines* 24, 171–180. doi:10.1142/S108842461950086X

Shinohara, A., and Shinmori, H. (2016). Controlled Generation of Singlet Oxygen by Porphyrin-Appended Gold Nanoparticles. *Bcsj* 89, 1341–1343. doi:10.1246/bcsj.20160254

Tanaka, S., Suzuki, H., Kamikado, T., Okuno, Y., and Mashiko, S. (2006). Conformation Control and High-Resolution Noncontact Atomic Force Microscopy Study of Porphyrin Derivatives on the Substrates. *J. Surf. Sci. Soc. Jpn.* 27, 72–78. doi:10.1380/jsssj.27.72

Terrill, R. H., Postlethwaite, T. A., Chen, C.-h., Poon, C.-D., Terzis, A., Chen, A., et al. (1995). Monolayers in Three Dimensions: NMR, SAXS, Thermal, and Electron Hopping Studies of Alkanethiol Stabilized Gold Clusters. *J. Am. Chem. Soc.* 117, 12537–12548. doi:10.1021/ja00155a017

Thomas, K. G., and Kamat, P. V. (2003). Chromophore-Functionalized Gold Nanoparticles. *Acc. Chem. Res.* 36, 888–898. doi:10.1021/ar030030h

Uznański, P., Kurjata, J., and Bryszewska, E. (2009). Modification of Gold Nanoparticle Surfaces with Pyrenedisulfide in Ligand-Protected Exchange Reactions. *Mater. Sci.* 27, 695–670.

Watanabe, Y., Sasabe, H., and Kido, J. (2019). Review of Molecular Engineering for Horizontal Molecular Orientation in Organic Light-Emitting Devices. *Bcsj* 92, 716–728. doi:10.1246/bcsj.20180336

Werts, M. H. V., Zaim, H., and Blanchard-Desce, M. (2004). Excimer Probe of the Binding of Alkyl Disulfides to Gold Nanoparticles and Subsequent Monolayer dynamicsElectronic Supplementary Information (ESI) Available: Absorption Spectra of Nanoparticle Solutions in Toluene. *Photochem. Photobiol. Sci.* 3, 29–32. See http://www.rsc.Org/suppdata/pp/b3/b310952f/. doi:10.1039/b310952f

Zhang, X.-F., Zhang, J., and Liu, L. (2014). Fluorescence Properties of Twenty Fluorescein Derivatives: Lifetime, Quantum Yield, Absorption and Emission Spectra. *J. Fluoresc.* 24, 819–826. doi:10.1007/s10895-014-1356-5

Zheng, N., Fan, J., and Stucky, G. D. (2006). One-Step One-phase Synthesis of Monodisperse Noble-Metallic Nanoparticles and Their Colloidal Crystals. *J. Am. Chem. Soc.* 128, 6550–6551. doi:10.1021/ja0604717

Zvyagina, A. I., Ezhov, A. A., Meshkov, I. N., Ivanov, V. K., Birin, K. P., König, B., et al. (2018). Plasmon-enhanced Light Absorption at Organic-Coated Interfaces: Collectivity Matters. *J. Mater. Chem. C* 6, 1413–1420. doi:10.1039/C7TC04905F

Conflict of Interest: The authors declare that the research was conducted in the absence of any commercial or financial relationships that could be construed as a potential conflict of interest.

Publisher's Note: All claims expressed in this article are solely those of the authors and do not necessarily represent those of their affiliated organizations, or those of the publisher, the editors, and the reviewers. Any product that may be evaluated in this article, or claim that may be made by its manufacturer, is not guaranteed or endorsed by the publisher.

Molecular Approaches to Protein Dimerization: Opportunities for Supramolecular Chemistry

Dung Thanh Dang*

Faculty of Biotechnology, Ho Chi Minh City Open University, Ho Chi Minh City, Vietnam

Protein dimerization plays a key role in many biological processes. Most cellular events such as enzyme activation, transcriptional cofactor recruitment, signal transduction, and even pathogenic pathways are significantly regulated via protein-protein interactions. Understanding and controlling the molecular mechanisms that regulate protein dimerization is crucial for biomedical applications. The limitations of engineered protein dimerization provide an opportunity for molecular chemistry to induce dimerization of protein in biological events. In this review, molecular control over dimerization of protein and activation in this respect are discussed. The well known molecule glue-based approaches to induced protein dimerization provide powerful tools to modulate the functionality of dimerized proteins and are shortly highlighted. Subsequently metal ion, nucleic acid and host-guest chemistry are brought forward as novel approaches for orthogonal control over dimerization of protein. The specific focus of the review will be on host-guest systems as novel, robust and versatile supramolecular approaches to modulate the dimerization of proteins, using functional proteins as model systems.

Keywords: approaches, inducers, protein, dimerization, supramolecular chemistry

INTRODUCTION

Protein dimerization is a crucial biological process in which proteins interact, as for example homo- or hetero-dimers, to form a functional assembly (**Figure 1**). In fact, proteins rarely show function and activity in their isolated form in a biological environment. The self-assembly of proteins to form dimers or higher oligomeric aggregates is a common biophysical phenomenon, which occurs in every cellular compartment such as cell membranes, the nucleus, and the cytosol. All cellular pathways such as enzymatic activation (Citri and Yarden, 2006; Baselga and Swain, 2009), signal transduction (Ferrer-Soler et al., 2007; Ahsan, 2016), and even pathogenic pathways (Hynes and Lane, 2005) are significantly regulated *via* protein dimerization.

Regulation of protein dimerization is an essential process for the growth and development of organisms under the stimuli of intrinsic or extrinsic factors in the natural environment (Marianayagam et al., 2004). Therefore, understanding and modulating the molecular mechanisms of protein dimerization and their function represents the cutting edge of research and provides multiple entries for biomedical applications. Protein engineering represents one approach to induce or control protein dimerization, thereby facilitating an increase in protein stability and/or function (Grueninger et al., 2008; Ardejani et al., 2011). For example, engineering a dimeric interface of initiator caspase-9 resulted in caspase activation through induced proximity. Shi and coworkers have generated a dimeric caspase-9 by replacing

FIGURE 1 | Schematic representation of protein homo-and hetero-dimerization.
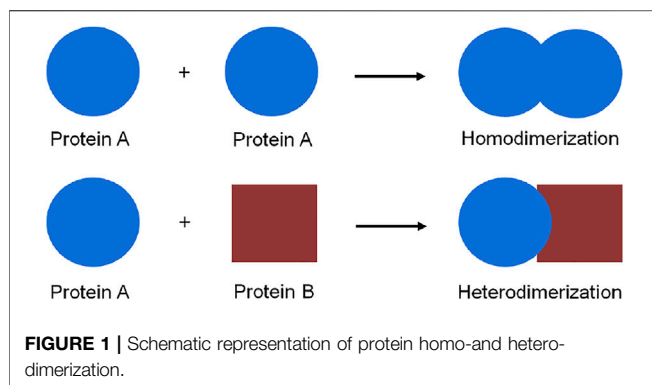
five residues in the β6 strand of caspase-9 (Gly^{402}-Cys-Phe-Asn-Phe^{406}) with those normally present in caspase-3 (Cys^{264}-Ile-Val-Ser-Met^{268}), resulting in a dimeric interface of an engineered caspase-9. The engineered caspase-9 functioned as homodimer in buffered solution, leading to an increase in enzymatic activity *in vitro* and in cell-based studies (Chao et al., 2005). Additionally, protein can be engineered to feature enhanced dimerization via the introduction of coiled-coil zipper sequences (Junius et al., 1996; Mason and Arndt, 2004). The coiled-coil zipper functions through hydrophobic interactions between leucine rich motifs which form homo- or hetero-dimeric states. An example in this respect is the dimer formation between c-Jun and c-Fos, to form functional DNA transcriptional factors (Mason and Arndt, 2004; Gazon et al., 2017). The dimer formation of leucine-rich zippers provides a bioengineering approach that enables induced dimerization of proteins bearing leucine-rich repeats. The introduction of a leucine zipper motif to quiescent cell proline dipeptidase (QPP), enabled QPP homodimerization, which is essential for QPP activation (Chiravuri et al., 2000). The leucine zipper motifs

were also applied to the induced dimerization of other proteins such as protein kinase (MLK-3) (Leung and Lassam, 1998) and tyrosine hydroxylase (Vrana et al., 1994) in which leucine zipper-induced protein dimerization showed a significant increase in enzymatic activity. Notwithstanding the great success achieved, the current approaches to engineered protein dimerization interfaces have their limitations, especially in terms of control over dimerization of protein dimerization event. Mutations made in the active domains of target proteins may change their biological structure and function. Approaches based on the addition of dimeric interfaces, such as *via* mutation interfaces or addition of leucine zipper-induced domains, do not provide a switching mechanism for temporal control or regulation of the dimerization. Therefore, the function of the resulting proteins in their biological processes is difficult to control. Protein dimerization approaches which are based on external molecular signals, capable of inducing or blocking dimerization, provide a strong point of entry to explore and control the molecular mechanisms of protein dimerization.

A powerful chemical approach currently used to control protein dimerization is via the use of molecular glues. More recently as well the use of metal ion, nucleic acid and synthetic host-guest systems has been explored (**Figure 2**). All these chemical elements act by bringing two proteins together to induce dimerization, resulting in the activation or inhibition of biological events. The reversibility of chemically-induced protein dimerization is attractive for biomedical research, as it enables an added degree of control over protein dimerization and activation. In this review, a schematic overview and selected examples of protein dimerization mediated by different molecular inducers of dimerization are provided, with a focus on the supramolecular chemistry based approaches. Synthetic host-guest systems are brought forward as novel, robust and versatile entries to modulate the dimerization of proteins.

FIGURE 2 | Schematic representation of dimerization of protein *via* molecular approaches.
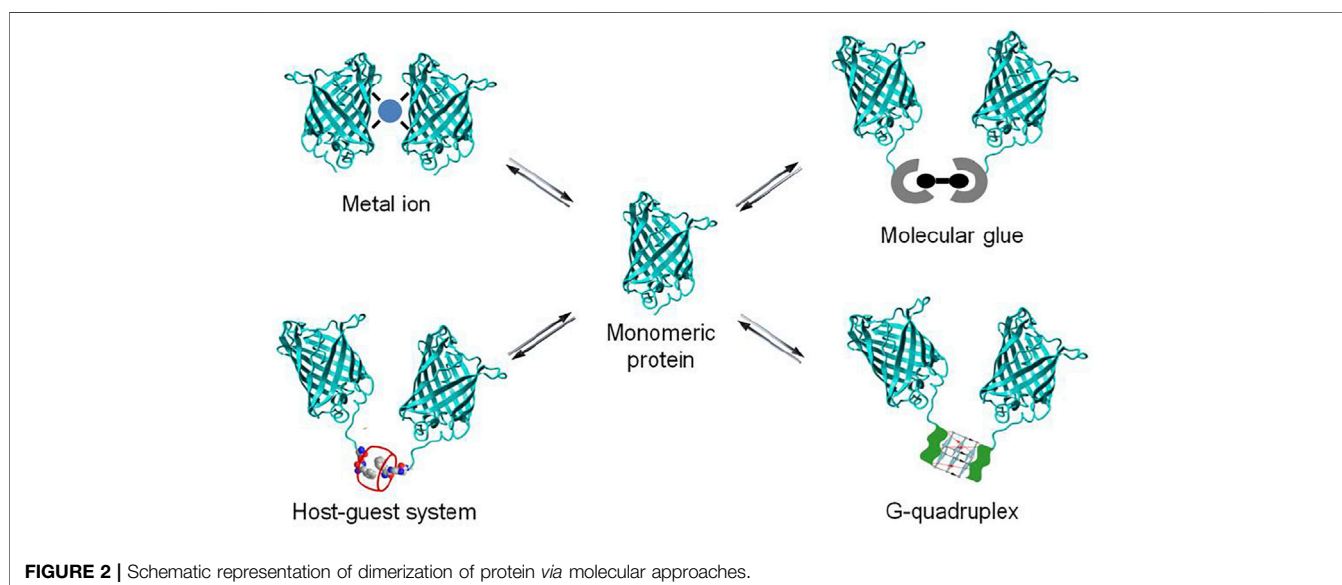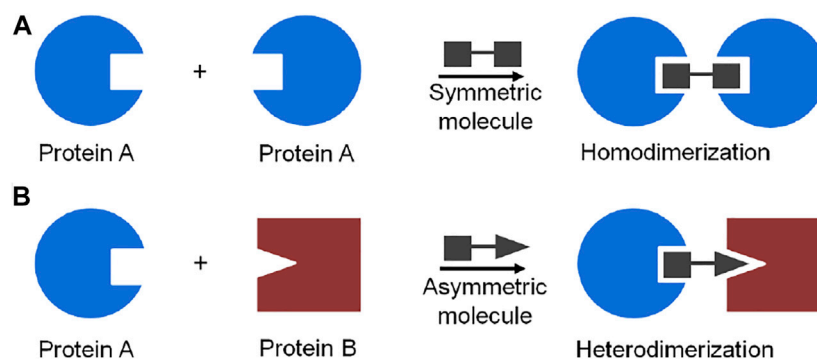
FIGURE 3 | Schematic representation of molecule glue induced dimerization of protein: **(A)** protein homodimerization induced by a symmetric bifunctional molecule, **(B)** protein heterodimerization induced by an asymmetric bifunctional molecule.

TABLE 1 | Molecule glues-induced dimerization of proteins.

Molecule glues	Induced protein dimerization
Cyclosporin A Liu et al. (199)1	Cyclophilin-Calcineurin
FK506 Liu et al. (1991); Ho et al. (1996)	FKBP-Calcineurin
FKCsA Belshaw et al. (1996a)	FKBP-CyPFas
Rapamycin Rivera et al. (1996)	FKBP-FRB domain of mTOR
Gibberellin Miyamoto et al. (2012)	Gal-GID1
Abscisic acid Liang et al. (2011)	ABI-PYL
HaXS Erhart et al. (2013)	SNAPTag-HaloTag
TMP-HTag Ballister et al. (2014)	eDHFR-HaloTag
ATB-737 Hill et al. (2018)	Bclxl-Fab (AZ1)
FK1012 Spencer et al. (1993)	FKBP-FKBP
Coumermycin Farrar et al. (1996)	GyrB-GyrB
(Cyclosporin A)$_2$ Belshaw et al. (1996b)	Cyclophilin- Cyclophilin

DIMERIZATION OF PROTEIN VIA MOLECULAR CHEMISTRY

Molecular Glue-Induced Dimerization of Protein

A powerful chemical approach currently used to control protein dimerization is via the use of molecular glues (Schreiber, 2021). The concept of molecular glue-induced protein dimerization is based on the use of low molecular weight organic compounds bearing bifunctional moieties which interact simultaneously with two proteins or protein domains (Boyd et al., 2021). A chemical inducer of protein dimerization acts as a dimerizer to bring protein molecules together and form either a homo- or a heterodimer (Corson et al., 2008; Fegan et al., 2010; Boyd et al., 2021) (**Figure 3**).

Molecule glue approaches to induce protein dimerization have been demonstrated into two groups: 1) Asymmetric molecules such as Cyclosporin A (Liu et al., 1991), FK506 (Liu et al., 1991; Ho et al., 1996), FKCsA (Belshaw et al., 1996a), rapamycin (Rivera et al., 1996), gibberellin (Miyamoto et al., 2012), abscisic acid (Liang et al., 2011), HaXS (Erhart et al., 2013), TMP-HTag (Ballister et al., 2014) and ATB-737 (Hill et al., 2018) induce hetero-dimerization of proteins; 2) Symmetric molecules such as FK1012 (Spencer et al., 1993), coumermycin (Farrar et al., 1996) and (cyclosporin A)$_2$ (Belshaw et al., 1996b) induce homo-

dimerization of proteins (**Table 1**). For example, the natural product rapamycin has emerged as the biofunctional dimerizer to induce heterodimerization of proteins (Choi et al., 1996; Liang et al., 1999; Bayle et al., 2006; Brown et al., 2015; Mangal et al., 2018; Courtney et al., 2021). The most prominent molecular feature of rapamycin is its two chemically distinct protein binding domains: one part of the molecule binds with high nanomolar affinity to the FK506-binding protein (FKBP12), the other molecular part to the FRB domain of mTOR, FRAP (FKBP-rapamycin associated protein), overall resulting in dimerization of the proteins involved. Rapamycin is thus capable of inducing heterodimerization of fusion proteins featuring FKBP and FRB domains. In contrast to rapamycin, coumermycin has two of the same protein-binding moieties and can be used to induce homodimerization of GyrB (bacterial DNA gyrase B) (Farrar et al., 1996; Farrar et al., 2000; Cele et al., 2016; Broeck et al., 2019). The concept of molecule glue-induced protein dimerization can be extended to novel synthetic compounds as well. For example, a synthetic dimer of FK506, named FK1012, promotes FKBP12 homodimerization (Schultz and Clardy, 1998), or a synthetic dimer of cyclosporine named (CsA)$_2$ can induce dimerization of cyclophilin (Belshaw et al., 1996b). These molecule glues are also capable of inducing protein dimerization in cases where the dimerizing protein of interest has been fused to a suitable protein ligand binding domain.

Protein dimerization induced by the specific binding of cell permeable high affinity small natural products or synthetic molecules represents a powerful tool for controlling dimerization of proteins in numerous biological processes such as gene expression (Rivera et al., 2012; Schreiber, 2021), proteolysis targeting chimera (PROTAC) (Mootz and Muir, 2002; Xu and Evans, 2005; Pratt et al., 2007; Foight et al., 2019), and signaling cascades (Shahi et al., 2012; Lecointre et al., 2018; Fujikawa et al., 2019). For example, control over gene expression was achieved with rapamycin by recruiting activation and repression protein domains to targeted loci (Schreiber, 2021). Fusion of an FRB domain to an activation domain (VP16) and a DNA-binding domain (Gal4) to an FKBP domain led to rapamycin-induced dimerization generating transcriptional activator functionality, and the promotion of

gene expression (Liberles et al., 1997; Hardwick et al., 1999). Since toxicity of the natural rapamycin inhibits cell proliferation, Crabtree and co-workers have developed non-toxic rapamycin analogs which were successfully used to control gene expression (Bayle et al., 2006). The use of molecule glues induced protein dimerization to control the stability or rescue of proteins in living cells has also been demonstrated. Crabtree and coworkers described that FRB* -not only bound to FKBP12 in the presence of a rapamycin analog (C20-MaRap) but also bore functionality which conferred reversible instability on the fusion proteins. In the absence of rapamycin analog, the glycogen synthase kinase-3β (GSK-3β) fused to FRB* (GSK-3βFRB*) was rapidly degraded (Stankunas et al., 2003). Interestingly, C20-MaRap induced dimerization of FKBP12 and GSK-3βFRB*, which might lock FRB* in a folded state, resulting in the stabilization of the GSK-3β protein. This system may provide a means to control the stability or degradation of target proteins. Another robust approach to rescue proteins from the proteasome is by using both molecule glue induced dimerization and splicing of ubiquitin hydrolysis. For example, split ubiquitin for the rescue of function (SURF) was based on the complementation of genetically split ubiquitin under the control of rapamycin-induced dimerization of FRB and FKBP. The strategy was as follows: 1) the FKBP was fused to the N-terminal fragment of ubiquitin to form FKBP-Ub^N, 2) the C-terminal fragment of ubiquitin was fused to a protein of interest and FRB to form the FRB-Ub^C-protein complex, and subsequently fused to a degradation signal (degron) which would cause degradation of the fusion protein by proteasome recognition. In the absence of rapamycin, the proteasome recognizes and "kills" the fusion protein through degron domain recognition, thereby promoting degradation of fusion protein. Addition of rapamycin caused dimerization of FRB and FKBP, which resulted in the reassembly and function of ubiquitin, thereby releasing the protein of interest from the degron and rescuing its function (Pratt et al., 2007). In addition, molecular glue-induced protein dimerization has also been investigated to control the activation of certain kinase family members, in order to study signal transduction (Belshaw et al., 1996b; Spencer et al., 1996; Kim et al., 2020). A synthetic molecule glue - FK1012 - induces homo-dimerization of FKBP and can also be used to gain control over programmed cell death. The Fas cytoplasmic domain was fused between poly FKBP and myristoyl group which located on the cell membrane. The presence of FK1012 mediated the aggregation of the Fas-poly FKBP receptor leading to activation of Fas signaling transduction, and eventually cell death (Spencer et al., 1996). An engineered rapamycin-induced dimerization approach of Fas consisting of FKBP and FRB proteins allowed rapamycin to specifically induce cellular apoptosis (Kim et al., 2020). Thus, the molecule glue approach is highly valuable for fundamental studies, drug development, and other biomedical applications. This approach, however, does require the construction of large fusion proteins, in which the required protein domains contribute substantial mass to the final protein construct, potentially affecting the biological activity of the target protein (Spencer et al., 1993; Fegan et al., 2010). Alternative methods for molecular control over protein

dimerization are additionally required. Apart from molecular glue based approaches, metal ion, nucleic acid and host-guest chemistry are brought forward as novel approaches for orthogonal control over dimerization of protein.

Metal Ion-Induced Dimerization of Protein

Metal ion-mediated protein dimerization has recently been demonstrated (Sinclair, 2012; Song et al., 2014; Kochanczyk et al., 2016). Tezcan and co-workers for example generated hybrid coordination motifs based on the simultaneous binding of a metal ion to a natural histidine amino acid and a non natural ligand on the α-helical surface of protein cytochrome cb_{562} (Radford et al., 2010). The ligand, 5-amino-8-hydroxyquinoline, which binds metal ions with high affinity, was covalently ligated to cysteine at position 70 of cytochrome cb_{562}. Addition of metal ions such as Ni^{2+}, Co^{2+}, Cu^{2+} and Zn^{2+} induced cytochrome cb_{562} dimerization, resulting in an increase of global protein stability. Zn ions were also exploited as powerful metal ions to assemble protein in a homodimer (Brodin et al., 2010; Churchfield et al., 2016) and tetramer, in which four Zn ions associated at the surface of each protein monomer. The design and synthesis of a helical coiled-coil by metal-induced folding has also been demonstrated; fusing the Cys-X-X-Cys metal binding domain of rubredoxin to a target random coil peptide enabled Cd^{2+} to induce peptide dimerization (Kharenko and Ogawa, 2004). Interestingly, metal ion-induced protein dimerization was used to generate a structural superposition closely resembling bZip-type transcriptional factors, suggesting potential applications for the recognition of biological targets. Using metal ions to induce protein dimerization represents a promising approach to controlling over biological processes (Zhang et al., 2005; Affandi and McEvoy, 2019).

Nucleic Acid-Induced Dimerization of Protein

G-quadruplex (G4)-induced protein dimerization has been recently reported (Truong et al., 2020). G4s are four-stranded structures formed by stacking of multiple G-tetrads. In cellular events, the formation of G4 involves in many biological processes such as replication, transcription, translation and telomeric maintenance (Lipps and Rhodes, 2009; Maizels and Gray, 2013). Therefore, specific interaction between G4 with proteins has emerged as a promising approach for regulation of biological processes. A G4-binding protein domain was also identified in N-terminus of RHAU (RHA helicase associated with AU rich element) (Heddi et al., 2015; Dang and Phan, 2019; Dang et al., 2021). Interestingly, NMR solution structure of a complex of an 18-residue peptide (RHAU18) consisting a G4-specific binding domain and a parallel G4 has showed G4 molecule can simultaneously binds two RHAU peptides at the 3′ and 5′ end G-tetrads (Heddi et al., 2015). The helical RHAU peptides covers and clamps the G4 with three-anchor-point electrostatic interactions between negatively charged phosphate groups of the G4 and the three positively charged amino acids (K_8, R_{10},
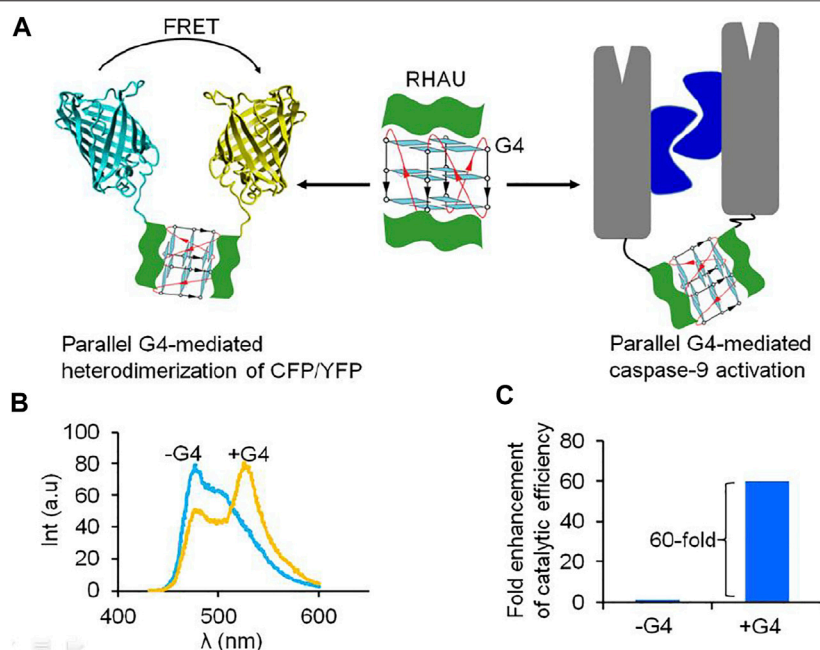
FIGURE 4 | Parallel G4 can act as a target-inducer of dimerization and activation of proteins fusing with RHAU peptide. **(A)** Schematic representation of dimerization of protein and activation *via* G4, **(B)** FRET signal was observe under addition of G4 to a mixture of RHAU-CFP/RHAU-YFP (Truong et al., 2020); **(C)** G4 can play as a target molecule for inducing both dimerization and rearrangement of the active site of RHAU-caspase-9, resulting in enhancement of catalytic efficiency of enzyme (Truong et al., 2020).

K_{19}) of the peptide. The specific binding of parallel G4 to two RHAU peptide provides a promising approach for G4-induced self assembly of protein by fusing a functional protein with RHAU peptide (Heddi et al., 2015). Incorporating a RHAU peptide with a fluorescent protein pair: cyan fluorescent protein/yellow fluorescent protein (CFP/YFP), resulting in generation of a pair of FRET (fluorescence resonance energy transfer) RHAU-CFP/RHAU-YFP. Upon addition of G4 to a mixture of RHAU-CFP and RHAU-YFP, the energy transfer from the donor CFP to the acceptor YFP was observed by G4-induced heterodimerization of proteins (Truong et al., 2020) (**Figure 4**). In addition, G4-induced dimerization protein approach was applied for dimer-driven activation of caspase-9. Inactivated monomeric caspase-9 incorporating with RHAU peptide allowed G4 to regenerate a catalytic activity. In the presence of G4, the catalytic efficiency of caspase-9 was 60-fold enhancement towards the natural substrate. G4 can play as a target molecule for inducing both dimerization and rearrangement of the active site of caspase-9. Another study showed oligonucleotides containing (GT) repeats could induce dimerization of HIV-1 Gag protein (Zhao et al., 2019). Short oligonucleotide as $(GT)_3$ or $(GT)_8$ bound to nucleocapsid (NC) domain of Gag protein leading to change conformation of Gag that is favor for Gag dimerization. Induction of dimerization of protein by nucleic acid is an alternative approach to study on function of protein and interplay between protein dimerization state and activation, not only enzyme, but also many other protein homodimerization events.

Supramolecular System-Induced Dimerization of Protein

Supramolecular chemistry was initially inspired by biomolecules and their higher order structures (Uhlenheuer et al., 2010; Khan and Lee, 2021). Recently, the supramolecular chemistry to modulate and control dimerization of protein have been reported. Supramolecular systems bearing natural or synthetic components have been engineered with desirable properties for use in biochemical research, such as improved water solubility and guest-specific binding (Oshovsky et al., 2007). The application of supramolecular chemistry for protein dimerization is based on the non-covalent interaction of supramolecular hosts with specific guest molecules, while being appended to proteins. Two supramolecular host molecules, cyclodextrin and cucurbit [8]uril, have been most intensively explored as tools for the selective and reversible control over protein dimerization in both buffered solution and living cells (Zhang et al., 2007; Nguyen et al., 2010). Cyclodextrins are naturally-derived sugar-based cone-shaped host molecules, which selectively bind hydrophobic guest molecules to form, typically, a 1:1 complex in aqueous solution. For example, the cavity of a *β*-cyclodextrin variant recognizes and binds lithocholic acid with high affinity ($K_a = 10^6 \, M^{-1}$) (Yang and Breslow, 1997) (**Figure 5A**), opening up the possibility for *β*-cyclodextrin to recognize and bind protein-lithocholic acid conjugates. Cucurbit [8]uril is the eight membered homologue of the cucurbit [n]uril family of glycoluril based macrocycles, which has shown highly
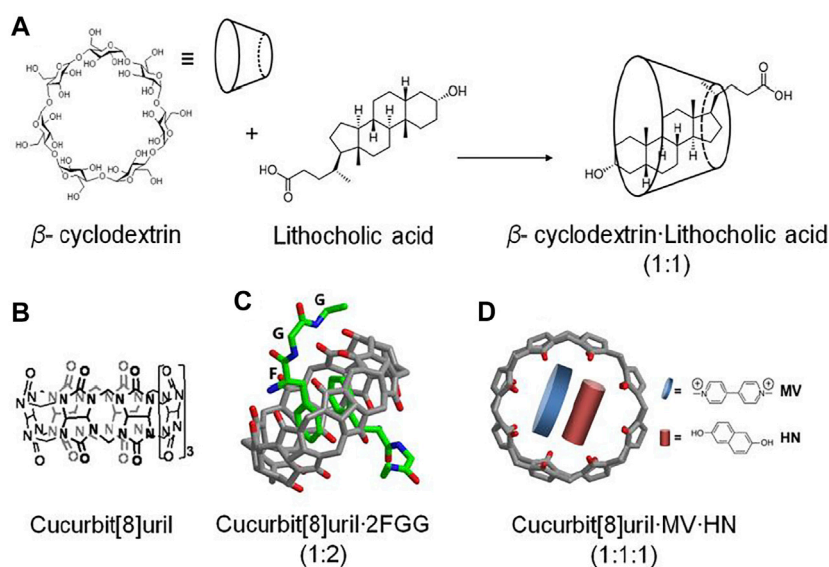
FIGURE 5 | (A) β-cyclodextrin recognizes and binds lithocholic acid forming a complex (1:1) (Yang and Breslow, 1997), **(B)** Chemical structure of cucurbit[8]uril, **(C)** cucurbit[8]uril selectively binds and dimerizes tripeptide phenylalanineglycine·glycine (FGG) (Heitmann et al., 2006), **(D)** ternary complex of cucurbit[8]urilmethylviologen·dihydroxynapthalene (Q8:MV:HN) (Ko et al., 2007; Rauwald et al., 2010).
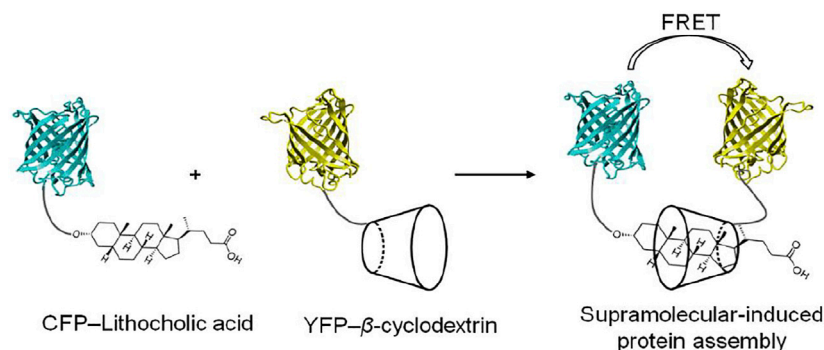
FIGURE 6 | Schematic representation of cyclodextrin-induced assembly of CFP and YFP functionalized with lithocholic acid and cyclodextrin, respectively (Zhang et al., 2007).

attractive biochemical applications due to its capacity to bind various cationic guest molecules, in addition to its good water-solubility and low toxicity (Urbach and Ramalingam, 2011; Masson et al., 2012). The cavity of cucurbit [8]uril is sufficiently large to bind two synthetic guest molecules simultaneously such as two equivalents of *N*-phenylpiperazine, aminoacridiziniums, naphthyl derivatives, coumarin and neutral red under acidic conditions (Urbach and Ramalingam, 2011) (**Figures 5B–D**). The favorable recognition of two guests by cucurbit [8]uril enables the formation of highly stable ternary complexes in aqueous solution. The selective non-covalent interaction of cucurbit [8]uril and guest elements provides a means to reversibly control dimerization of proteins incorporating these supramolecular guest elements. The easy design and synthesis of supramolecular host-guest systems

opens up the possibility of modulating and controlling dimerization of protein.

The concept of supramolecular induced protein-protein interactions was first probed using supramolecular host-guest elements attached to synthetic peptides (Ueno et al., 1993). The specific recognition of the adamantyl group by β-cyclodextrin permitted a β-cyclodextrin-conjugated synthetic peptide to selectively recognize and bind an adamantane-conjugated peptide. This self-assembled peptide dimer enabled strong and selective DNA recognition. DNA recognition by supramolecular peptide dimerization could be reversed by inhibiting the supramolecular dimerization with either free β-cyclodextrin or adamantane. The fluorescent proteins were conjugated to the β-cyclodextrin and lithocholic acid host guest system at the C-terminus of the proteins (Zhang et al., 2007) (**Figure 6**). A high affinity and selective recognition of lithocholic acid by β-

cyclodextrin enabled the association of the two fluorescent proteins. In this case, the degree of protein association could be monitored by donor-receptor fluorescence resonance energy transfer (FRET), both in buffer and in cells. Increasing the affinity of the synthetic host-guest complex would enhance the interaction of host-guest conjugated proteins and would thus be attractive from the point of view of studying protein-protein interactions at lower concentrations. This concept could be shown using a β-cyclodextrin host which was modified to heptakis-[6-deoxy-6-(2-aminoethyl-sulfanyl]-β-cyclodextrin (Gomez-Biagi et al., 2008). This molecular upgrading of the β-cyclodextrin side-chains brought about a 10 fold increase in binding to lithocholic acid and enhanced FRET (Uhlenheuer et al., 2011a). The optimization of synthetic host-guest systems is not a unique approach to increase the affinity of protein-protein interactions: engineering of the dimeric interface of the proteins can also been used to increase and stabilize the supramolecular protein dimerization. For example, point-mutated (S208F and V224L) fluorescent CFP and YFP proteins, so called dimerizing proteins (dCFP and dYFP) which normally show weak intrinsic affinity for dimerization, formed strong and stable supramolecular protein complexes on ligation of host-guest elements with a concomitant very strong FRET (Uhlenheuer et al., 2009). The reversibility of the supramolecular protein dimerization, could be probed by addition of β-cyclodextrin to the supramolecular protein dimers, resulting in inhibition of protein dimerization for all types of protein pairs (Zhang et al., 2007; Uhlenheuer et al., 2009; Uhlenheuer et al., 2010). β-Cyclodextrin can also be used to induce homodimerization of proteins (Kitagishi et al., 2012). For example, surface functionalization of bovine serum albumin protein (BSA) with TMe-β-cyclodextrin enabled 5,10,15,20-tetrakis (4-sulfonatophenyl)porphyrin to reversibly control BSA homodimerization via complexation with the TMe-β-cyclodextrin. The resulting supramolecular protein dimer is stable and can be separated from monomeric proteins via size exclusion chromatography.

Cucurbit [8]uril is a second attractive supramolecular host molecule for use in reversible protein dimerization studies (Bai et al., 2016; Cao et al., 2021; Liu et al., 2021). Cucurbit [8]uril selectively binds and dimerizes two guest molecules simultaneously within its hydrophobic cavity, and with high affinity (Heitmann et al., 2006; Ko et al., 2007). For example, cucurbit [8]uril recognizes and binds methyl viologen (MV) and naphthalene (Np) simultaneously to form a ternary cucurbit [8] uril·MV·Np complex (Ko et al., 2007). This concept could be applied to induce heterodimerization of CFP and YFP. For this, CFP and YFP were chemically outfitted with Np and MV, resulting in synthetic CFP-Np and YFP-MV mutants, respectively. The addition of cucurbit [8]uril mediated heterodimerization of CFP-Np with YFP-MV, resulting in an energy transfer from donor CFP to acceptor YFP (Uhlenheuer et al., 2011b). Incorporation of a 4,4′-bipyridinium scaffold at the C-teminus of transcription factor (GCN4) opened up a new approach to the supramolecular control of peptide assemblies (Novo et al., 2021). Cucurbit [8]uril-induced GCN4 dimerization by the formation of a homoternary supramolecular complex (1 cucurbit[8]uril:2 bipyridinium) could specifically bind to its targeted double-strand DNA. This binding complex was easily disassembled in a reversible manner upon addition of a specific competitor guest. Interestingly, cucrbit[8]uril-induced dimerization of antimitotic peptide-conjugated benzylimidazolium could recognize the microtubules and convert from fibrous to nanoparticulate aggregates through cross-linkage of host-guest complex. The cucurbit[8]uril-induced intertubular aggregation was applied to regulate cell apoptosis and tumor ablation at the cellular level and in the mouse (Zhang et al., 2019). Chemical conjugation of specific guest molecules with proteins or peptides provides a facile supramolecular method to enhance protein-protein interactions which may open up new opportunities for biomedical applications.

The supramolecular host cucurbit[8]uril can as well be efficiently used to reversibly switch the dimerization of fluorescent proteins incorporating a genetically encoded N-terminal phenylalanine-glycine-glycine (FGG) peptide motif (Nguyen et al., 2010; Dang et al., 2014) (**Figure 7**). The proteins with an FGG-tag are easily generated by autocleavage of an intein system under control of pH and temperature. Selective binding of the FGG-tag to the hydrophobic cavity of cucurbit[8]uril induces protein dimerization and is mediated via a key interaction between the N-terminal amine functionality of the peptide and the carbonyl rim of cucurbit [8]uril (**Figure 5C**), resulting in protein homo- or heterodimerization. Cucurbit[8]uril-induced dimerization of proteins bearing an FGG-tag via a supramolecular host-guest interaction can be fully reversed through the addition of a small synthetic competitor (methyl viologen) (Nguyen et al., 2010). In addition, cucurbit[8]uril has been used as an inducer of protein tetramerization (dimer of dimer), by combining the two-fold binding of an FGG motif to cucurbit[8]uril with intrinsic affinities between the proteins domains as a stepwise assembly process (Dang et al., 2012). The incorporation of a dimerizing interface at the fluorescent protein surface (dYFP, dCFP) combined with an encoded N-terminal phenylalanine-glycine-glycine (FGG) peptide motif allowed cucurbit[8]uril to selectively recognize and induce FGG-dYFP or FGG-dCFP homotetramerization. The concept of cucurbit[8]uril-induced protein homotetramerization was elucidated using a combination of dynamic light scattering and size exclusion chromatography experiments. Addition of cucurbit[8]uril to a solution of FGG-dYFP, pre-dimerized in solution, resulted in the automatic generation of the tetrameric protein assembly.

Cucurbit[8]uril-induced self assembly of protein dimerization approach has been applied to study molecular mechanisms of dimerization and activation of caspase-9 (Dang et al., 2013) (**Figure 8**). Caspase-9 consisting of FGG motif (FGG-caspase-9) at the N-terminus allows cucurbit[8]uril to induce protein dimerization which was confirmed by dynamic light scattering (DLS). The catalytic activity of enzyme increases upon increased addition of cucurbit[8]uril until a maximal activity is reached when all FGG-caspase-9 is dimerized. The activity of the cucurbit [8]uril-induced FGG-caspase-9 dimer is not only significantly greater than that of the isolated protein, but is also superior to proteins mutated to have an engineered hydrophobic
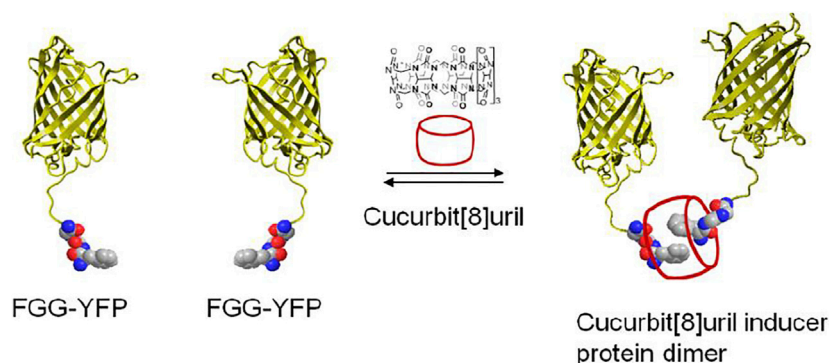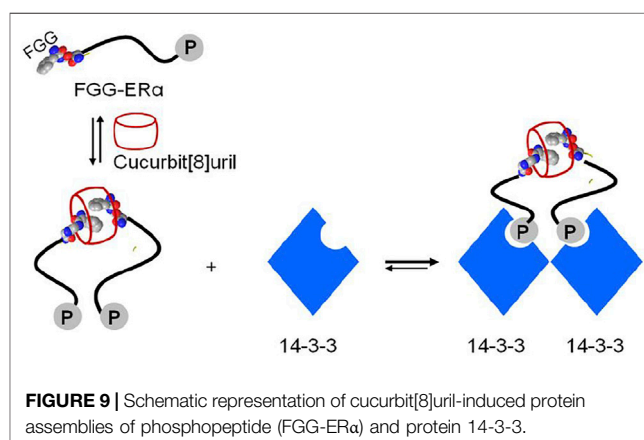
FIGURE 7 | Schematic representation of two yellow fluorescent proteins having an N-terminal FGG peptide motif and their dimerization which is induced by cucurbit[8]uril (Nguyen et al., 2010).
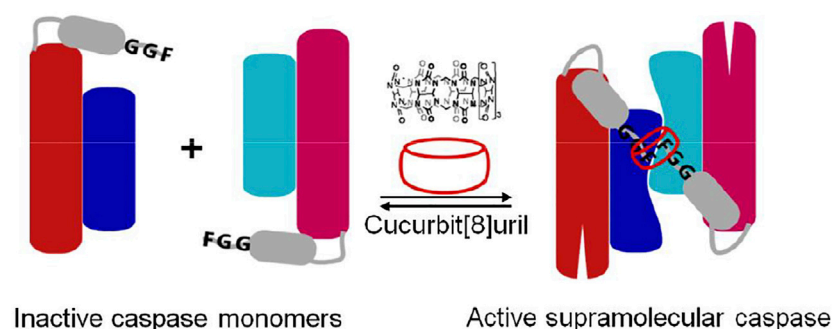
FIGURE 8 | Schematic representation of N-terminal FGG-bearing (grey) monomeric caspase-9 (red: large subunit, blue: small subunit) and its dimerization into an enzymatically active homodimer by cucurbit[8]uril (Dang et al., 2013).

dimerization interface. Upon addition of a competitor peptide (FGG) to the active cucurbit[8]uril-induced FGG-caspase-9 dimer, the enzymatic activity of enzyme was decreased in a dose-dependent fashion (Dang et al., 2013). The reversibility of the cucurbit [8]uril–FGG system thus shows the full control achievable over dimerization of FGG-caspase-9 dimerization and activation via supramolecular host–guest approach and the potential to either induce or inhibit protein dimerization with specific small guest molecules. Moreover, light-triggered supramolecular cucurbit[8]uril activation of FGG-caspase-9 has been demonstrated (de Vink et al., 2021). Cucurbit [8]uril was temporarily caged by bivalent FGG peptide with high affinity. The UV light induced release of cucurbit[8]uril from a bivalent cage molecule, resulting in activation of cucurbit[8]uril-induced FGG-caspase-9 dimerization. The concept of light-responsive caged cucurbit[8]uril also provides a new platform for application of switchable approaches. Supramolecular reactivation of inactivated enzymes have been studied on inactivated caspase-8 mutant and split-luciferase fragments. A mutated caspase-8 (D384A) featuring FGG motif at the N-terminus which shows enzymatically inactive towards its natural substrate caspase-3, could be fully reactivated upon addition of cucurbit[8]uril (Dang et al., 2018). The FGG motif

FIGURE 9 | Schematic representation of cucurbit[8]uril-induced protein assemblies of phosphopeptide (FGG-ERα) and protein 14-3-3.

was applied to split-luciferase fragment pairs at the N-terminus that allowed cucurbit[8]uril to induce dimerization of luciferase and regenerate enzymatic activity (Bosmans et al., 2016). Cucurbit[8]uril can act as a supramolecular inducer of dimerization, thus leading to optimal protein reorganization and enzymatic activation that holds great promises for studying many other protein homodimerization events in a

reversible manner, such as dimerizing enzymes and membrane receptor proteins.

Crystal structure of the supramolecular-mediated protein complex has been studied on cucurbit[8]uril-induced dimerization of protein 14-3-3 (involved in human disease including the breast-cancer target) (de Vink et al., 2017; Liu et al., 2021). Fusion of FGG motif to the N-terminus of the 14-3-3 binding epitope of the estrogen receptor alpha (ERα) could be simply formed into a dimeric peptide in the presence of cucurbit [8]uril. Cucurbit[8]uril-induced ERα peptide dimerization significantly enhanced its affinity towards protein 14-3-3 *via* a binary bivalent binding manner (**Figure 9**). Molecular insight into the supramolecular interaction of the complex of protein, peptide and cucurbit[8]uril was clarified by the first crystal structure (de Vink et al., 2017). The crystal structure showed that the complex was favorably stabilized by multiple intermolecular interactions. The cucurbit[8]. FGG system has also been applied to generate protein nanowires (Hou et al., 2013; Bai et al., 2016). Genetic generation of the dimeric glutathione S-transferase (GST) surfaces consisting of FGG motif at the symmetric N-terminus allowed cucurbit[8]uril to induce self-assembly of protein into high molecular nanowires (Hou et al., 2013). The incorporation of Se-containing active center to FGG-GST resulted in a functionalized Se-FGG-GST. The Se-FGG-GST could be easily formed into high molecular nanowires in the presence of cucurbit[8]uril which was shown to be a better antioxidant than Se-FGG-GST monomers. That holds a great promise for the design of functional proteins such as biosensors, catalysis and pharmaceuticals.

Approaches of controlling protein dimerization reveals diversity in the regulation of protein activity both *in vitro* and *in vivo*. It is necessary to apply these approaches to therapeutic applications. Some molecule glues-induced protein dimerization have been used as drugs in clinical treatment. For example, rapamycin and its analog have been approved by FDA (Food and Drug Administration) as an immunosuppressive drug for transplantation and cancer therapy (Schreiber, 2021). Interestingly, ARV-110 is the first "PROTAC" molecule glue

which entered phase I clinical trials (Schreiber, 2021). In addition, supramolecular system-induced protein dimerization also shows great potential for therapeutic applications. The administration of cucurbit [8]uril-induced aggregation of tubulin-targeted antimitotic peptides could induce apoptosis and suppress tumor growth which can be developed as a therapeutic supramolecular approach for cancer treatment (Zhang et al., 2019). The host-guest cucurbit [8]uril:FGG (1:2) complex has been widely used to regulate numerous functional proteins such as caspase-9, caspase-8, protein 14-3-3, nanowires that also holds a great promise for design of functional proteins such as biosensors, catalysis and pharmaceuticals (Liu et al., 2021).

Protein dimerization plays a key role in almost all biological processes. Control over protein dimerization using molecules is an important concept for studying the fundamental underlying molecular processes. The use of molecules to induce protein dimerization in part overcomes the limitations of protein engineering approaches. In particular, the selective recognition of small guests by synthetic host molecules to form 1:1 complexes or 1:2 ternary complexes enables the reversible control of protein dimerization using proteins prefunctionalized with small guest elements. The supramolecular induced dimerization of protein represents orthogonal approaches for studying functional protein dimerization and aggregation, thus opening up new opportunities for biomedical applications.

AUTHOR CONTRIBUTIONS

The author confirms being the sole contributor of this work and has approved it for publication.

ACKNOWLEDGMENTS

REFERENCES

Affandi, T., and McEvoy, M. M. (2019). Mechanism of Metal Ion-Induced Activation of a Two-Component Sensor Kinase. *Biochem. J.* 476 (1), 115–135. doi:10.1042/BCJ20180577

Ahsan, A. (2016). Mechanisms of Resistance to EGFR Tyrosine Kinase Inhibitors and Therapeutic Approaches: An Update. *Adv. Exp. Med. Biol.* 893, 137–153. doi:10.1007/978-3-319-24223-1_7

Ardejani, M. S., Li, N. X., and Orner, B. P. (2011). Stabilization of a Protein Nanocage through the Plugging of a Protein-Protein Interfacial Water Pocket. *Biochemistry* 50 (19), 4029–4037. doi:10.1021/bi200207w

Bai, Y., Luo, Q., and Liu, J. (2016). Protein Self-Assembly via Supramolecular Strategies. *Chem. Soc. Rev.* 45 (10), 2756–2767. doi:10.1039/c6cs00004e

Ballister, E. R., Aonbangkhen, C., Mayo, A. M., Lampson, M. A., and Chenoweth, D. M. (2014). Localized Light-Induced Protein Dimerization in Living Cells Using a Photocaged Dimerizer. *Nat. Commun.* 5, 5475. doi:10.1038/ncomms6475

Baselga, J., and Swain, S. M. (2009). Novel Anticancer Targets: Revisiting ERBB2 and Discovering ERBB3. *Nat. Rev. Cancer* 9 (7), 463–475. doi:10.1038/nrc2656

Bayle, J. H., Grimley, J. S., Stankunas, K., Gestwicki, J. E., Wandless, T. J., and Crabtree, G. R. (2006). Rapamycin Analogs with Differential Binding Specificity Permit Orthogonal Control of Protein Activity. *Chem. Biol.* 13 (1), 99–107. doi:10.1016/j.chembiol.2005.10.017

Belshaw, P. J., Ho, S. N., Crabtree, G. R., and Schreiber, S. L. (1996a). Controlling Protein Association and Subcellular Localization with a Synthetic Ligand that Induces Heterodimerization of Proteins. *Proc. Natl. Acad. Sci.* 93 (10), 4604–4607. doi:10.1073/pnas.93.10.4604

Belshawl, P. J., Spencer, D. M., Crabtree, G. R., and Schreiber, S. L. (1996b). Controlling Programmed Cell Death with a Cyclophilincyclosporin-Based Chemical Inducer of Dimerization. *Chem. Biol.* 3 (9), 731–738. doi:10.1016/s1074-5521(96)90249-5

Bosmans, R. P. G., Briels, J. M., Milroy, L.-G., de Greef, T. F. A., Merkx, M., and Brunsveld, L. (2016). Supramolecular Control over Split-Luciferase Complementation. *Angew. Chem. Int. Ed.* 55 (31), 8899–8903. doi:10.1002/anie.201602807

Boyd, S. R., Chang, L., Rezende, W., Raji, I. O., Kandel, P., Holmes, S. L., et al. (2021). Design and Applications of Bifunctional Small Molecules in Biology. *Biochim. Biophys. Acta (Bba) - Proteins Proteomics* 1869 (1), 140534. doi:10.1016/j.bbapap.2020.140534

Brodin, J. D., Medina-Morales, A., Ni, T., Salgado, E. N., Ambroggio, X. I., and Tezcan, F. A. (2010). Evolution of Metal Selectivity in Templated Protein Interfaces. *J. Am. Chem. Soc.* 132 (25), 8610–8617. doi:10.1021/ja910844n

Broeck, A. V., McEwen, A. G., Chebaro, Y., Potier, N., and Lamour, V. (2019). Structural Basis for DNA Gyrase Interaction with Coumermycin A1. *J. Med. Chem.* 62 (8), 4225–4231. doi:10.1021/acs.jmedchem.8b01928

Brown, K. A., Zou, Y., Shirvanyants, D., Zhang, J., Samanta, S., Mantravadi, P. K., et al. (2015). Light-cleavable Rapamycin Dimer as an Optical Trigger for Protein Dimerization. *Chem. Commun.* 51 (26), 5702–5705. doi:10.1039/c4cc09442e

Cao, W., Qin, X., and Liu, T. (2021). When Supramolecular Chemistry Meets Chemical Biology: New Strategies to Target Proteins through Host-Guest Interactions. *Chembiochem* 22 (20), 2914–2917. doi:10.1002/cbic.202100357

Cele, F. N., Kumalo, H., and Soliman, M. E. S. (2016). Mechanism of Inhibition of Hsp90 Dimerization by Gyrase B Inhibitor Coumermycin A1 (C-A1) Revealed by Molecular Dynamics Simulations and Thermodynamic Calculations. *Cell Biochem. Biophys.* 74 (3), 353–363. doi:10.1007/s12013-016-0743-8

Chao, Y., Shiozaki, E. N., Srinivasula, S. M., Rigotti, D. J., Fairman, R., and Shi, Y. (2005). Engineering a Dimeric Caspase-9: a Re-evaluation of the Induced Proximity Model for Caspase Activation. *Plos Biol.* 3 (6), e183. doi:10.1371/journal.pbio.0030183

Chiravuri, M., Lee, H., Mathieu, S. L., and Huber, B. T. (2000). Homodimerization via a Leucine Zipper Motif Is Required for Enzymatic Activity of Quiescent Cell Proline Dipeptidase. *J. Biol. Chem.* 275 (35), 26994–26999. doi:10.1074/jbc.M00544520010.1016/s0021-9258(19)61470-5

Choi, J., Chen, J., Schreiber, S. L., and Clardy, J. (1996). Structure of the FKBP12-Rapamycin Complex Interacting with Binding Domain of Human FRAP. *Science* 273 (5272), 239–242. doi:10.1126/science.273.5272.239

Churchfield, L. A., Medina-Morales, A., Brodin, J. D., Perez, A., and Tezcan, F. A. (2016). De Novo Design of an Allosteric Metalloprotein Assembly with Strained Disulfide Bonds. *J. Am. Chem. Soc.* 138 (40), 13163–13166. doi:10.1021/jacs.6b08458

Citri, A., and Yarden, Y. (2006). EGF-ERBB Signalling: towards the Systems Level. *Nat. Rev. Mol. Cel. Biol.* 7 (7), 505–516. doi:10.1038/nrm1962

Corson, T. W., Aberle, N., and Crews, C. M. (2008). Design and Applications of Bifunctional Small Molecules: Why Two Heads Are Better Than One. *ACS Chem. Biol.* 3 (11), 677–692. doi:10.1021/cb8001792

Courtney, T. M., Darrah, K. E., Horst, T. J., Tsang, M., and Deiters, A. (2021). Blue Light Activated Rapamycin for Optical Control of Protein Dimerization in Cells and Zebrafish Embryos. *ACS Chem. Biol.* 16, 2434–2443. doi:10.1021/acschembio.1c00547

Dang, D. T., Bosmans, R. P. G., Moitzi, C., Voets, I. K., and Brunsveld, L. (2014). Solution Structure of a Cucurbit[8]uril Induced Compact Supramolecular Protein Dimer. *Org. Biomol. Chem.* 12 (46), 9341–9344. doi:10.1039/c4ob01729c

Dang, D. T., Nguyen, H. D., Merkx, M., and Brunsveld, L. (2013). Supramolecular Control of Enzyme Activity through Cucurbit[8]uril-Mediated Dimerization. *Angew. Chem. Int. Ed.* 52 (10), 2915–2919. doi:10.1002/anie.201208239

Dang, D. T., Nguyen, L. T. A., Truong, T. T. T., Nguyen, H. D., and Phan, A. T. (2021). Construction of a G-quadruplex-specific DNA Endonuclease. *Chem. Commun.* 57 (37), 4568–4571. doi:10.1039/d0cc05890d

Dang, D. T., and Phan, A. T. (2019). Development of a Ribonuclease Containing a G4-specific Binding Motif for Programmable RNA Cleavage. *Sci. Rep.* 9 (1), 7432. doi:10.1038/s41598-019-42143-8

Dang, D. T., Schill, J., and Schill, L. (2012). Cucurbit[8]uril-mediated Protein Homotetramerization. *Chem. Sci.* 3 (9), 2679–2684. doi:10.1039/c2sc20625k

Dang, D. T., van Onzen, A. H. A. M., Dorland, Y. L., and Brunsveld, L. (2018). Cucurbit[8]uril Reactivation of an Inactivated Caspase-8 Mutant Reveals Differentiated Enzymatic Substrate Processing. *Chembiochem* 19 (23), 2490–2494. doi:10.1002/cbic.201800521

de Vink, P. J., van der Hek, T., and Brunsveld, L. (2021). Light-driven Release of Cucurbit[8]uril from a Bivalent Cage. *Chem. Sci.* 12 (19), 6726–6731. doi:10.1039/d1sc01410b

de Vink, P. J., Briels, J. M., Schrader, T., Milroy, L.-G., Brunsveld, L., and Ottmann, C. (2017). A Binary Bivalent Supramolecular Assembly Platform Based on Cucurbit[8]uril and Dimeric Adapter Protein 14-3-3. *Angew. Chem. Int. Ed.* 56 (31), 8998–9002. doi:10.1002/anie.201701807

Erhart, D., Zimmermann, M., Jacques, O., Wittwer, M. B., Ernst, B., Constable, E., et al. (2013). Chemical Development of Intracellular Protein Heterodimerizers. *Chem. Biol.* 20 (4), 549–557. doi:10.1016/j.chembiol.2013.03.010

Farrar, M. A., Alberola-lla, J., and Perlmutter, R. M. (1996). Activation of the Raf-1 Kinase cascade by Coumermycin-Induced Dimerization. *Nature* 383 (6596), 178–181. doi:10.1038/383178a0

Farrar, M. A., Olson, S. H., and Perlmutter, R. M. (2000). [31] Coumermycin-Induced Dimerization of GyrB-Containing Fusion Proteins. *Methods Enzymol.* 327, 421–IN5. doi:10.1016/s0076-6879(00)27293-5

Fegan, A., White, B., Carlson, J. C. T., and Wagner, C. R. (2010). Chemically Controlled Protein Assembly: Techniques and Applications. *Chem. Rev.* 110 (6), 3315–3336. doi:10.1021/cr8002888

Ferrer-Soler, L., Vazquez-Martin, A., Brunet, J., Menendez, J., De Llorens, R., and Colomer, R. (2007). An Update of the Mechanisms of Resistance to EGFR-Tyrosine Kinase Inhibitors in Breast Cancer: Gefitinib (Iressa)-Induced Changes in the Expression and Nucleo-Cytoplasmic Trafficking of HER-Ligands (Review). *Int. J. Mol. Med.* 20 (1), 3–10. doi:10.3892/ijmm.20.1.3

Foight, G. W., Wang, Z., Wei, C. T., Jr Greisen, P., Warner, K. M., Cunningham-Bryant, D., et al. (2019). Multi-input Chemical Control of Protein Dimerization for Programming Graded Cellular Responses. *Nat. Biotechnol.* 37 (10), 1209–1216. doi:10.1038/s41587-019-0242-8

Fujikawa, A., Sugawara, H., Tanga, N., Ishii, K., Kuboyama, K., Uchiyama, S., et al. (2019). A Head-To-Toe Dimerization Has Physiological Relevance for Ligand-Induced Inactivation of Protein Tyrosine Receptor Type Z. *J. Biol. Chem.* 294 (41), 14953–14965. doi:10.1074/jbc.RA119.007878

Gazon, H., Barbeau, B., Mesnard, J.-M., and Peloponese, J.-M., Jr. (2017). Hijacking of the AP-1 Signaling Pathway during Development of ATL. *Front. Microbiol.* 8, 2686. doi:10.3389/fmicb.2017.02686

Gómez-Biagi, R. F., Jagt, R. B. C., and Nitz, M. (2008). Remarkably Stable Inclusion Complexes with Heptakis-[6-Deoxy-6-(2-Aminoethylsulfanyl)]-β-Cyclodextrin. *Org. Biomol. Chem.* 6 (24), 4622–4626. doi:10.1039/b813999g

Grueninger, D., Treiber, N., Ziegler, M. O. P., Koetter, J. W. A., Schulze, M.-S., and Schulz, G. E. (2008). Designed Protein-Protein Association. *Science* 319 (5860), 206–209. doi:10.1126/science.1150421

Hardwick, J. S., Kuruvilla, F. G., Tong, J. K., Shamji, A. F., and Schreiber, S. L. (1999). Rapamycin-modulated Transcription Defines the Subset of Nutrient-Sensitive Signaling Pathways Directly Controlled by the Tor Proteins. *Proc. Natl. Acad. Sci.* 96 (26), 14866–14870. doi:10.1073/pnas.96.26.14866

Heddi, B., Cheong, V. V., Martadinata, H., and Phan, A. T. (2015). Insights into G-Quadruplex Specific Recognition by the DEAH-Box Helicase RHAU: Solution Structure of a Peptide-Quadruplex Complex. *Proc. Natl. Acad. Sci. USA* 112 (31), 9608–9613. doi:10.1073/pnas.1422605112

Heitmann, L. M., Taylor, A. B., Hart, P. J., and Urbach, A. R. (2006). Sequence-specific Recognition and Cooperative Dimerization of N-Terminal Aromatic Peptides in Aqueous Solution by a Synthetic Host. *J. Am. Chem. Soc.* 128 (38), 12574–12581. doi:10.1021/ja064323s

Hill, Z. B., Martinko, A. J., Nguyen, D. P., and Wells, J. A. (2018). Human Antibody-Based Chemically Induced Dimerizers for Cell Therapeutic Applications. *Nat. Chem. Biol.* 14 (2), 112–117. doi:10.1038/nchembio.2529

Ho, S. N., Biggar, S. R., Spencer, D. M., Schreiber, S. L., and Crabtree, G. R. (1996). Dimeric Ligands Define a Role for Transcriptional Activation Domains in Reinitiation. *Nature* 382 (6594), 822–826. doi:10.1038/382822a0

Hou, C., Li, J., Zhao, L., Zhang, W., Luo, Q., Dong, Z., et al. (2013). Construction of Protein Nanowires through Cucurbit[8]uril-Based Highly Specific Host-Guest Interactions: an Approach to the Assembly of Functional Proteins. *Angew. Chem. Int. Ed.* 52 (21), 5590–5593. doi:10.1002/anie.201300692

Hynes, N. E., and Lane, H. A. (2005). ERBB Receptors and Cancer: the Complexity of Targeted Inhibitors. *Nat. Rev. Cancer* 5 (5), 341–354. doi:10.1038/nrc1609

Junius, F. K., O'Donoghue, S. I., Nilges, M., Weiss, A. S., and King, G. F. (1996). High Resolution NMR Solution Structure of the Leucine Zipper Domain of the C-Jun Homodimer. *J. Biol. Chem.* 271 (23), 13663–13667. doi:10.1074/jbc.271.23.13663

Khan, S. B., and Lee, S.-L. (2021). Supramolecular Chemistry: Host-Guest Molecular Complexes. *Molecules* 26 (13), 3995. doi:10.3390/molecules26133995

Kharenko, O. A., and Ogawa, M. Y. (2004). Metal-induced Folding of a Designed Metalloprotein. *J. Inorg. Biochem.* 98 (11), 1971–1974. doi:10.1016/j.jinorgbio.2004.07.015

Kim, S., Shin, J., Oh, H., Ahn, S., Kim, N., and Heo, W. D. (2020). An Inducible System for *In Vitro* and *In Vivo* Fas Activation Using FKBP-FRB-Rapamycin Complex. *Biochem. Biophysical Res. Commun.* 523 (2), 473–480. doi:10.1016/j.bbrc.2019.12.072

Kitagishi, H., Kashiwa, K., and Kano, K. (2012). Functionalization of a Protein Surface with Per-O-Methylated β-cyclodextrin. *Biopolymers* 97 (1), 11–20. doi:10.1002/bip.21695

Ko, Y. H., Kim, E., Hwang, I., and Kim, K. (2007). Supramolecular Assemblies Built with Host-Stabilized Charge-Transfer Interactions. *Chem. Commun.* (13), 1305–1315. doi:10.1039/b615103e

Kochańczyk, T., Nowakowski, M., Wojewska, D., Kocyła, A., Ejchart, A., Koźmiński, W., et al. (2016). Metal-coupled Folding as the Driving Force for the Extreme Stability of Rad50 Zinc Hook Dimer Assembly. *Sci. Rep.* 6, 36346. doi:10.1038/srep36346

Lecointre, C., Simon, V., Kerneur, C., Allemand, F., Fournet, A., Montarras, I., et al. (2018). Dimerization of the Pragmin Pseudo-kinase Regulates Protein Tyrosine Phosphorylation. *Structure* 26 (4), 545–554. doi:10.1016/j.str.2018.01.017

Leung, I. W.-L., and Lassam, N. (1998). Dimerization via Tandem Leucine Zippers Is Essential for the Activation of the Mitogen-Activated Protein Kinase Kinase Kinase, MLK-3. *J. Biol. Chem.* 273 (49), 32408–32415. doi:10.1074/jbc.273.49.32408

Liang, F.-S., Ho, W. Q., and Crabtree, G. R. (2011). Engineering the ABA Plant Stress Pathway for Regulation of Induced Proximity. *Sci. Signal.* 4 (164), rs2. doi:10.1126/scisignal.2001449

Liang, J., Choi, J., and Clardy, J. (1999). Refined Structure of the FKBP12-Rapamycin-FRB Ternary Complex at 2.2 Å Resolution. *Acta Crystallogr. D Biol. Cryst.* 55 (Pt 4), 736–744. doi:10.1107/s0907444998014747

Liberles, S. D., Diver, S. T., Austin, D. J., and Schreiber, S. L. (1997). Inducible Gene Expression and Protein Translocation Using Nontoxic Ligands Identified by a Mammalian Three-Hybrid Screen. *Proc. Natl. Acad. Sci.* 94 (15), 7825–7830. doi:10.1073/pnas.94.15.7825

Lipps, H. J., and Rhodes, D. (2009). G-quadruplex Structures: *In Vivo* Evidence and Function. *Trends Cel. Biol.* 19 (8), 414–422. doi:10.1016/j.tcb.2009.05.002

Liu, J., Farmer, J. D., Jr., Lane, W. S., Friedman, J., Weissman, I., and Schreiber, S. L. (1991). Calcineurin Is a Common Target of Cyclophilin-Cyclosporin A and FKBP-Fk506 Complexes. *Cell* 66 (4), 807–815. doi:10.1016/0092-8674(91)90124-h

Liu, Y. H., Zhang, Y. M., Yu, H. J., and Liu, Y. (2021). Cucurbituril-Based Biomacromolecular Assemblies. *Angew. Chem. Int. Ed.* 60 (8), 3870–3880. doi:10.1002/anie.202009797

Maizels, N., and Gray, L. T. (2013). The G4 Genome. *Plos Genet.* 9 (4), e1003468. doi:10.1371/journal.pgen.1003468

Mangal, S., Zielich, J., Lambie, E., and Zanin, E. (2018). Rapamycin-induced Protein Dimerization as a Tool for *C. elegans* Research. *Micropubl. Biol.* doi:10.17912/W2BH3H

Marianayagam, N. J., Sunde, M., and Matthews, J. M. (2004). The Power of Two: Protein Dimerization in Biology. *Trends Biochem. Sci.* 29 (11), 618–625. doi:10.1016/j.tibs.2004.09.006

Mason, J. M., and Arndt, K. M. (2004). Coiled Coil Domains: Stability, Specificity, and Biological Implications. *Chembiochem* 5 (2), 170–176. doi:10.1002/cbic.200300781

Masson, E., Ling, X. X., Joseph, R., Kyeremeh-Mensah, L., and Lu, X. Y. (2012). Cucurbituril Chemistry: a Tale of Supramolecular success. *Rsc Adv.* (2), 1213–1247. doi:10.1039/c1ra00768h

Miyamoto, T., DeRose, R., Suarez, A., Ueno, T., Chen, M., Sun, T.-p., et al. (2012). Rapid and Orthogonal Logic Gating with a Gibberellin-Induced Dimerization System. *Nat. Chem. Biol.* 8 (5), 465–470. doi:10.1038/nchembio.922

Mootz, H. D., and Muir, T. W. (2002). Protein Splicing Triggered by a Small Molecule. *J. Am. Chem. Soc.* 124 (31), 9044–9045. doi:10.1021/ja026769o

Nguyen, H. D., Dang, D. T., van Dongen, J. L. J., and Brunsveld, L. (2010). Protein Dimerization Induced by Supramolecular Interactions with Cucurbit[8]uril. *Angew. Chem. Int. Edition* 49 (5), 895–898. doi:10.1002/anie.200904413

Novo, P., García, M. D., Peinador, C., and Pazos, E. (2021). Reversible Control of DNA Binding with Cucurbit[8]uril-Induced Supramolecular 4,4'-Bipyridinium-Peptide Dimers. *Bioconjug. Chem.* 32 (3), 507–511. doi:10.1021/acs.bioconjchem.1c00063

Oshovsky, G. V., Reinhoudt, D. N., and Verboom, W. (2007). Supramolecular Chemistry in Water. *Angew. Chem. Int. Ed.* 46 (14), 2366–2393. doi:10.1002/anie.200602815

Pratt, M. R., Schwartz, E. C., and Muir, T. W. (2007). Small-molecule-mediated rescue of Protein Function by an Inducible Proteolytic Shunt. *Proc. Natl. Acad. Sci.* 104 (27), 11209–11214. doi:10.1073/pnas.0700816104

Radford, R. J., Nguyen, P. C., Ditri, T. B., Figueroa, J. S., and Tezcan, F. A. (2010). Controlled Protein Dimerization through Hybrid Coordination Motifs. *Inorg. Chem.* 49 (9), 4362–4369. doi:10.1021/ic100534y

Rauwald, U., Biedermann, F., Deroo, S., Robinson, C. V., and Scherman, O. A. (2010). Correlating Solution Binding and ESI-MS Stabilities by Incorporating Solvation Effects in a Confined Cucurbit[8]uril System. *J. Phys. Chem. B* 114 (26), 8606–8615. doi:10.1021/jp102933h

Rivera, V. M., Berk, L., and Clackson, T. (2012). Dimerizer-mediated Regulation of Gene Expression. *Cold Spring Harb. Protoc.* 2012 (7), pdb.top070128-770. doi:10.1101/pdb.top070128

Rivera, V. M., Clackson, T., Natesan, S., Pollock, R., Amara, J. F., Keenan, T., et al. (1996). A Humanized System for Pharmacologic Control of Gene Expression. *Nat. Med.* 2 (9), 1028–1032. doi:10.1038/nm0996-1028

Schreiber, S. L. (2021). The Rise of Molecular Glues. *Cell* 184 (1), 3–9. doi:10.1016/j.cell.2020.12.020

Shahi, P., Park, D., Pond, A. C., Seethammagari, M., Chiou, S.-H., Cho, K., et al. (2012). Activation of Wnt Signaling by Chemically Induced Dimerization of LRP5 Disrupts Cellular Homeostasis. *PLoS One* 7 (1), e30814. doi:10.1371/journal.pone.0030814

Sinclair, J. C. (2012). Proteins on Parade. *Nat. Chem.* 4 (5), 346–347. doi:10.1038/nchem.1337

Song, W. J., Sontz, P. A., Ambroggio, X. I., and Tezcan, F. A. (2014). Metals in Protein-Protein Interfaces. *Annu. Rev. Biophys.* 43, 409–431. doi:10.1146/annurev-biophys-051013-023038

Spencer, D. M., Belshaw, P. J., Chen, L., Ho, S. N., Randazzo, F., Crabtree, G. R., et al. (1996). Functional Analysis of Fas Signaling *In Vivo* Using Synthetic Inducers of Dimerization. *Curr. Biol.* 6 (7), 839–847. doi:10.1016/s0960-9822(02)00607-3

Spencer, D. M., Wandless, T. J., Schreiber, S. L., and Crabtree, G. R. (1993). Controlling Signal Transduction with Synthetic Ligands. *Science* 262 (5136), 1019–1024. doi:10.1126/science.7694365

Stankunas, K., Bayle, J. H., Gestwicki, J. E., Lin, Y.-M., Wandless, T. J., and Crabtree, G. R. (2003). Conditional Protein Alleles Using Knockin Mice and a Chemical Inducer of Dimerization. *Mol. Cel.* 12 (6), 1615–1624. doi:10.1016/s1097-2765(03)00491-x

Truong, T. T. T., Cao, C., and Dang, D. T. (2020). Parallel G-Quadruplex-Mediated Protein Dimerization and Activation. *RSC Adv.* 10, 29957–29960. doi:10.1039/d0ra06173e

Ueno, M., Murakami, A., Makino, K., and Morii, T. (1993). Arranging Quaternary Structure of Peptides by Cyclodextrin Guest Inclusion Complex - Sequence-specific Dna-Binding by A Peptide Dimer with Artificial Dimerization Module. *J. Am. Chem. Soc.* (115), 12575–12576. doi:10.1021/ja00079a043

Uhlenheuer, D. A., Milroy, L.-G., Neirynck, P., and Brunsveld, L. (2011a). Strong Supramolecular Control over Protein Self-Assembly Using a Polyamine Decorated Beta-Cyclodextrin as Synthetic Recognition Element. *J. Mater. Chem.* (21), 18919–18922. doi:10.1039/c1jm12736e

Uhlenheuer, D. A., Petkau, K., and Brunsveld, L. (2010). Combining Supramolecular Chemistry with Biology. *Chem. Soc. Rev.* 39 (8), 2817–2826. doi:10.1039/b820283b

Uhlenheuer, D. A., Wasserberg, D., Nguyen, H., Zhang, L., Blum, C., Subramaniam, V., et al. (2009). Modulation of Protein Dimerization by a Supramolecular Host-Guest System. *Chem. Eur. J.* 15 (35), 8779–8790. doi:10.1002/chem.200900462

Uhlenheuer, D. A., Young, J. F., Nguyen, H. D., Scheepstra, M., and Brunsveld, L. (2011b). Cucurbit[8]uril Induced Heterodimerization of Methylviologen and Naphthalene Functionalized Proteins. *Chem. Commun.* 47 (24), 6798–6800. doi:10.1039/c1cc11197c

Urbach, A. R., and Ramalingam, V. (2011). Molecular Recognition of Amino Acids, Peptides, and Proteins by Cucurbit[n]uril Receptors. *Isr. J. Chem.* 51 (51), 664–678. doi:10.1002/ijch.201100035

Vrana, K. E., Walker, S. J., Rucker, P., and Liu, X. (1994). A Carboxyl Terminal Leucine Zipper Is Required for Tyrosine Hydroxylase Tetramer Formation. *J. Neurochem.* 63 (6), 2014–2020. doi:10.1046/j.1471-4159.1994. 63062014.x

Wayne Schultz, L., and Clardy, J. (1998). Chemical Inducers of Dimerization: the Atomic Structure of FKBP12-Fk1012a-FKBP12. *Bioorg. Med. Chem. Lett.* 8 (1), 1–6. doi:10.1016/s0960-894x(97) 10195-0

Xu, M.-Q., and Evans, T. C., Jr. (2005). Recent Advances in Protein Splicing: Manipulating Proteins *In Vitro* and *In Vivo*. *Curr. Opin. Biotechnol.* 16 (4), 440–446. doi:10.1016/j.copbio.2005.06.012

Yang, Z. W., and Breslow, R. (1997). Very strong Binding of Lithocholic Acid to Beta-Cyclodextrin. *Tetrahedron Lett.* (38), 6171–6172. doi:10.1016/S0040-4039(97)01427-5

Zhang, L., Lookene, A., Wu, G., and Olivecrona, G. (2005). Calcium Triggers Folding of Lipoprotein Lipase into Active Dimers. *J. Biol. Chem.* 280 (52), 42580–42591. doi:10.1074/jbc.M507252200

Zhang, L., Wu, Y., and Brunsveld, L. (2007). A Synthetic Supramolecular Construct Modulating Protein Assembly in Cells. *Angew. Chem. Int. Ed.* 46 (11), 1798–1802. doi:10.1002/anie.200604222

Zhang, Y. M., Liu, J. H., Yu, Q., Wen, X., and Liu, Y. (2019). Targeted Polypeptide-Microtubule Aggregation with Cucurbit[8]uril for Enhanced Cell Apoptosis. *Angew. Chem. Int. Ed.* 58 (31), 10553–10557. doi:10.1002/ anie.201903243

Zhao, H., Datta, S. A. K., Kim, S. H., To, S. C., Chaturvedi, S. K., Rein, A., et al. (2019). Nucleic Acid-Induced Dimerization of HIV-1 Gag Protein. *J. Biol. Chem.* 294 (45), 16480–16493. doi:10.1074/jbc.RA119.010580

Advantages of publishing in Frontiers

OPEN ACCESS
Articles are free to read
for greatest visibility
and readership

FAST PUBLICATION
Around 90 days
from submission
to decision

HIGH QUALITY PEER-REVIEW
Rigorous, collaborative,
and constructive
peer-review

TRANSPARENT PEER-REVIEW
Editors and reviewers
acknowledged by name
on published articles

Frontiers
Avenue du Tribunal-Fédéral 34
1005 Lausanne | Switzerland

Visit us: www.frontiersin.org
Contact us: frontiersin.org/about/contact

**REPRODUCIBILITY OF
RESEARCH**
Support open data
and methods to enhance
research reproducibility

DIGITAL PUBLISHING
Articles designed
for optimal readership
across devices

FOLLOW US
@frontiersin

IMPACT METRICS
Advanced article metrics
track visibility across
digital media

EXTENSIVE PROMOTION
Marketing
and promotion
of impactful research

LOOP RESEARCH NETWORK
Our network
increases your
article's readership